City Research Online

City, University of London Institutional Repository

AdS$_3$/CFT$_2$ from integrability and ML applications in theoretical physics

Suvajit Majumder[*]

Department of Mathematics, City University of London, EC1V 0HB, UK

September, 2023

Thesis submitted in partial fulfillment of
the requirements for a doctorate of philosophy

[*]E-mail address: `majumder.suvajit95@gmail.com`

Declaration

I, Suvajit Majumder confirm that the work presented in this thesis is my own. Where information has been derived from other sources, I confirm that this has been indicated in the thesis.

Acknowledgements

Abstract

This thesis explores AdS_3/CFT_2 dualities in string theory using techniques from integrability, and machine-learning applications in Lie algebras and in quantum integrability. Introductory chapters on string theory and holography, AdS_3/CFT_2, and machine-learning are followed by 3 chapters, each presenting a different work of original research: protected spectrum using Algebraic Bethe ansatz in AdS_3 backgrounds, supervised learning tensor-products of Lie algebra representations, and searching for quantum integrable models using neural networks. We conclude with a discussion of ongoing and unpublished works.

Contents

1   String theory and integrable holography

1.1   String theory and AdS/CFT

String theory has provided us with a lot of tools to understand physics beyond standard model and classical gravity. A major breakthrough in this regard came with the AdS/CFT correspondence, which provided us a window to probe non-perturbative regimes of a diverse array of QFTs by mapping them to weakly-coupled dual theories. Integrability has been another highly useful theme in theoretical physics, that has enabled very powerful non-perturbative computations within classical and quantum systems. In the context of string theory, integrable structures were first discovered in the 4 dimensional $\mathcal{N} = 4$ super Yang-Mills (SYM) [1], which appears as gauge theory dual to strings on $\mathrm{AdS}_5 \times \mathrm{S}^5$. While investigating the one-loop spectrum of the dilatation operator, the authors realised that the problem could be mapped to a spin chain Hamiltonian, and solved using Bethe ansatz. Later, string theory in $\mathrm{AdS}_5 \times \mathrm{S}^5$ background has been shown to be classically integrable [2] by exhibiting the zero curvature representation of the string equations of motion [3]. Classical integrability of the string action allowed the construction of soliton solutions to the equations of motion, known as "giant magnons" (see [4]). They were shown to satisfy the same dispersion relation as the spin chain magnons in the dual gauge theory. An all-loop integrable S-matrix for these magnons in the *decompactification limit* of the string world-sheet were obtained in [5]. This matched the S-matrix proposal from the gauge theory side, made earlier in [6, 7, 8]. It is assumed that this integrability survives quantisation, at least in certain corners of the moduli space

(e.g. planar limit of the dual CFT). Hence, the various tools developed in the context of integrable spin chains, such as the Bethe ansatz, finite-gap equations and the quantum spectral curve can be applied to string theory. This allows for huge improvement in computability as it produces results *exact* to all orders of the string coupling α'. Using the AdS/CFT correspondence this translates to computation exact to all orders in 't Hooft coupling λ of the dual CFT.

Besides AdS$_5$, integrable holography has been explored extensively for AdS$_4$, AdS$_3$ backgrounds as well. In AdS$_4$ case, the dual CFT is ABJM theory, and the integrability picture follows closely with AdS$_5$(see [9]). It is beyond the scope of this thesis. We shall focus on AdS$_3$ integrability in the following sections. Classical integrability of the superstring action in AdS$_3$/CFT$_2$ backgrounds supported by pure Ramond-Ramond (RR) flux was confirmed by working out the appropriate coset descriptions in [10, 11]. [11] further proved semi-classical integrability in these backgrounds by constructing the relevant finite-gap equations. The Lax representations were obtained for more general mixed-flux backgrounds with both RR and Neveu-Schwarz-Neveu-Schwarz (NSNS) flux fields in [12], and the corresponding finite-gap equations were worked out in [13]. Progress towards quantum integrability was achieved with the construction of the all-loop S-matrices, thermodynamic Bethe ansatz (TBA) and quantum spectral curve. Relevant literature and in-depth developments of these backgrounds will be discussed in the next section.

In this section, we shall review the fundamentals of superstring theory in 10-D space-time and how the AdS/CFT conjecture arises from D-brane setups in this background. Next, we outline the basics of classical and quantum integrability that are relevant for our discussions. Following that, we write down the non-linear sigma model action for the superstring, impose the lightcone gauge and κ symmetry, and explore the Lax reformulation of the classical equations of motion. We discuss the spectral curve and how classical string configurations are realised as branch-cut solutions in the spectral plane. Then we write down the quantum all-loop worldsheet S-matrices in AdS$_5 \times$ S^5 in terms of suitable reparameterisation of the momentum of the scatterers. This will prepare us for the AdS$_3 \times$ S$^3 \times$ M^4 backgrounds in the following section.

1.1.1 Superstring theory in 10 dimensions

String theory involves the study of 1-dimensional strings as the fundamental dynamical objects modelling small-scale physics, instead of 0-dimensional point particles in QFTs. As such we have world-sheets instead of worldlines for the fundamental objects, which are parameterised by two real parameters (τ, σ), or one complex parameter $z = \tau + i\sigma$ which is referred to as the worldsheet coordinates. The space-time (say $\mathcal{M}$) coordinates emerges as fields of the world-sheet (say Σ) coordinates

$$X^i(\tau, \sigma): \quad \Sigma \to \mathcal{M}, \quad i = 1, \dots D \tag{1.1}$$

where D denotes the dimensionality of the spacetime $\mathcal{M}$. There are two parameters relevant to the study of fundamental strings: string tension T ($\sim \frac{1}{\alpha'}$), and string coupling g_s. The former characterises the energy quantum of vibrational modes of excitations along the string, while the latter denotes the strength of string-string interactions. Perturbative expansion in g_s corresponds to a genus expansion of string worldsheet topologies. For a fixed topology, one can further expand string theory amplitudes/correlators in terms of expansion in inverse string tension/ Regge slope α', which corresponds to a momentum/derivative expansion in the low-energy effective action.

Worldsheet conformal invariance and anomaly cancellation leads to strict constraints on the spacetime dimensions that the strings can live in, alongwith conditions on the strings themselves. If we assume supersymmetry, which is a symmetry between particles of integer spins (bosons) and half-integer spins (fermions), there are 5 consistent theories: type I, type IIA, type IIB, heterotic SO(32), and heterotic $E_8 \times E_8$ all living in $D = 10$ spacetime dimensions. While type IIA, IIB theories only have closed oriented strings, type I has both closed and open unoriented strings, and heterotic theories include a hybrid of closed bosonic and superstrings. A web of dualities connect these different theories to each other. Furthermore, they are realised as special limits in corners of the moduli space of M-theory which lives in 11 dimensions. We shall focus our discussion on type IIB string theory since that is the one relevant for our future sections.

In the Green-Schwarz (GS) formalism wherein spacetime supersymmetry is manifest, type IIB string theory includes two superspace fermion fields $\theta^1(\tau, \sigma), \theta^2(\tau, \sigma)$ alongwith the bosonic fields $X^m(\tau, \sigma)$ mentioned earlier. These fermion fields are Majorana-Weyl spinors of the same chirality. The low-energy (massless) spectrum of states include the symmetric 2-tensor graviton G_{MN}, antisymmetric 2-tensor Kalb-Ramond field B_{MN}, and a scalar dilaton field Φ. The expectation value of the scalar field dynamically fixed the string coupling g_s. Furthermore, we have higher form Ramond-Ramond (RR) flux-fields of odd, even dimensions for type IIB, IIA respectively. In the low energy limit $\alpha' \to 0$, type II superstring theories give rise to supergravity with the above fields as the higher mass modes are suppressed.

We can include open strings in type IIB string theory by introducing extended objects known as Dirichlet branes. The open string end-points lie on the Dirichlet Dp branes, with p denoting the space dimensionality of the brane. The Dp branes are themselves dynamical objects in superstring theory, being solutions to supergravity equations. They couple to the RR fields mentioned above. Since open strings stretch between Dp branes, the distance between them affects the spectrum of open string states. The mass squared of the open string sectors is proportional to the square of the brane separation. As a result, when two Dp branes come together one ends up with many more massless non-abelian open strings. The gauge symmetry sees an enhancement from U(1)×U(1) to U(2) as the branes merge. More generally, stacking a bunch of N Dp branes on top of one another leads to an enhancement of gauge symmetry from $U(1)^N$ to U(N).

1.1.2 AdS/CFT correspondence

AdS/CFT or the gauge-gravity correspondence has been a cornerstone in the development of theoretical physics for over two decades. It was first conjectured by Maldacena in [14] to arise at the low energy limit of type IIB string theory in ten dimensions. His original proposal stated that the theory of closed strings propagating in the background of $\text{AdS}_5 \times \text{S}^5$, and the theory of $\mathcal{N} = 4$ SYM in 3+1 dimensional flat spacetime are dual to each other. Here, *duality* refers to different descriptions of the same physical system. In the same work, similar such dualities were conjectured for other AdS_{d+1} string theories as well. We will focus on the 3D-2D version of this duality, where the spacetime background is of the type $\text{AdS}_3 \times \text{S}^3 \times M^4$ with $M^4 = \text{T}^4, \text{S}^3 \times \text{S}^1$. The specific choice of the compact manifold M^4 ensures that maximal supersymmetry is preserved (in $\text{AdS}_3 \times M^7$ the maximum number of supercharges is 16). The central idea behind all such constructions rely on engineering a specific brane setup.

Lets briefly review the setup for $d = 4$ before heading to $d = 2$ which is relevant

for this work. There are different equivalent descriptions to account for the Dp branes: via the open or closed string channels. In case of AdS$_5$/CFT$_4$, the brane construction involves a stack of N D3 branes at the origin of the 10D flat spacetime. The world-volume theory of open strings ending on these D3 branes is $\mathcal{N} = 4$ SYM with gauge group SU(N). At low energies, these open strings decouple from the closed strings propagating in the background. Another way to account for the D3-branes is to consider their back-reaction on the spacetime in which the closed strings propagate. This is the closed-string channel. The geometry near the D3 branes gets drastically modified from the flat background to a black p-brane with singularity at the origin. The supergravity metric is given by

$$ds^2_{p-brane} = \frac{1}{\sqrt{f(r)}}(-dt^2 + \sum_{i=1}^{3} dx_i^2) + \sqrt{f(r)}(dr^2 + r^2 d\Omega_5^2)\,, \quad f(r) = 1 + \frac{R^4}{r^4}\,, \quad (1.2)$$

where $d\Omega_5^2$ is the metric on S^5. The background further supports a constant 5-form RR flux F_5 such that

$$\int_{S^5} F_5 = N \tag{1.3}$$

In the low energy limit, the closed strings far away from the origin (where the D3 branes were located) become decoupled from the ones near the horizon. Thus, we are lead to the equivalence conjecture:

$$\text{type IIB strings in AdS}_5 \times S_5 \quad \equiv \quad \mathcal{N} = 4 \text{ SYM in 4 dimensions} \tag{1.4}$$

This is a strong-weak duality which means that the strongly coupled regime on one side is mapped to weakly coupled regime on the other side and vice-versa. This is reflected in the mapping of the coupling parameters on both sides: Yang-Mills coupling (g_{YM}), and number of colours (N) respectively on the gauge theory side, to string coupling (g_s), and string tension (α') respectively, on the gravity side

$$g_s = \frac{g_{YM}^2}{4\pi}\,, \qquad \frac{R^4}{\alpha'^2} = g_{YM}^2 N, \tag{1.5}$$

where R is the radius of curvature of the AdS$_5$(see equation (1.2). For the supergravity description to make sense on the string theory side, R needs to be much bigger than the string length $\sqrt{\alpha'}$. According to the above map, this corresponds to the limit where the 't Hooft coupling $g_{YM}^2 N$ is large. So the dual CFT is strongly coupled when the string theory simplifies. Conversely for weakly coupled regime in the CFT $g_{YM}^2 N << 1$, the gravity side becomes very *stringy*. This lack of control on at least one side of the duality makes it very difficult to prove this duality, or even check for its validity. There is a limit, however, in which one can check for its validity- the *planar* limit. It is a double scaling limit, where the Yang-Mills coupling is vanishing, and number of colour charges approaches infinity, while the 't Hooft coupling λ is kept finite

$$g_{YM} \to 0\,, \quad N \to \infty\,, \quad \lambda \equiv g_{YM}^2 N = \frac{R^4}{\alpha'^2} = \text{fixed} \tag{1.6}$$

In this large N regime, the dominant Feynman diagrams contributing to correlation functions in the CFT are planar, i.e. they can be drawn in 2D without crossing. The non-planar diagram contributions are suppressed as $N^{-\chi}$, where χ is the genus of the Riemann surface corresponding to the diagram. By the above dictionary in (1.5), we can

see that the large N expansion of the gauge theory is mapped to small g_s expansion of the string theory

$$\frac{1}{N} = \left(\frac{4\pi}{\lambda}\right) g_s \tag{1.7}$$

The improvement in computational ability in this regime happens because of the emergence of integrability. This enhancement of symmetries has been exploited to compute (and match) all-loop exact quantities on both sides of the duality, e.g. anomalous dimension of single-trace operators.

1.1.3 AdS$_3$/CFT$_2$

An analogous story to the above AdS$_5$ case, also holds true in three dimensions [14]. However, there are two consistent choices of supergravity backgrounds in AdS$_3$ preserving maximal supersymmetry (SUSY), distinguished by their compact seven dimensional complement M_7 (target spacetime being the Cartesian product AdS$_3 \times M_7$). The first one is AdS$_3 \times$ S$^3 \times$ T^4 and it arises from the near horizon limit of a system of N_1 D1 branes and N_5 D5 branes in type IIB string theory. The D5 branes are wrapped around the T^4, and has one remaining spatial direction which is non-compact. The D1 branes are extended along the non-compact direction of the D5 branes. The orientation of the branes is shown in table 1.

	0	1	2	3	4	5	6	7	8	9
D1	x	x								
D5	x	x	x	x	x	x				

Table 1: D1-D5 system of branes. The numbers at the top label the spatial directions, and the crosses indicate the coordinates spanned by the brane.

The AdS/CFT conjecture maps the closed string theory in this background to a dual CFT with small $\mathcal{N} = (4, 4)$ supersymmetry. As in the 5d case, the duality arises from the decoupling of the near horizon degrees of freedom from the asymptotic bulk. The radius of the AdS$_3$ and S^3 are equal and is given in terms of the string coupling, string tension, the number of D1,D5 branes (N_1, N_5 resp.), and the volume of T^4 V_{T^4} as follows

$$R = \frac{g_s \alpha' \sqrt{N_1 N_5}}{\sqrt{v}}, \tag{1.8}$$

where $v = \frac{V_{\mathrm{T}^4}}{(2\pi)^4 \alpha'^2}$ is a parameter in the bulk metric, proportional to the volume of T^4. The resultant supergravity metric is

$$ds^2 = \frac{1}{\sqrt{f_1 f_5}}(-dt^2 + dx_1^2) + \sqrt{f_1 f_5}(dr^2 + r^2 d\Omega_3^2) + \sqrt{\frac{f_1}{f_5}}\sum_{i=6}^{9} dx_i^2, \tag{1.9}$$

where

$$f_1(r) = 1 + \frac{g_s \alpha' N_1}{v r^2}, \quad f_5(r) = 1 + \frac{g_s \alpha' N_5}{r^2}. \tag{1.10}$$

This has a non-trivial dilaton Φ as well as a 3-form RR field $F^{(3)}$

$$\Phi(r) = \frac{1}{2} \log \frac{f_1(r)}{f_5(r)}, \quad F^{(3)} = -df_1^{-1} \wedge dt \wedge dx_1 + 2\alpha' N_5 \Omega_{\mathrm{S}^3} \tag{1.11}$$

8

More generally, one can construct superstring backgrounds supported by a 3-form NSNS flux alongwith the above mentioned 3-form RR flux. These supergravity backgrounds are generated in the near-horizon limit of NS5-branes and fundamental strings, alongwith the D1-D5 brane system. Overall, we have a one parameter family of mixed flux backgrounds with non-trivial NSNS and RR fluxes

$$H^{(3)} = 2qR^2(\text{Vol}(\text{AdS}_3) + \text{Vol}(S^3)), \quad F^{(3)} = \frac{\tilde{q}}{q}H^{(3)}, \quad q^2 + \tilde{q}^2 = 1, \tag{1.12}$$

with $\text{Vol}(\text{AdS}_3), \text{Vol}(S^3)$ as the volume forms on AdS_3, S^3 respectively.

The second maximally supersymmetric background is $\text{AdS}_3 \times S^3 \times S^3 \times S^1$ and it arises from a D1-D5-D5′ system in type IIB. As in the previous setup, the first set of D5 branes share a common spatial direction with the D1 branes. The second stack of D5 branes, labelled D5′, share one spacelike coordinate with the common direction of D1, and D5, while the remaining four spacelike directions are transverse to the ones occupied by the first set of D5 branes. The configuration of the branes along the standard spatial coordinates are listed in table 2

	0	1	2	3	4	5	6	7	8	9
D1	x	x								
D5	x	x	x	x	x	x				
D5′	x	x					x	x	x	x

Table 2: D1-D5-D5′ system of branes. The numbers at the top label the spatial directions, and the crosses indicate the coordinates spanned by the brane.

The resultant geometry is $\text{AdS}_3 \times S^3 \times S^3 \times \mathbb{R}$

$$ds^2 = ds^2_{\text{AdS}_3} + ds^2_{S^3_+} + ds^2_{S^3_-} + dw^2, \tag{1.13}$$

where $S^3_\pm$ are used to distinguish the two 3-spheres. One should further compactify $\mathbb{R} \to S^1$ to get the dual CFT. The radii of the two 3-spheres $R_{S^3_+}, R_{S^3_-}$ are related to the AdS_3 radius R_{AdS_3} as follows

$$\frac{1}{R^2_{\text{AdS}_3}} = \frac{1}{R^2_{S^3_+}} + \frac{1}{R^2_{S^3_-}}. \tag{1.14}$$

Due to this relation, we can write a one-parameter family of such backgrounds parameterised by α(or φ) as follows

$$\alpha \equiv \cos^2\varphi = \frac{R^2_{\text{AdS}_3}}{R^2_{S^3_+}}, \qquad 1 - \alpha \equiv \sin^2\varphi = \frac{R^2_{\text{AdS}_3}}{R^2_{S^3_-}}, \qquad 0 < \alpha < 1. \tag{1.15}$$

The above background has a non-trivial RR 3-form flux. Analogous to the T^4 case, we can generalise this brane system to end up with near-horizon geometries with both a 3-form NSNS and a 3-form RR flux field. One ends up with a 1-parameter family of backgrounds with fluxes

$$H^{(3)} = 2qR^2(\text{Vol}(\text{AdS}_3) + \frac{1}{\cos^2\varphi}\text{Vol}(S^3_+) + \frac{1}{\sin^2\varphi}\text{Vol}(S^3_-)), \quad F^{(3)} = \frac{\tilde{q}}{q}H^{(3)}, \quad q^2 + \tilde{q}^2 = 1, \tag{1.16}$$

where $\mathrm{Vol}(\mathrm{AdS}_3), \mathrm{Vol}(\mathrm{S}_+^3), \mathrm{Vol}(\mathrm{S}_-^3)$ are the volume forms on AdS_3, $\mathrm{S}_+^3, \mathrm{S}_-^3$ respectively. The AdS/CFT conjecture maps the closed string theory in this background to a dual CFT with large $\mathcal{N} = (4, 4)$ supersymmetry.

The dual CFT_2 description is a much harder problem to solve in the above AdS_3 backgrounds than in $\mathrm{AdS}_5 \times \mathrm{S}^5$. Firstly, the low energy effective gauge theory for the open strings in not conformal. The dual CFT_2 is supposed to emerge as an infra-red fixed point of the renormalisation group flow from the gauge theory describing the open string dynamics. In the case of $\mathrm{AdS}_3 \times \mathrm{S}^3 \times \mathrm{S}^3 \times \mathrm{S}^1$ one has the further complication of dealing with compactification of $\mathbb{R} \to \mathrm{S}^1$. First attempts to find this dual theory was made in [15].

The current algebra of the CFT dual to strings on $\mathrm{AdS}_3 \times M^7$ for $M^7 = \mathrm{S}^3 \times \mathrm{T}^4$, and $\mathrm{S}^3 \times \mathrm{S}^3 \times \mathrm{S}^1$ respectively, is (small, large respectively) $\mathcal{N} = (4, 4)$ SUSY with global symmetry as $\mathrm{psu}(1, 1|2)^2$ and $\mathrm{d}(2, 1; \alpha)^2$. Note the α here is the same parameter as defined earlier in (1.15). It was argued in [14] that the dual CFT should arise in the infra-red limit of renormalisation group flow along the Higgs branch (i.e. flow directions of the superconformal field theory (SCFT) moduli space along which the hypermultiplets of the free theory attain vacuum expectation value) of the above gauge theories. Another approach to study the dual CFT_2 comes from treating the D1 branes as instantons on the D5 branes, and it has been argued that the integrable spin-chain picture arises in the limit of vanishing instanton size. $\mathrm{AdS}_3/\mathrm{CFT}_2$ has another major difference with $\mathrm{AdS}_5/\mathrm{CFT}_4$: the presence of a large moduli space. In $\mathrm{AdS}_3 \times \mathrm{S}^3 \times \mathrm{T}^4$, there is a 20 dimensional moduli space, corresponding to vacuum expectation values for the massless scalars of the theory. Of these, 16 parameterise the T^4 degrees of freedom. Integrability only accesses the zero-winding, zero-momentum sector along the T^4. As such, these moduli do not affect the spectrum in the integrable limit, while the remaining 4 do [16]. The duality maps these 4d spaces on the two sides. Recently, there has been substantial development in understanding this duality at a specific point of this enormous moduli space: called the symmetric product orbifold point. The correspondence is between: string theory on $\mathrm{AdS}_3 \times \mathrm{S}^3 \times \mathrm{T}^4$ with 1 unit of NSNS flux, and symmetric orbifold CFT $\mathrm{Sym}^N(\mathrm{T}_4)$ on N copies of T^4, where $N = N_1 N_5$(for N_1, N_5 number of D1, D5 branes respectively). More generally it is believed that for a generic point on the moduli space, the dual CFT lies on the same conformal manifold as the symmetric product orbifold $\mathrm{Sym}^N(T_4)$. It is unclear how to identify points in the moduli space on both sides of the duality with each other and how to find the planar limit (and hence integrability) amongst the degrees of freedom of $\mathrm{Sym}^N(T_4)$.

1.2 Integrability

In this section, we shall review the basics of classical and quantum integrability that are relevant for our discussion in the context of string integrability in the later parts of the section, as well as integrable spin chains in later sections.

1.2.1 Classical integrability

Here we will discuss the technology of integrability in classical mechanics and field theories. A thorough review of these topics can be found in [17]. This will be useful when discussing classical integrability of the GS superstring later in this section.

A Hamiltonian dynamical system with phase space coordinates (q_μ, p_μ), $\mu = 1 \dots D$,

is said to be (Liouville) integrable if it has D independent integrals of motion $F_1, \ldots F_D$ in involution, i.e. they mutually Poisson commute $\{F_\mu, F_\nu\} = 0 \, \forall \, \mu \neq \nu$. In such systems, one can do a canonical change of coordinates to the action-angle pairs (ψ_μ, F_μ), $\mu = 1 \ldots D$, such that the equations of motion reads

$$\frac{d\psi_\mu}{dt} = \text{const.}, \quad \frac{dF_\mu}{dt} = 0 \tag{1.17}$$

Integrating the above equations gives the time-evolution trajectories in the phase space. This generalises to (1+1)-dimensional field theories via the Lax formalism. We call a classical field theory integrable if the equations of motion can be reformulated in terms of some pair of functions $L(\sigma, \tau, z), M(\sigma, \tau, z)$, as a one parameter family of equations

$$\partial_\tau L(\sigma, \tau, z) - \partial_\sigma M(\sigma, \tau, z) + [L(\sigma, \tau, z), M(\sigma, \tau, z)] = 0, \quad \forall \, z \in \mathbb{C}, \tag{1.18}$$

where the Lie bracket $[A, B]$ is defined as the commutator of A, B

$$[A, B] = A \circ B - B \circ A. \tag{1.19}$$

We further require the following condition in order to have the conserved charges as mutually Poisson commuting

$$\{L_1(\sigma, \tau, u), L_2(\sigma', \tau, u')\} = [L_1(\sigma, \tau, u) + L_2(\sigma', \tau, u'), r_{12}(u - u')]\delta(\sigma - \sigma') \tag{1.20}$$

where $L_1 = L \otimes \mathbb{I}$ and $L_2 = \mathbb{I} \otimes L$ and $r_{12} \in \mathfrak{g} \otimes \mathfrak{g}$. The charges can be constructed from the monodromy matrix, defined as the path ordered exponential of the Lax-operator $L(\sigma, \tau, z)$

$$T(b, a; z) = \overleftarrow{\text{Pexp}} \left(\int_a^b d\sigma L(\sigma, \tau, z) \right) \tag{1.21}$$

Assuming periodic boundary conditions along $\sigma \in (0, 2\pi)$ direction, we get the following conservation law for $T(2\pi, 0; z)$ from its time evolution equation

$$\partial_\tau T(2\pi, 0; z) = [M(0, \tau, z), T(2\pi, 0; z)] \Rightarrow \partial_\tau \text{Tr} \, T(2\pi, 0; z)^n = 0 \, \forall \, n \in \mathbb{N}, \, z \in \mathbb{C}. \tag{1.22}$$

The local charges in involution can be obtained by expanding trace of the monodromy matrix near generic point in the $z-$plane, commonly $z = 0$

$$\text{Tr} \, T(2\pi, 0; z) = \sum_{i=0}^\infty Q_i z^i, \quad \partial_\tau Q_i = 0, \, \forall \, i \tag{1.23}$$

1.2.2 Quantum integrability: spin chains and field theories

Next, lets look at how the above discussion can be extended to a quantum picture. For finite dimensional quantum mechanics, the natural setting for integrable systems are spin chains. A good reference on this topic is [18].

The Hilbert space of the spin chain is a L-fold tensor product $\mathbb{V} = V_1 \otimes \ldots \otimes V_L$ of d-dimensional vector spaces $V_i \sim V = \mathbb{C}^d$. The Hamiltonian H of a spin chain with nearest-neighbour interaction is a sum of two-site Hamiltonians $H_{i,i+1}$:

$$H = \sum_{i=1}^L H_{i,i+1}, \tag{1.24}$$

where we assume periodic boundary conditions : $H_{L,L+1} \equiv H_{L,1}$. The chrestomathic example of the integrable spin-chain is spin-1/2 XYZ model :

$$H = \sum_{i=1}^{L} \sum_{\alpha} J^{\alpha} S_i^{\alpha} S_{i+1}^{\alpha}, \tag{1.25}$$

where $\alpha = \{x, y, z\}$ and S_i^{α} are Pauli matrices acting in the two-dimensional space $V_i = \mathbb{C}^2$ of i-th site. In particular case when $J^x = J^y$ it reproduces XXZ model, while in the case of three equal coupling constants $J^x = J^y = J^z = J$ the Hamiltonian reduces to the XXX spin chain. These famous magnet models are just a few examples of integrable spin chains and now we turn to the general construction.

The central element for the whole construction and proof of quantum integrability is the R-matrix operator $R_{ij}(u)$ which acts in the tensor product $V_i \otimes V_j$ of two spin sites [1] and satisfies the Yang-Baxter equation:

$$R_{ij}(u-v)R_{ik}(u)R_{jk}(v) = R_{jk}(v)R_{ik}(u)R_{ij}(u-v) \tag{1.26}$$

where the operators on the left and right sides act in the tensor product $V_i \otimes V_j \otimes V_k$. The R-matrix is assumed to be an analytic function of the spectral parameter u. Further, in order to guarantee locality of the interaction in (1.24), it must reduce to the permutation operator P_{ij} when evaluated at $u = 0$, i.e.

$$R_{ij}(0) = P_{ij}. \tag{1.27}$$

This condition will be referred to as *regularity* in the following sections. We next turn to defining the monodromy matrix $\mathcal{T}_a(u)$. This matrix, denoted by $\mathcal{T}_a(u) \in \text{End}(V_a \otimes \prod_{i=1}^{L} \otimes_i V_i) \times \mathbb{C}$, acts on the spin chain plus an auxiliary spin site labeled by a with Hilbert space as $V_a \sim \mathbb{C}^d$. It is defined as a product of R-matrices $R_{a,i}(u)$ acting on the auxiliary site and one of the spin chain sites and is given by

$$\mathcal{T}_a(u) = R_{a,L}(u)R_{a,L-1}(u)\ldots R_{a,1}(u). \tag{1.28}$$

The transfer matrix $T(u) \in \text{End}(\prod_{i=1}^{L} \otimes_i V_i) \times \mathbb{C}$ is obtained by taking a trace over the auxiliary vector space V_a :

$$T(u) = \text{tr}_a(\mathcal{T}_a(u)). \tag{1.29}$$

From the Yang-Baxter equation one can derive the following $R\mathcal{T}\mathcal{T}$ relation constraining monodromy matrix entries

$$R_{12}(u-v)\mathcal{T}_1(u)\mathcal{T}_2(v) = \mathcal{T}_2(v)\mathcal{T}_1(u)R_{12}(u-v). \tag{1.30}$$

This condition can be used to prove that the transfer matrices commute at different values of the momenta

$$[T(u), T(v)] = 0. \tag{1.31}$$

---

[1] In general, the R-matrix is an analytic function of two complex arguments u, v, which can be viewed as momenta of two particles at the two sites. Here, we shall exclusively focus our analysis to a restricted class of R-matrices of *difference form* $R(u, v) = R(u - v)$ depending only on a single complex argument $w = u - v$.

The above condition implies that the transfer matrix $T(u)$ encodes all the commuting charges $\mathbb{Q}_i$ as series-expansion in u :

$$\log T(u) = \sum_{n=0}^{\infty} \mathbb{Q}_{n+1} \frac{u^n}{n!} \, . \tag{1.32}$$

Hence we have [2]

$$\mathbb{Q}_{n+1} = \frac{d^n}{du^n} \log T(u)|_{u=0} = \frac{d^{n-1}}{du^{n-1}} \left(T^{-1}(u) \frac{d}{du} T(u) \right) \Bigg|_{u=0} . \tag{1.33}$$

The Hamiltonian density $H_{i,i+1}$ introduced earlier in equation (1.24) can be generated from the R-matrix using

$$H_{i,i+1} = R_{i,i+1}^{-1}(0) \frac{d}{du} R_{i,i+1}(u)|_{u=0} = P_{i,i+1} \frac{d}{du} R_{i,i+1}(u)|_{u=0} \tag{1.34}$$

where $P_{i,i+1}$ is the permutation operator between sites $i, i+1$. Also, we emphasize that while the charges are conventionally computed in Equation (1.33) at $u = 0$, this computation can equally well be done at generic values of u to extract mutually commuting charges. The only difference is we no longer recover the Hamiltonian directly as one of the commuting charges.

Given an integrable spin chain, the energy eigenvalues can be obtained by solving a set of coupled polynomial equations known as Bethe equations. The corresponding eigenstates can be obtained by using the formalism of algebraic Bethe ansatz (ABA). One starts with an ansatz for the energy eigenstates, starting from a reference ground state say $|\Omega\rangle$. Excited states are created by acting with $B-$operators, which are certain off-diagonal entries of the monondromy matrix, when written out explicitly in the auxiliary space representation. Then one uses the fundamental commutation relations (FCRs) to obtain the algebraic conditions known as Bethe equations as requirements for the excited states to be eigenstates of the transfer matrix. This in turn causes the obtained states to be eigenstates of a tower of commuting charges, including the spin chain Hamiltonian. Let us illustrate this through the concrete example of XXX spin-chain. Let us consider a spin chain of size L, each site in spin-$\frac{1}{2}$ representation of $SU(2)$ gauge group. The R-matrix is given by

$$R_{XXX}(u) = u\mathbb{I}_{4\times 4} + i\mathbb{P}_{4\times 4}, \quad \mathbb{P}_{4\times 4} = \begin{pmatrix} 1 & 0 & 0 & 0 \\ 0 & 0 & 1 & 0 \\ 0 & 1 & 0 & 0 \\ 0 & 0 & 0 & 1 \end{pmatrix} \tag{1.35}$$

The spin-chain monodromy matrix, written in the basis of the spin-$\frac{1}{2}$ auxiliary site, reads

$$\mathcal{T}(u) = \begin{pmatrix} A(u) & B(u) \\ C(u) & D(u) \end{pmatrix} \tag{1.36}$$

where $A(u), B(u), C(u), D(u)$ are matrices of size $2^L \times 2^L$ that act on the spin chain sites. The resultant transfer matrix is $T(u) = A(u) + D(u)$. The reference state for ABA is

$$|\Omega\rangle = |\uparrow\rangle^{\otimes L} \tag{1.37}$$

---

[2]In practice, numerically it's more stable to work with the second formula on the right hand side than the first.

The Bethe ansatz for the eigenstates generated on top of the above reference state is given by

$$|\{u_i\}_{i=1}^M\rangle = B(u_1)B(u_2)\ldots B(u_M)|\Omega\rangle \tag{1.38}$$

where the set $\{u_j\}_{j=1}^M$, for integer $0 < M \leqslant L$ must satisfy the Bethe equations

$$\left(\frac{u_j + \frac{i}{2}}{u_j - \frac{i}{2}}\right)^L = \prod_{k=1,\neq j}^M \frac{u_j - u_k + i}{u_j - u_k - i}, \quad j = 1\ldots M. \tag{1.39}$$

This equation is obtained by using the FCRs for $A - B$, and $D - B$(which in turn are obtained from the RTT relation) to commute the transfer matrix past the B-operators in $|\Psi\rangle$ and then using $A(u)|\Omega\rangle \propto |\Omega\rangle$, $D(u)|\Omega\rangle \propto |\Omega\rangle$. Solving the above equation for fixed M, gives us the energy eigenstates. The corresponding eigenvalue is

$$E(|\{u_i\}_{i=1}^M\rangle) = \sum_{i=1}^M \frac{1}{u_i^2 + \frac{1}{4}}. \tag{1.40}$$

There is an interesting limit known as the thermodynamic limit where one takes $L \to \infty$, $M \to \infty$ while keeping $\frac{M}{L} = $ finite. In this limit, its natural to look at root densities instead of roots, and the solutions (known as Bethe strings) to the Bethe equations show up as finite-length cuts in the spectral-parameter complex plane.

Next, lets briefly review (1+1)D integrable quantum field theories (IQFTs). One can define S-matrices for scattering of asymptotic states in the decompactification limit of the spatial (σ) direction $\sigma \in (-R, R)$, $R \to \infty$. Such a quantum field theory is said to be integrable if the S-matrix satisfies the following properties: there is no particle production/annihilation, the incoming momenta match the outgoing momenta upto permutation, and the $3 \to 3$ and higher point S-matrices factorise into product of $2 \to 2$ ones. A corollary of the factorisation is the Yang-Baxter equation which constrains the $2 \to 2$ S-matrix entries $S_{\alpha\beta}^{\gamma\delta}(p_i, p_j)$ where α, β label the incoming particles, while γ, δ labels the outgoing ones and p_i, p_j label the momenta of the scatterers

$$S_{ij}^{\beta\alpha}(p_1, p_2)S_{\beta k}^{n\gamma}(p_1, p_3)S_{\alpha\gamma}^{ml}(p_2, p_3) = S_{jk}^{\beta\gamma}(p_2, p_3)S_{i\gamma}^{\alpha l}(p_1, p_3)S_{\alpha\beta}^{nm}(p_1, p_2) \tag{1.41}$$

This is the same relation as satisfied by the R-matrices in quantum spin chains. A natural problem to study in IQFTs is the spectrum of states in finite volume, i.e. the σ endpoints $\pm R = $ finite. This can be done by starting from the asymptotic Bethe equations whose solutions give the exact spectrum in the limit $R \to \infty$. Picking a basis where the 2-particle S-matrix is diagonal (so only the 2 in-state indices are sufficient), the Bethe equations read

$$e^{ip_j R}\prod_{k\neq j} S_{\alpha_j\alpha_k}(p_j, p_k) = 1, \quad j = 1\ldots M \tag{1.42}$$

One can account for exponentially suppressed corrections known as wrapping as described by Luscher [19, 20]. Alternatively, one can solve the (much harder) mirror-channel thermodynamic Bethe equations to get the exact spectrum at finite R. Going to the mirror-channel involves double Wick rotating the space and time directions (σ, τ) to $(\bar{\sigma}, \bar{\tau}) = (-i\sigma, i\tau)$. This maps the finite volume IQFT to one at finite temperature with decompactified spatial direction. Hence we can employ the technology of asymptotic Bethe ansatz mentioned above. A comprehensive review of mirror TBA and related literature can be found in [21, 22].

1.3 String theory in AdS and integrability

Thus far, we have reviewed AdS/CFT and integrability. This section will be focused on connecting the two fields by looking at integrable structures within string theory and AdS/CFT. [23] is a good reference for the topics we discuss here. Integrability becomes evident in the Green-Schwarz (GS) formalism for describing superstrings, wherein spacetime SUSY is manifestly preserved (instead of world-sheet SUSY, as in Ramond-Neveu-Schwarz (RNS) formalism). The RNS formalism is useful to study string theory in AdS spacetime with pure NSNS flux. However, this formalism is not very helpful when dealing with the D3 branes in AdS_5 or the D1-D5 system of branes in AdS_3, as there is non-zero RR flux in such cases. Integrability comes to the rescue, at least in the 't Hooft (planar) limit $N \to \infty, g_{YM} \to 0, \lambda = g_{YM}^2 N = \text{finite}$. GS formalism is the natural candidate to study string theory in pure RR background. It can be used to study other backgrounds with NSNS flux, as well as a mix of both NSNS and RR fluxes, but we cannot use world-sheet (WS) CFT techniques which comes handy in the RNS formalism[24]. Also, GS superstring in AdS is integrable at the level of the classical action. Assuming that integrability survives quantisation as suggested by [25], we can work out results exact in the coupling parameters. We shall focus on $\text{AdS}_5/\text{CFT}_4$ in the rest of this section, and leave the discussion of $\text{AdS}_3/\text{CFT}_2$ for the next section.

We shall begin with the GS action, go to the uniform light-cone gauge (necessary generalisation of phase space light-cone gauge to curved backgrounds, as discussed below equation (1.57)) and then fix κ-symmetry. The bosonic part of the GS action S_{bos} is given by a nonlinear sigma model on a background with spacetime metric $G_{mn}(X)$ and B-field $B_{mn}(X)$ as functions of spacetime coordinates X^M, $M = 0, \dots, 9$

$$S_{bos} = -\frac{g}{2} \int d^2\sigma (\sqrt{-\gamma}\gamma^{\alpha\beta} G_{MN}(X) + \epsilon^{\alpha\beta} B_{MN}(X))\partial_\alpha X^M \partial_\beta X^N , \quad g = \frac{1}{2\pi\alpha'} \quad (1.43)$$

where $\gamma^{\alpha\beta}$ denotes the worldsheet (WS) metric in coordinates $\sigma^\alpha = (\tau, \sigma)$. Lets assume σ takes values in the range $(-r, r)$. This action is invariant under WS coordinate reparametrisation

$$\sigma^\alpha \to f^\alpha(\tau, \sigma) \quad (1.44)$$

as well as under WS scaling transformations

$$\gamma_{\alpha\beta} \to \Omega^2(\tau, \sigma)\gamma_{\alpha\beta} \quad (1.45)$$

Using the above symmetry we shall set the determinant of the WS metric to -1. In order to go to uniform light-cone gauge we re-write the above action in the first-order formalism

$$S_{bos} = \int d^2\sigma \left(p_M \dot{X}^M + \frac{\gamma^{01}}{\gamma^{00}} C_1 + \frac{1}{2g\gamma^{00}} C_2 \right) , \quad \dot{X}^M \equiv \partial_0 X^M , \; X^{M\prime} \equiv \partial_1 X^M \quad (1.46)$$

by introducing the momenta p_M conjugate to the coordinates X^M

$$p_M \equiv \frac{\delta S_{bos}}{\delta \dot{X}^M} = -g \left(\gamma^{0\beta} G_{MN} \partial_\beta X^N + B_{MN} X^{N\prime} \right) . \quad (1.47)$$

This first order action is complemented by the Virasoro constraints on the fields which arise due to the two dimensional WS reparametrization $((\sigma, \tau) \to (f(\sigma, \tau), g(\sigma, \tau))$, for generic smooth functions f, g) invariance of the string action

$$C_1 = p_M X^{M\prime} , \quad (1.48)$$

15

$$C_2 = G^{MN}p_M p_N + g^2 G_{MN} X^{M\prime} X^{N\prime} + 2g G^{MN} p_N B_{MO} X^{O\prime} + g^2 G^{MN} B_{MO} B_{NP} X^{O\prime} X^{P\prime}.$$
(1.49)

The above Virasoro constraints $C_1 = C_2 = 0$ can be simplified to

$$\gamma^{11} G_{MN} \dot{X}^M X^{N\prime} + \gamma^{01} G_{MN} \dot{X}^M \dot{X}^N = 0$$
$$\gamma^{00} G_{MN} \dot{X}^M \dot{X}^N - \gamma^{11} G_{MN} X^{M\prime} X^{N\prime} = 0$$
(1.50)

The fermionic fields θ^I couple with themselves and with the bosonic fields X^M via the rest of the GS action, which includes kinetic term for the fermions S_{kin} and a Wess-Zumino (WZ) term S_{WZ}

$$S_{GS} = S_{bos} + S_{kin} + S_{WZ}.$$
(1.51)

The WZ term is responsible for restoring a local fermionic symmetry known as κ-symmetry. This step is essential to reduce the fermionic degrees of freedom to the physical ones. The above action can be re-formulated as a coset action on $PSU(2,2|4)/(SO(4,1)\times SO(5))$. The action written in terms of the one-form current $A = -\mathfrak{g}^{-1} d\mathfrak{g} \in \mathfrak{su}(2,2|4)$, which is constructed from the supergroup valued element $\mathfrak{g} \in PSU(2,2|4)$

$$S_{coset} = \int d^2\sigma \mathcal{L}, \quad \mathcal{L} = -\frac{g}{2}\left(\gamma^{\alpha\beta}\mathrm{str}(A^{(2)}_\alpha A^{(2)}_\beta) + \kappa\epsilon^{\alpha\beta}\mathrm{str}(A^{(1)}_\alpha A^{(3)}_\beta)\right), \quad \kappa \in \mathbb{R} \quad (1.52)$$

with a $\mathbb{Z}_4$ decomposition of A under an automorphism Ω of order 4 (equivalent to "minus supertransposition", $\Omega(M) = -\mathcal{K}M^{\mathrm{st}}\mathcal{K}^{-1}$ for some $\mathcal{K} \in \mathfrak{su}(2,2|4)$)

$$A = A^{(0)} + A^{(1)} + A^{(2)} + A^{(3)}, \quad \Omega(A^{(k)}) = i^k A^{(k)}$$
(1.53)

The WZ level $\kappa = \pm 1$ due to κ-symmetry (local symmetry under right action by fermionic element $\mathfrak{g} \to \mathfrak{g} \circ \exp(\epsilon(\tau,\sigma))$, see below equation (1.63)). The above action has a central $\mathfrak{u}(1)$ symmetry under $A^{(2)} \to A^{(2)} + c.i\,\mathbb{I}$, which we fix by imposing $\mathrm{tr}(A^{(2)}) = 0$. This action has a gauge symmetry $SO(4,1) \times SO(5)$ under

$$\mathfrak{g} \to \mathfrak{g}H, \quad H \in SO(4,1) \times SO(5),$$
(1.54)

and global symmetry $PSU(2,2|4)$ under

$$G.\mathfrak{g} = \mathfrak{g}'H, \quad G \in PSU(2,2|4), \, H \in SO(4,1) \times SO(5).$$
(1.55)

One nice choice for $\mathfrak{g}$ suitable for working in the light-cone gauge is

$$\mathfrak{g}(X^M, \Theta) = \exp\begin{pmatrix} \frac{it\gamma^5}{2} & 0 \\ 0 & \frac{i\phi\gamma^5}{2} \end{pmatrix} \exp\begin{pmatrix} 0 & \Theta \\ -\Theta^\dagger\Sigma & 0 \end{pmatrix} \exp\begin{pmatrix} \frac{z^i\gamma^i}{2} & 0 \\ 0 & \frac{iy^i\gamma^i}{2} \end{pmatrix}, \quad \Sigma = \begin{pmatrix} \mathbb{I}_2 & 0 \\ 0 & -\mathbb{I}_2 \end{pmatrix}$$
(1.56)

where we have assumed $X^M = \{t, \phi, z^i, y^i\}$, where $\{t, z^i\}, i = 1,2,3,4$ are the AdS$_5$ coordinates and $\{\phi, y^i\}, i = 1,2,3,4$ are the S^5 coordinates, with t, ϕ being the AdS$_5$ time and S^5 equatorial angle respectively. By construction the above one-form A satisfies the zero curvature condition

$$dA - A \wedge A = 0 \quad \Leftrightarrow \quad \partial_\alpha A_\beta - \partial_\beta A_\alpha - [A_\alpha, A_\beta] = 0.$$
(1.57)

For light-cone gauge fixing the superstring action, let us first consider flat Minkowski spacetime. In this case, we can impose light-cone gauge one of two ways. Either we impose

16

conformal gauge for the WS metric $\gamma^{\alpha\beta} = \eta^{\alpha\beta}$ followed by fixing the residual conformal diffeomorphism by equating light-cone coordinate x^+ with WS time. Alternatively, one can rewrite the action in the first-order formalism(discussed below) and fixing $x^+ = \tau$, lightcone momentum $p_+ = \frac{\delta S}{\delta \dot{x}^-} = $ constant. Both approaches are equivalent for flat space, but the former is not possible in AdS backgrounds due to absence of covariantly constant null Killing vectors. As such, the only option is to work with the first-order formalism. Below, we review the more general uniform light-cone gauge, that includes a 1-parameter family of interesting gauge choices. The light-cone coordinates x^+, x^-(and conjugate momenta p_-, p_+ respectively) are defined as

$$x^- = \phi - t, \quad x^+ = (1-a)t + a\phi, \quad p_- = p_\phi + p_t, \quad p_+ = (1-a)p_\phi - ap_t, \quad a \in \mathbb{C} \quad (1.58)$$

The uniform light-cone gauge is fixed by imposing

$$x^+ = \tau + a\,m\,\sigma, \quad p_+ = 1, \quad (1.59)$$

where $m \in \mathbb{Z}$ is the winding number for the string around the ϕ direction. Some preferred choices of a include $a = 0$ for the temporal gauge, $a = \frac{1}{2}$ for the usual light-cone gauge, and $a = 1$ where the angular coordinate ϕ acts as WS time. Consistency of above gauge choice fixes the end-points of σ to $r = \frac{P_+}{2}$, where P_+ is the total light-cone momentum. Solving the Virasoro constraints and substituting them into the action, we get the string Hamiltonian H. The gauge choice means H is related to the target space-time energy E and U(1) charge J as

$$H = E - J, \quad H = -\int d\sigma\, p_-, \quad E = -\int d\sigma\, p_t, \quad J = \int d\sigma\, p_\phi \quad (1.60)$$

Integrating over the Virasoro constraint C_1, one gets the level-matching condition for physical states

$$\Delta x_- = \int_{-r}^{r} d\sigma x'_- = 2\pi m, \quad m \in \mathbb{Z} \quad (1.61)$$

This condition forces the total world-sheet momentum of physical states to be 2π times the winding number $m \in \mathbb{Z}$. One can use the above relation, alongwith the mapping $E \equiv \Delta$, the conformal dimension of operators in the dual CFT, to solve for them from the spectrum of H. For the full GS superstring action in $\mathrm{AdS}_5 \times \mathrm{S}^5$, imposing the lightcone gauge is somewhat more difficult due to the non-trivial interactions between the bosons and fermions affecting the expressions for the conjugate momenta. It is useful to introduce a Lie-algebra valued auxiliary field Π into the coset Lagrangian, and gauge-fix that instead.

Next, let us fix the κ-symmetry. This local supersymmetry is responsible for reducing the independent fermion degrees of freedom by half. It was first discovered in [26] for superparticles, extended to flat space superstring action in [27] and for general backgrounds in [28]. As mentioned earlier below equation (1.53), κ symmetry transformation is given by $\mathfrak{g} \to \mathfrak{g} \circ \exp(\epsilon(\tau, \sigma))$. The one-form A in the coset action transforms under infinitesimal local right multiplication by a fermionic element ϵ as

$$\delta_\epsilon A = -d\epsilon + [A, \epsilon], \quad \epsilon = \epsilon^{(1)} + \epsilon^{(3)} \quad (1.62)$$

where $\epsilon^{(i)}, i = 1, 3$, refers to the $\mathbb{Z}_4$ grading. The coset action remains invariant under such a right action, provided the WS metric is also varied suitably. Further, the invariance of

the action requires $P_\pm^{\alpha\beta} = \frac{1}{2}(\gamma^{\alpha\beta} \pm \kappa\epsilon^{\alpha\beta})$ to be a projection operator which only happens for $\kappa = \pm 1$. One common κ-gauge choice is to bring the odd-elements of $\mathfrak{su}(2,2|4)$ to the form

$$
\begin{pmatrix}
0 & 0 & 0 & 0 & 0 & 0 & \cdot & \cdot \\
0 & 0 & 0 & 0 & 0 & 0 & \cdot & \cdot \\
0 & 0 & 0 & 0 & \cdot & \cdot & 0 & 0 \\
0 & 0 & 0 & 0 & \cdot & \cdot & 0 & 0 \\
0 & 0 & \cdot & \cdot & 0 & 0 & 0 & 0 \\
0 & 0 & \cdot & \cdot & 0 & 0 & 0 & 0 \\
\cdot & \cdot & 0 & 0 & 0 & 0 & 0 & 0 \\
\cdot & \cdot & 0 & 0 & 0 & 0 & 0 & 0
\end{pmatrix} ,
\tag{1.63}
$$

thus reducing to 16 fermionic degrees of freedom.

Classical integrability, i.e. demanding a flat Lax connection, also fixes κ to be the same values as κ-symmetry, $\kappa = \pm 1$. The Lax connection $L(z)$ for $\mathrm{AdS}_5 \times \mathrm{S}^5$ superstring is given by the following meromorphic function on the Riemann sphere parameterised by z [2]

$$
L(z) = A^{(0)} + z^{-1}A^{(1)} + \frac{z^2 + z^{-2}}{2} A^{(2)} + \left(\frac{z^2 - z^{-2}}{2} \right) \star A^{(2)} + zA^{(3)} ,
\tag{1.64}
$$

where $\star$ denotes the WS Hodge star. Provided $\kappa = \pm 1$, the flatness condition for $L(\tau, \sigma, z)$ is satisfied due to the Maurer-Cartan equation for A (see equation (1.57))

$$
\partial_\alpha L_\beta - \partial_\beta L_\alpha - [L_\alpha, L_\beta] = 0 , \quad \alpha, \beta \in (\tau, \sigma) .
\tag{1.65}
$$

Thus, we have the result that the GS superstring action on $\mathrm{AdS}_5 \times \mathrm{S}^5$ is classically integrable. The above Lax connection L depends on one complex spectral parameter z. We can write down the monodromy matrix as path-ordered exponential of the above Lax connection L along a closed path encircling the compact worldsheet direction. We define quasimomenta $p_k(z)$, $k = 1, 2, \ldots 8$ as $-i$ times logarithm of the eigenvalues of the monodromy matrix. They are multi-valued on the z−plane and define the spectral curve. Classical solutions to the string equations of motion [29, 30, 31, 32] can be characterized by the analytic properties of the spectral curve like cuts and poles[33, 34, 35]. For instance, the circular string solution in $\mathbb{R} \times \mathrm{S}^3$ corresponds to the following one-cut solution

$$
p_1 = p_2 = -p_3 = -p_4 = \frac{2\pi\kappa z}{z^2 - 1} ,
\tag{1.66}
$$

$$
p_5 = \frac{z}{z^2 - 1} K\left(\frac{1}{z}\right) ,
$$
$$
p_6 = \frac{z}{z^2 - 1} K(z) - m ,
$$
$$
p_7 = \frac{z}{1 - z^2} K(z) + m ,
$$
$$
p_8 = \frac{z}{1 - z^2} K\left(\frac{1}{z}\right) ,
\tag{1.67}
$$

with $K(z) = \sqrt{m^2 z^2 + J}$, where m, J are the mass and angular momentum along the sphere. These classical solutions satisfy the finite gap equations, which arise in the thermodynamic limit of the dual $\mathcal{N} = 4$ SYM spin chain description. The spectral curve

also captures quantum fluctuations as shifts in the quasimomenta around the classical solutions perturbatively

$$p_i(x) \rightarrow p_i(x) + \delta^{ij} p_j(x). \tag{1.68}$$

This can be used to calculate one-loop energy shift around generic classical solutions, as discussed in the review [36] with further literature references.

One can further develop this integrability picture into a quantum version, by working in the decompactification limit where one goes from the WS cylinder to the plane by letting $P_+ = (1-a)J + aE \rightarrow \infty$, while keeping string tension fixed. Finiteness of $H = E - J$ requires $J \rightarrow \infty$ as well. In this limit, we have well-defined asymptotic states and WS S-matrix for their scattering. The S-matrix can be computed perturbatively as $\frac{1}{g}$-expansion in large tension regime $g >> 1$. This S-matrix factorises i.e. $n \rightarrow n$ S-matrix can be re-expressed as product of $2 \rightarrow 2$ S-matrices and are schematically of the form

$$e^{2ip_k r} \prod_{j \neq k}^{M} S(p_k, p_j) = 1. \tag{1.69}$$

This is the hallmark of quantum integrability. As we shall see in the next sub-section, the S-matrix is fully determined by the centrally extended $\mathfrak{psu}(2|2) \oplus \mathfrak{psu}(2|2)$ symmetry of the theory. The spectrum for H is calculated by solving the Bethe-Yang equations in this limit, which involve the 2-particle S-matrices. The Bethe equations turn out to admit a quantum spin-chain description, which in the weak-coupling limit of the dual $\mathcal{N} = 4$ SYM becomes the Heisenberg spin chain described in the previous sub-section. Finite-size corrections can then be included (to go back to finite P_+) by using TBA.

The lightcone string sigma model admits soliton solutions, such as the 1-soliton giant magnon solution which satisfy the dispersion relation [4]

$$\omega_{classical}(p_{WS}) = E - J = 2g \sin \frac{p_{WS}}{2}, \tag{1.70}$$

where the WS momentum $p_{WS} = 2\cos^{-1} v$, for v velocity of the soliton. This dispersion relation shows that the light-cone model is not Lorentz-invariant. Furthermore, it is independent of the gauge-parameter a. This dispersion relation is classical, and gets modified in the full quantum theory to [7]

$$\omega_{quantum}(p_{WS}) = \sqrt{1 + 4g^2 \sin^2 \frac{p_{WS}}{2}} \tag{1.71}$$

This dispersion relation gets fixed by the symmetries of the quantum theory as we shall see in the next sub-section.

Before we discuss the quantum theory, let us focus on the symmetry algebra of the light-cone gauge-fixed model. For $P_+ = $ finite, we have the symmetry algebra $\mathcal{A}$

$$\mathcal{A} = \mathfrak{psu}(2|2) \oplus \mathfrak{psu}(2|2) \oplus \Sigma_+ \oplus \Sigma_- \tag{1.72}$$

where Σ_+, Σ_- are the lightcone directions with corresponding charges H, P_+ respectively. The symmetry algebra $\mathfrak{psu}(2|2) \oplus \mathfrak{psu}(2|2)$ arises from the elements of $\mathfrak{psu}(2,2|4)$ that commute with Σ_+. In the decompactification limit, we no longer have P_+. However, we have two new central charges $C, C^\dagger$ for the off-shell theory that appear in the Poisson bracket of odd elements with

$$C = \frac{i\sqrt{\lambda}}{4\pi}(e^{ip_{WS}} - 1). \tag{1.73}$$

For the on-shell theory $p_{WS} = 0$, we have vanishing $C, C^\dagger$.

1.4 All-loop S-matrices

In this sub-section, we shall review the full quantum integrable model that arises in the $\mathrm{AdS}_5 \times \mathrm{S}^5$ superstring theory in the planar limit. A good review of this topic is in [37]. The full S-matrix $\mathbb{S}_{\mathrm{AdS}_5 \times \mathrm{S}^5}$ can be written as tensor-product of two identical copies of S-matrices $S_{\mathfrak{su}(2|2)}$ acting on each centrally extended $\mathfrak{su}(2|2)$

$$\mathbb{S}_{\mathrm{AdS}_5 \times \mathrm{S}^5} = S_{\mathfrak{su}(2|2)} \otimes S_{\mathfrak{su}(2|2)} \,. \tag{1.74}$$

So we can focus on a single copy of centrally-extended $\mathfrak{su}(2|2)$ algebra and its representations. This algebra consists of rotation generators $\mathbb{L}_a{}^b$, $\mathbb{R}_\alpha{}^\beta$, SUSY generators $\mathbb{Q}_\alpha{}^a$, $\mathbb{Q}^\dagger{}_a{}^\alpha$ and central elements $\mathbb{C}, \mathbb{C}^\dagger, \mathbb{H}$ with Latin indices $a, b, \dots$ taking values $\{1, 2\}$ and Greek indices $\alpha, \beta, \dots$ taking values $\{3, 4\}$. The fundamental excitations corresponding to the asymptotic states transform in the fundamental representation of $\mathfrak{su}(2|2)$ $\mathcal{V}_{fund}$

$$\mathcal{V}_{fund} = \mathrm{span}(|e_a\rangle, |e_\alpha\rangle), \quad a = \{1, 2\}, \, \alpha = \{3, 4\}, \tag{1.75}$$

where $|e_M\rangle$ are the basis elements with $M = 1, 2$ being bosons, and $M = 3, 4$ being fermions. The S-matrix can be fixed, upto a phase, by requiring it to commute with the above symmetry generators $\mathbb{L}, \mathbb{R}, \mathbb{Q}, \mathbb{Q}^\dagger$. The 16×16 $\mathfrak{su}(2|2)$ S-matrix in fundamental representation can be written in terms of components

$$S_{\mathfrak{su}(2|2)} = S_{ij}^{kl} e_i^k \otimes e_j^l, \quad i, j, k, l = 1, 2, 3, 4, \tag{1.76}$$

where e_i^j is a 4×4 matrix with 1 in the $(i, j)^{th}$ entry and zeros elsewhere. It is useful to go to the Zhukovsky variables $x^\pm$ when solving for the S-matrix components. They are related to the momentum variable p and the rapidity variables u as follows:

$$x^\pm(u) = x(u \pm \frac{i}{2}), \quad x(u) = \frac{u}{2} + \frac{1}{2}\sqrt{u^2 - 2g^2}, \quad u(p) = \frac{1}{2}\cot\left(\frac{p}{2}\right)\sqrt{1 + 8g^2 \sin^2 \frac{p}{2}} \tag{1.77}$$

For the S-matrix components $S_{ij}^{kl}(p_1, p_2)$ corresponding to in-states denoted by labels i, j and out-states by k, l, we have

$$S_{aa}^{aa} = A, \; S_{\alpha\alpha}^{\alpha\alpha} = D, \; S_{ab}^{ab} = \frac{A - B}{2}, \; S_{ab}^{ba} = \frac{A + B}{2}, \; S_{\alpha\beta}^{\alpha\beta} = \frac{D - E}{2}, \; S_{\alpha\beta}^{\beta\alpha} = \frac{D + E}{2},$$

$$S_{ab}^{\alpha\beta} = -\frac{\epsilon_{ab}\epsilon^{\alpha\beta}}{2}C, \; S_{\alpha\beta}^{ab} = -\frac{\epsilon^{ab}\epsilon_{\alpha\beta}}{2}F, \; S_{a\alpha}^{a\alpha} = G, \; S_{a\alpha}^{\alpha a} = H, \; S_{\alpha a}^{\alpha a} = K, \; S_{\alpha a}^{a\alpha} = L. \tag{1.78}$$

where

$$A = S_0 \frac{x_2^- - x_1^+}{x_2^+ - x_1^-} \frac{\eta_1 \eta_2}{\tilde{\eta}_1 \tilde{\eta}_2}\,,$$

$$B = -S_0 \left(\frac{x_2^- - x_1^+}{x_2^- - x_1^+} + 2 \frac{(x_1^- - x_1^+)(x_2^- - x_2^+)(x_2^- + x_1^+)}{(x_1^- - x_2^+)(x_1^- x_2^- - x_1^+ x_2^+)} \right) \frac{\eta_1 \eta_2}{\tilde{\eta}_1 \tilde{\eta}_2}\,,$$

$$C = S_0 \frac{2i x_1^- x_2^- (x_1^+ - x_2^+)\eta_1 \eta_2}{x_1^+ x_2^+ (x_1^- - x_2^+)(1 - x_1^- x_2^-)}\,, \quad D = -S_0\,,$$

$$E = S_0 \left(1 - 2 \frac{(x_1^- - x_1^+)(x_2^- - x_2^+)(x_1^- + x_2^+)}{(x_1^- - x_2^+)(x_1^- x_2^- - x_1^+ x_2^+)} \right),$$

$$F = S_0 \frac{2i(x_1^- - x_1^+)(x_2^- - x_2^+)(x_1^+ - x_2^+)}{(x_1^- - x_2^+)(1 - x_1^+ x_2^+)\tilde{\eta}_1 \tilde{\eta}_2}\,,$$

$$G = S_0 \frac{x_2^- - x_1^-}{x_2^+ - x_1^-} \frac{\eta_1}{\tilde{\eta}_1}\,, \quad H = S_0 \frac{x_2^+ - x_2^-}{x_1^- - x_2^+} \frac{\eta_1}{\tilde{\eta}_2}\,,$$

$$K = S_0 \frac{x_1^+ - x_1^-}{x_1^- - x_2^+} \frac{\eta_2}{\tilde{\eta}_1}\,, \quad L = S_0 \frac{x_1^+ - x_2^+}{x_1^- - x_2^+} \frac{\eta_2}{\tilde{\eta}_2} \tag{1.79}$$

with $x_i^\pm = x^\pm(p_i)$ satisfying the shortening conditions

$$x^+ + \frac{1}{x^+} - x^- - \frac{1}{x^-} = \frac{i}{g}\,, \quad \frac{x^+}{x^-} = e^{ip} \tag{1.80}$$

and

$$\eta_1 = \eta(p_1)e^{ip_2/2}\,, \ \eta_2 = \eta(p_2)\,, \ \tilde{\eta}_1 = \eta(p_1)\,, \ \tilde{\eta}_2 = \eta(p_2)e^{ip_1/2}\,, \ \eta(p) = e^{ip/4}\sqrt{x^- - x^+}\,. \tag{1.81}$$

The dressing phase S_0 satisfies unitarity and crossing constraints which we will present in detail in the context of AdS$_3$ backgrounds in the next section. Crossing symmetry refers to the symmetry under scattering of a physical particle against a spurious bound state of another particle and its antiparticle. Unitarity is the requirement for the S-matrix to be unitary for real momenta. Solving these constraints [38], one ends up with

$$S_0(p_1, p_2)^2 = \frac{x_1^- - x_2^+}{x_1^+ - x_2^-} \frac{1 - \frac{1}{x_1^+ x_2^-}}{1 - \frac{1}{x_1^- x_2^+}} \sigma^2(p_1, p_2)\,, \tag{1.82}$$

where σ is called BES phase factor which has several interesting representations in terms of asymptotic series (c_{rs} charge expansion), and the DHM double contour integral. Again, we shall revisit these representations in the next section. One also has an infinite tower of bound-states on top of the above mentioned fundamental excitations. They all have non-trivial scattering matrices $S_{PQ}(P \geqslant 1, Q \geqslant 1$ labelling the number of particles forming each bound state), which go into the final construction of the (mirror)TBA equations. We shall omit their discussion here as they are not actively used in our works, but shall point to [39, 40, 41] for further discussion and relevant references.

2 Strings on AdS$_3$ backgrounds

This section will review AdS$_3 \times M^7$ backgrounds preserving 16 supercharges, which appear as near-horizon geometry of the brane-constructions in type IIB string theory discussed

earlier in section (1.1.3). The resultant supergravity backgrounds are supported by RR and NSNS 3-form fluxes. Integrability in these backgrounds, was first hinted from the presence of giant magnon solutions in $\text{AdS}_3 \times \text{S}^3 \times \text{T}^4$ [42, 43]. Another hint of integrability came from the GKP spinning string solution [44]. As mentioned in the previous section, classical integrability of the GS action was worked out in [10, 11, 12, 13]. Upto some $U(1)$ factors, the string action in $\text{AdS}_3 \times \text{S}^3 \times \text{T}^4$ background with pure RR flux is equivalent to the super-coset action on $PSU(1,1|2)^2/(SO(1,2) \times SO(3))$. On the other hand, GS action on $\text{AdS}_3 \times \text{S}^3 \times \text{S}^3 \times \text{S}^1$ with pure RR flux can be mapped to the $D(2,1;\alpha)^2/(SO(1,2) \times SO(3) \times SO(3))$[45] super-coset action(again upto some $U(1)$ factors). Unlike strings in $\text{AdS}_5 \times \text{S}^5$(or $\text{AdS}_4 \times CP^3$), there are massless modes (alongwith massive ones) in the string spectrum which are harder to include in the semi-classical picture. Major progress in this direction happened in [46] followed by [47], where the authors managed to incorporate massless modes in the finite gap equations by imposing a less restrictive Virasoro constraint. These massless modes are crucial in computation of protected spectrum, as was first discussed in [48] and further refined in [49] and [50]. All-loop S-matrices for the fundamental excitations were worked out for the massive modes in $\text{AdS}_3 \times \text{S}^3 \times \text{S}^3 \times \text{S}^1$ in [51, 52], and for $\text{AdS}_3 \times \text{S}^3 \times \text{T}^4$ in [53, 54]. The massless modes were later included in [55, 56, 57](for $\text{AdS}_3 \times \text{S}^3 \times \text{T}^4$) and [58](for $\text{AdS}_3 \times \text{S}^3 \times \text{S}^3 \times \text{S}^1$). These works still had some undetermined overall factors in the S-matrix, which have been identified for $\text{AdS}_3 \times \text{S}^3 \times \text{T}^4$ background with RR flux in [59]. TBA and quantum spectral curve have also been constructed for this background in [60], [61] respectively.

In this section, we shall review the fundamentals of string theory in $\text{AdS}_3 \times \text{S}^3 \times M^4$ backgrounds with $M^4 = \text{T}^4, \text{S}^3 \times \text{S}^1$, and how classical and quantum integrability emerges in these backgrounds. We will write down the gauge-fixed action, take its decompactification limit, and work out the all-loop S-matrices for the scattering of the massive/massless states and the Bethe equations for the spectrum of single-trace operators.

2.1 GS action and gauge-fixing

Let us begin with the light-cone gauge-fixing of the GS action and its decompactification limit. The bosonic and GS actions were reviewed in the previous section in equation (1.43), (1.51). Explicitly, the terms S_{kin} and S_{WZ} written upto quadratic order in fermions reads[62]

$$S_{kin} = -i \int d^2\sigma \gamma^{\alpha\beta} \bar{\tilde{\Theta}}_I \slashed{E}_\alpha (\delta^{IJ} D_\beta + \frac{1}{48}\sigma_3^{IJ} \slashed{F} \slashed{E}_\beta + \frac{1}{8}\sigma_1^{IJ} \slashed{H}_\beta)\tilde{\Theta}_J \tag{2.1}$$

$$S_{WZ} = i \int d^2\sigma \epsilon^{\alpha\beta} \sigma_1^{IJ} \bar{\tilde{\Theta}}_I \slashed{E}_\alpha (\delta^{JK} D_\beta + \frac{1}{48}\sigma_3^{JK} \slashed{F} \slashed{E}_\beta + \frac{1}{8}\sigma_1^{JK} \slashed{H}_\beta)\tilde{\Theta}_K \,, \tag{2.2}$$

where $\alpha, \beta \in \{\tau, \sigma\}$, $I, J, K \in \{1, 2\}$. The vielbeins E_μ^A satisfy

$$E_\mu^A E_\nu^B \eta_{AB} = G_{\mu\nu} \,, \quad \slashed{E}_\alpha = \partial_\alpha X^\mu \slashed{E}_\mu \,, \quad \slashed{E}_\mu = \sum_{A=0}^{9} E_\mu^A \eta_{AB} \Gamma^B \tag{2.3}$$

while the background 3-form fluxes are given by

$$\slashed{F} = F_{ABC}\Gamma^{ABC} \,, \quad \slashed{H}_\alpha = \partial_\alpha X^\mu \slashed{H}_\mu \,, \quad \slashed{H}_\mu = H_{\mu AB}\Gamma^{AB} \,. \tag{2.4}$$

The main difference with respect to the $\text{AdS}_5 \times \text{S}^5$ discussion, appears at the level of gauge-fixing. We will discuss the lightcone gauge-fixing for $\text{AdS}_3 \times \text{S}^3 \times \text{S}^3 \times \text{S}^1$, from

which the $\text{AdS}_3 \times \text{S}^3 \times \text{T}^4$ result can be obtained in the $\varphi \to 0$ limit. We will broadly follow [58, 63] for the rest of this sub-section.

The light-cone coordinates $x^\pm$ are defined as linear combination of the AdS_3 time coordinate t, and angular coordinates ϕ^5, ϕ^8, one from each S^3

$$x^+ = (1-a)t + a\frac{\cos\vartheta}{\cos\varphi}\phi^5 + a\frac{\sin\vartheta}{\sin\varphi}\phi^8, \quad x^- = \frac{1}{2}(-t + \frac{\cos\vartheta}{\cos\varphi}\phi^5 + \frac{\sin\vartheta}{\sin\varphi}\phi^8) \qquad (2.5)$$

where $0 \leqslant a \leqslant 1$ and ϑ parametrizes 1-parameter family of null geodesics, which is forced to be $\vartheta = \varphi$ for BPS state condition. We further define a transverse angular coordinate ψ to the light-cone directions as follows

$$\psi = -\frac{\sin\vartheta}{\cos\varphi}\phi^5 + \frac{\cos\vartheta}{\sin\varphi}\phi^8 \qquad (2.6)$$

Uniform light-cone gauge fixes x^+ and p_- as before

$$x^+ = \tau, \quad p_- = 1 \qquad (2.7)$$

in the zero winding sector. The worldsheet length $2R$ is related to the spin J and the worldsheet Hamiltonian as

$$2R = J + aH \qquad (2.8)$$

The decompactification limit corresponds to $P_- = \int d\sigma p_- = 2R \to \infty$ as in the AdS_5 case in last section. The lightcone energy H is given by

$$H = l + \tilde{l} - J, \quad J = (j_1 + \tilde{j}_1)\cos\vartheta\cos\varphi + (j_2 + \tilde{j}_2)\sin\vartheta\sin\varphi \qquad (2.9)$$

where $l, \tilde{l}$ are AdS spins, $j_i, \tilde{j}_i, i = 1, 2$ are spins on the two S^3. κ symmetry is fixed by setting

$$(\cos\vartheta\,\Gamma^{\phi_5} + \sin\vartheta\,\Gamma^{\phi_8} + \Gamma^t)\Theta_I = 0, \quad I = 1, 2, \qquad (2.10)$$

where $\Gamma^{\phi_5}, \Gamma^{\phi_8}, \Gamma^t$ are 10-dimensional Gamma matrices

$$\Gamma^t = -i\,\sigma_1 \otimes \sigma_2 \otimes \sigma_3 \otimes \mathbb{I} \otimes \mathbb{I}, \; \Gamma^{\phi_5} = \sigma_1 \otimes \sigma_1 \otimes \mathbb{I} \otimes \sigma_3 \otimes \mathbb{I}, \; \Gamma^8 = \sigma_1 \otimes \sigma_3 \otimes \mathbb{I} \otimes \mathbb{I} \otimes \sigma_3 \quad (2.11)$$

where σ_i are the Pauli matrices. One can further expand the action in the decompactification limit in a large-tension expansion (near-BMN expansion). This allows us to determine the perturbative S-matrix.

Classical integrability of the AdS_3 backgrounds can be proven by the Lax reformulation of the string equations of motion via their coset descriptions. We will discuss the case of $\text{AdS}_3 \times \text{S}^3 \times \text{S}^3 \times \text{S}^1$ where the coset is $D(2, 1; \alpha) \times D(2, 1; \alpha)/(SU(1, 1) \times SU(2) \times SU(2))$, as the $\text{AdS}_3 \times \text{S}^3 \times \text{T}^4$ can be realised in the limit of $\alpha \to 0$. The left and right copies of $d(2, 1; \alpha)$, i.e. Lie algebra for $D(2, 1; \alpha)$, can each be realised as 4×4 matrices. The full algebra is their direct sum leading to a 8×8 representation. The $\mathbb{Z}_4$ coset is generated by acting with order 4 element Ω

$$\Omega = \begin{pmatrix} 0 & \text{id} \\ (-1)^F & 0 \end{pmatrix} \Rightarrow \Omega^4 = \text{id} \qquad (2.12)$$

and the general coset representative $g(X, \Theta)$ is obtained by exponentiating Lie algebra elements, similar to equation (1.56). The Lie algebra $d(2, 1; \alpha)$, where $\alpha = \cos^2\varphi = \frac{R_{AdS}^2}{R_{\text{S}^3_+}^2}$,

is generated by bosonic elements $S_\mu(\mu = 0, 1, 2)$, $L_n(n = 3, 4, 5)$ and $R_{\dot n}(\dot n = 6, 7, 8)$, plus fermionic elements $Q_{a\alpha\dot\alpha}(a, \alpha, \dot\alpha \in \{+, -\})$. The bosonic elements generate $sl(2, \mathbb{R}) \oplus su(2) \oplus su(2)$ algebra amongst themselves

$$[S_\mu, S_\nu] = \epsilon_{\mu\nu\lambda}S^\lambda, \quad [L_m, L_n] = \epsilon_{mnp}S^\lambda, \quad [R_{\dot m}, R_{\dot n}] = \epsilon_{\dot m\dot n\dot p}S^{\dot p}, \tag{2.13}$$

while the supercharges satisfy (graded-)commutation relations

$$\{Q_{a\alpha\dot\alpha}, Q_{b\beta\dot\beta}\} = -i(\epsilon\gamma^\mu)_{ab}\epsilon_{\alpha\beta}\epsilon_{\dot\alpha\dot\beta}S_\mu - \cos^2\varphi\epsilon_{ab}(\epsilon\gamma^m)_{\alpha\beta}\epsilon_{\dot\alpha\dot\beta}L_m - \sin^2\varphi\epsilon_{ab}\epsilon_{\alpha\beta}(\epsilon\gamma^{\dot m})_{\dot\alpha\dot\beta}R_{\dot m}, \tag{2.14}$$

$$[S_\mu, Q_{a\alpha\dot\alpha}] = -\frac{1}{2}Q_{b\alpha\dot\alpha}\gamma^b_{\mu a}, \quad [L_m, Q_{a\alpha\dot\alpha}] = -\frac{i}{2}Q_{a\beta\dot\alpha}\gamma^\beta_{m\alpha}, \quad [R_{\dot m}, Q_{a\alpha\dot\alpha}] = -\frac{i}{2}Q_{a\alpha\dot\beta}\gamma^{\dot\beta}_{\dot m\dot\alpha} \tag{2.15}$$

Here, the vector indices are raised and lowered using $\eta_{\mu\nu} = \mathrm{diag}(- + +)$, δ_{mn}, $\delta_{\dot m\dot n}$. The two copies of $d(2, 1; \alpha)$ are distinguished using an additional label L, R. The Lax representation proving classical integrability, is the same as in equation (1.64), as that representation solely relies on the existence of the $\mathbb{Z}_4$ automorphism, and not the specifics of the AdS background.

Light-cone gauge fixed Hamiltonian commutes with a sub-algebra of the full $d(2, 1; \alpha)^2$

$$\mathrm{su}(1|1)^2 \subset d(2, 1; \alpha)^2 \tag{2.16}$$

Relaxing level-matching condition leads to the above off-shell algebra $\mathcal{A}$ extended by two central charges $\mathbf{C}, \bar{\mathbf{C}}$ which are related to the world-sheet momentum

$$\mathcal{A} = \mathrm{psu}(1|1)^2_{\mathrm{c.e.}} \tag{2.17}$$

The graded commutation relations amongst the supercharges $\mathbf{Q}_\mathrm{L}, \mathbf{S}_\mathrm{L}, \mathbf{Q}_\mathrm{R}, \mathbf{S}_\mathrm{R}$ generating this algebra is given by

$$\{\mathbf{Q}_\mathrm{L}, \mathbf{S}_\mathrm{L}\} = \mathbf{H}_\mathrm{L}, \qquad \{\mathbf{Q}_\mathrm{R}, \mathbf{S}_\mathrm{R}\} = \mathbf{H}_\mathrm{R}, \qquad \{\mathbf{Q}_\mathrm{L}, \mathbf{Q}_\mathrm{R}\} = \mathbf{C}, \qquad \{\mathbf{S}_\mathrm{L}, \mathbf{S}_\mathrm{R}\} = \bar{\mathbf{C}}, \tag{2.18}$$

with $\mathbf{H}_\mathrm{L}$, $\mathbf{H}_\mathrm{R}$, $\mathbf{C}$, $\bar{\mathbf{C}}$ central elements. The algebra furthermore comes equipped with a non-trivial coproduct of the form

$$\begin{aligned}
\Delta(\mathbf{Q}_\mathrm{L}) &= \mathbf{Q}_\mathrm{L} \otimes 1 + e^{+\frac{i}{2}\mathbf{P}} \otimes \mathbf{Q}_\mathrm{L}, &\qquad \Delta(\mathbf{S}_\mathrm{L}) &= \mathbf{S}_\mathrm{L} \otimes 1 + e^{-\frac{i}{2}\mathbf{P}} \otimes \mathbf{S}_\mathrm{L}, \\
\Delta(\mathbf{Q}_\mathrm{R}) &= \mathbf{Q}_\mathrm{R} \otimes 1 + e^{+\frac{i}{2}\mathbf{P}} \otimes \mathbf{Q}_\mathrm{R}, &\qquad \Delta(\mathbf{S}_\mathrm{R}) &= \mathbf{S}_\mathrm{R} \otimes 1 + e^{-\frac{i}{2}\mathbf{P}} \otimes \mathbf{S}_\mathrm{R},
\end{aligned} \tag{2.19}$$

where $\mathbf{P}$ is the world-sheet momentum. Near BMN analysis in [58] shows that the excitations transform in short representation of the off-shell symmetry algebra $\mathcal{A}$. One assumes that it remains short at higher orders in order to use them to write down the all-loop S-matrices and solve for the spectrum of excitations. Each of the representations is 2-dimensional, and transforms under one of the two copies of $su(1|1)$, and has a boson/fermion as the highest weight state. So we have 4 possible short representations $\rho_\mathrm{L,R}, \tilde\rho_\mathrm{L,R}$. These representations act on 2D graded vector spaces with basis states as

$$\mathcal{V}_{\rho_\mathrm{L,R}} = \{|\phi^{L,R}\rangle, |\psi^{L,R}\rangle\}, \quad \mathcal{V}_{\tilde\rho_\mathrm{L,R}} = \{|\tilde\psi^{L,R}\rangle, |\tilde\phi^{L,R}\rangle\} \tag{2.20}$$

There is an additional mass label m carried by these representations, that dictate the value of the central charges H, M, C. The short representations ρ_L, labeled by momentum

24

p, act as

$$\mathbf{Q}_{\mathrm{L}} |\phi_p^L\rangle = \eta_p^L |\psi_p^L\rangle, \qquad\qquad \mathbf{Q}_{\mathrm{R}} |\psi_p^L\rangle = -\frac{\eta_p^L}{x_{Lp}^-} e^{-ip/2} |\phi_p^L\rangle,$$

$$\mathbf{S}_{\mathrm{L}} |\psi_p^L\rangle = \eta_p^L e^{-ip/2} |\phi_p^L\rangle, \qquad \mathbf{S}_{\mathrm{R}} |\phi_p^L\rangle = -\frac{\eta_p^L}{x_{Lp}^+} |\psi_p^L\rangle, \tag{2.21}$$

where

$$\eta_p^L = e^{\frac{ip}{4}} \sqrt{\frac{ih}{2}(x_{Lp}^- - x_{Lp}^+)}, \tag{2.22}$$

h being the integrable-interaction coupling constant, which is a function of the moduli. The representations $\tilde{\rho}_{\mathrm{L}}$ act on $\mathcal{V}_{\tilde{\rho}_{\mathrm{L}}} = \{|\tilde{\psi}_p\rangle, |\tilde{\phi}_p\rangle\}$ as

$$\mathbf{Q}_{\mathrm{L}} |\tilde{\psi}_p^L\rangle = \eta_p |\tilde{\phi}_p^L\rangle, \qquad \mathbf{Q}_{\mathrm{R}} |\tilde{\phi}_p\rangle = -\frac{\eta_p^L}{x_{Lp}^-} e^{-ip/2} |\tilde{\psi}_p^L\rangle,$$

$$\mathbf{S}_{\mathrm{L}} |\tilde{\phi}_p\rangle = \eta_p^L e^{-ip/2} |\tilde{\psi}_p^L\rangle, \quad \mathbf{S}_{\mathrm{R}} |\tilde{\psi}_p^L\rangle = -\frac{\eta_p^L}{x_{Lp}^+} |\tilde{\phi}_p^L\rangle, \tag{2.23}$$

and are obtained from ρ_{L} by swapping the grading of the two excitations. The right representations $\rho_R, \tilde{\rho}_R$ are obtained by swapping out L with R in the above functions with

$$\eta_p^R = e^{\frac{ip}{4}} \sqrt{\frac{ih}{2}(x_{Rp}^- - x_{Rp}^+)}. \tag{2.24}$$

The Zhukovski variables $x_{Lp}^\pm, x_{Rp}^\pm$ are related to the momentum p through the relations

$$\frac{x_{Lp}^+}{x_{Lp}^-} = e^{ip}, \qquad x_{Lp}^+ + \frac{1}{x_{Lp}^+} - x_{Lp}^- - \frac{1}{x_{Lp}^-} = \frac{2i(|m| + \mathrm{\textit{k}}p)}{h}. \tag{2.25}$$

$$\frac{x_{Rp}^+}{x_{Rp}^-} = e^{ip}, \qquad x_{Rp}^+ + \frac{1}{x_{Rp}^+} - x_{Rp}^- - \frac{1}{x_{Rp}^-} = \frac{2i(|m| - \mathrm{\textit{k}}p)}{h}. \tag{2.26}$$

which are solved in the physical region by

$$x_{Lp}^\pm = \frac{(|m| + \mathrm{\textit{k}}p) + \sqrt{(|m| + \mathrm{\textit{k}}p)^2 + 4h^2 \sin^2 \frac{p}{2}}}{2h \sin \frac{p}{2}} e^{\pm \frac{ip}{2}}, \tag{2.27}$$

$$x_{Rp}^\pm = \frac{(|m| - \mathrm{\textit{k}}p) + \sqrt{(|m| - \mathrm{\textit{k}}p)^2 + 4h^2 \sin^2 \frac{p}{2}}}{2h \sin \frac{p}{2}} e^{\pm \frac{ip}{2}}. \tag{2.28}$$

Above $\mathrm{\textit{k}} = \frac{k}{2\pi}$, $k \in \mathbf{Z}$ is the NSNS charge of the background and m is the mass of the excitations.

Again comparing with the BMN analysis, we end up with a total of 8 exact representations for fundamental modes: ρ_L, ρ_R for masses $|m| = \alpha, 1 - \alpha$, $\tilde{\rho}_L, \tilde{\rho}_R$ for masses $|m| = 0, 1$. The heaviest $m = 1$ modes are expected to be composite particles or bound states, meaning their S-matrices would be either non-existent (composite scenario) or redundant (bound-state scenario, fixed uniquely by others via fusion). The $m = 0$ representations are special, since the L, R representations are isomorphic to the transpose of each other. In the T^4 limit $\alpha \to 0$, we end up with modes of two mass values 0 and 1, which is compatible with the symmetry enhancement to $\mathrm{psu}(1|1)_{\mathrm{c.e.}}^4$. In the next subsection, we shall review the all-loop S-matrices for the scattering of the above excitations and the crossing and unitarity constraints on overall phases that remain undetermined by symmetries alone.

2.2 All-loop S-matrices

The central charges impose conditions on the $2 \to 2$ scattering processes allowed. For in-coming particles of momenta and masses p_1^{in}, p_2^{in} and m_1^{in}, m_2^{in} and outgoing momenta and masses p_1^{out}, p_2^{out} and m_1^{out}, m_2^{out}, we have constraints

$$p_1^{in} + p_2^{in} = p_1^{out} + p_2^{out} , \quad m_1^{in} + m_2^{in} = m_1^{out} + m_2^{out} , \quad E_1^{in} + E_2^{in} = E_1^{out} + E_2^{out} \quad (2.29)$$

where the energy of 1-particle states is given by

$$E(p) = \sqrt{(m + \hbar p)^2 + 4h^2 \sin^2 \frac{p}{2}} \qquad (2.30)$$

with $m = |m|, -|m|$ for the left, right representations respectively. The above constraints can be used to split the full S-matrix into smaller blocks of 4 types: same mass and chirality, same mass but opposite chirality, different mass but same chirality, different mass and opposite chirality. The S-matrices can be further sub-divided into overall factors Σ for each block, known as dressing factor, and a matrix-part $\mathcal{S}$ that is fixed entirely by the symmetries

$$S(p, q) = \bigoplus_{m_1, m_2, \alpha, \beta} \Sigma_{m_1, m_2}^{\alpha\beta} \mathcal{S}_{m_1, m_2}^{\alpha\beta} , \qquad (2.31)$$

where $m_1, m_2 \in \{0, \alpha, 1-\alpha\}$ and $\alpha, \beta \in \{L, R\}$. For same chirality scattering, the matrix part of the S-matrix is given by

$$\mathcal{S}^{LL} |\phi_p^L \phi_q^L\rangle = A_{pq}^{LL} |\phi_q^L \phi_p^L\rangle , \quad \mathcal{S}^{LL} |\phi_p^L \psi_q^L\rangle = B_{pq}^{LL} |\psi_q^L \phi_p^L\rangle + C_{pq}^{LL} |\phi_q^L \psi_p^L\rangle ,$$
$$\mathcal{S}^{LL} |\psi_p^L \psi_q^L\rangle = F_{pq}^{LL} |\psi_q^L \psi_p^L\rangle , \quad \mathcal{S}^{LL} |\psi_p^L \phi_q^L\rangle = D_{pq}^{LL} |\phi_q^L \psi_p^L\rangle + E_{pq}^{LL} |\psi_q^L \phi_p^L\rangle . \qquad (2.32)$$

We can rewrite $\mathcal{S}$ as a R-matrix by (graded-)permuting the out-states to yield

$$R^{\text{LL}}(p, q) = \begin{pmatrix} A_{pq}^{LL} & 0 & 0 & 0 \\ 0 & B_{pq}^{LL} & E_{pq}^{LL} & 0 \\ 0 & C_{pq}^{LL} & D_{pq}^{LL} & 0 \\ 0 & 0 & 0 & -F_{pq}^{LL} \end{pmatrix} \qquad (2.33)$$

where the functions on the RHS are given by

$$A_{pq}^{LL} = 1, \qquad\qquad B_{pq}^{LL} = \left(\frac{x_{Lp}^-}{x_p^+}\right)^{1/2} \frac{x_{Lp}^+ - x_{Lq}^+}{x_{Lp}^- - x_{Lq}^+},$$

$$C_{pq}^{LL} = \left(\frac{x_{:p}^- x_{Lq}^+}{x_{Lp}^+ x_{Lq}^-}\right)^{1/2} \frac{x_{Lq}^- - x_{Lq}^+}{x_{Lp}^- - x_{Lq}^+} \frac{\eta_p^L}{\eta_q^L}, \qquad D_{pq}^{LL} = \left(\frac{x_{Lq}^+}{x_{Lq}^-}\right)^{1/2} \frac{x_{Lp}^- - x_{Lq}^-}{x_{Lp}^- - x_{Lq}^+}, \qquad (2.34)$$

$$E_{pq}^{LL} = \frac{x_{Lp}^- - x_{Lp}^+}{x_{Lp}^- - x_{Lq}^+} \frac{\eta_q^L}{\eta_p^L}, \qquad\qquad F_{pq}^{LL} = -\left(\frac{x_{Lp}^- x_{Lq}^+}{x_{Lp}^+ x_{Lq}^-}\right)^{1/2} \frac{x_{Lp}^+ - x_{Lq}^-}{x_{Lp}^- - x_{Lq}^+}.$$

Similarly for same chirality scattering of two $\tilde{\rho}_L$ particles, we have

$$R^{\tilde{L}\tilde{L}}(p, q) = \begin{pmatrix} A_{pq}^{LL} & 0 & 0 & 0 \\ 0 & B_{pq}^{LL} & -E_{pq}^{LL} & 0 \\ 0 & -C_{pq}^{LL} & D_{pq}^{LL} & 0 \\ 0 & 0 & 0 & -F_{pq}^{LL} \end{pmatrix} \qquad (2.35)$$

and for scattering of right particles of same chirality, we can swap L with R in the above equations. We can also have scattering between the two different gradings within same chirality, i.e. $L\tilde{L}$ or $\tilde{L}L$(same with R)

$$R^{\mathrm{L}\tilde{\mathrm{L}}}(p,q) = \begin{pmatrix} A_{pq}^{LL} & 0 & 0 & 0 \\ 0 & B_{pq}^{LL} & E_{pq}^{LL} & 0 \\ 0 & C_{pq}^{LL} & D_{pq}^{LL} & 0 \\ 0 & 0 & 0 & -F_{pq}^{LL} \end{pmatrix} , \; R^{\tilde{\mathrm{L}}\mathrm{L}}(p,q) = \begin{pmatrix} A_{pq}^{LL} & 0 & 0 & 0 \\ 0 & B_{pq}^{LL} & -E_{pq}^{LL} & 0 \\ 0 & -C_{pq}^{LL} & D_{pq}^{LL} & 0 \\ 0 & 0 & 0 & -F_{pq}^{LL} \end{pmatrix}$$
(2.36)

The right chirality matrices can again be obtained by switching L with R above. A slightly different set of functions appear in the mixed chirality S-matrices.

$$R^{\mathrm{LR}}(p,q) = \begin{pmatrix} A_{pq}^{LR} & 0 & 0 & F_{pq}^{LR} \\ 0 & C_{pq}^{LR} & 0 & 0 \\ 0 & 0 & D_{pq}^{LR} & 0 \\ -B_{pq}^{LR} & 0 & 0 & -E_{pq}^{LR} \end{pmatrix} , \; R^{\mathrm{RL}}(p,q) = \begin{pmatrix} A_{pq}^{LR} & 0 & 0 & F_{pq}^{LR} \\ 0 & C_{pq}^{LR} & 0 & 0 \\ 0 & 0 & D_{pq}^{LR} & 0 \\ -B_{pq}^{LR} & 0 & 0 & -E_{pq}^{LR} \end{pmatrix}$$
(2.37)

where the RHS functions is given by

$$A_{pq}^{LR} = \zeta_{pq}^{LR} \left(\frac{x_{Lp}^+}{x_{Lp}^-} \right)^{1/2} \frac{1 - \frac{1}{x_{Lp}^+ x_{Rq}^-}}{1 - \frac{1}{x_{Lp}^- x_{Rq}^-}} , \qquad B_{pq}^{LR} = -\frac{2i}{h} \left(\frac{x_{Lp}^- x_{Rq}^+}{x_p^+ x_{Rq}^-} \right)^{1/2} \frac{\eta_p^L \eta_q^R}{x_{Lp}^- x_{Rq}^+} \frac{\zeta_{pq}^{LR}}{1 - \frac{1}{x_{Lp}^- x_{Lq}^-}} ,$$

$$C_{pq}^{LR} = \zeta_{pq}^{LR} , \qquad D_{pq}^{LR} = \zeta_{pq}^{LR} \left(\frac{x_{Lp}^+ x_{Rq}^+}{x_{Lp}^- x_{Rq}^-} \right)^{1/2} \frac{1 - \frac{1}{x_{Lp}^+ x_{Rq}^+}}{1 - \frac{1}{x_{Lp}^- x_{Rq}^-}} ,$$

$$E_{pq}^{LR} = -\zeta_{pq}^{LR} \left(\frac{x_{Rq}^+}{x_{Rq}^-} \right)^{1/2} \frac{1 - \frac{1}{x_{Lp}^- x_{Rq}^+}}{1 - \frac{1}{x_{Lp}^- x_{Rq}^-}} , \qquad F_{pq}^{LR} = \frac{2i}{h} \left(\frac{x_{Lp}^+ x_{Rq}^+}{x_p^- x_{Rq}^-} \right)^{1/2} \frac{\eta_p^L \eta_q^R}{x_{Lp}^+ x_{Rq}^+} \frac{\zeta_{pq}^{LR}}{1 - \frac{1}{x_{Lp}^- x_{Lq}^-}} .$$
(2.38)

where $\zeta_{pq}^{LR} = e^{-i\frac{p+q}{4}} \sqrt{\frac{1 - \frac{1}{x_{Lp}^- x_{Rq}^-}}{1 - \frac{1}{x_{Lp}^+ x_{Rq}^+}}}$. The remaining choices of chiralities and grading, for instance $(L\tilde{R})$, $(\tilde{L}R)$, $(\tilde{L}\tilde{R})$ are given in terms of the same functions as in equation (2.38)(see appendix G of [58]). Using the above R-matrices, one can go ahead and write down the asymptotic Bethe equations and solve for the spectrum. Wrapping effects can then be incorporated via Luscher corrections or solving the TBA for ground state and excited states (using the contour deformation trick).

The dressing factors that come as overall functions outside the above matrix blocks, have to satisfy physical constraints of crossing and unitarity. Braiding unitarity requires the S-matrix $S(p,q)$ defined in equation (2.31) to satisfy

$$S(p,q)S(q,p) = 1 \tag{2.39}$$

which implies the associated dressing phases have to obey

$$\Sigma_{m_2,m_1}^{LL}(p_2,p_1)\Sigma_{m_1,m_2}^{LL}(p_1,p_2) = 1 , \; \Sigma_{m_2,m_1}^{RR}(p_2,p_1)\Sigma_{m_1,m_2}^{RR}(p_1,p_2) = 1 ,$$
$$\Sigma_{m_2,m_1}^{LR}(p_2,p_1)\Sigma_{m_1,m_2}^{RL}(p_1,p_2) = 1 . \tag{2.40}$$

We also impose reality for the S-matrix by requiring physical unitarity

$$S^\dagger(p,q)S(p,q) = 1 \tag{2.41}$$

27

which gives the dressing constraints

$$(\Sigma^{LL}_{m_1,m_2}(p_1,p_2))^\star \Sigma^{LL}_{m_1,m_2}(p_1,p_2) = 1 \,, \quad (\Sigma^{RR}_{m_1,m_2}(p_1,p_2))^\star \Sigma^{RR}_{m_1,m_2}(p_1,p_2) = 1$$
$$(\Sigma^{LR}_{m_1,m_2}(p_1,p_2))^\star \Sigma^{LR}_{m_1,m_2}(p_1,p_2) = 1 \,, \quad (\Sigma^{RL}_{m_1,m_2}(p_1,p_2))^\star \Sigma^{RL}_{m_1,m_2}(p_1,p_2) = 1 \qquad (2.42)$$

Furthermore, we have crossing constraints that relate the S-matrix in the physical region on the spectral plane to other sheets accessible by crossing branch-cuts on the physical sheet, commonly referred to as the crossed regions. Identifying the charge conjugation matrix that transforms particles to anti-particles as $\mathcal{C}$ (see [58] for details), we get the following identity for crossing

$$\mathcal{C}_1.S^{t_1}(\bar{p},q).\mathcal{C}_1^{-1}.S(p,q) = \mathbf{I} \,, \qquad (2.43)$$

where $\mathcal{C}_1 = \mathcal{C} \otimes \mathbf{I}$ acts only on the first particle, and t_1 refers to matrix transposition in the first space. The Zhukovski variables corresponding to the crossed momenta can be related to the physical ones as

$$x^\pm_L(\bar{p}) = \frac{1}{x^\pm_R(p)} \,, \quad x^\pm_R(\bar{p}) = \frac{1}{x^\pm_L(p)} \,. \qquad (2.44)$$

One can similarly write a crossing equation for the second particle. Writing down the crossing equations separately for each pair of chirality and extracting contributions from the matrix parts, we are left with the following conditions for the dressing phases

$$\Sigma^{RL}_{m_1,m_2}(x_R(\bar{p}_1), x_L(p_2))\Sigma^{LL}_{m_1,m_2}(x_L(p_1), x_L(p_2)) = c(x_{L1}, x_{L2}) \,,$$
$$\Sigma^{LL}_{m_1,m_2}(x_L(\bar{p}_1), x_L(p_2))\Sigma^{RL}_{m_1,m_2}(x_R(p_1), x_L(p_2)) = \tilde{c}(x_{R1}, x_{L2}) \,,$$
$$\Sigma^{LR}_{m_1,m_2}(x_L(\bar{p}_1), x_R(p_2))\Sigma^{RR}_{m_1,m_2}(x_R(p_1), x_R(p_2)) = c(x_{R1}, x_{R2}) \,,$$
$$\Sigma^{RR}_{m_1,m_2}(x_R(\bar{p}_1), x_R(p_2))\Sigma^{LR}_{m_1,m_2}(x_L(p_1), x_R(p_2)) = \tilde{c}(x_{L1}, x_{R2}) \,, \qquad (2.45)$$

where

$$c(x_1, x_2) = \left(\frac{x_1^+}{x_1^-}\right)^{1/4} \left(\frac{x_2^+}{x_2^-}\right)^{-1/4} \frac{x_1^- - x_2^-}{x_1^+ - x_2^-} \sqrt{\frac{x_1^+ - x_2^+}{x_1^- - x_2^-}} \,,$$

$$\tilde{c}(x_1, x_2) = \left(\frac{x_1^+}{x_1^-}\right)^{-1/4} \left(\frac{x_2^+}{x_2^-}\right)^{-3/4} \frac{1 - x_1^- x_2^+}{1 - x_1^- x_2^-} \sqrt{\frac{1 - \frac{1}{x_1^- - x_2^-}}{1 - \frac{1}{x_1^+ - x_2^+}}} \qquad (2.46)$$

The all-loop Bethe ansatz equations for $d(2,1;\alpha)^2$ using these S-matrices was first proposed in [11]. The overall normalisations that reflect the correct bound-state pole structure and are consistent with DHM-type double poles still need to be identified in the context of $AdS_3 \times S^3 \times S^3 \times S^1$. On the other hand, the crossing equations in $AdS_3 \times S^3 \times T^4$ have been solved in pure RR backgrounds recently in [59]. For more general mixed flux backgrounds, it is an active area of research right now.

2.2.1 $\quad \mathbf{AdS}_3 \times \mathbf{S}^3 \times \mathbf{T}^4$

Let us briefly review the $AdS_3 \times S^3 \times T^4$ S-matrices and asymptotic Bethe equations. This will be useful in setting up Algebraic Bethe ansatz for the computation of protected states in section (4). As we discussed earlier, the $AdS_3 \times S^3 \times T^4$ S-matrices arise in the

limits $\alpha \to 0, 1$ of the $\text{AdS}_3 \times \text{S}^3 \times \text{S}^3 \times \text{S}^1$ S-matrices. The off-shell symmetry algebra $\mathcal{A}$ is

$$\mathcal{A} = \text{psu}(1|1)^4_{\text{c.e.}} \subset \text{psu}(1,1|2)^2 \tag{2.47}$$

The $\text{psu}(1|1)^4_{\text{c.e.}}$ S-matrices are obtained by tensoring two copies of the above $\text{psu}(1|1)^2_{\text{c.e.}}$ S-matrices

$$\mathcal{S}_{\text{psu}(1|1)^4_{\text{c.e.}}} = \mathcal{S}_{\text{psu}(1|1)^2_{\text{c.e.}}} \check{\otimes} \mathcal{S}_{\text{psu}(1|1)^2_{\text{c.e.}}} , \tag{2.48}$$

where $\check{\otimes}$ refers to the graded tensor-product operation. The full S-matrix can be subdivided into blocks: massive ($\mathcal{S}^{\bullet\bullet}$), mixed-mass ($\mathcal{S}^{\bullet\circ}$), and massless ($\mathcal{S}^{\circ\circ}$)

$$\mathcal{S}^{\bullet\bullet} = \begin{pmatrix} \sigma^{\bullet\bullet}_{LL} \mathcal{S}^{LL} \check{\otimes} \mathcal{S}^{LL} & \tilde{\sigma}^{\bullet\bullet}_{RL} \mathcal{S}^{RL} \check{\otimes} \mathcal{S}^{RL} \\ \tilde{\sigma}^{\bullet\bullet}_{LR} \mathcal{S}^{LR} \check{\otimes} \mathcal{S}^{LR} & \sigma^{\bullet\bullet}_{RR} \mathcal{S}^{RR} \check{\otimes} \mathcal{S}^{RR} \end{pmatrix} ,$$

$$\mathcal{S}^{\circ\circ} = \sigma^{\circ\circ} \mathcal{S}_{su(2)} \otimes (\mathcal{S}^{LL} \check{\otimes} \mathcal{S}^{LL}) ,$$

$$\mathcal{S}^{\bullet\circ} = [\sigma^{\bullet\circ}_L (\mathcal{S}^{LL} \otimes \mathcal{S}^{L\tilde{L}})^{\oplus 2}] \oplus [\sigma^{\bullet\circ}_R (\mathcal{S}^{RL} \otimes \mathcal{S}^{R\tilde{L}})^{\oplus 2}] ,$$

$$\mathcal{S}^{\circ\bullet} = [\sigma^{\circ\bullet}_L (\mathcal{S}^{LL} \otimes \mathcal{S}^{\tilde{L}L})^{\oplus 2}] \oplus [\sigma^{\circ\bullet}_R (\mathcal{S}^{LR} \otimes \mathcal{S}^{\tilde{L}R})^{\oplus 2}] , \tag{2.49}$$

where $\mathcal{S}^{AB}, A, B \in \{L, R, \tilde{L}, \tilde{R}\}$ are the different $\text{su}(1|1)^2_{\text{c.e.}}$ S-matrices from last subsection, and $\mathcal{S}_{su(2)}$ is the S-matrix of the Heisenberg spin chain, and $\sigma^{\bullet\bullet}, \tilde{\sigma}^{\bullet\bullet}$ are massive, $\sigma^{\bullet\circ}, \sigma^{\circ\bullet}$ are mixed-mass, and $\sigma^{\circ\circ}$ is the massless dressing factor. $\sigma^{\bullet\circ}, \sigma^{\circ\bullet}$ are related by unitarity, thus leaving 4 undetermined functions that need to be solved using crossing equations.

The Bethe equations in bosonic grading (see [64]) comprise of those for massive momentum-carrying L, and R roots with rapidities $x_k^\pm$ and $\bar{x}_k^\pm$ respectively, and massless roots with rapidities $w_k^\pm$, plus auxiliary roots $y_{I,k}, I = 1, 3$

$$\left(\frac{x_k^+}{x_k^-}\right)^L = \prod_{j\neq k}^{N_2} \nu_k^{-1} \nu_j \frac{x_k^+ - x_j^-}{x_k^- - x_j^+} \frac{1 - \frac{1}{x_k^+ x_j^-}}{1 - \frac{1}{x_k^- x_j^+}} (\sigma_{kj}^{\bullet\bullet})^2 \prod_j^{N_1} \nu_k^{1/2} \frac{x_k^- - y_{1,j}}{x_k^+ - y_{1,j}} \prod_j^{N_3} \nu_k^{1/2} \frac{x_k^- - y_{3,j}}{x_k^+ - y_{3,j}}$$

$$\times \prod_j^{N_{\bar{2}}} \nu_j \frac{1 - \frac{1}{x_k^+ \bar{x}_j^+}}{1 - \frac{1}{x_k^- \bar{x}_j^-}} \frac{1 - \frac{1}{x_k^+ \bar{x}_j^-}}{1 - \frac{1}{x_k^- \bar{x}_j^+}} (\tilde{\sigma}_{kj}^{\bullet\bullet})^2$$

$$\times \prod_j^{N_0} \nu_k^{-1/2} \nu_j \frac{x_k^+ - z_j^-}{x_k^- - z_j^+} \left(\frac{1 - \frac{1}{x_k^- z_j^-}}{1 - \frac{1}{x_k^+ z_j^+}}\right)^{1/2} \left(\frac{1 - \frac{1}{x_k^+ z_j^-}}{1 - \frac{1}{x_k^- z_j^+}}\right)^{1/2} (\sigma_{kj}^{\bullet\circ})^2 \tag{2.50}$$

$$\left(\frac{\bar{x}_k^+}{\bar{x}_k^-}\right)^L = \prod_{j\neq k}^{N_{\bar{2}}} \frac{\bar{x}_k^+ - \bar{x}_j^-}{\bar{x}_k^- - \bar{x}_j^+} \frac{1 - \frac{1}{\bar{x}_k^+ \bar{x}_j^-}}{1 - \frac{1}{\bar{x}_k^- \bar{x}_j^+}} (\sigma_{kj}^{\bullet\bullet})^2 \prod_j^{N_1} \nu_k^{1/2} \frac{1 - \frac{1}{\bar{x}_k^+ y_{1,j}}}{1 - \frac{1}{\bar{x}_k^- y_{1,j}}} \prod_j^{N_3} \nu_k^{1/2} \frac{1 - \frac{1}{\bar{x}_k^+ y_{3,j}}}{1 - \frac{1}{\bar{x}_k^- y_{3,j}}}$$

$$\times \prod_j^{N_2} \nu_k^{-1} \frac{1 - \frac{1}{\bar{x}_k^- x_j^-}}{1 - \frac{1}{\bar{x}_k^+ x_j^+}} \frac{1 - \frac{1}{\bar{x}_k^+ x_j^-}}{1 - \frac{1}{\bar{x}_k^- x_j^+}} (\tilde{\sigma}_{kj}^{\bullet\bullet})^2$$

$$\times \prod_j^{N_0} \nu_k^{-1/2} \nu_j \frac{x_k^+ - z_j^-}{x_k^- - z_j^+} \left(\frac{1 - \frac{1}{\bar{x}_k^- z_j^-}}{1 - \frac{1}{\bar{x}_k^+ z_j^+}}\right)^{3/2} \left(\frac{1 - \frac{1}{\bar{x}_k^+ z_j^-}}{1 - \frac{1}{\bar{x}_k^- z_j^+}}\right)^{1/2} (\sigma_{kj}^{\bullet\circ})^2 \tag{2.51}$$

29

$$\left(\frac{z_k^+}{z_k^-}\right)^L = \prod_{j\neq k}^{N_0} \nu_k^{-1/2}\nu_j^{1/2}\frac{z_k^+ - z_j^-}{z_k^- - z_j^+}(\sigma_{kj}^{\circ\circ})^2 \prod_{j}^{N_1} \nu_k^{1/2}\frac{z_k^- - y_{1,j}}{z_k^+ - y_{1,j}} \prod_{j}^{N_3} \nu_k^{1/2}\frac{z_k^- - y_{3,j}}{z_k^+ - y_{3,j}}$$

$$\prod_{j}^{N_2} \nu_k^{-1}\nu_j^{1/2}\frac{z_k^+ - x_j^-}{z_k^- - x_j^+}\left(\frac{1-\frac{1}{z_k^+ x_j^-}}{1-\frac{1}{z_k^- x_j^+}}\right)^{1/2}\left(\frac{1-\frac{1}{z_k^+ x_j^-}}{1-\frac{1}{z_k^- x_j^+}}\right)^{1/2}(\sigma_{kj}^{\circ\bullet})^2$$

$$\prod_{j}^{N_{\bar 2}} \nu_j^{1/2}\left(\frac{1-\frac{1}{z_k^+ \bar x_j^+}}{1-\frac{1}{z_k^- \bar x_j^-}}\right)^{3/2}\left(\frac{1-\frac{1}{z_k^+ \bar x_j^-}}{1-\frac{1}{z_k^- \bar x_j^+}}\right)^{1/2}(\sigma_{kj}^{\circ\bullet})^2 \tag{2.52}$$

$$1 = \prod_{j=1}^{N_2} \nu_j^{-1/2}\frac{y_{I,k}-x_j^+}{y_{I,k}-x_j^-} \prod_{j=1}^{N_{\bar 2}} \nu_j^{-1/2}\frac{1-\frac{1}{y_{I,k}-\bar x_j^-}}{1-\frac{1}{y_{I,k}\bar x_j^-}} \prod_{j=1}^{N_0} \nu_j^{-1/2}\frac{y_{I,k}-z_j^+}{y_{I,k}-z_j^-}, \quad I = 1,3 \tag{2.53}$$

where $N_2, N_{\bar 2}, N_0$ are the number of massive L, massive R, and massless Bethe roots while N_1, N_3 are the number of auxiliary roots. Physical states further satisfy level-matching condition

$$1 = \prod_{j=1}^{N_2}\frac{x_j^+}{x_j^-} \prod_{j=1}^{N_{\bar 2}}\frac{\bar x_j^+}{\bar x_j^-} \prod_{j=1}^{N_0}\frac{z_j^+}{z_j^-} \tag{2.54}$$

Solution to the above set of equation gives rise to a state with energy

$$D - J = N_2 + N_{\bar 2} + ih\sum_{k=1}^{N_2}\left(\frac{1}{x_k^+}-\frac{1}{x_k^-}\right) + ih\sum_{k=1}^{N_{\bar 2}}\left(\frac{1}{\bar x_k^+}-\frac{1}{\bar x_k^-}\right) + ih\sum_{k=1}^{N_0}\left(\frac{1}{z_k^+}-\frac{1}{z_k^-}\right) \tag{2.55}$$

In section 4, we will be using the above Bethe equations, especially the auxiliary and massless Bethe equations. We will see how zero-momentum limit for the massless modes affects the auxiliary roots. This will then allow us to generate protected states on top of the BMN vacuum in $\text{AdS}_3 \times \text{S}^3 \times \text{T}^4$ supported by mixed-flux, plus its orbifolds. Derivation of the auxiliary Bethe equation is given in Appendix A.

3 Tools from machine learning: neural networks and more

We shall discuss the fundamentals of neural networks in this section that will be relevant for their applications in later sections. We begin with a *dense neural networks*, also known as *multi-layer perceptrons* (MLPs), schematically displayed in Figure 1.

These networks consist of an *input layer* $a^{in} = (a_0^{in}, a_1^{in}, \dots a_{n_0}^{in})^{\text{T}} \in \mathbb{R}^{n_0}$, followed by a series of *fully connected layers* known as *hidden layers*, and terminate in an *output layer* $a^{out} = (a_0^{out}, a_1^{out}, \dots a_{n_{L+1}}^{out})^{\text{T}} \in \mathbb{R}^{n_{L+1}}$. Data is read in to the network at the input layer and the output is collected at the output layer. There are L fully connected layers in this network, where the ℓ-th layer contains n_ℓ neurons. Each neuron $a_m^{(l)}$ in a l-th fully connected layer receives inputs from *all* the neurons in the previous $(l-1)$-th layer and the output of the neuron is in turn fed as an input to neurons in the succeeding layer:
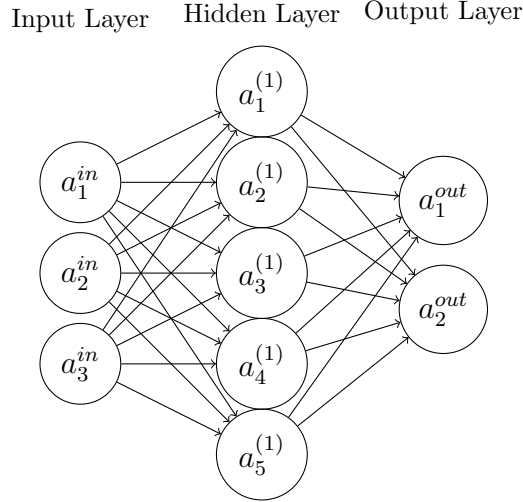
Figure 1: Multilayer Perceptron with one hidden layer $L = 1$ of width $n_1 = 5$, input of size $n_0 = 3$ and output of size $n_2 = 2$

$$
\begin{pmatrix} a_1^{(\ell)} \\ a_2^{(\ell)} \\ \vdots \\ a_{n_\ell}^{(\ell)} \end{pmatrix} = h \left[\begin{pmatrix} w_{1,0}^{(\ell)} & w_{1,1}^{(\ell)} & \cdots & w_{1,n_{\ell-1}}^{(\ell)} \\ w_{2,0}^{(\ell)} & w_{2,1}^{(\ell)} & \cdots & w_{2,n_{\ell-1}}^{(\ell)} \\ \vdots & \vdots & \ddots & \vdots \\ w_{n_\ell,0}^{(\ell)} & w_{n_\ell,1}^{(\ell)} & \cdots & w_{n_\ell,n_{\ell-1}}^{(\ell)} \end{pmatrix} \begin{pmatrix} a_1^{(\ell-1)} \\ a_2^{(\ell-1)} \\ \vdots \\ a_{n_{\ell-1}}^{(\ell-1)} \end{pmatrix} + \begin{pmatrix} b_1^{(\ell)} \\ b_2^{(\ell)} \\ \vdots \\ b_{n_\ell}^{(\ell)} \end{pmatrix} \right] , \quad \ell = 1, \ldots L + 1 ,
$$

(3.1)

where $w^{(l)} \in \mathcal{M}(n_l, n_{l-1}, \mathbb{R})$ is a *weight matrix*, $b^{(l)} \in \mathbb{R}^{n_l}$ - *bias vector*, $h(z)$ is in general a non-linear, non-polynomial function known as the *activation function* acting component-wise :

$$
h \begin{pmatrix} z_1 \\ z_2 \\ \vdots \\ z_n \end{pmatrix} = \begin{pmatrix} h(z_1) \\ h(z_2) \\ \vdots \\ h(z_n) \end{pmatrix} .
$$

(3.2)

In (3.1) we also identify $a^{(0)} = a^{in}$ and $a^{(L+1)} = a^{out}$ with input and output layers respectively. Introducing shorthand notation for the affine transformations in equation (3.1) as $A^{(\ell)}(a^{(\ell-1)}) \equiv w^{(\ell)}a^{(\ell-1)} + b^{(\ell)}$, the neural network $a^{out}(a^{in}) : \mathbb{R}^{n_0} \to \mathbb{R}^{n_{L+1}}$ can be expressed as compositions of affine transformations, and activation functions:

$$
a^{out} = h \circ A^{L+1} \circ h \circ A^L \circ \ldots \circ h \circ A^1 \circ a^{in}
$$

(3.3)

The output function of the neural network is tuned by tuning the weights and biases. It is by now well established that such neural networks are a highly expressive framework capable of approximation of extremely complex functions, and indeed there exists a series of mathematical proofs which attest to their *universal approximation* property, e.g. [65, 66, 67, 68, 69]. This property, along with the feature learning capability of deep neural networks is the key driver to the automated search for R-matrices which we have implemented here.

A natural generalisation of the MLPs involve removing some of the neuron connections of the aforementioned dense network. This is called pruning and is usually done in

larger networks. Such sparse networks tend to lead to better generalisation to unseen datasets, while being harder/slower to train than MLPs. Besides the MLP, other popular neural network (NN) architectures include the convolutional neural network (for natural language processing and computer vision), the recurrent neural networks (for sequential data), and transformers (for text-classification and generation). We shall avoid discussing these in any detail since they are not used in our research works.

3.1 Supervised learning: loss functions

Supervised learning involves training the neural network on input-output dataset $\mathcal{D} = \{(x, y)\}$, where y is the target output for given input vector x. *Training* involves updating the network weights and biases (symbolically represented below as θ) in order to fit the above data $\mathcal{D}$

$$f_\theta(x) \approx y \qquad \forall \qquad (x, y) \in \mathcal{D}, \tag{3.4}$$

by minimising some target loss-function $\mathcal{L}(\mathcal{D}, f_\theta)$ which provides a measure of the discrepancy between the actual and desired properties of the function f. For regression tasks, a popular class of such loss-functions are the powers of absolute error

$$\mathcal{L}(\mathcal{D}, f_\theta) = \sum_{(x,y)\in\mathcal{D}} |y - f_\theta(x)|^q, \tag{3.5}$$

where $q = 1$ corresponds to the *mean average error*(MAE) or L1 loss, and $q = 2$ to the *mean square error*(MSE) or L2 loss, respectively. Another popular choice is the log cosh error

$$\mathcal{L}_{log-cosh}(\mathcal{D}, f_\theta) = \sum_{(x,y)\in\mathcal{D}} \log(\cosh(y - f_\theta)). \tag{3.6}$$

The network parameters θ get updated iteratively following gradient descent methods like stochastic gradient descent. For classification tasks, i.e. when the output takes discrete set of values (binary or multi-class), some popular choices of loss functions are the cross-entropy loss $\mathcal{L}_{c.e.}$ and the hinge loss $\mathcal{L}_{hinge}$. For binary classification with outputs 0 and 1, these are

$$\mathcal{L}_{c.e.}(\mathcal{D}, f_\theta) = -\sum_{(x,y)\in\mathcal{D}} (y \log(f_\theta(x)) + (1 - y) \log(1 - f_\theta(x))), \tag{3.7}$$

$$\mathcal{L}_{hinge}(\mathcal{D}, f_\theta) = \sum_{(x,y)\in\mathcal{D}} \max(0, 1 - (2y - 1)(2f_\theta(x) - 1)). \tag{3.8}$$

Evolution of training and test loss functions during training of the neural network provides information about the degree of learning and ability to generalise to unseen data. For small networks, one usually ends up with training losses that saturate at high non-zero values due to under-fitting of the training data. On the other hand, using very deep/big networks can lead to over-parameterisation, which is usually indicated by high test losses. This is depicted in figure 2 of training and validation accuracy curves on a image-classification task using a convolutional neural network known as LeNet [70] on the CIFAR-10 dataset [71].

Aside from the NN architecture, hyperparameter-tuning plays an important role on the evolution of the losses. We shall discuss this in the following sub-section on optimisation algorithms.
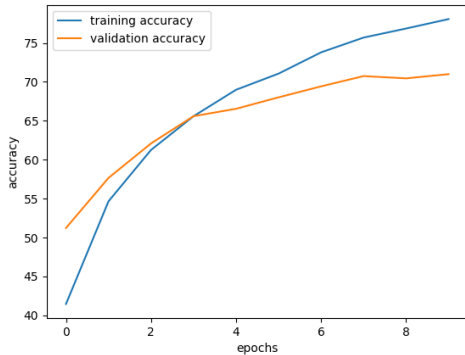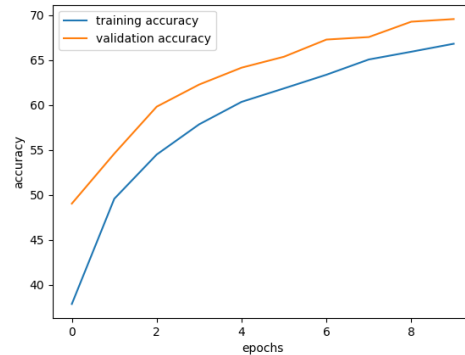
Figure 2: Overfitting during training (for 10 epochs) remedied by enlarging the CIFAR-10 dataset using data-augmentation techniques. Here, we measure the training and validation accuracies in percentage.

3.2 Activation functions

Activation functions introduce non-linearity in the hypothesis space for the neural network, and play a crucial role in feature learning. They are crucial in gradient propagation during back-propagation, and absence of vanishing or exploding gradient of these functions is integral to effective training. Popular choices of activation functions for classification tasks include sigmoid (binary) and softmax (multi-class) activations

$$\sigma_{sigmoid}(x) = \frac{1}{1 + e^{-x}} \tag{3.9}$$

$$\sigma_{softmax}(\vec{x})_i = \frac{e^{x_i}}{\sum_{j=1}^{N} e^{x_j}} \tag{3.10}$$

while for regression tasks some popular options are tanh, (leaky)ReLU and swish activations

$$\sigma_{tanh}(x) = \tanh(x) \tag{3.11}$$

$$\sigma_{relu}(x; \alpha) = \max(\alpha x, x), \quad 0 \leqslant \alpha \leqslant 1 \tag{3.12}$$

$$\sigma_{swish}(x; \beta) = x \times \sigma_{sigmoid}(\beta x) \tag{3.13}$$

Note the ReLU activation becomes linear in the limit $\alpha = 1$. We will compare their relative performance on different experiments in the later sections.

3.3 Optimisation algorithms

Optimisation algorithms are key to the training of the network parameters to better approximate the target function. Common algorithms include stochastic gradient descent (SGD), stochastic gradient descent with momentum (SGDM), and adaptive learning methods (AdaGrad, RMSProp, and ADAM). Stochastic gradient descent updates the weights and biases after a forward pass of mini-batches of training data through the network, by a term proportional to the gradient of the loss function with respect to the corresponding parameter

$$\Delta\theta_{t+1} \equiv \theta_{t+1} - \theta_t = -\eta \frac{\partial \mathcal{L}}{\partial \theta_t} \tag{3.14}$$

where the hyperparameter η is known as the learning rate. This protocol performs well to find points with vanishing gradients. Stochastic gradient descent with momentum helps to avoid being stuck on local minima and saddle points in SGD, by weighted-averaging over previous gradient steps. This is done by introducing auxiliary momentum variables π_t for each of the physical weight and bias parameters θ_t and using update rule

$$\Delta\pi_{t+1} \equiv \pi_{t+1} - \pi_t = -(1-\beta)\pi_t - \frac{\partial\mathcal{L}}{\partial\theta_t}\,, \quad \Delta\theta_t \equiv \theta_{t+1} - \theta_t = \eta\pi_{t+1}\,, \tag{3.15}$$

where $\beta \in (0,1)$ is called the momentum parameter, with $\beta = 0$ realising the naive SGD limit. Adaptive algorithms such as AdaGrad, RMSProp, and ADAM change the learning rate η for each of the weight and bias parameters separately based on prior training history. They use moving average estimates (mean and higher moments) for the loss-gradients to inform these updates. We will mostly be employing ADAM optimizer in our experiments. The corresponding update equations[72] for the network parameters are

$$\theta_{t+1} = \theta_t - \alpha\frac{\hat{m}_{t+1}}{\sqrt{\hat{v}_{t+1}} + \epsilon}\,, \tag{3.16}$$

where

$$\hat{m}_{t+1} = \frac{m_{t+1}}{1 - \beta_1^{t+1}}\,, \quad m_{t+1} = \beta_1 m_t + (1-\beta_1)g_t\,,$$
$$\hat{v}_{t+1} = \frac{v_{t+1}}{1 - \beta_2^{t+1}}\,, \quad v_{t+1} = \beta_2 v_t + (1-\beta_2)g_t^2\,, \tag{3.17}$$

with $g_t = \frac{\partial\mathcal{L}}{\partial\theta_t}$, hyperparameters $\alpha, \beta_1, \beta_2 \in [0,1)$ and small regularisation paramater $\epsilon << 1$. Their default values are $\alpha = 0.001$, $\beta_1 = 0.9$, $\beta_2 = 0.999$, $\epsilon = 10^{-8}$. The default initial values are $m_0 = v_0 = 0$. We get back SGDM in the limit $\beta_2 = 1$ and SGD by further setting $\beta_1 = 0$.

There are interesting alternative optimisation algorithms that have been proposed recently[73, 74]. One can use an energy functional to flow down the loss landscape along constant-energy orbits. In this picture, the SGD is a friction-dominated energy-losing trajectory. It is unclear as of now, which problems are better-suited to this kind of approach versus aforementioned standard protocols.

In all the above protocols, finding the optimal hyperparameters for a given task that efficiently minimises the losses during training is a bottleneck. Usually one selects them by experimenting with a spread of values. However, there are interesting features and possibilities that might be missed without exploring a big enough search space. For instance, the catapult mechanism in overparametrised networks at super-critical learning rate $\eta > 1$ in SGD and similar algorithms that leads to better generalisation than sub-critical values $\eta << 1$. In our works, such issues have not been very visible - nonetheless important to keep in mind.

3.4   Physics Inspired Neural Networks (PINNs)

PINNs are a special class of NN architectures wherein one uses custom loss functions to drive the NN function approximator to desired solution of target optimisation problem. One starts with a system of constraint equations C_j for a set of functions f_i

$$C_j(\{f_i\}_{i=1}^N) = 0\,, \tag{3.18}$$

where f_i can include fields as well as their space-time derivatives. One implements these constraints/ equations of motions as loss terms

$$\mathcal{L} = \sum_j |C_j|^{a_j}, \quad a_j > 0.$$ (3.19)

Although this term is specifically used for solving differential and integral equations, I am abusing it here to include functional equations as well. This method has been successfully employed for well-known problems such as heat equation, Poisson equation, and fluid dynamics [75, 76]. In more specialised settings, they have been employed to learn about string field theory amplitudes by studying Strebel differentials [77], quasinormal modes of near-extremal black holes [78], and time-dependent Schrodinger equations [79]. We employ a similar strategy to set up a search program for quantum integrable spin chains in the function space modelling R-matrices.

3.5   Beyond MLPs and supervised learning

Unsupervised learning provides a complementary set of tools to discover features in generic datasets. Unlike supervised learning, there is no apriori input-output form of the data. The popular tools within this framework that were used in the research works include K-means clustering and principal component analysis (PCA). K-means clustering is an algorithm to segregrate the dataset into finite number of distinct clusters by optimising their distance from certain central points. One needs to specify the number of clusters k beforehand for this method to work. The algorithm then finds central points m_i, such that the following distance is minimized

$$\mathcal{D} = \sum_j \min_i(||x_j - m_i||)$$ (3.20)

where $||.||$ is usually the L2 norm, and the sum on the RHS runs over all the dataset points x_j. One initialises the centers randomly, and clusters the dataset points by computing their distances from each of the centers and choosing the minimal one. Then one keeps updating the centers as the mean of the respective clusters, and re-evaluating the cluster-assignment for the dataset points from the new centers. Iterating this process, we get to the desired configuration of k centers that minimise $\mathcal{D}$. Some popular generalisations/variations of this algorithm are K-means minibatch clustering, K-median clustering, and mean shift clustering, the last of which does not require us to fix the number of clusters k apriori. Other standard methods of clustering include Gaussian expectation-maximization, BIRCH and DBSCAN. One major problem that appears when using this technique is known as the curse of dimensionality which happens when the feature space grows in dimension. This refers to the fact that distances between points distributed uniformly in some compact ball of say radius 1, grows as one increases the number of dimensions, tending to 1 asymptotically. As we shall see in later sections, this issue does not affect us since the solution spaces we encounter are relatively low-dimensional.

PCA is a feature-extraction technique from the dataset that allows one to identify low-dimensional subspaces containing most of the useful information. One projects the dataset from the full feature space to a few linear combinations of the basis vectors. This is done by first computing the $F \times F$ covariance matrix C of the dataset $\{\vec{x}_i\}_{i=1}^N$ of size

N, F being the feature space dimensionality, i.e. size of each vector $\vec{x}_i = (x_i^1, \ldots x_i^F)^T$

$$C = A^T A, \qquad A_{ij} = x_i^j - \frac{1}{N} \sum_{k=1}^{N} x_k^j. \tag{3.21}$$

Then we project the dataset along the eigendirections corresponding to the largest set of m (fixed) eigenvalues. The value of m is set by requiring that the m largest eigenvalues of the covariance matrix C, denoted by the ordered set $\{\lambda_i\}_{i=1}^F$, add up to some threshold fraction f_{th} of the total sum of eigenvalues

$$\frac{\sum_{i \leqslant m} \lambda_i}{\sum_{i=1}^{N} \lambda_i} \geqslant f_{th} \tag{3.22}$$

This measure is known as maximum variance explained (MVE). PCA is a crucial tool that people often use to bypass the curse of dimensionality, which refers to the issues in training input datasets with too many feature dimensions. As part of the PhD work, PCA has been used in the analysis of polytopes and their properties, but this topic is not included in this thesis.

Reinforcement learning, although introduced naturally in the context of robotics, games and strategies, has seen diverse applications in theoretical and mathematical physics. Varying degrees of success have been achieved via the use of actor critic algorithms like SAC and A3C, Trust Region Policy Optimisation (TRPO) and Proximal Policy Optimisation (PPO) among others, in CFT bootstrap[80, 81, 82], string vacua searches[83], knot theory[84], quantum computing and quantum error correction[85]. In all these scenarios, one begins by posing a Markov decision problem (MDP), which is then solved by optimising neural network components modelling the value and policy functions. We shall not delve further into these topics since they are not used in the works discussed in the upcoming sections, and instead are part of ongoing research directions.

4   Protected states in AdS$_3$ backgrounds from integrability

In this work [50], we write down the Algebraic Bethe Ansatz for string theory on AdS$_3$ × S^3 × T^4 and AdS$_3$ × S^3 × K3 in its orbifold limits. We use it to determine the wavefunctions of protected closed strings in these backgrounds and prove that their energies are protected to all orders in α'. We further apply the ABA to find the wave functions of protected states of AdS$_3$ × S^3 × S^3 × S^1 and its $\mathbf{Z}_2$ orbifold. Our findings match with protected spectrum calculations from supergravity, Sym^N orbifolds and apply to the complete moduli space of these theories, excluding orbifold blow-up modes for which further analysis is necessary. The author is the main contributor to the ABA analysis from section 4.1-4.4, which is the central focus of the paper. This work builds upon the previous work of the other collaborators in [49] where they argue for the presence of the protected states in AdS$_3$ × S^3 × T^4 and AdS$_3$ × S^3 × S^3 × S^1 backgrounds based on the all-loop Bethe equations. We provide a novel formalism to understand these states as wavefunctions using ABA and also construct these states on integrable orbifolds.

Integrability offers a novel way to prove non-renormalization theorems, since one can show exactly in λ that certain BPS operators' dimensions do not receive quantum

corrections. In the planar limit, integrable $\text{AdS}_5 \times \text{S}^5$ and $\text{AdS}_4 \times \text{CP}^3$ backgrounds have only one protected multiplet for each value of global charges[3]. Geometrically, this corresponds to the supersymmetric light-ray, or Berenstein-Maldacena-Nastase (BMN) geodesic [29], while in the gauge theory language protected operators are the (unique) ferromagnetic groundstates of the Minahan-Zarembo spin-chains [1].[4]

The protected-spectrum of integrable $\text{AdS}_3/\text{CFT}_2$ backgrounds [10, 11, 12] is much richer, with several multiplets for a given set of charges. In the integrable formulation, these extra multiplets appear because the worldsheet theory has fermionic massless excitations [48]. Such excitations have zero energy in the zero-momentum limit but are not descendents of the BMN vacuum. Further, for each set of charges one can find solutions of the exact Bethe equations [87, 64] with the correct multiplicities to match the supergravity and Sym^N orbifold calculations [88, 89]. Since integrability methods are exact in α', they give $\text{AdS}_3 \times \text{S}^3 \times \mathcal{M}_4$ non-renormalization theorems for *all* half- and quarter-BPS states of $\mathcal{M}_4 = \text{T}^4$ and $\mathcal{M}_4 = \text{S}^3 \times \text{S}^1$, respectively [87, 49]. These backgrounds have a 20, respectively 2, dimensional moduli space on which integrability continues to hold [16]. From this we can immediately conclude that half-, respectively quarter-BPS, states are protected across the whole moduli space, matching in particular the Wess-Zumino-Witten (WZW) point results [90, 89]. These findings are also in agreement with the non-renormalization results [91] applicable to the $\mathcal{M}_4 = \text{T}^4$ case.

As in other integrable models, Bethe equations (BEs) are valid in the large worldsheet radius limit with generic states receiving wrapping corrections. These are especially important when the theory has massless modes [92, 93]. It is known that protected states do not receive wrapping corrections at leading-order [49] and it is likely that the argument can be generalised to all orders of wrapping using the exact massless TBA [94, 95].

In this work we find the Bethe eigenvectors for massless low-magnon excitations using the Algebraic Bethe Ansatz (ABA). Low-lying states in integrable field theories are analogous to conventional Minkowski spacetime string states with a few oscillator excitations above the vacuum, for example

$$|v\rangle \equiv \left(\alpha_{p_1}^i\right)^\dagger \left(\text{S}_{p_2}^{\dot{a}}\right)^\dagger \left(\tilde{\alpha}_{p_3}^j\right)^\dagger |0\rangle. \tag{4.1}$$

Each of the three magnons above sits in a short representation of the supersymmetry algebra $\text{psu}(1|1)_{\text{c.e.}}^4$ unbroken by the BMN vacuum.[5] The indices i and $\dot{a}$ are the usual transverse $\mathbf{8}_v$ and $\mathbf{8}_c$ indices of the light-cone $\text{so}(8)$ algebra [96], which now break-up into several representations of the (abelian) bosonic subalgebra of $\text{psu}(1|1)_{\text{c.e.}}^4$, depending on the mass m of the magnon. The energy of the above state is the sum of the energies of the individual magnons

$$E(v) = E(p_1) + E(p_2) + E(p_3), \tag{4.2}$$

each of which satisfies the exact dispersion relation dictated by the shortening condition [97, 57]

$$E(p_i) = \sqrt{(m_i + k p_i)^2 + 4h^2 \sin^2 \tfrac{p_i}{2}}. \tag{4.3}$$

Above, $2\pi k \in \mathbf{Z}$ is the WZW level of the background and h encodes the strength of the integrable interaction, and is a function of the RR charge and moduli values [16]. In the

---

[3]See the review [86] and references in it.

[4]In the case of planar $\mathcal{N} = 4$ this is the $\text{tr}(Z^J)$ family, while in ABJM theory it is $\text{tr}((AB)^J)$.

[5]The global symmetry of $\text{AdS}_3 \times \text{S}^3 \times \text{T}^4$ is $\text{psu}(1,1|2)^2$ and the vacuum-preserving symmetry sub-algebra is $\text{p}(\text{su}(1|1)^2)^2$. Since individual magnons do not satisfy the level-matching condition, they transform in representations of a triple central extension of $\text{p}(\text{su}(1|1)^2)^2$, which we denote by $\text{psu}(1|1)_{\text{c.e.}}^4$.

large worldsheet radius limit, low-lying physical states are made from a few magnons just like in flat space (4.1).[6]

Throughout this work we will only be interested in $m = 0$ states, since these are the only states that can give rise to extra protected multiplets.[7] In the ABA a generic state is constructed in two steps. Firstly, one considers states made of N_0 massless magnons, each a *fermionic* highest-weight state of a $m = 0$ $\text{psu}(1|1)^4_{\text{c.e.}}$ module with momentum p_i (with $i = 1, \ldots, N_0$)[8] Such states are physical if they satisfy the *momentum carrying* BEs. Secondly, one acts with so-called $\mathcal{B}$ operators, which play the role of raising operators of the underlying Yangian algebra. They generate states whose constituent magnons include descendants of the $m = 0$ $\text{psu}(1|1)^4_{\text{c.e.}}$ modules. These descendants should be thought of as further magnons on top of the N_0 magnons, as introduced in the famous nesting procedure (see [98] for a recent review). As such, they too carry momenta, which for physical states are constrained by *auxiliary* BEs. The algebra $\text{psu}(1|1)^4_{\text{c.e.}}$, has four (fermionic) raising operators, but only two linear combinations of these act non-trivially on the *short* magnon multiplets. We will label by N_1 and N_3 the number of times the corresponding $\mathcal{B}^I$ raising operators were used to produce a particular state and by $y_{I,k}$ the corresponding auxiliary momenta (with $I = 1, 3$ and $k = 1, \ldots, N_I$).

For example, taking each of the three magnons in (4.1) to be massless, with the fermionic magnon further chosen as highest-weight in $\text{psu}(1|1)^4_{\text{c.e.}}$ [9], the state $|v\rangle$ has $N_0 = 3$ and $N_1 = N_3 = 1$, since each of the bosons is an $\text{psu}(1|1)^4_{\text{c.e.}}$ descendant. It will be convenient to write the state in terms of its Bethe roots as

$$|v\rangle \equiv |\vec{p}; y_1; y_3\rangle \tag{4.4}$$

where $\vec{p} = (p_1, p_2, p_3)$. If we had instead chosen the fermion to be lowest-weight, the state would still have $N_0 = 3$, but now it would have four auxiliary roots, with $N_1 = N_3 = 2$. In flat space and in plane-wave backgrounds, the magnon S-matrix becomes the identity. As a result, the momentum carrying BEs reduce to the familiar integrality requirement on the momenta $p_i = \frac{n_i}{L}$ that follows from the periodicity of the worldsheet. The auxiliary BEs on the other hand trivialise completely to $1 = 1$. This is why auxiliary Bethe roots don't have a natural interpretation in the familiar flat space or plane-wave setting, their multiplicity simply counting the number of times raising supercharges were used in any given state.

The $\text{psu}(1, 1|2)^2$ charges of the ABA states can be determined from N_i, p_i and an auxiliary integer parameter L related to the length of the worldsheet by the gauge-fixing

---

[6]For more energetic states or at smaller worldsheet radius, this flat spacetime magnon picture is less useful.

[7]Extending the ABA to massive and mixed mass sectors is straightforward.

[8]As in any super-module, the highest-weight state can be chosen to be bosonic or fermionic, depending on the choice of raising operators. In AdS/CFT, it is conventional to take the lightest $m > 0$ excitations to be bosonic, in order to identify them with Hofman-Maldacena magnons. With this choice, the $m = 0$ highest weight states then have to be fermionic.

[9]This would be done by suitably restricting the $\mathbf{8}_v$ and $\mathbf{8}_c$ labels.

condition

$$2D_{\mathrm{L}} = L + N_1 + N_3 - N_0 + \sum_{i=1}^{N_0} \sqrt{k^2 p_i^2 + 4h^2 \sin^2 \tfrac{p_i}{2}}$$

$$2D_{\mathrm{R}} = L + \sum_{i=1}^{N_0} \sqrt{k^2 p_i^2 + 4h^2 \sin^2 \tfrac{p_i}{2}} \tag{4.5}$$

$$2J_{\mathrm{L}} = L + N_1 + N_3 - N_0$$

$$2J_{\mathrm{R}} = L,$$

where D and J are, respectively, the sl(2) and su(2) Cartan generators of $\mathrm{psu}(1,1|2)_{\mathrm{L}} \times \mathrm{psu}(1,1|2)_{\mathrm{R}}$. The AdS$_3$ backgrounds considered in this work have *small* $(4,4)$ superconformal symmetry. Protected states satisfy shortening conditions on both the left- and right-moving parts of the algebra

$$D_{\mathrm{L}} = J_{\mathrm{L}}, \qquad\qquad D_{\mathrm{R}} = J_{\mathrm{R}}. \tag{4.6}$$

Such half-BPS multiplets are often written in the following notation

$$(2D_{\mathrm{L}} + 1, 2D_{\mathrm{R}} + 1)_{\mathrm{S}} \tag{4.7}$$

as, for example, reviewed in section 5.8 of [99].

In this work we use the ABA, to construct all such low-magnon number eigenvectors and show how they organise themselves into $\mathrm{psu}(1|1)^4_{\mathrm{c.e.}}$ multiplets. We then investigate the $p_i \longrightarrow 0$ limit of these Bethe eigenvectors in order to identify the protected states. We show that in the strict $p_i = 0$ limit all states become $\mathrm{psu}(1|1)^4_{\mathrm{c.e.}}$ singlets and the protected states are indeed made up of purely fermionic excitations, as anticipated in [48]. It is interesting to note that these protected states come from both highest-weight and descendant states of the $p_i \neq 0$ modules. The construction of the eigenvectors provided by the ABA allows us to straightforwardly generalise this analysis to AdS$_3 \times$ S$^3 \times$ T$^4/\mathbf{Z}_k$, in other words the orbifold limit of AdS$_3 \times$ S$^3 \times$ K3, and show that the protected spectrum is again the same as found using supergravity and dual CFT$_2$ methods [88].

This work is organised as follows. In Section 4.1 we review the protected spectrum of closed strings on AdS$_3 \times$ S$^3 \times$ T^4 and AdS$_3 \times$ S$^3 \times$ K3 in its orbifold limits. In Section 4.2 we review the general ABA construction and apply it to the AdS$_3$ backgrounds of interest in the present work. We end the section with a few examples of low-magnon number excitations and discuss their representation-theoretic properties. In Section 4.3 we apply the ABA methods to find the protected multiplets in AdS$_3 \times$ S$^3 \times$ T^4. We demonstrate that, in addition to taking the zero-momentum limit for momentum carrying roots, auxiliary roots for protected states also need to take special values given in equation (4.73). The short representations of the protected states follow from the number of momentum-carrying and auxiliary roots of a given multiplet as described in equation (4.67). In Section 4.4, we use the explicit expressions for the protected eigenstates found in Section 4.3 to determine the spectrum of protected states in AdS$_3 \times$ S$^3 \times$ K3 orbifold backgrounds. In Section 4.5 we briefly apply our ABA analysis to the AdS$_3 \times$ S$^3 \times$ S$^3 \times$ S^1 background and its $\mathbf{Z}_2$ orbifold. Since none of the protected states involve auxiliary roots the analysis is much simpler, essentially following from the results in [49], taking into account the zero-momentum limit discussed in equation (4.68). Finally, we present our conclusions and include four appendices to which the technical details of some of our results are relegated. We also include a Mathematica notebook which generates explicit expressions for wavefunctions of states with up to four magnons and their descendants.

4.1 Protected Spectrum of $\mathbf{AdS}_3 \times \mathbf{S}^3 \times \mathbf{T}^4$ and $\mathbf{AdS}_3 \times \mathbf{S}^3 \times \mathbf{K3}$

In this section we briefly review the spectrum of protected closed string states on $AdS_3 \times S^3 \times T^4$ and $AdS_3 \times S^3 \times K3$, originally found from Kaluza-Klein supergravity reductions in [88]. In the planar limit, holographic backgrounds with more supersymmetry, such as $AdS_5 \times S^5$ or $AdS_4 \times CP^3$ have a single family of half-BPS BMN vacua, labelled by an integer L equal to the angular momentum and conformal dimension of the dual operator $e.g.$, $\text{tr}(Z^L)$ in $\mathcal{N} = 4$ super-Yang-Mills theory. The corresponding string state is often written as

$$|Z^L\rangle \, . \tag{4.8}$$

The backgrounds considered in this work have less supersymmetry and, as a result, have *multiple* families of half-BPS vacua. Each family can be obtained by starting with the BMN vacuum (4.8) and adding zero-momentum massless fermionic magnons [48].

In the case of $AdS_3 \times S^3 \times T^4$, the protected multiplets organise themselves into a family of Hodge diamonds labelled by L, which we write following [49] as[10]

$$|Z^L\rangle \tag{4.9a}$$

$$|Z^L \chi^{\dot a}\rangle \qquad\qquad |Z^L \tilde\chi^{\dot a}\rangle \tag{4.9b}$$

$$\epsilon_{\dot a \dot b}\,|Z^L \chi^{\dot a}\chi^{\dot b}\rangle \qquad\qquad |Z^L \chi^{\dot a}\tilde\chi^{\dot b}\rangle \qquad\qquad \epsilon_{\dot a \dot b}\,|Z^L \tilde\chi^{\dot a}\tilde\chi^{\dot b}\rangle \tag{4.9c}$$

$$\epsilon_{\dot a \dot b}\,|Z^L \chi^{\dot a}\chi^{\dot b}\tilde\chi^{\dot c}\rangle \qquad\qquad \epsilon_{\dot a \dot b}\,|Z^L \chi^{\dot a}\tilde\chi^{\dot b}\tilde\chi^{\dot c}\rangle \tag{4.9d}$$

$$\epsilon_{\dot a \dot b}\epsilon_{\dot c \dot d}\,|Z^L \chi^{\dot a}\chi^{\dot b}\tilde\chi^{\dot c}\tilde\chi^{\dot d}\rangle \tag{4.9e}$$

Above, the index $\dot a = \pm$ labels a $\mathbf{2}$ representation of the $su(2)_\circ$ algebra that is part of the rotations which act on the decompactified T^4

$$so(4) \sim su(2)_\circ \oplus su(2)_\bullet \, . \tag{4.10}$$

Upon compactification, it is useful to continue labeling the zero winding and zero momentum excitations in this way. In terms of the notation (4.7), these multiplets can be written as

$$
\begin{array}{ccccc}
& & (L,L)^{\mathbf{1}}_{\text{s}} & & \\
& (L,L+1)^{\mathbf{2}}_{\text{s}} & & (L+1,L)^{\mathbf{2}}_{\text{s}} & \\
(L,L+2)^{\mathbf{1}}_{\text{s}} & & (L+1,L+1)^{\mathbf{1}\oplus\mathbf{3}}_{\text{s}} & & (L+2,L)^{\mathbf{1}}_{\text{s}} \\
& (L+1,L+2)^{\mathbf{2}}_{\text{s}} & & (L+2,L+1)^{\mathbf{2}}_{\text{s}} & \\
& & (L+2,L+2)^{\mathbf{1}}_{\text{s}} & &
\end{array}
\tag{4.11}
$$

with the superscripts denoting the $su(2)_\circ$ representation and for compactness we have changed $L \to L - 1$. In other words, for each L, the multiplets organise themselves into the Hodge diamond of T^4

$$
\begin{array}{ccccc}
& & h^{0,0} & & \\
& h^{1,0} & & h^{0,1} & \\
h^{2,0} & & h^{1,1} & & h^{0,2} \\
& h^{2,1} & & h^{1,2} & \\
& & h^{2,2} & &
\end{array}
\;=\;
\begin{array}{ccccc}
& & 1 & & \\
& 2 & & 2 & \\
1 & & 4 & & 1 \\
& 2 & & 2 & \\
& & 1 & &
\end{array}
\tag{4.12}
$$

---

[10]Z, $\chi^{\dot a}$ and $\tilde\chi^{\dot a}$ respectively correspond to Φ^{++}, $\chi_{\text{R}}^{+\dot a}$ and $\chi_{\text{L}}^{+\dot a}$ in [49].

The appearance of the cohomology of T^4 is to be expected given the conjectured connection of the protected operators of the dual CFT_2 to the Sym^N orbifold [14]. It is well known that for such CFTs, the chiral ring of the theory is closely related to that of the Hodge diamond of the seed theory, which in this case is T^4 [100]. Because of this structure, in this work we often express the protected spectrum of the theory in terms of the Hodge diamond of the seed theory.

Turning to the $AdS_3 \times S^3 \times K3$ background, we blow down the K3 to an orbifold $T/\mathbf{Z}_n$ ($n = 2, 3, 4, 6$). The $\mathbf{Z}_n$ orbifold action acts only on the $su(2)_\circ$ index as

$$\begin{pmatrix} \omega_n & 0 \\ 0 & \omega_n^{-1} \end{pmatrix}, \tag{4.13}$$

where $\omega_n = e^{2\pi i/n}$. A simple way to see that this has to be the action of $\mathbf{Z}_n$ is to note that these orbifolds do not break any supersymmetry and the supercharges are singlets of $su(2)_\circ$, but doublets of $su(2)_\bullet$. It is then clear that the states in equation (4.9b) and (4.9d) are projected out in all $\mathbf{Z}_n$ orbifolds. The states in equations (4.9a) and (4.9e) on the other hand are always kept in all $\mathbf{Z}_n$ orbifolds. All six states in equation (4.9c) are additionally kept in the $\mathbf{Z}_2$ orbifold, while in $\mathbf{Z}_n$ orbifolds with $n > 2$ only the four states

$$|Z^L \chi^+ \chi^-\rangle, \qquad |Z^L \chi^+ \tilde{\chi}^-\rangle, \qquad |Z^L \chi^- \tilde{\chi}^+\rangle, \qquad |Z^L \tilde{\chi}^+ \tilde{\chi}^-\rangle, \tag{4.14}$$

are kept. In summary, for each L in the $\mathbf{Z}_2$ orbifold the untwisted sector Hodge numbers $h^{0,0} = h^{2,2} = h^{2,0} = h^{0,2} = 1$ and $h^{1,1} = 4$ while in $\mathbf{Z}_{n>2}$ orbifolds we have from the untwisted sector the Hodge numbers $h^{0,0} = h^{2,2} = h^{2,0} = h^{0,2} = 1$ and $h^{1,1} = 2$.

The twisted sectors' Hodge numbers are well known (see for example [101])

- $\mathbf{Z}_2$ There are 16 identical twisted sectors. Each twisted sector is a blow-down of an A_1 two-cycle, giving a contribution to $h^{1,1} = 16 \times 1$ overall.

- $\mathbf{Z}_3$ There are 9 identical twisted sectors. Each twisted sector is a blow-down of an A_2 two cycle , giving a contribution to $h^{1,1} = 9 \times 2 = 18$ overall.

- $\mathbf{Z}_4$ There are 4 A_3 fixed points and 6 A_1 fixed points, giving a contribution to $h^{1,1} = 4 \times 3 + 6 \times 1 = 18$ overall.

- $\mathbf{Z}_6$ There is one A_5 fixed point and 4 A_2 fixed points and 5 A_1 fixed point, giving a contribution to $h^{1,1} = 1 \times 5 + 4 \times 2 + 5 \times 1 = 18$ overall.

In the $\mathbf{Z}_2$ orbifold we therefore have the twisted sector Hodge numbers $h^{1,1} = 16$, while in $\mathbf{Z}_{n>2}$ orbifolds we have $h^{1,1} = 18$. Adding the twisted and untwisted Hodge numbers in all cases gives the standard K3 Hodge diamond of the seed theory

$$\begin{matrix} & & 1 & & \\ & 0 & & 0 & \\ 1 & & 20 & & 1 \\ & 0 & & 0 & \\ & & 1 & & \end{matrix}. \tag{4.15}$$

The protected spectrum of the $AdS_3 \times S^3 \times K3$ theory is then a family of Hodge diamonds

labelled by L

$$(L, L)_{\mathrm{s}}$$

$$\varnothing \qquad\qquad\qquad\qquad \varnothing$$

$$(L, L+2)_{\mathrm{s}} \qquad (L+1, L+1)_{\mathrm{s}}^{\oplus 20} \qquad (L+2, L)_{\mathrm{s}} \qquad\qquad (4.16)$$

$$\varnothing \qquad\qquad\qquad\qquad \varnothing$$

$$(L+2, L+2)_{\mathrm{s}}$$

Since the orbifold action breaks $\mathrm{su}(2)_{\circ}$, we have removed the representation-theoretic superscript compared to equation (4.11), listing instead multiplicity in the superscript where it is non-trivial.

4.2 Algebraic Bethe ansatz for $\mathbf{AdS}_3 \times \mathbf{S}^3 \times \mathbf{T}^4$

In this section we present the Algebraic Bethe ansatz for strings on $\mathrm{AdS}_3 \times \mathrm{S}^3 \times \mathrm{T}^4$. We shall summarise the general Bethe ansatz prescription for eigenstates in terms of the transfer matrix in Section 4.2.2 and ABA construction of eigenstates using the monodromy matrix in Section 4.2.3. We end with some examples of low-magnon states in the massless sector of $\mathrm{AdS}_3 \times \mathrm{S}^3 \times \mathrm{T}^4$ in Section 4.2.4.

4.2.1 Massless representations of $\mathrm{psu}(1|1)^4_{\mathbf{c.e.}}$

The $\mathrm{psu}(1|1)^2_{\mathrm{c.e.}}$ algebra, which tensor to give the full $\mathrm{psu}(1|1)^4_{\mathrm{c.e.}}$ symmetry algebra, was introduced earlier in equation (2.18). Throughout this section, we will use the two left chirality families of short representations of $\mathrm{psu}(1|1)^2_{\mathrm{c.e.}}$ ρ_{L} and $\tilde{\rho}_{\mathrm{L}}$. Since, the right chirality representations do not show up in this discussion, we shall omit the L label on basis states, and Zhukovski variables for the rest of this section for brevity.

The $\mathrm{psu}(1|1)^4_{\mathrm{c.e.}}$ algebra is a tensor product of two commuting copies of $\mathrm{psu}(1|1)^2_{\mathrm{c.e.}}$, and throughout this paper we will use the short representation $\rho_{\mathrm{psu}(1|1)^4}$

$$\rho_{\mathrm{psu}(1|1)^4} = \rho_{\mathrm{L}} \otimes \tilde{\rho}_{\mathrm{L}}, \qquad\qquad (4.17)$$

which acts on $\mathcal{V}_p \equiv \mathcal{V}_{\rho_{\mathrm{L}}} \otimes \mathcal{V}_{\tilde{\rho}_{\mathrm{L}}}$ whose basis elements we write as

$$|\chi\rangle \equiv |\phi\rangle\,|\tilde{\psi}\rangle\,, \qquad |T^2\rangle \equiv |\phi\rangle\,|\tilde{\phi}\rangle\,, \qquad |T^1\rangle \equiv |\psi\rangle\,|\tilde{\psi}\rangle\,, \qquad |\tilde{\chi}\rangle \equiv |\psi\rangle\,|\tilde{\phi}\rangle\,, \qquad (4.18)$$

in order to emphasize their connection to the massless worldsheet excitations that appear

in the gauge-fixed Lagrangian [55, 56].[11] In the basis (4.18), the supercharges act as[12]

$$\mathbf{Q}_{\mathrm{L}}^1 = -x_p^+ \mathbf{S}_{\mathrm{R}}^1 = \eta_p^L \begin{pmatrix} 0 & 0 & 0 & 0 \\ 0 & 0 & 0 & 0 \\ 1 & 0 & 0 & 0 \\ 0 & 1 & 0 & 0 \end{pmatrix}, \qquad \mathbf{S}_{\mathrm{L}}^1 = -x_p^- \mathbf{Q}_{\mathrm{R}}^1 = e^{-\frac{ip}{2}} \eta_p^L \begin{pmatrix} 0 & 0 & 1 & 0 \\ 0 & 0 & 0 & 1 \\ 0 & 0 & 0 & 0 \\ 0 & 0 & 0 & 0 \end{pmatrix},$$

$$\mathbf{Q}_{\mathrm{L}}^2 = -x_p^+ \mathbf{S}_{\mathrm{R}}^2 = \eta_p^L \begin{pmatrix} 0 & 0 & 0 & 0 \\ 1 & 0 & 0 & 0 \\ 0 & 0 & 0 & 0 \\ 0 & 0 & -1 & 0 \end{pmatrix}, \qquad \mathbf{S}_{\mathrm{L}}^2 = -x_p^- \mathbf{Q}_{\mathrm{R}}^2 = e^{-\frac{ip}{2}} \eta_p^L \begin{pmatrix} 0 & 1 & 0 & 0 \\ 0 & 0 & 0 & 0 \\ 0 & 0 & 0 & -1 \\ 0 & 0 & 0 & 0 \end{pmatrix}.$$

(4.19)

The $\mathrm{psu}(1|1)^4$ R-matrix is the graded tensor product of the $\mathrm{psu}(1|1)^2$ R-matrices

$$R_{\mathrm{psu}(1|1)^4} = R_{\mathrm{psu}(1|1)^2}^{\mathrm{LL}} \otimes R_{\mathrm{psu}(1|1)^2}^{\tilde{\mathrm{L}}\tilde{\mathrm{L}}}, , \tag{4.20}$$

where $R_{\mathrm{psu}(1|1)^2}^{\mathrm{LL}}, R_{\mathrm{psu}(1|1)^2}^{\tilde{\mathrm{L}}\tilde{\mathrm{L}}}$ are given by equations 2.33, 2.35. For the special case of pure RR background ($k = 0$) and massless excitations the above R-matrices can be written in a difference-form using relativistic γ variables [102]. We discuss the pure RR results in those variables in Appendix C. In the remainder of this section, we use the R-matrix in equation (4.20) to find the string spectrum using the Bethe Ansatz.

4.2.2 Bethe ansatz eigenstates

The spectrum of $\mathrm{AdS}_3 \times \mathrm{S}^3 \times \mathrm{T}^4$ can be obtained through a Bethe ansatz. In this work we are mainly interested in protected states, which are built by adding fermionic zero modes on top of BMN ground states. To understand how such protected states are obtained we first review how to construct generic wave functions using the Bethe ansatz before specialising to the protected states.[13]

The basic building block of the Bethe ansatz for the wave functions are asymptotic states with well-separated excitations carrying momenta p_i. We write such a state as

$$\left| \Phi_{p_1}^{\alpha_1} \cdots \Phi_{p_N}^{\alpha_N} \right\rangle, \tag{4.21}$$

where Φ^α represents any type of excitation. Note that there is an implied ordering of the excitations, which can be highlighted by going to a position basis

$$\left| \Phi_{p_1}^{\alpha_1} \cdots \Phi_{p_N}^{\alpha_N} \right\rangle = \int\limits_{\sigma_1 \ll \cdots \ll \sigma_N} d\sigma_1 \cdots d\sigma_N \, e^{i(p_1\sigma_1 + \cdots + p_N\sigma_N)} \left| \Phi^{\alpha_1}(\sigma_1) \cdots \Phi^{\alpha_N}(\sigma_N) \right\rangle. \tag{4.22}$$

In order to build a full eigenstate from such asymptotic states we make an ansatz where

---

[11] The massless worldsheet excitations additionally all transform in the fundamental representation of $\mathrm{su}(2)_\circ$ and in total there are four bosons and four fermions in the massless sector. However, $\mathrm{su}(2)_\circ$ does not enter the Bethe equations or the R-matrix and we will drop the corresponding index (denoted by ^{a} in [55, 56]) in this section to declutter the notation. This multiplicity will be important when counting the number of protected states and so we will re-instate the $\mathrm{su}(2)_\circ$ index in Section 4.3.

[12] This matches equation (3.35) of [57] with the phase $\xi = 0$.

[13] For more details in the $\mathrm{AdS}_3/\mathrm{CFT}_2$ context see for example reference [103].

we sum over all orderings of the excitations[14]

$$|\Psi\rangle = \sum_{\tau \in S_N} \psi^{\tau}_{\alpha_1 \cdots \alpha_N}(\vec{p}) \, |\Phi^{\alpha_1}_{p_{\tau(1)}} \cdots \Phi^{\alpha_N}_{p_{\tau(N)}}\rangle \,, \qquad (4.23)$$

where we use $\vec{p}$ as a shorthand for $p_1, \ldots, p_N$. The partial wave functions $\psi^{\tau}_{\alpha_1 \cdots \alpha_N}(\vec{p})$ are related by the two-particle S matrix, which acts on two neighbouring excitations as[15]

$$\mathcal{S}_{12} \, |\Phi^{\alpha_1}_{p_1} \Phi^{\alpha_2}_{p_2}\rangle = S^{\alpha_1 \alpha_2}_{\beta_1 \beta_2}(p_1, p_2) \, |\Phi^{\beta_2}_{p_2} \Phi^{\beta_1}_{p_1}\rangle \,. \qquad (4.24)$$

For the wave function corresponding to a permutation τ we have relations of the form

$$\psi^{\tau}_{\alpha_1 \cdots \alpha_{i+1} \alpha_i \cdots \alpha_N}(\vec{p}) = S^{\beta_i \beta_{i+1}}_{\alpha_i \alpha_{i+1}}(p_i, p_{i+1}) \psi^{(i\,i+1)\circ\tau}_{\alpha_1 \cdots \beta_i \beta_{i+1} \cdots \alpha_N}(\vec{p}), \qquad (4.25)$$

where the wave function on the right-hand side corresponds to the composition of the transposition $(i\,i+1)$ and τ. Since any permutation can be factored into a series of transpositions of nearest neighbours all of the partial wave functions can be related to each other in this way. Such a decomposition is in general not unique, but if the two-particle S matrix satisfies the Yang-Baxter equation, all possible decompositions of a permutation lead to the same wave function. This construction furthermore assumes integrability, which implies that any interaction can be separated into distinct two-particle interactions.

As an example of the above construction, let us consider the simplest case of a model with a single type of bosonic excitation ϕ, and a state with two excitations ($N = 2$) with momenta p_1 and p_2, with $p_1 > p_2$. We then have two possible orderings: the incoming wavepacket

$$|\phi_{p_1} \phi_{p_2}\rangle = \int\limits_{\sigma_1 \ll \sigma_2} d\sigma_1 d\sigma_2 \, e^{i(p_1 \sigma_1 + p_2 \sigma_2)} \, |\phi(\sigma_1)\phi(\sigma_2)\rangle \,, \qquad (4.26)$$

and the outgoing wavepacket

$$|\phi_{p_2} \phi_{p_1}\rangle = \int\limits_{\sigma_1 \ll \sigma_2} d\sigma_1 d\sigma_2 \, e^{i(p_2 \sigma_1 + p_1 \sigma_2)} \, |\phi(\sigma_1)\phi(\sigma_2)\rangle \,. \qquad (4.27)$$

The state in equation (4.23) is now a sum over two terms

$$|\Psi_2\rangle = \psi^e(p_1, p_2) \, |\phi_{p_1} \phi_{p_2}\rangle + \psi^{(12)}(p_1, p_2) \, |\phi_{p_2} \phi_{p_1}\rangle \,, \qquad (4.28)$$

where e denotes the identity permutation. As in equation (4.25) the two wavefunctions above are related by

$$\psi^{(12)}(p_1, p_2) = S(p_1, p_2) \psi^e(p_1, p_2), \qquad (4.29)$$

where the S matrix is now replaced by the scattering phase $S(p_1, p_2)$. Using this, the state $|\Psi\rangle$ is, up to an overall factor, just the sum over the incoming and outgoing components

$$|\Psi_2\rangle = \psi^e(p_1, p_2) \Big(|\phi_{p_1} \phi_{p_2}\rangle + S(p_1, p_2) \, |\phi_{p_2} \phi_{p_1}\rangle \Big). \qquad (4.30)$$

---

[14]This ansatz does not give a complete description of the eigenstate, since we only consider excitations that are well separated, and thus ignore any region where the excitations come close enough to each other to interact. As we will see below, interactions are taken into account when we glue the different regions together using the two-particle S matrix.

[15]The S matrix is related to the R matrix by the relation $\mathcal{R} = \Pi \circ \mathcal{S}$, where Π is a (graded) permutation.

The above wave functions describe the system on an infinite line. For a closed string we want to impose periodic boundary conditions on a circle of some length L. To do this it is useful to introduce the <u>full</u> spatial wave function $\Psi_{\alpha_1\cdots\alpha_N}(\sigma_1,\ldots,\sigma_N)$ in terms of which the state $|\Psi\rangle$ can be written as

$$|\Psi\rangle = \int\limits_{\sigma_1\ll\cdots\ll\sigma_N} d\sigma_1\cdots d\sigma_N\, \Psi_{\alpha_1\cdots\alpha_N}(\sigma_1,\ldots,\sigma_N)\,|\Phi^{\alpha_1}(\sigma_1)\cdots\Phi^{\alpha_N}(\sigma_N)\rangle. \qquad (4.31)$$

Periodic boundary conditions then imply that

$$\Psi_{\alpha_1\cdots\alpha_{N-1}\alpha_N}(\sigma_1,\ldots,\sigma_{N-1},\sigma_N) = \Psi_{\alpha_2\cdots\alpha_N\alpha_1}(\sigma_2,\ldots,\sigma_N,\sigma_1+L). \qquad (4.32)$$

Expanding out the full wave function using equations (4.22) and (4.31), and repeatedly using relation (4.25) so that all the partial wave functions are written in terms of the wave function corresponding to the same permutation τ we find that demanding periodicity gives a set of equations of the form

$$\psi^\tau_{a_1\cdots a_N}(\vec{p}) = -e^{ip_k L}\mathcal{T}^{b_1\cdots b_N}_{a_1\cdots a_N}(p_k|\vec{p})\psi^\tau_{b_1\cdots b_N}(\vec{p}), \quad k=1,\ldots N, \qquad (4.33)$$

where the matrix $\mathcal{T}$ is the <u>transfer matrix</u>, which we will discuss in more detail below.

For the simple $N=2$ example with a single flavour of excitations, the full state can be written as

$$|\Psi_2\rangle = \int\limits_{\sigma_1\ll\sigma_2} d\sigma_1 d\sigma_2\, \psi^e(p_1,p_2)\left(e^{i(p_1\sigma_1+p_2\sigma_2)} + S(p_1,p_2)e^{i(p_2\sigma_1+p_1\sigma_2)}\right)|\phi(\sigma_1)\phi(\sigma_2)\rangle, \quad (4.34)$$

from which we identify the wave function

$$\Psi(\sigma_1,\sigma_2) = \psi^e(p_1,p_2)\left(e^{i(p_1\sigma_1+p_2\sigma_2)} + S(p_1,p_2)e^{i(p_2\sigma_1+p_1\sigma_2)}\right). \qquad (4.35)$$

Periodic boundary conditions now gives us that

$$\Psi(\sigma_1,\sigma_2) = \Psi(\sigma_2,\sigma_1+L), \qquad (4.36)$$

which leads to the two conditions

$$\psi^e(p_1,p_2) = e^{ip_1 L}S(p_1,p_2)\psi^e(p_1,p_2), \qquad \psi^{(12)}(p_1,p_2) = e^{ip_2 L}S(p_2,p_1)\psi^{(12)}(p_1,p_2). \qquad (4.37)$$

Assuming that $S(p,p)=-1$, this can be written as the constraint[16]

$$1 + e^{ip_k L}\prod_{j=1}^{2} S(p_k,p_j) = 0, \qquad (4.38)$$

which for $k=1,2$ gives the quantisation conditions for the two momenta p_1 and p_2.

To solve the equations (4.33) we first need to diagonalise $\mathcal{T}$. Once we have found the eigenvalues and eigenvectors of $\mathcal{T}$, equation (4.33) gives quantisation conditions on the momenta p_j. For a given set of momenta solving these Bethe equations, we can finally reconstruct the full eigenstate by summing over all permutations of the momenta with coefficient obtained from equation (4.25).

---

[16]In this simple example there is only a single flavour and hence $\mathcal{T}(p_1|p_1,p_2)$ and $\mathcal{T}(p_2|p_1,p_2)$ are just numbers

$$\mathcal{T}(p_1|p_1,p_2) = S(p_1,p_1)S(p_1,p_2) = -S(p_1,p_2),$$

$$\mathcal{T}(p_2|p_1,p_2) = S(p_2,p_1)S(p_2,p_2) = -S(p_2,p_1) = -\frac{1}{S(p_1,p_2)}.$$

4.2.3 The algebraic Bethe ansatz

There are many ways to diagonalise $\mathcal{T}$. Here we will mainly focus on the algebraic Bethe ansatz (ABA) construction, while in Appendix D we present a complementaty coordinate Bethe ansatz construction. In the ABA in order to diagonalize $\mathcal{T}$, one introduces a more general object, the monodromy matrix $\mathcal{M}$. To construct $\mathcal{M}$ we consider a state with some number of physical excitations, and add to it an additional excitation, referred to as an auxiliary excitation. The auxiliary excitation starts out to the left of all the excitations, and we let it scatter once with physical excitation until it sits to the right of all of them.

For concreteness we will now consider states consisting of massless $\mathrm{AdS}_3 \times \mathrm{S}^3 \times \mathrm{T}^4$ excitations. We take the auxiliary excitation to sit in a $\rho_{\mathrm{psu}(1|1)^4}$ representation[17] of $\mathrm{psu}(1|1)^4_{\text{c.e.}}$. Viewed as a linear map on the auxiliary space, the monodromy matrix $\mathcal{M}$ can then be written as a 4×4 matrix whose entries are operators acting on the physical excitations. Since the $\mathrm{psu}(1|1)^4_{\text{c.e.}}$ algebra is a direct product of two copies of the $\mathrm{psu}(1|1)^2_{\text{c.e.}}$ algebra, the $\mathrm{psu}(1|1)^4_{\text{c.e.}}$ monodromy matrix can be written as a product of two 2×2 $\mathrm{psu}(1|1)^2_{\text{c.e.}}$ monodromy matrices.[18] We denote the components of this smaller matrix by

$$\mathcal{M}^I(p_0) = \begin{pmatrix} \mathcal{A}^I(p_0) & \mathcal{B}^I(p_0) \\ \mathcal{C}^I(p_0) & \mathcal{D}^I(p_0) \end{pmatrix}, \tag{4.39}$$

where the index $I = 1, 3$ labels the two copies of $\mathrm{psu}(1|1)^2_{\text{c.e.}}$ and we have indicated the dependence on the momentum p_0 of the auxiliary excitations. The transfer matrix is the supertrace of the monodromy matrix over the auxiliary space[19]

$$\mathcal{T}^I(p_0) = \mathrm{str}_0 \, \mathcal{M}^I(p_0). \tag{4.40}$$

Using the Yang-Baxter equation one can show that the transfer matrix commutes with itself for any value of the auxiliary momentum

$$\left[\mathcal{T}^I(p_0), \mathcal{T}^I(p_0') \right] = 0. \tag{4.41}$$

In the Bethe equation (4.33) we need the eigenvalues of $\mathcal{T}^I(p_0)$ when the auxiliary momentum coincides with one of the physical momenta p_i, but because of the above equation we can diagonalise $\mathcal{T}$ for all auxiliary momenta simultaneously.

The simplest eigenvectors of $\mathcal{T}$ are states made of N_0 $\mathrm{psu}(1|1)^4_{\text{c.e.}}$ highest-weight excitations χ, since these all scatter diagonally

$$|\chi_{p_1} \cdots \chi_{p_{N_0}}\rangle. \tag{4.42}$$

Other eigenvectors are obtained by acting with N_I $\mathcal{B}^I$ operators with $I = 1, 3$, which act as raising operators in the algebraic Bethe Ansatz. For example, given the above

---

[17]The transfer matrix obtained for any short representation has the same set of eigenvectors, and hence the same final physical spectrum. It is convenient to pick the auxiliary excitations to be in a *massive* representation even if all physical excitations are massless. With this choice, the descendent states arise from auxiliary roots in the conventional fashion [6].

[18]As discussed in section 4.2.1 the massless excitations transform in the $\rho_{\mathrm{L}} \otimes \rho_{\bar{\mathrm{L}}}$ representation of $\mathrm{psu}(1|1)^4_{\text{c.e.}}$, and hence in slightly different representations under the two copies of $\mathrm{psu}(1|1)^2_{\text{c.e.}}$. It is therefore also convenient to also pick the representations of two auxiliary spaces 1 and 3 to be massive versions of the ρ_{L} and $\rho_{\bar{\mathrm{L}}}$. The spectra of the two transfer matrices will be almost the same up to some fermion minus signs.

[19]Here, we have suppressed the dependence of $\mathcal{T}$ on the momenta $p_1, \ldots, p_N$ for brevity.

reference state, we obtain a new state with $N_0 - 1$ χ excitations and one T^1, by acting with a single $\mathcal{B}^1$ operator

$$\mathcal{B}^1(y) |\chi_{p_1} \cdots \chi_{p_{N_0}}\rangle \,, \tag{4.43}$$

where now the argument of $\mathcal{B}^1$ is the auxiliary Zhukovski parameter $y \equiv x_q^-$ for the auxiliary momentum q.[20] The other eigenstates can be built by acting with more creation operators

$$|\vec{p}; \vec{y_1}; \vec{y_3}\rangle \equiv \mathcal{B}^1(y_{1,1}) \cdots \mathcal{B}^1(y_{1,N_1}) \mathcal{B}^3(y_{3,1}) \cdots \mathcal{B}^3(y_{3,N_3}) |\chi_{p_1} \cdots \chi_{p_{N_0}}\rangle \,. \tag{4.44}$$

where $\vec{p} = \{p_1, \ldots, p_{N_0}\}$ and $\vec{y_I} = \{y_{I,1}, \ldots, y_{I,N_I}\}$ Acting with the two transfer matrices on such a state gives

$$\mathcal{T}^1(p_0)\mathcal{T}^3(p_0) |\vec{p}; \vec{y_1}; \vec{y_3}\rangle = \Lambda^1(p_0|\vec{y_1}|\vec{p})\Lambda^3(p_0|\vec{y_3}|\vec{p}) |\vec{p}; \vec{y_1}; \vec{y_3}\rangle + |X\rangle \,. \tag{4.45}$$

The underlined term $|X\rangle$ is a linear combination of states with one less auxiliary root than $|\vec{p}; \vec{y_1}; \vec{y_3}\rangle$ on which a single $\mathcal{B}^J(p_0)$ acts. These vanish provided the $y_{I,k}$ satisfy the auxiliary Bethe equations

$$1 = \prod_{j=1}^{N_0} \sqrt{\frac{x_j^+}{x_j^-}} \frac{y_{I,k} - x_j^-}{y_{I,k} - x_j^+}, \qquad k = 1, \ldots, N_I, \qquad I = 1, 3 \,. \tag{4.46}$$

The eigenvalue in equation (4.45) is given by

$$\Lambda^1(p_0|\vec{y_1}|\vec{p})\Lambda^3(p_0|\vec{y_3}|\vec{p}) = -\left(1 - \prod_{i=1}^{N_0} \sqrt{\frac{x_i^+}{x_i^-}} \frac{x_0^- - x_i^-}{x_0^- - x_i^+}\right)^2 \prod_{I=1,3} \prod_{j=1}^{N_I} \frac{x_0^+ - y_{I,j}^-}{x_0^- - y_{1,j}^-} \sqrt{\frac{x_0^-}{x_0^+}} \,. \tag{4.47}$$

In the Bethe equation (4.33) Λ^I is evaluated for p_0 equal to one of the physical momenta p_i, in which case the above expression reduces to

$$\Lambda^1(p_k|\vec{y_1}|\vec{p})\Lambda^3(p_k|\vec{y_3}|\vec{p}) = -\prod_{I=1,3} \prod_{j=1}^{N_I} \frac{x_k^+ - y_{I,j}^-}{x_k^- - y_{1,j}^-} \sqrt{\frac{x_k^-}{x_k^+}} \,, \tag{4.48}$$

since now $x_0^- = x_i^-$ for one of the i. Using the normalisation in the S matrix of [64], this leads to the momentum carrying Bethe equation

$$\left(\frac{x_k^+}{x_k^-}\right)^L = \prod_{\substack{j=1 \\ j \neq k}}^{N_0} \sqrt{\frac{x_k^-}{x_k^+} \frac{x_j^+}{x_j^-}} \frac{x_k^+ - x_j^-}{x_k^- - x_j^+} (\sigma_{kj}^{\circ\circ})^2 \prod_{j=1}^{N_1} \sqrt{\frac{x_k^+}{x_k^-}} \frac{x_k^- - y_{1,j}}{x_k^+ - y_{1,j}} \prod_{j=1}^{N_3} \sqrt{\frac{x_k^+}{x_k^-}} \frac{x_k^- - y_{3,j}}{x_k^+ - y_{3,j}} \,. \tag{4.49}$$

Above, $\sigma_{kj}^{\circ\circ}$ is the massless dressing factor [87].

---

[20]The S matrix, and hence also the monodromy matrix and transfer matrix, depend on the Zhukovski parameters $x_q^\pm$ of the auxiliary excitation. However, the state generated by the action of $\mathcal{B}^1(y)$ can always be written in a form such that the x_q^+ dependence enters only in the overall normalisation of the state, while the relative coefficients only depend explicitly on x_q^-. For a state of the form

$$\mathcal{B}^1(y_1) \cdots \mathcal{B}^1(y_{N_1}) |\chi_{p_1} \cdots \chi_{p_{N_0}}\rangle \,,$$

the $x_{q_i}^+$ dependence is captured by a factor of the form

$$\prod_{i=1}^{N_1} \sqrt{\frac{x_{q_i}^-}{x_{q_i}^+}} \frac{\eta_{q_i}}{\prod_{j<i} D_{q_i q_j}} \,,$$

with η and D defined in equations (2.22) and (2.34), respectively. Since the normalisation of states is not important in our discussion, we will write the argument of $\mathcal{B}$ as $y = x_q^-$ only, and drop the above normalization factor when writing out explicit expressions for the action of $\mathcal{B}$.

4.2.4 Examples of unprotected $AdS_3 \times S^3 \times T^4$ states

We illustrate the above ABA construction by presenting a few examples of unprotected $AdS_3 \times S^3 \times T^4$ states made up of massless magnon excitations. To begin with we need to study the solutions to the auxiliary Bethe equation (4.46). Since physical states satisfy the level-matching constraint[21]

$$1 = \prod_{j=1}^{N_0} \frac{x_j^+}{x_j^-}\,, \tag{4.50}$$

we can write (4.46) as

$$1 = \prod_{j=1}^{N_0} \frac{y_{I,k} - x_j^-}{y_{I,k} - x_j^+}\,. \tag{4.51}$$

For level-matched states, this equation has two solutions independent of the $x_j^{\pm}$: $y_{I,k} \to \infty$ or $y_{I,k} = 0$. For these two solutions the action of the creation operators $\mathcal{B}^I(y)$ on the state is proportional to that of a supercharge, for example

$$\begin{aligned}
\mathcal{B}^1(y \gg 1) &= -\frac{2i}{h}\frac{1}{y}\,\mathbf{Q}_{\mathrm{L}}^1 + \mathcal{O}\Big(\frac{1}{y^2}\Big)\,, & \mathcal{B}^1(y \ll 1) &= +\frac{2y}{h}\,\mathbf{S}_{\mathrm{R}}^1 + \mathcal{O}(y^2)\,, \\
\mathcal{B}^3(y \gg 1) &= +\frac{2i}{h}\frac{1}{y}\,\mathbf{Q}_{\mathrm{L}}^2 + \mathcal{O}\Big(\frac{1}{y^2}\Big)\,, & \mathcal{B}^3(y \ll 1) &= -\frac{2y}{h}\,\mathbf{S}_{\mathrm{R}}^2 + \mathcal{O}(y^2)\,.
\end{aligned} \tag{4.52}$$

Hence, any state with an auxiliary root $y_{I,k}$ at 0 or ∞ is a descendent. In addition to these two special solutions, the auxiliary Bethe equation has $N_0 - 2$ additional solutions, which give rise to highest-weight states. Below we consider some simple examples.

Example 1: $N_0 = 2$. We start with a reference state with $N_0 = 2$, for which level-matching means that the two excitations have momenta $p_2 = -p_1$

$$|\chi_{p_1}\chi_{p_2}\rangle\,. \tag{4.53}$$

For $N_0 = 2$ the only solutions to the auxiliary Bethe equations are located at 0 and ∞. The $\mathcal{B}^I(y_{I,k})$ are now proportional to raising supercharges of $\mathfrak{psu}(1|1)^4_{\mathrm{c.e.}}$ and acting with them on the above eigenstate generates a long, 16-dimensional $\mathfrak{psu}(1|1)^4_{\mathrm{c.e.}}$ multiplet with $N_I = 0, 1, 2$. This matches the representation theory expectation, since each excitation transforms in a short four-dimensional representation and the tensor product of two such representations generically gives a single long 16-dimensional representation.

For example, acting with a single $\mathcal{B}^1$ operator on the highest-weight state we find

$$\mathcal{B}^1(y)\,|\chi_{p_1}\chi_{p_2}\rangle \propto \frac{\eta_1}{y - x_1^+}\,|T_{p_1}^1 \chi_{p_2}\rangle - \frac{\eta_2}{y - x_2^+}\frac{y - x_1^-}{y - x_1^+}\sqrt{\frac{x_1^+}{x_1^-}}\,|\chi_{p_1}T_{p_2}^1\rangle\,. \tag{4.54}$$

At large y this reduces to

$$\mathcal{B}^1(\infty)\,|\chi_{p_1}\chi_{p_2}\rangle \propto \frac{\eta_1}{y}\,|T_{p_1}^1 \chi_{p_2}\rangle - \frac{\eta_2}{y}\sqrt{\frac{x_1^+}{x_1^-}}\,|\chi_{p_1}T_{p_2}^1\rangle\,, \tag{4.55}$$

---

[21]The square-root branch cuts in (4.46) are chosen so that the level-matching constraint also implies $\prod_{j=1}^{N_0}\sqrt{x_j^+/x_j^-} = 1$.

and for small y we get

$$\mathcal{B}^1(0) \left| \chi_{p_1} \chi_{p_2} \right\rangle \propto -\frac{\eta_1}{x_1^+} \left| T_{p_1}^1 \chi_{p_2} \right\rangle + \frac{\eta_2}{x_2^+} \sqrt{\frac{x_1^-}{x_1^+}} \left| \chi_{p_1} T_{p_2}^1 \right\rangle . \tag{4.56}$$

Up to overall normalizations, these two expressions agree with the action on a level-matched $N_0 = 2$ state of the supercharges $\mathbf{Q}_{\mathrm{L}}^1$ and $\mathbf{S}_{\mathrm{R}}^1$, respectively. This can be verified by using the coproduct (2.19) together with the explicit expressions for the supersymmetry generators given in equation (4.19).

As another example, consider acting with one $\mathcal{B}^1$ operator and one $\mathcal{B}^3$ operator to find $N_1 = N_3 = 1$ states

$$\begin{aligned}
\mathcal{B}^3(\infty)\mathcal{B}^1(\infty) \left| \chi\chi \right\rangle &\propto \left| \chi\tilde{\chi} \right\rangle + f_p^2 \left| \tilde{\chi}\chi \right\rangle - f_p \left| T^1 T^2 \right\rangle + f_p \left| T^2 T^1 \right\rangle , \\[4pt]
\mathcal{B}^3(0)\mathcal{B}^1(\infty) \left| \chi\chi \right\rangle &\propto \left| \chi\tilde{\chi} \right\rangle - \left| \tilde{\chi}\chi \right\rangle - f_p \left| T^1 T^2 \right\rangle - \frac{1}{f_p} \left| T^2 T^1 \right\rangle , \\[4pt]
\mathcal{B}^3(\infty)\mathcal{B}^1(0) \left| \chi\chi \right\rangle &\propto \left| \chi\tilde{\chi} \right\rangle - \left| \tilde{\chi}\chi \right\rangle + \frac{1}{f_p} \left| T^1 T^2 \right\rangle + f_p \left| T^2 T^1 \right\rangle , \\[4pt]
\mathcal{B}^3(0)\mathcal{B}^1(0) \left| \chi\chi \right\rangle &\propto \left| \chi\tilde{\chi} \right\rangle + \frac{1}{f_p^2} \left| \tilde{\chi}\chi \right\rangle + \frac{1}{f_p} \left| T^1 T^2 \right\rangle - \frac{1}{f_p} \left| T^2 T^1 \right\rangle ,
\end{aligned} \tag{4.57}$$

where

$$f_p = \sqrt{x_p^- x_p^+} \tag{4.58}$$

and we have suppressed the momenta p_i of the two excitations for brevity. As expected for descendants, these states can also be obtained by acting with supercharges[22]

$$\begin{aligned}
\mathbf{Q}_{\mathrm{L}}^2\mathbf{Q}_{\mathrm{L}}^1 \left| \chi\chi \right\rangle &\propto \mathcal{B}^3(\infty)\mathcal{B}^1(\infty) \left| \chi\chi \right\rangle , & \mathbf{S}_{\mathrm{R}}^2\mathbf{Q}_{\mathrm{L}}^1 \left| \chi\chi \right\rangle &\propto \mathcal{B}^3(0)\mathcal{B}^1(\infty) \left| \chi\chi \right\rangle , \\
\mathbf{Q}_{\mathrm{L}}^2\mathbf{S}_{\mathrm{R}}^1 \left| \chi\chi \right\rangle &\propto \mathcal{B}^3(\infty)\mathcal{B}^1(0) \left| \chi\chi \right\rangle , & \mathbf{S}_{\mathrm{R}}^2\mathbf{S}_{\mathrm{R}}^1 \left| \chi\chi \right\rangle &\propto \mathcal{B}^3(0)\mathcal{B}^1(0) \left| \chi\chi \right\rangle .
\end{aligned} \tag{4.59}$$

Example 2: $N_0 = 3$. Next, consider three-magnon excitations. In addition to the solutions $y = 0$ and $y = \infty$, the auxiliary Bethe equation has the additional solution

$$y_* = \frac{\sum_{i<j} x_i^+ x_j^+ - \sum_{i<j} x_i^- x_j^-}{\sum_i x_i^+ - \sum_i x_i^-} . \tag{4.60}$$

In the pure RR case this reduces to $y_* = 1$. There are now four highest weight states

$$\left| \chi_{p_1} \chi_{p_2} \chi_{p_3} \right\rangle , \qquad \mathcal{B}^I(y_*) \left| \chi_{p_1} \chi_{p_2} \chi_{p_3} \right\rangle , \qquad \mathcal{B}^1(y_*)\mathcal{B}^3(y_*) \left| \chi_{p_1} \chi_{p_2} \chi_{p_3} \right\rangle , \tag{4.61}$$

where $p_1 + p_2 + p_3 = 0$. Explicitly, we have for example

$$\begin{aligned}
\mathcal{B}^1(y_*) \left| \chi_{p_1} \chi_{p_2} \chi_{p_3} \right\rangle \propto{} & \frac{\eta_1}{y_* - x_1^+} \left| T_{p_1}^1 \chi_{p_2} \chi_{p_3} \right\rangle - \frac{\eta_2}{y_* - x_2^+} \frac{y_* - x_1^-}{y_* - x_1^+} \sqrt{\frac{x_1^+}{x_1^-}} \left| \chi_{p_1} T_{p_2}^1 \chi_{p_3} \right\rangle \\
& + \frac{\eta_3}{y_* - x_3^+} \frac{y_* - x_1^-}{y_* - x_1^+} \frac{y_* - x_2^-}{y_* - x_2^+} \sqrt{\frac{x_1^+ x_2^+}{x_1^- x_2^-}} \left| \chi_{p_1} \chi_{p_2} T_{p_3}^1 \right\rangle .
\end{aligned} \tag{4.62}$$

---

[22]We label the supercharges of the two copies of $\mathrm{psu}(1|1)_{\mathrm{c.e.}}^2$ as 1 and 2, but the corresponding auxiliary roots as 1 and 3. The latter choice is motivated by the Dynkin diagram of $\mathrm{psu}(1,1|2)$, which underlies the structure of our Bethe equations as discussed in Figure 7 of [64].

The remaining highest-weight state is obtained by acting with two $\mathcal{B}^I(y_*)$ operators and is given explicitly in equation (B.1) in Appendix B.

As in the $N_0 = 2$ case, we can fill out the full representations by adding additional roots at 0 and ∞, where the action of $\mathcal{B}^I(y)$ reduces to that of a supercharge. For example, for $y = \infty$

$$\mathcal{B}^1(\infty) \left| \chi_{p_1} \chi_{p_2} \chi_{p_3} \right\rangle \propto \frac{\eta_1}{y} \left| T^1_{p_1} \chi_{p_2} \chi_{p_3} \right\rangle - \frac{\eta_2}{y} \sqrt{\frac{x_1^+}{x_1^-}} \left| \chi_{p_1} T^1_{p_2} \chi_{p_3} \right\rangle + \frac{\eta_3}{y} \sqrt{\frac{x_1^+ x_2^+}{x_1^- x_2^-}} \left| \chi_{p_1} \chi_{p_2} T^1_{p_3} \right\rangle ,$$
(4.63)

and we can check again that this state is a descendant

$$\mathcal{B}^1(\infty) \left| \chi_{p_1} \chi_{p_2} \chi_{p_3} \right\rangle \propto \mathbf{Q}^1_{\mathrm{L}} \left| \chi_{p_1} \chi_{p_2} \chi_{p_3} \right\rangle .$$
(4.64)

As before, this matches the representation theory of $\mathrm{psu}(1|1)^4_{\mathrm{c.e.}}$, since the product of three short representations can be generically decomposed into a sum of four long representations, $(2|2)^{\otimes 3} = (8|8)^{\oplus 4}$.

4.3   Protected states from Bethe ansatz wave functions

In this section we find the wave-functions of protected states in $\mathrm{AdS}_3 \times \mathrm{S}^3 \times \mathrm{T}^4$ using the ABA constructed in the previous section. A generic unprotected ABA state of the form discussed in the previous section is built from N_0 momentum-carrying roots p_k and N_I auxiliary roots $y_{I,j}$

$$\left| \vec{p}; \vec{y_1}; \vec{y_3} \right\rangle ,$$
(4.65)

as introduced in equation (4.44). Protected states do not receive corrections to their energies and since the dispersion relation (4.3) depends on the magnon momentum p_k, protected states come from zero-momentum magnons only. As we show below, the auxiliary roots $y_{I,j}$ also take special values for protected states $y_{I,j} = s_\pm$ with $s_\pm$ defined in equation (4.68). In order not to over-load the notation and to distinguish them from unprotected states, we will label protected states by the number of momentum-carrying and auxiliary roots

$$\left| N_0, N_1, N_3 \right\rangle \equiv \left| \vec{p} = \vec{0}; \vec{y_1} = \vec{s}_\pm; \vec{y_3} = \vec{s}_\pm \right\rangle .$$
(4.66)

Since the charges of these states follow from equation (4.5), we can equivalently write these states in the notation of equation (4.7)

$$\left| N_0, N_1, N_3 \right\rangle \equiv (L + N_1 + N_3 - N_0 + 1, L + 1)_{\mathrm{s}} .$$
(4.67)

On the right-hand side above, we have re-introduced the L-dependence of the BMN vacuum $\left| 0, 0, 0 \right\rangle$ that is suppressed in equations like (4.66) for compactness.

4.3.1   Fermionic zero modes

In order to find the protected states, we send magnon momenta to zero. Since the massless dispersion relation (4.3) has a cusp at $p = 0$ we get potentially different results if we send $p \to 0$ from above or below. For $p = 0$, the Zhukovski variables satisfy $x_p^+ = x_p^-$ and we will denote by s_+ or s_- their value as p goes to zero from above or below

$$s_+ \equiv \lim_{p \to 0^+} x_p^\pm = \frac{\hbar + \sqrt{\hbar^2 + h^2}}{h} , \qquad s_- \equiv \lim_{p \to 0^-} x_p^\pm = \frac{\hbar - \sqrt{\hbar^2 + h^2}}{h} = -\frac{1}{s_+} , \quad (4.68)$$

which become ± 1 for $\Bbbk = 0$.

The simplest zero-momentum states have no auxiliary excitations and setting $x_\pm = s_+$ or $x^\pm = s_-$ leads to the same state, hence denoting the corresponding excitation by $\chi_{p=0}$ is unambiguous. For example, a single excitation ($N_0 = 1$) with zero momentum[23] written in the notation of equation (4.66) is

$$|1,0,0\rangle^{\dot{a}} = |\chi_0^{\dot{a}}\rangle \,, \tag{4.69}$$

where we reintroduced the su(2)$_\circ$ index of χ, as discussed in footnote 11. Hence, the $N_0 = 1$ reference state gives an su(2)$_\circ$ doublet of protected states. Similarly, for $N_0 = 2$ we have

$$|2,0,0\rangle^{\dot{a}\dot{b}} = |\chi_0^{\dot{a}}\chi_0^{\dot{b}}\rangle \,. \tag{4.70}$$

This is not yet a full physical state, since we still have to sum over all permutations of the excitations as described in equation (4.35). At zero momentum, the S matrix reduces to a graded permutation, so the full state is given by

$$\epsilon_{\dot{a}\dot{b}}|2,0,0\rangle^{\dot{a}\dot{b}} = |\chi_0^{\dot{a}}\chi_0^{\dot{b}}\rangle - |\chi_0^{\dot{b}}\chi_0^{\dot{a}}\rangle \,. \tag{4.71}$$

Hence, the $N_0 = 2$ reference state give rise to a single protected state, which is an su(2)$_\circ$ singlet.

The remaining protected states carry auxiliary roots. But where should these roots sit? If we take the auxiliary Bethe equation (4.46) and send all momenta to zero, we find it is trivially satisfied for any y. Naively then we might conclude that acting with $\mathcal{B}^I(y)$ for any y gives a physical protected state. However, this cannot be correct, since at $y = 0, \infty$ the $\mathcal{B}^I(y)$ reduce to psu(1|1)$^4_{\text{c.e.}}$ supercharges (see equation (4.52)), which by definition annihilate all protected states. As we show below, there are natural values for y to take for protected states.

To determine which value the auxiliary roots need to take, consider the $N_0 = 3$ states discussed in Section 4.2.4 in the limit $p_1 \to 0$, for which $x_1^\pm$ goes to either s_+ or s_- (see equation (4.68)). In this limit the auxiliary root solution (4.60) becomes

$$y_* = s_\pm + \frac{x_2^+ x_3^+ - x_2^- x_3^-}{x_2^+ + x_3^+ - x_2^- - x_3^-} + \mathcal{O}(p_1) \,. \tag{4.72}$$

Since the level-matching condition reduces to $p_2 + p_3 = 0$, for which $x_2^+ x_3^+ - x_2^- x_3^- = 0$, the auxiliary root for $p_1 = 0$ is

$$y_* = s_\pm \,. \tag{4.73}$$

In other words, in this limit the auxiliary root takes the *same* value as the momentum-carrying root

$$y_{I,1} = x_1^+ = x_1^- = s_\pm \,. \tag{4.74}$$

For example, consider the highest-weight state in equation (4.62). Inserting $y_* = s_\pm$ and sending $p_1 \to 0$, we see that the coefficient of the first term on the right-hand side of (4.62) diverges, since $\eta_{p_1} = \mathcal{O}(\sqrt{p_1})$, while the remaining two terms stay finite. For a normalized state this means that we can neglect the latter terms in the limit, leading to

$$\lim_{p_1 \to 0} |p_1, p_2, p_3; y_{1,1} = y_*\rangle = |0, p_2, p_3; s_\pm\rangle \propto |T_0^1 \chi_{p_2} \chi_{-p_2}\rangle \,. \tag{4.75}$$

---

[23]Because of the level-matching constraint $\sum_i p_i = 0$, for $N_0 = 1$ we have to set $p_1 = 0$.

This is a highest-weight two-magnon state, similar to the state in equation (4.53), but with an additional T_0^1 zero mode. While such *bosonic* zero modes will not play a role in the protected spectrum, this example illustrates an important feature of the special value of the auxiliary root $y = s_\pm$: the operator $\mathcal{B}(s_\pm)$ acts *only* on the corresponding zero momentum site changing the highest weight state $\chi_{p=0}$ to a $\rho_{\mathrm{psu}(1|1)^4}$ descendant, in this case $T_{p=0}^1$.

Similarly, if we considered the highest-weight state (B.1) in the $p_1 \to 0$ limit, we find

$$\lim_{p_1 \to 0} |p_1, p_2, p_3; y_{1,1} = y_*; y_{3,1} = y_*\rangle = |0, p_2, -p_2; s_\pm; s_\pm\rangle \propto |\tilde{\chi}_0 \chi_{p_2} \chi_{-p_2}\rangle . \qquad (4.76)$$

This too is a highest-weight two magnon state, similar to the state in equation (4.53), now with an additional $\tilde{\chi}_0$ zero mode. As we discuss in the next subsection, sending $p_2 \to 0$ will lead to further protected states.

The above examples illustrate how our ABA takes into account the further ground-states which exist in AdS_3 integrable backgrounds in addition to the BMN vacuum on which the generic state (4.44) is constructed. For such a state, sending one of the momenta p_k to zero and setting one auxiliary root $y_{I,j}$ to $s_\pm$ leads to a state with $N_0 - 1$ magnons and $N_I - 1$ auxiliary roots in the presence of a massless bosonic zero-mode, while setting $y_{1,j} = y_{3,j} = s_\pm$ gives a state with $N_0 - 1$ magnons as well as $N_1 - 1$ and $N_3 - 1$ auxiliary roots.

On the other hand, states whose auxiliary roots are not $s_\pm$ in a zero-momentum limit, become states with $N_0 - 1$ magnons, N_I auxiliary roots and a χ_0 zero-mode, which is highest-weight in $\rho_{\mathrm{psu}(1|1)^4}(p_k = 0)$. For example, consider the $N_0 = 3$ descendant state in equation (4.63). There, the first term is suppressed in the $p_1 \to 0$ limit by a factor $\sqrt{p_1}$, giving

$$\lim_{p_1 \to 0} |p_1, p_2, p_3; y_{1,1} = \infty\rangle = |0, p_2, p_3; \infty\rangle \propto -\eta_2 |\chi_0 T_{p_2}^1 \chi_{p_3}\rangle + \eta_3 \sqrt{\frac{x_2^+}{x_2^-}} |\chi_0 \chi_{p_2} T_{p_3}^1\rangle , \quad (4.77)$$

with $p_3 = -p_2$ due to level-matching. This state is a descendant of the highest-weight state $|\chi_0 \chi_{p_2} \chi_{-p_2}\rangle$ and in this way is similar to the $N_0 = 2$ descendant in equation (4.55), with an additional χ_0 zero mode inserted. In the $p_2 \to 0$ limit, this state goes to zero as expected for a $\mathrm{psu}(1|1)_{\mathrm{c.e.}}^4$ descendant. This example illustrates the fact that, in the zero-momentum limit, states whose auxiliary roots do not become $s_\pm$ will not give rise to protected states. This example illustrates a second important feature of the massless ABA: in the limit where one momentum goes to zero, the operator $\mathcal{B}(y_{I,j})$ for $y_{I,j} \neq s_\pm$ acts on all sites *except* the zero momentum site.

From the above discussion, we conclude that protected states involving $\tilde{\chi}_0$ zero modes have auxiliary roots at $y = s_\pm$ as $p \to 0^\pm$. For the $N_0 = 2$ state (4.70), we can add at most two auxiliary roots of each I-type[24]

$$|2, 2, 2\rangle^{\dot{a}\dot{b}} = \mathcal{B}^1(s_+)\mathcal{B}^3(s_+)\mathcal{B}^1(s_-)\mathcal{B}^3(s_-) |\chi_0^{\dot{a}} \chi_0^{\dot{b}}\rangle \sim |\tilde{\chi}_0^{\dot{a}} \tilde{\chi}_0^{\dot{b}}\rangle , \qquad (4.78)$$

which leads to a single protected state

$$\epsilon_{\dot{a}\dot{b}} |2, 2, 2\rangle^{\dot{a}\dot{b}} = \epsilon_{\dot{a}\dot{b}} |\tilde{\chi}_0^{\dot{a}} \tilde{\chi}_0^{\dot{b}}\rangle \qquad (4.79)$$

---

[24]Since we are only interested in fermionic zero modes we always turn on the auxiliary roots pairwise, with one root of type 1 and one root of type 3 sitting at the same point.

which is a singlet under $su(2)_\circ$ once we sum over all permutations of the excitations as in equation (4.35). In equation (4.78), we have chosen a particular ordering of s_+ and s_- in the arguments of the $\mathcal{B}$ operators as well as implicitly setting $x_1^\pm = s_+$ and $x_2^\pm = s_-$. One can check that different choices of $s_\pm$ lead to the same protected states as long as this is done consistently with equation (4.74).

More interesting is the case where we turn on one auxiliary root of each type. We now have two possibilities[25]

$$\mathcal{B}^1(s_+)\mathcal{B}^3(s_+)\,|\chi^{\dot{a}}\chi^{\dot{b}}\rangle \sim |\tilde{\chi}^{\dot{a}}\chi^{\dot{b}}\rangle \qquad \text{or} \qquad \mathcal{B}^1(s_-)\mathcal{B}^3(s_-)\,|\chi^{\dot{a}}\chi^{\dot{b}}\rangle \sim |\chi^{\dot{a}}\tilde{\chi}^{\dot{b}}\rangle\,. \tag{4.80}$$

These states are described by two distinct sets of Bethe roots, and at first sight we would expect them to represent different states. However, summing over all permutations of the excitations as in equation (4.35) gives

$$|\tilde{\chi}_0^{\dot{a}}\chi_0^{\dot{b}}\rangle - |\chi_0^{\dot{b}}\tilde{\chi}_0^{\dot{a}}\rangle \qquad \text{or} \qquad |\chi_0^{\dot{a}}\tilde{\chi}_0^{\dot{b}}\rangle - |\tilde{\chi}_0^{\dot{b}}\chi_0^{\dot{a}}\rangle\,, \tag{4.81}$$

which are the same states. The protected states at this level can thus be decomposed into a triplet and a singlet of $su(2)_\circ$. Hence, we find that two different solutions to the Bethe equations can lead to the same physical protected state.

We end this subsection by noting that when performing explicit computations of how the $\mathcal{B}(s_\pm)$ operators act on states of the form (4.42) it is important to take an *ordered* zero-momentum limit $0 \leftarrow |p_1| < |p_2| < \dots$. This is because, as we discussed below equation (4.76), one needs to re-normalize the eigenstates as each momentum reaches zero. One can check that in the end different orderings lead to the same protected eigenstates, but at intermediate stages of the calculation care must be taken with expressions involving multiple $\mathcal{B}$ operators.

In the next subsection we summarize the complete set of protected states obtained by picking an ordering of the $\mathcal{B}$ operators, as well as making particular choices for the each zero-momentum Zhukovsky variable as discussed in equation (4.68) in a way that is consistent with equation (4.74). We have checked that all other allowed choices lead to the same physical protected eigenstates just as the $N_0 = 2$ cases described above.

4.3.2 Protected states

In this sub-section, we write down the complete closed-string protected spectrum for $\text{AdS}_3 \times \text{S}^3 \times \text{T}^4$, using the ABA procedure described in detail above. As discussed there, the Bethe equations' solutions corresponding to these states are not unique, and for each protected state we have the freedom to choose a useful way of taking the zero momentum limit. All such choices lead to the same physical protected states. Below we make one such choice and list the states ordered by the number of zero modes they contain. Furthermore, we do not explicitly write down the sum over permutations of the zero modes, as described in equation (4.35), for simplicity listing a single representative for each state.[26]

$\underline{N_0 = 0}$

---

[25]Other combinations of $\mathcal{B}$ operators, such as $\mathcal{B}^1(s_+)\mathcal{B}^3(s_-)$ would lead to states with two zero-momentum bosons instead of fermions.

[26]For a state with only zero modes, the sum over permutations just gives the obvious fermionic minus signs.

Without any zero modes we have just the family of BMN ground states

$$|0, 0, 0\rangle, \tag{4.82}$$

labelled by L with $2D_\mathrm{L} = 2D_\mathrm{L} = 2J_\mathrm{L} = 2J_\mathrm{R} = L$, which are $\mathrm{su}(2)_\circ$ singlets.

$\underline{N_0 = 1}$

The protected states with a single $\chi^{\dot{a}}$ zero-mode were introduced in (4.69)

$$|1, 0, 0\rangle^{\dot{a}} = |\chi_0^{\dot{a}}\rangle, \tag{4.83}$$

while those with a single $\tilde{\chi}^{\dot{a}}$ zero-mode have two $\mathcal{B}$ operators

$$|1, 1, 1\rangle^{\dot{a}} = \mathcal{B}^1(s_+)\mathcal{B}^3(s_+)|1, 0, 0\rangle \propto |\tilde{\chi}_0^{\dot{a}}\rangle. \tag{4.84}$$

Both types of states are $\mathrm{su}(2)_\circ$ doublets.

$\underline{N_0 = 2}$

Here we start with the reference state introduced in (4.71)

$$\epsilon_{\dot{a}\dot{b}}|2, 0, 0\rangle^{\dot{a}\dot{b}} = \epsilon_{\dot{a}\dot{b}}|\chi_{0+}^{\dot{a}}\chi_{0-}^{\dot{b}}\rangle, \tag{4.85}$$

which is a $\mathrm{su}(2)_\circ$-singlet. Adding one set of $\mathcal{B}$ operators we have[27]

$$|2, 1, 1\rangle^{\dot{a}\dot{b}} = \mathcal{B}^1(s_+)\mathcal{B}^3(s_+)|2, 0, 0\rangle^{\dot{a}\dot{b}} \propto |\tilde{\chi}_{0+}^{\dot{a}}\chi_{0-}^{\dot{b}}\rangle, \tag{4.86}$$

which is a triplet and a singlet under $\mathrm{su}(2)_\circ$. With two sets of $\mathcal{B}$ operators we find

$$\epsilon_{\dot{a}\dot{b}}|2, 2, 2\rangle^{\dot{a}\dot{b}} = \epsilon_{\dot{a}\dot{b}}\mathcal{B}^1(s_+)\mathcal{B}^3(s_+)\mathcal{B}^1(s_-)\mathcal{B}^3(s_-)|2, 0, 0\rangle^{\dot{a}\dot{b}} \propto \epsilon_{\dot{a}\dot{b}}|\tilde{\chi}_{0+}^{\dot{a}}\tilde{\chi}_{0-}^{\dot{b}}\rangle^{\dot{a}\dot{b}}, \tag{4.87}$$

which is a $\mathrm{su}(2)_\circ$ singlet.

$\underline{N_0 = 3}$

With three fermions the reference state would take the form

$$|\chi_{0+}^{\dot{a}}\chi_{0-}^{\dot{b}}\chi_{0-}^{\dot{c}}\rangle. \tag{4.88}$$

However, since the fermions are doublets under $\mathrm{su}(2)_\circ$, fermion statistics will kill the corresponding full physical state. To get a non-vanishing state we need to include at least one set of $\mathcal{B}$ operators

$$|3, 1, 1\rangle^{\dot{a}} = \mathcal{B}^1(s_+)\mathcal{B}^3(s_+)\epsilon_{\dot{b}\dot{c}}|\chi_{0+}^{\dot{a}}\chi_{0-}^{\dot{b}}\chi_{0-}^{\dot{c}}\rangle \propto \epsilon_{\dot{b}\dot{c}}|\tilde{\chi}_{0+}^{\dot{a}}\chi_{0-}^{\dot{b}}\chi_{0-}^{\dot{c}}\rangle, \tag{4.89}$$

We can also include two sets of $\mathcal{B}$ operators to get

$$|3, 2, 2\rangle^{\dot{a}} = \mathcal{B}^1(s_+)\mathcal{B}^3(s_+)\mathcal{B}^1(s_-)\mathcal{B}^3(s_-)\epsilon_{\dot{b}\dot{c}}|\chi_{0+}^{\dot{a}}\chi_{0+}^{\dot{b}}\chi_{0-}^{\dot{c}}\rangle \propto \epsilon_{\dot{b}\dot{c}}|\tilde{\chi}_{0+}^{\dot{a}}\tilde{\chi}_{0-}^{\dot{b}}\chi_{0-}^{\dot{c}}\rangle. \tag{4.90}$$

Both types of states are $\mathrm{su}(2)_\circ$ doublets. A state with more than two sets of $\mathcal{B}$ operators would again vanish because of fermion statistics.

$\underline{N_0 = 4}$

The four fermion zero momentum reference state

$$|\chi_{0+}^{\dot{a}}\chi_{0+}^{\dot{b}}\chi_{0-}^{\dot{c}}\chi_{0-}^{\dot{d}}\rangle, \tag{4.91}$$

---

[27]In obtaining this state, it is important to first act with the $\mathcal{B}$ operators and then sum over permutations, as described in equation (4.35).

for which the full physical state vanishes due to Fermi statistics. To get a physical state we now need to include two sets of $\mathcal{B}$ operators

$$
\begin{aligned}
|4,2,2\rangle &= \mathcal{B}^1(s_+)\mathcal{B}^3(s_+)\mathcal{B}^1(s_-)\mathcal{B}^3(s_-)\epsilon_{\dot{a}\dot{b}}\epsilon_{\dot{c}\dot{d}}\,|\chi^{\dot{a}}_{0+}\chi^{\dot{b}}_{0+}\chi^{\dot{c}}_{0-}\chi^{\dot{d}}_{0-}\rangle \\
&\propto \epsilon_{\dot{a}\dot{b}}\epsilon_{\dot{c}\dot{d}}\,|\chi^{\dot{a}}_{0+}\tilde{\chi}^{\dot{b}}_{0+}\tilde{\chi}^{\dot{c}}_{0-}\chi^{\dot{d}}_{0-}\rangle\,,
\end{aligned}
\tag{4.92}
$$

which is a $su(2)_\circ$ singlet.

Summary of protected states

The protected states found in this section are summarised below, where superscripts indicate the $su(2)_\circ$ representations

$$
\begin{array}{ccccc}
& & |0,0,0\rangle^{\mathbf{1}} & & \\
& |1,0,0\rangle^{\mathbf{2}} & & |1,1,1\rangle^{\mathbf{2}} & \\
|2,0,0\rangle^{\mathbf{1}} & & |2,1,1\rangle^{\mathbf{1}\oplus\mathbf{3}} & & |2,2,2\rangle^{\mathbf{1}} \\
& |3,1,1\rangle^{\mathbf{2}} & & |3,2,2\rangle^{\mathbf{2}} & \\
& & |4,2,2\rangle^{\mathbf{1}} & &
\end{array}
\tag{4.93}
$$

These states match the Hodge diamond of the seed T^4 theory (4.12) and, since they depend additionally on L through the BMN vacuum $|0,0,0\rangle$ (see equation (4.67)), we match the expected protected spectrum in (4.11).[28]

4.4 Protected states in $\mathrm{AdS}_3 \times \mathrm{S}^3 \times \mathrm{K3}$ orbifolds

In this section, we discuss the ABA spectrum of strings in $\mathrm{AdS}_3 \times \mathrm{S}^3 \times \mathrm{T}^4/\mathbf{Z}_n$ orbifolds, with $n = 2,3,4,6$. As reviewed in Section 4.1, $\mathbf{Z}_n$ acts only on $su(2)_\circ$. Since the massive sector is not charged under the $su(2)_\circ$ symmetry, there is no impact of the action of the orbifold group on the massive ABA states, nor on the massive Bethe equations [54]. In particular, the massive excitation Z which generates the BMN-like vacuum $|Z^L\rangle$, is invariant under the orbifold action.

On the other hand, massless modes transform as doublets under $su(2)_\circ$. Since we are only considering states with zero winding and momentum on T^4, the untwisted sector states simply have to be invariant under the projection (4.13). In particular, protected states listed in equation (4.93) survive the $\mathbf{Z}_{n>2}$ projections only if they are $su(2)_\circ$ singlets. The $n > 2$ untwisted sector protected spectrum is

$$
\begin{array}{ccccc}
& & |0,0,0\rangle & & \\
& \varnothing & & \varnothing & \\
|2,0,0\rangle & & |2,1,1\rangle & & |2,2,2\rangle \\
& \varnothing & & \varnothing & \\
& & |4,2,2\rangle & &
\end{array}
\tag{4.94}
$$

Compared to (4.93), we have dropped the superscript denoting the $su(2)_\circ$ representations, since $su(2)_\circ$ is broken by the orbifold and each multiplet above has multiplicity one. For

---

[28]Recall that, as we have shown in this sub-section, $(N_0, N_1 + N_3)$ can only take the following values $(0,0),(1,0),(1,2),(2,0),(2,2),(2,4),(3,2),(3,4),(4,4)$. Since $L \in \mathbb{N}^+$, we have additionally shifted L by suitable discrete amounts when matching the two expressions.

$n = 2$, the orbifold acts as a minus sign for each $su(2)_\circ$ doublet index and as a result all four $|2, 1, 1\rangle$ multiplets are $\mathbf{Z}_2$-invariant. The $n = 2$ untwisted sector protected spectrum is

$$
\begin{array}{ccccc}
& & |0, 0, 0\rangle & & \\
& \varnothing & & \varnothing & \\
|2, 0, 0\rangle & & |2, 1, 1\rangle^{\oplus 4} & & |2, 2, 2\rangle \\
& \varnothing & & \varnothing & \\
& & |4, 2, 2\rangle & &
\end{array}
\qquad (4.95)
$$

Next consider the twisted sectors. The massive ABA and Bethe equations remain unchanged, since those excitations are $su(2)_\circ$ singlets. In fact, since the orbifold leaves the $psu(1|1)_{\text{c.e.}}^4$ symmetry invariant, only the massless momentum-carrying Bethe equations change. The twisted-sector boundary conditions are implemented in the Bethe equations by an additional phase

$$
\left(\frac{x_k^+}{x_k^-} \right)^L = e^{-i\phi_0} \prod_{\substack{j=1 \\ j \neq k}}^{N_0} \sqrt{\frac{x_k^- x_j^+}{x_k^+ x_j^-}} \frac{x_k^+ - x_j^-}{x_k^- - x_j^+} (\sigma_{kj}^{\circ\circ})^2 \prod_{j=1}^{N_1} \sqrt{\frac{x_k^+}{x_k^-}} \frac{x_k^- - y_{1,j}}{x_k^+ - y_{1,j}} \prod_{j=1}^{N_3} \sqrt{\frac{x_k^+}{x_k^-}} \frac{x_k^- - y_{3,j}}{x_k^+ - y_{3,j}} .
$$

$$(4.96)$$

where ϕ_0 is

$$
\phi_0 = \pm \frac{2\pi}{n} , \qquad (4.97)
$$

with the sign choice determined by the value of the $su(2)_\circ$ index of the momentum-carrying massless excitation in question. Because of this phase, in the zero momentum limit, there are no $N_0 > 0$ solutions to the above Bethe equation and only the BMN vacuum state $|0, 0, 0\rangle$ without any fermionic zero modes is protected in each twisted sector. As a result, the counting of pretected multiplets in the twisted sectors matches the Hodge number counting reviewed in Section 4.1: there are 16, respectively 18, twisted sector multiplets in the $\mathbf{Z}_2$, respectively $\mathbf{Z}_{n>2}$, orbifolds. Combining these with the untwisted sector states above, we match the Hodge diamond of the seed K3 theory (4.15). Remembering the additional dependence on L through the BMN vacuum $|0, 0, 0\rangle$ (see equation (4.67)), we match the expected protected spectrum in (4.16).

4.5   Protected states in $\mathbf{AdS}_3 \times \mathbf{S}^3 \times \mathbf{S}^3 \times \mathbf{S}^1$ and its orbifold

The ABA and Bethe equations for closed strings on $\text{AdS}_3 \times \text{S}^3 \times \text{S}^3 \times \text{S}^1$ are based on a single $psu(1|1)_{\text{c.e.}}^2$ algebra. There are two massless ρ_{L} multiplets, with highest-weight fermions denoted as χ_{L} and χ_{R}. There is now a single auxiliary variable y, whose Bethe equation is the same as (4.46). The two massless momentum-carrying Bethe equations are like equation (4.49), but with only a single auxiliary-root product. As already shown in [49], the protected states come from the BMN vacuum with up to two fermionic zero modes inserted

$$
|Z^L\rangle , \qquad |Z^L \chi_{\text{L}}\rangle , \qquad |Z^L \chi_{\text{R}}\rangle , \qquad |Z^L \chi_{\text{L}} \chi_{\text{R}}\rangle , \qquad (4.98)
$$

where, as in the T^4 case, the Zhukovski variables can take either of the two values s_+ in equation (4.68) to give the same physical state. Unlike the T^4 case, here there are no protected multiplets involving auxiliary roots. The spectrum found in this way [49] agrees with the supergravity calculation and WZW point analysed in [89].

When $\alpha = 1/2$ the two S^3s in the geometry have the same radius and one can define a $\mathbf{Z}_2$ orbifold whose action swaps the two three-spheres and inverts the circle [104]. These authors showed that it is possible to extend the orbifold action in a way that preserves $\mathcal{N} = (3, 3)$ super-conformal symmetry, whose global symmetry is $\mathrm{osp}(3|2) \subset \mathrm{osp}(4|2) \equiv \mathrm{d}(2, 1; \alpha = \frac{1}{2})$. The protected spectrum of this orbifold was found in [105]. The $\mathrm{psu}(1|1)^2_{\mathrm{c.e.}}$ algebra used to construct the ABA of the unorbifolded background is contained in the $\mathrm{osp}(3|2)$ symmetry of the orbifolded background. This suggests that the orbifolded theory could also be integrable, with the same ABA as the parent theory, if suitable integrability-preserving quasi-periodicity conditions for the twisted sectors can be found. Further, since the $\mathrm{psu}(1|1)^2_{\mathrm{c.e.}}$ algebra is invariant under the orbifold action so too must be the $\mathrm{psu}(1|1)^2_{\mathrm{c.e.}}$ supercurrents given in equations (2.38)–(2.41) of [58]. The massless bosons are the S^1 boson w and the difference of the great circles on the two S^3s ψ. The $\mathbf{Z}_2$ action on these is

$$w \longrightarrow -w \,, \qquad \psi \longrightarrow -\psi \,, \tag{4.99}$$

and in order to preserve the supercurrents the orbifold must act as a

$$\chi_{\mathrm{L}} \longrightarrow -\chi_{\mathrm{L}} \,, \qquad \chi_{\mathrm{R}} \longrightarrow -\chi_{\mathrm{R}} \tag{4.100}$$

on the massless fermions. The untwisted protected spectrum of $\mathrm{AdS}_3 \times (\mathrm{S}^3 \times \mathrm{S}^3 \times \mathrm{S}^1)/\mathbf{Z}_2$ follows immediately: the states

$$|Z^L \chi_{\mathrm{L}}\rangle \,, \qquad |Z^L \chi_{\mathrm{R}}\rangle \,, \tag{4.101}$$

are projected out, while

$$|Z^L\rangle \,, \qquad |Z^L \chi_{\mathrm{L}} \chi_{\mathrm{R}}\rangle \,, \tag{4.102}$$

survive the projection. The orbifold also has two twisted sectors, one each for the two S^1 fixed points. Each twisted sector's ground state gives rise to a single protected state for fixed L. This is to be be expected in the twisted ABA which does not contain any zero-momentum massless fermions, much like in the case of the twisted sectors in $\mathrm{T}^4/\mathbf{Z}_n$ orbifolds. This protected spectrum agrees with the one found in [105] using supergravity and WZW methods.

4.6   Conclusions and outlook

In this work, we have constructed the exact ABA for closed strings on $\mathrm{AdS}_3 \times \mathrm{S}^3 \times \mathrm{T}^4$ and $\mathrm{AdS}_3 \times \mathrm{S}^3 \times \mathrm{K3}$ in its orbifold limits. The ABA is valid for these geometries supported by any combination of NSNS and RR charges as well as any value of non-blow up moduli since all such theories are integrable [16]. Because of the relatively low amount of supersymmetry, these theories have multiple families of groundstates in addition to the familiar BMN vacua. We have shown how generic closed string states can be constructed in the ABA on top of each of these groundstates by inserting fermionic zero-modes. This novel feature, not found in higher-dimensional integrable holographic models, relies on the presence of massless momentum carrying roots, as well as new special points in the auxiliary Bethe variables.

As we showed in equation (4.74), starting with a Bethe state containing a massless momentum-carrying excitation at zero momentum $x^\pm = s_\pm$, we can create another state by acting with a $\mathcal{B}$ operator with auxiliary root $y = s_\pm$. This leads to an excited state on

top of a different vacuum with other zero-modes inserted. Such a feature of the ABA is unique for $m = 0$ momentum carrying excitations, because the zero-momentum limit in equation (4.68) gives a finite answer only when $m = 0$. This should be contrasted with adding auxiliary roots at $\pm\infty$ to a generic Bethe state [6]. In this more familiar case, the resulting states are descendents in the same multiplet of the global superconformal algebra, in contrast to the massless states with zero-momentum roots, which are in different multiplets.

Using the ABA we constructed the explicit low-magnon number eigenstates and showed how, in the zero-momentum limit, they give rise to protected half-BPS states in these backgrounds. The protected spectrum was first found using supergravity Kaluza-Klein reduction in [88] and we reproduce it with the ABA here. Our analysis proves that such states are protected to all orders in α' in the planar theory and amounts to a non-renormalization theorem based on integrability. By constructing the explict wavefunctions of states, we were able to perform the $T/\mathbf{Z}_n$ orbifolds in a straightforward way, obtaining for the first time the protected spectrum of the $\mathrm{AdS}_3 \times \mathrm{S}^3 \times \mathrm{K3}$ theories from exact integrable methods. Additionally, our wavefunction construction demonstrates explicitly that each protected state can be obtained from a number of distinct solutions of the Bethe equations, as was anticipated in [49].

It is not clear to us whether integrability continues to hold away from the orbifold limit of K3. While this would not affect the protected spectrum analysis, since blow-up modes are moduli, a generic K3 has a complicted metric making the integrability of string theory on it less likely. To test this, one might, for example, compute the magnon dispersion relation or generalise the analysis of [106] in the presence of a few blow-up mode insertions. At the same time, as the analysis in [16] showed, integrability is valid across the whole moduli space of $\mathrm{AdS}_3 \times \mathrm{S}^3 \times \mathrm{T}^4$ theories. We might optimistically hope for the same to be true for $\mathrm{AdS}_3 \times \mathrm{S}^3 \times \mathrm{K3}$.

We have also generalised our analysis of the protected string spectrum to the quarter-BPS protected states for the $\mathrm{AdS}_3 \times \mathrm{S}^3 \times \mathrm{S}^3 \times \mathrm{S}^1$ background and its $\mathbf{Z}_2$ orbifold. The protected eigenstates are much simpler since they do not involve any auxiliary roots and for the unorbifolded theory was already presented in [49].

It would be interesting to use these results to better understand the Thermodynamic Bethe Ansatz (TBA) for these backgrounds, building on the massless TBA of the pure RR theory found in [94]. The role of the auxiliary roots we have presented may help to clarify how mixed-mass interactions can be incorporated into the TBA following also the observations in [93].

5 Machine learning Lie structures and applications to physics

In this work [107], we are motivated by the question of whether and how much one can machine-learn the essential information about classical, and exceptional Lie algebras as tabulated in standard texts such as Slansky [108]. Specifically, we address the two fundamental problems in the representation theory of Lie algebras that is crucial to physics – the tensor product decomposition and the branching rules to a sub-algebra – and show that these salient structures are machine learnable. The author of the thesis is responsible for implementing both experiments.

In particular we show that a relatively simple forward-feeding neural network can pre-

dict to high accuracy and confidence, the number of irreducible representations ("irreps") that appear in a tensor product decomposition, which we refer to as the *length* of the decomposition. Our findings for classical and exceptional algebras are summarized in Table 3 . We subsequently show that a neural network can also predict with high accuracy, the presence or absence of a given irreducible representation of a maximal sub-algebra within an irreducible representation of a parent algebra. The neural network is capable of predicting, for example, the presence of bi-fundamentals in $SU(3) \times SU(2)$ for a given representation of $SU(5)$ to an accuracy of 88% and a confidence of 0.735.

We remark that our classification problems were also addressed with various standard classifiers, such as Naive Bayes, nearest neighbours and support vector machines. We found that the NN with the architecture shown below in Fig. 4 significantly out-performed them. For example, using Logistic Regression for the analysis of Table 4 for the A_m algebra yields a test accuracy of 0.823 and a confidence of 0.64. The results from support vector machines are similar. This is in line with previous observations where NNs with similar architures perform well for a variety of problems, such as the computation of topological invariants of manifolds [109, 110], and finite graph invariants [111].

5.1   Tensor Products

Let us begin with a simple ML experiment. One of the most important computations for Lie groups/algebras is the decomposition of the tensor product of two representations into a direct sum of irreducible representations for a given group G: $R_1 \otimes R_2 = \bigoplus\limits_{r\in \text{ irreps}} a_r R_r$, where $a_r \in \mathbb{Z}_{\geqslant 0}$ are the multiplicity factors. To be concrete, let us first consider $A_m = SU(m + 1)$. Every irreducible representation ("irrep") of A_m is specified by a highest-weight vector $\vec{v}$, which is a rank m vector of non-negative integer components. Throughout this section, we will use

$$\vec{v} \equiv (v_1, \ldots, v_r) \tag{5.1}$$

to denote the weight vector for a Lie algebra of rank r. When the context is clear, an integer with the vector over-script is understood to be a vector of the same integer entry, e.g., $\vec{4} = (4, 4, \ldots, 4)$.

As the entries of $\vec{v}$ increase in magnitude, the dimension of the corresponding irrep $R_{\vec{v}}$ can grow dramatically. For instance, for $A_3 = SU(4)$, $\dim R_{\vec{v}=(a,b,c)} = \frac{1}{12}(a + 1)(b + 1)(c + 1)(a + b + 2)(b + c + 2)(a + b + c + 3)$. This makes the task of identifying the precise irreps contained in a tensor decomposition rather laborious.

We start with two weight-vectors $\vec{v}_1, \vec{v}_2$. Their rank m is chosen randomly from {1,2,...,8}. Then, we randomly generate a pair quinary vectors $\vec{v}_1, \vec{v}_2$ of rank m, and compute their tensor decomposition into irreducible representations:

$$R_{\vec{v_1}} \otimes R_{\vec{v_2}} = \bigoplus\limits_{r \, \in \, \text{irreps}} a_r R_r \; . \tag{5.2}$$

This computation, although algorithmic, is non-trivial. Even the relatively simple question of *how many distinct irreps, along with their multiplicities, are there on the RHS* or what we call the <u>length</u> of a given tensor decomposition, is not immediately obvious just by looking at the the vectors $\vec{v}_1$ and $\vec{v}_2$. For example,

$$R_{[0,1]} \otimes R_{[2,1]} = \mathbf{8} \oplus \mathbf{10} \oplus \mathbf{27} \; ;$$
$$R_{[1,0,1]} \otimes R_{[0,2,0]} = \overline{\mathbf{45}} \oplus \mathbf{20'} \oplus \mathbf{175} \oplus \mathbf{45} \oplus \mathbf{15} \; . \tag{5.3}$$

It is difficult to see a priori that one decomposition would be of length 3 while the other would be of length 5; and one needs to actually compute the respective tensor decomposition to know the answer. It took several hours using LieART to perform five thousands decompositions[29]. To get an idea of their distributions, we show the histogram of the length: indeed there is a huge variation from 1 to over 350. A significant improvement in the running time (from hours to a few minutes) can be attained by capping off the maximum dimension of the irreps (say to 10,000). The distribution of the lengths of the decompositions vs frequency histogram, is depicted in figure 3.
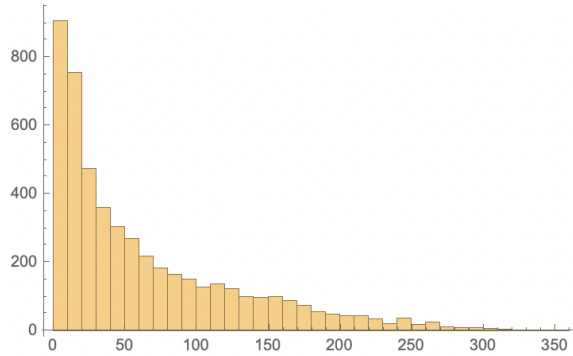
Figure 3: Distribution of the number of distinct irreps in the tensor decomposition of $R_{\vec{v}_1} \otimes R_{\vec{v}_2}$ for A_m with randomized $1 \leqslant m \leqslant 8$ and randomized ternary weight vectors $\vec{v}_{1,2}$. The horizontal axis denotes the length of $R_{\vec{v}_1} \otimes R_{\vec{v}_2}$ and the vertical axis denotes the corresponding frequency.

Let us next consider a simple binary classification problem using the data generated by LieART: can ML distinguish tensor decompositions of length $\geqslant 70$ and of length < 70? The length 70 is chosen since it splits the data rather evenly into around five thousands each. To uniformize the input vectors, for the rank $m < 8$, we also pad both $\vec{v}_{1,2}$ to the right with -1 (a meaningless number in this context) and stack them on top of each other. Thus, our input is a 2×8 matrix with integer entries for $1 \leq m \leq 8$. This step is essential for using a single NN for learning data for Lie algebras of varying ranks (it is for $A_m, 1 < m < 8$ here). For the majority of our experiments, we use a feed-forward neural network classifier built in `Mathematica` with the architecture shown in Figure 4. We also reproduced these results with a similar 2-layer architecture on `Keras`, with `selu` activated neurons to obtain similar accuracy and confidence. Finally, we need to ensure that the last softmax is rounded to 0 or 1 according to our binary categories.

The results of our training and learning for A_m are depicted in figure 5. The data was partitioned into 64% training, 16% validation, and 20% test splits. The network was trained on the training and validation sets and the test set was used purely for

---

[29]Care must be taken to find five thousands distinct pairs $(\vec{v_1}, \vec{v_2})$ amidst the randomizations so as not to bias the input.
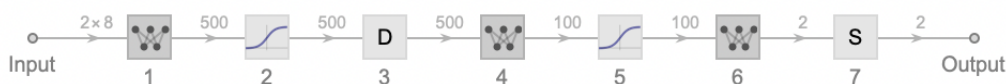
Figure 4: The neural network architecture. S is the softmax activation and D is a dropout layer with probability 0.2. The hidden-layer neurons $(1,2)$ and $(4,5)$ are fully connected and sigmoid activated.
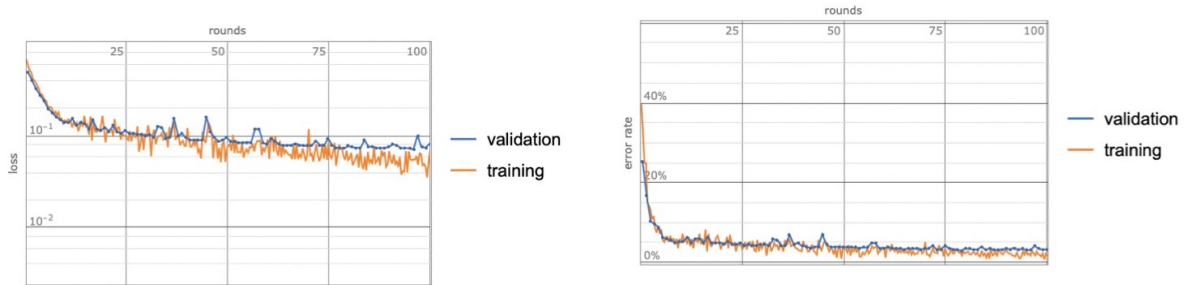
Figure 5: Loss-function (top), and error-rate (below) for training and validation for A_m are plotted against number of epochs.

evaluating the trained network. The plots show a steady lowering in both the error-rate and loss-function as we increase the number of rounds of training and validation. We achieved accuracy 0.969, confidence 0.930, 5% error rate, and 0.1 loss function within one minute by training for 100 epochs using learning rate 10^{-3}, ADAM optimizer; which is excellent indeed. Throughout this work, we will use "accuracy" to mean percentage agreement of predicted and actual values. In addition, in discrete classification problems it is also important to have a measure of "confidence" so that false positives/negatives can be noted. A widely used one is the so-called Matthews' Phi-coefficient ϕ (essentially a signed square-root of the chi-squared of the contingency table) [112], which is $\lesssim 1$ for predictions with good confidence.

The above experiment was also carried out with other classical, as well as exceptional Lie algebras with comparable success. The results are given in table 3. We generated the same data size as in the A_m case, i.e. 5000, and used the same cap on the maximum dimension of the irreps (10,000). In contrast, though the dimension cap for exceptional groups was set to 120,000, it yielded far fewer data points. The lengths we split the data-sets on were chosen to generate a balanced data-set in each case. The accuracy of ML prediction was above .95 for each of these cases. The relatively lower accuracy

Group	Data Size	Splitting Length	Accuracy	Confidence
A_m	5000	70	0.969	0.930
B_m	5000	40	0.959	0.878
C_m	5000	40	0.969	0.921
D_m	5000	35	0.965	0.908
G_2	1275	110	0.946	0.891
E_6	903	30	0.898	0.795

Table 3: The binary classification of product decomposition lengths. The splitting lengths yield a balanced dataset.

for E_6 is caused by the low number of points available at low dimensions due to its relatively high rank: 903 data points below dimension of 120,000. Raising the dimension cap would improve the machine-learning, bringing it up to par with others, however the corresponding data generation using LieART would take days.

We also note that partitioning the data-sets at the 'midpoint' to generate balanced data-sets as we have done above is by no means necessary. As an example, we explored this classification problem for the A_m algebras but now organizing the data into partitions

of varying lengths, *viz.* 20/80 through to 80/20. Here by a partition of length 20/80 we mean that a 'cutoff' decomposition length was chosen such that 20% of the decomposition lengths in the dataset are below this length, i.e. are denoted by the target variable Y = 0 and the remaining 80% are above, and hence denoted by Y = 1. In every case the Matthews' Phi-coefficient remains close to 1. In particular, for the 20/80 and 80/20 partition it is 0.98.

We can take this experiment one step further and train the neural net on low dimensional tensor decomposition data, then test its performance on higher dimensional cases. If successful this would immensely reduce the computation time. For example, obtaining the length of decomposition for two A_6 weight vectors $\vec{v}_1 = \vec{v}_2 = (2, 2, 2, 2, 2, 2)$ by brute force takes over 15 minutes on LieART while machine learning should estimate the length in a matter of seconds.

We retrained the NN in figure 4 on the same data for the classical and G_2 algebras generated by LieART for the previous experiment. However, the training set is now restricted to have both input weight vectors of dimension less than certain cut-off value, here taken to be 2,000. The *trained* neural network was subsequently evaluated on the test dataset consisting of input weight vectors of dimension ranging between 2,000 and 10,000. Our results are presented in Table 4 and Figure 6.

Group	Train/Val Accuracy	Test Accuracy	Confidence
A_m	0.974/0.957	0.961	0.907
B_m	0.972/0.963	0.957	0.845
C_m	0.969/0.970	0.892	0.792
D_m	0.971/0.940	0.956	0.817
G_2	0.969/0.963	0.968	0.922
E_6	0.963/0.947	0.875	0.751

Table 4: Training on low dimensional irreps, and testing on high dimensional ones.
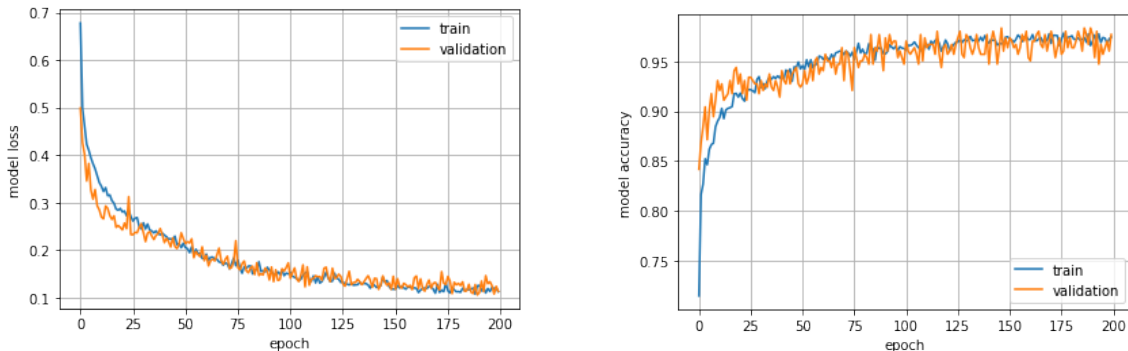
Figure 6: Loss-function (top), and model accuracy (below) for training on A_m irreps, plotted against number of epochs.

5.2   Beyond Binary Classification

We now move beyond the simpler binary classification experiments done previously to a multi-class classification task, with the aim of predicting a range for the length of

the product decomposition as opposed to the over/under estimates obtained above. For definiteness, let us take the A_m data and classify it into five classes, depending on whether the length of the product decomposition lies in the ranges 0 to 10, 10 to 25, 25 to 55, 55 to 115 and greater than 115. Figure 7 shows a histogram with the class populations, and the training curves are displayed in Figure 8. The neural network reaches a ϕ-coefficient
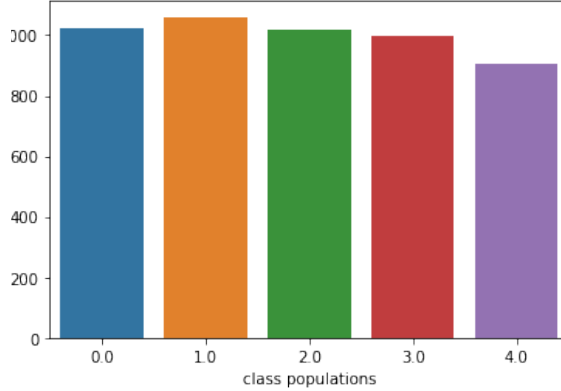
Figure 7: Class Populations of length bins for A_m irreps.

of 0.917 on the test set, and the confusion matrix (measuring the frequency of the truth label against the predicted label) is given by

$$
\begin{pmatrix}
96 & 3 & 0 & 0 & 0 \\
1 & 92 & 3 & 0 & 0 \\
0 & 2 & 109 & 4 & 0 \\
0 & 0 & 7 & 86 & 7 \\
0 & 0 & 0 & 6 & 84
\end{pmatrix}
\tag{5.4}
$$

5.3   Branching Rules

The next task on which we train our neural network of Figure 4 is to learn about the branching rules for Lie algebras. Suppose we take a weight-vector of $SU(5)$, and restrict its entries from 0 to 4 (i.e., as quinary 4-vectors). Even though this may look rather harmless, the dimension of the corresponding irrep ranges from 1 for $\vec{0}$, to 9765625 for $\vec{4}$. When we decomposed these irreps of $SU(5)$ to those of its maximal sub-algebra $SU(3) \times$
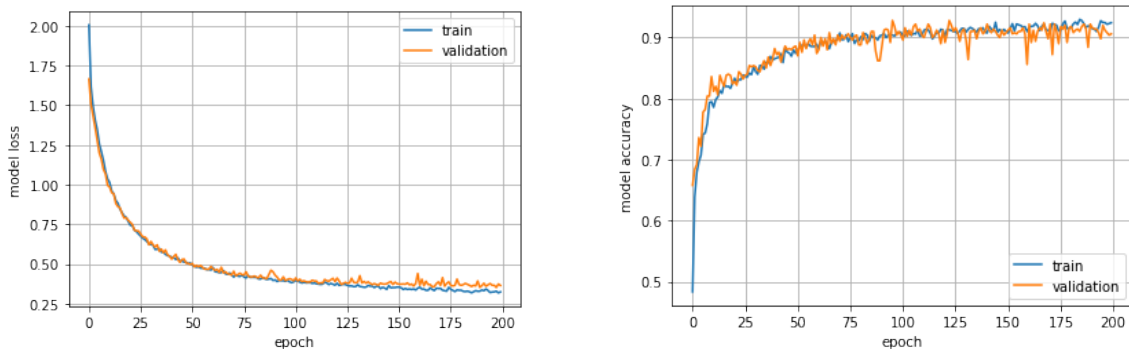
Figure 8: Training curves for the quinary classification problem for A_m, plotted against number of epochs.
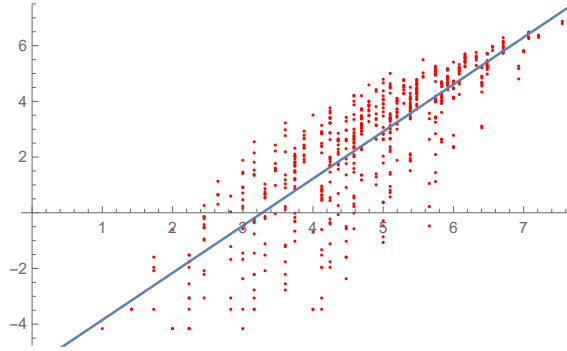
Figure 9: Plot and fit of log of the time in seconds of the branching of irreps of $SU(5)$ versus the length of the weight-vector.

$SU(2) \times U(1)$, and found their explicit branching products, the time taken on LieART was easily seen to be exponential[30]. In figure 9, we plot the log of the time taken in seconds, versus the length of the weight-vector. The best fit is the line $-5.54361 + 1.69186x$. By extrapolation, the single irrep of $SU(5)$ corresponding to weight vector $\overrightarrow{10}$ would take over 20 years just to compute its branching products into $SU(3) \times SU(2) \times U(1)$.

In the rest of this section, we shall show the efficacy of using ML to predict presence/absence of any given representation of the maximal sub-algebra in a given irrep of $SU(5)$ and G_2 algebras. For concreteness, we look for bi-fundamental representations of $SU(3) \times SU(2)$ (with arbitrary values of $U(1)$ charges) in any given $SU(5)$ irrep. In the G_2 case, we restrict ourselves to bi-fundamental representation of $SU(2) \times SU(2)$ maximal sub-algebra.

For the $SU(5)$ branching, we use first 800 irreps of smallest dimension as input vectors with binary output depending on presence/absence of a bi-fundamental rep of $SU(3) \times SU(2)$. The data was split into train/validation/test sets in the ratio 80/10/10. The neural network reached a test accuracy of 0.899 and a confidence of 0.813. The next best results were arrived at by a support vector classifier which reached an test accuracy of 0.838 and confidence of 0.677.

For the G_2 branching, we used 400 weight input vectors with dimensions below 4.7 million. Analogous to the $SU(5)$ case, the output was binary, depending on presence/absence of a bi-fundamental rep of $SU(2) \times SU(2)$. All classifiers, neural nets and otherwise, performed at the level of blind guessing in this case, which is possibly due to the relatively fewer input data as well as smaller number of features in the data.

5.4 Outlook

Given the ubiquity of Lie algebras and groups in physics, we conclude this section with some comments about the vast possibilities in applications to physics of our results, exemplifying with two which immediately come to mind.

In scattering processes, given a pair of incoming particles transforming under the irreps of certain global symmetry group, the outgoing particles can be classified via their tensor decompositions. The tensor decomposition prediction and extrapolation results in section 5.1 thus allow us to efficiently estimate the number of distinct outgoing particles.

---

[30]Notice that as LieART is only capable of generating branching rule data for maximal subgroups, here we will focus on this simplest set of branching training data to illustrate the capability of neural network.

It would also be exciting to see if the NN upper bound estimate of the length of a given decomposition can help LieART package to work out its explicit terms within significantly shorter period.

Our choice of studying the branching of $SU(5)$ into its maximal subgroup $SU(3) \times SU(2) \times U(1)$ in section 5.3 was phenomenologically motivated. This hopefully can lead to an useful algorithm for testing whether a field transforming under $SU(5)$ GUT gauge group can yield descendants transforming under standard model gauge groups upon spontaneous symmetry breaking. We hope this will be useful for particle physics model building purposes.

6 The R-mAtrIx Net

In this work [113], we demonstrate how neural networks and deep learning provide an efficient way to numerically solve the Yang-Baxter equation for integrable quantum spin chains. On an immediate front, we are motivated by recent interesting work on classical integrable systems using machine learning [114, 115, 116, 117]. The approach taken in the work [117] of learning classical Lax pairs for integrable systems by minimization of the loss functions encoding a flatness condition has a particularly close parallel to our approach. However, to the best of our knowledge, the present work is the first attempt to apply machine learning to quantum integrability, the analysis of R-matrices and the Yang-Baxter equation. The author of thesis is responsible for the implementation of all the experiments including the design of architecture, hyperparameter tuning, and extracting meaningful predictions.

Our analysis utilizes neural networks to construct an approximator for the R-matrix and thereby solve functional Yang-Baxter equation while also allowing for the imposition of additional constraints. We look into the sub-class of all possible R-matrices, namely those that are regular and holomorphic, and incorporate the Yang-Baxter equation into the loss function. Upon training for the given integrable Hamiltonian, we successfully learn the corresponding R-matrix to a prescribed precision. Using spin chains with two-dimensional space as a main playground we reproduce all R-matrices of difference form which was recently classified in [118]. Moreover, this *Solver* can be turned into an *Explorer* which scans the space (or a certain subspace) of all Hamiltonians looking for integrable models, which in principle allows us to discover new integrable models inaccessible to other methods. Below we provide the summary of the Neural Network and its training, as well as an overview of the paper.

Summary of Neural Network and Training: The functional Yang-Baxter equation, see Equation (1.26) below, is holomorphic in the spectral parameter $u \in \mathbb{C}$ and as such, holds over the entire complex plane. In this paper, we shall restrict our training to the interval $\Omega = (-1, 1)$ on the real line, but design our neural network so that it analytically continues to a holomorphic function over the complex plane. Each entry into the R-matrix is separately modeled by multi-layer perceptrons (MLP) with two hidden layers of 50 neurons each, taking as input parameters the variable $u \in \Omega$. More details are available in Section 6.2 and Appendix F. All the neurons are `swish` activated [119], except for the output neurons which are `linear` activated. Training proceeds by optimizing the loss functions that encode the Yang-Baxter equations (6.5), regularity (6.10), and constraints on the form of the spin chain Hamiltonian, for instance *via* (6.11). Hermiticity of the

Hamiltonian, if applicable, is imposed by the loss (6.13). Optimization is done using Adam [72] with a starting learning rate of $\eta = 10^{-3}$ which is annealed $\eta = 10^{-8}$ in steps of 10^{-1} by monitoring the Yang-Baxter loss (6.5) on validation data for saturation. Adam's hyperparameters β_1 and β_2 are fixed to 0.9 and 0.999 respectively. In the following, we will refer to this learning rate policy as the *standard schedule*. We apply this framework to explore the space of R-matrices using the following strategies:

1. **Exploration by Attraction**: The Hamiltonian loss (6.11) is imposed by specifying target numerical values for the two-particle Hamiltonian, or some ansatz/ symmetries instead (like 6-vertex, 8-vertex, etc.). We also formally include here the ultimate case of *general search* when no restrictions are imposed on the Hamiltonian at all. This strategy is predominantly used in our Section 6.3.

2. **Exploration by Repulsion**: We can generate new solutions by *repelling away* from an ansatz or a given spin chain. This requires us to activate the loss function (6.15) for a few epochs in order to move from the specific Hamiltonian. This strategy is employed in Section 6.4.

Further, we also have two schemes for initializing training.

1. **Random initialization**: We randomly initialize the weights of the neural network using He initialization [120]. This samples the weights from either a uniform or a normal distribution centered around 0 but with a variance that scales as the inverse power of the layer width.

2. **Warm-start**: we use the weights and biases for an already learnt solution .

A brief overview of this section is as follows. In subsection 6.1, we review the classification program of 2-D spin chains of difference form through the boost automorphism method [118]. Then we outline our methodology for learning the R-matrix given an ansatz for the two-particle Hamiltonian in Section 6.2. We present our results in sections 6.3, 6.4. Section 6.3 focuses on hermitian XYZ and XXZ models (section 6.3.1), and prototype examples from the 14 gauge-inequivalent classes of models in [118](section 6.3.2). The latter sub-section also contrasts training behaviour for integrable and non-integrable models. Section 6.4 presents a preliminary search strategy for new models which we illustrate within a toy-model setting: rediscovering the two integrable subclasses of 6-vertex Hamiltonians. Section 6.5 discusses ongoing and future research directions.

6.1   Reviewing two-dimensional R-matrices of difference form

We will illustrate the work of our neural network using two-dimensional spin chains as a playground. The regular difference-form integrable models in this context have recently been classified using the Boost operator in [118]. Here, we present a brief overview of the methods and results of this paper. Boost automorphism method allows one to find integrable Hamiltonians by reducing the problem to a set of algebraic equations. Let us focus on a spin chains with two-dimensional space $V = \mathbb{C}^2$ and nearest-neighbour Hamiltonian (1.24). One formally defines the boost operator $\mathcal{B}$ [121] as

$$\mathcal{B} = \sum_{a=-\infty}^{\infty} a H_{a,a+1}\,, \tag{6.1}$$

which generates higher charges $\mathbb{Q}_n$, $n \geqslant 3$, from the Hamiltonian $\mathbb{Q}_2$ via action by commutation:

$$\mathbb{Q}_{r+1} = [\mathcal{B}, \mathbb{Q}_r]. \tag{6.2}$$

This was used in [118] to successfully classify all 2-dimensional integrable Hamiltonians by solving the system of algebraic equations arising from imposing vanishing conditions on commutators between $\mathbb{Q}_i$, upto some finite value of i. Surprisingly it turns out that for the considered models, the vanishing of the first non-trivial commutator $[\mathbb{Q}_2, \mathbb{Q}_3] = 0$ is a sufficient condition to ensure the vanishing of all other commutators. Then making an ansatz for the R-matrices and solving Yang-Baxter equation in the small u limit, the authors constructed the corresponding R-matrices and confirmed the integrability of the discovered Hamiltonians. The solutions can be organized into two classes: XYZ-type, and non-XYZ type, distinguished by the non-zero entries appearing in the Hamiltonian.

$$H_{\text{XYZ type}} = \begin{pmatrix} a_1 & 0 & 0 & d_1 \\ 0 & b_1 & c_1 & 0 \\ 0 & c_2 & b_2 & 0 \\ d_2 & 0 & 0 & a_2 \end{pmatrix}, \qquad H_{\text{non-XYZ type}} = \begin{pmatrix} a_1 & a_2 & a_3 & a_4 \\ 0 & b_1 & b_3 & b_3 \\ 0 & c_1 & c_2 & c_3 \\ 0 & 0 & 0 & d_1 \end{pmatrix}. \tag{6.3}$$

Generically, all non-zero entries would be complex valued. Hermiticity, for the actual XYZ model and its XXZ and XXX limits, places additional constraints. Integrability also imposes additional algebraic constraints between the non-zero entries, none of which involve complex conjugation in contrast to hermiticity. Amongst the XYZ type models, there are 8 distinct solutions each corresponding to some set of algebraic constraints among the matrix elements of H. In particular, there is one 4-vertex model (H_{4v}) which is purely diagonal (see (E.1)). Next, there are two 6-vertex models ($H_{6v,1}$, $H_{6v,2}$) where d_1 and d_2 are constrained to vanish, among other conditions (see (E.2), (E.4)). One of these, namely $H_{6v,1}$, is a non-hermitian generalisation of the XXZ model. There are also two 7-vertex models ($H_{7v,1}$, $H_{7v,2}$) where only d_2 vanishes (see (E.6), (E.8)), and three 8-vertex models ($H_{8v,1}$, $H_{8v,2}$, $H_{8v,3}$) where all entries are non-zero (see (E.10), (E.13), (E.17)). Here, $H_{8v,1}$ is the non-hermitian generalization of the XYZ model. Among these classes the Hamiltonians are distinguished by additional algebraic constraints on the non-zero elements which we have enumerated in Appendix E. The corresponding R-matrices for these models were obtained in [122]. The non-XYZ models are similarly divided into 6-classes with Hamiltonians $H_{class-1}, \ldots H_{class-6}$ which have been explicitly enumerated in Equation (E.19). Among these, the class 1 and class 2 Hamiltonians have rank less than four. For convenience, we also explicitly write down all of these R-matrices, both for the XYZ type and non-XYZ type models, in Appendix E.

6.2 Machine Learning the R-Matrix

In this sub-section, we shall describe our proposed methodology for constructing R-matrices $\mathcal{R}(u)$ by optimizing a neural network using appropriate loss functions. An R-matrix has elements $R_{ij}(u)$ at least some of which are non-zero. In the following, we shall focus solely on the $R_{ij}(u)$ which are not identically zero as functions of u. We also restrict the training to the real values of spectral parameter $u \in \Omega = (-1, 1)$ and exclusively use holomorphic activations function in order to guarantee the holomorphy of the resulting R-matrix $\mathcal{R}(u)$. The matrix elements $\mathcal{R}_{ij}(u)$ of this R-matrix are modeled

by neural networks as

$$\mathcal{R}_{ij}(u) = a_{ij}(u) + i\, b_{ij}(u) :$$

$$; \quad r_{ij} = \{a_{ij}, b_{ij}\}\,. \quad (6.4)$$
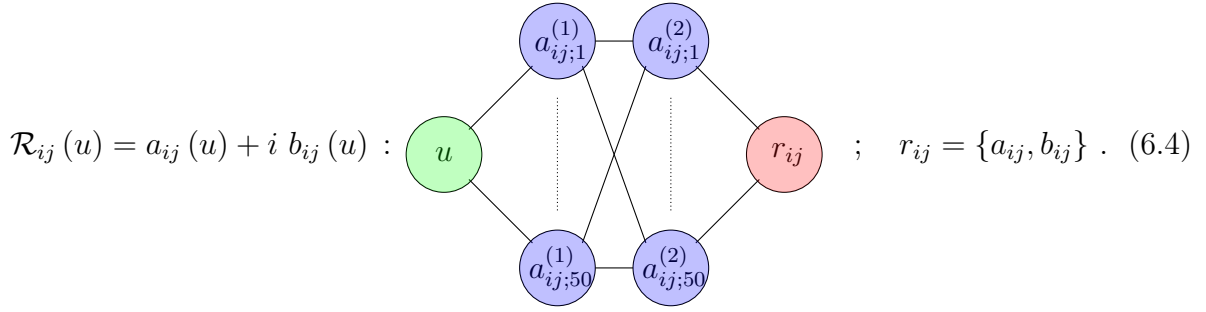
We have decomposed the matrix element $\mathcal{R}_{ij}(u)$ into $a_{ij}(u) + i\, b_{ij}(u)$ in order to learn complex-valued functions $\mathcal{R}_{ij}$ while training with real MLPs on the real interval Ω. In this paper, purely for uniformity, we have modeled each such $a_{ij}(u)$ and $b_{ij}(u)$ using an MLP containing two hidden layers of 50 neurons each and one `linear` activated output neuron. We emphasize that the identification of $a_{ij}(u)$ and $b_{ij}(u)$ to real and imaginary parts of $\mathcal{R}_{ij}(u)$ is only valid over the real line, and these functions separately continue into holomorphic functions over the complex plane whose sum $\mathcal{R}_{ij}(u)$ is holomorphic by construction. Now, $\mathcal{R}_{ij}(u)$ is required to solve the the Yang-Baxter equation (1.26) subject to (1.27). We may also place constraints on the corresponding two-particle H given by (1.34). These criteria are encoded into loss functions which the R-matrix $\mathcal{R}_{ij}(u)$ aims to minimize by training. For example, in order to train $\mathcal{R}_{ij}(u)$ to satisfy Yang-Baxter equation (1.26) for all values of spectral parameter u from the set $\Omega \subset \mathbb{C}$ we introduce the following loss function :

$$\mathcal{L}_{YBE} = ||\mathcal{R}_{12}(u-v)\mathcal{R}_{13}(u)\mathcal{R}_{23}(v) - \mathcal{R}_{23}(v)\mathcal{R}_{13}(u)\mathcal{R}_{12}(u-v)||\,, \quad (6.5)$$

where $||...||$ is a matrix norm defined as $||A|| = \sum_{\alpha,\beta=1}^{n} |A_{\alpha\beta}|$ for an complex-valued $n \times n$ matrix A. During the forward propagation we sample a mini-batch of u and v values, from which the corresponding $u - v$ is constructed. Along this paper, the spectral parameters u and v run over the discrete set of 20000 points randomly chosen from the interval Ω. [31] The loss function $\mathcal{L}_{YBE}$ is positive semi-definite, vanishing only when $\mathcal{R}(u)$ solves the Yang-Baxter equation. In principle, one may imagine a scan across the space of all functions in which case, solutions of the Yang-Baxter equation would minimize the loss (6.5) to zero.

In practice of course, one cannot scan across the space of all functions and is restricted to a hypothesis class. Here the hypothesis class is implicitly defined by the design of the neural network, the choice of numbers of layers, number of neurons in each layer, as well as the activation function. Varying the weights and biases of the neural network allows us to scan across this hypothesis space. While in general the exact R-matrix may not belong to this hypothesis class, and the loss function would then be strictly positive, deep learning may allow us to approach the desired functions $\mathcal{R} \to R$ to a high degree of accuracy. In summary, if we restrict to a hypothesis class which does not include an actual solution of the Yang-Baxter equation then

$$\mathcal{L}_{YBE} \geqslant \epsilon = \min_{\{w',b'\}} \mathcal{L}_{YBE}\left(\{w',b'\}\right) > 0\,, \quad (6.6)$$

---

[31] The number of points used during the training bounds the precision which one can reach and in our case it will be of order 10^{-4}.

where ideally ϵ would be small, indicating that we have obtained a good approximation to the true solution. We expect that scanning across wider and wider hypothesis classes would bring ϵ closer and closer to zero. Further, while the RTT equation (1.30) follows from the Yang-Baxter equation (1.26), it can also be imposed separately as a loss function on the network in order to improve the training :

$$\mathcal{L}_{RTT} = ||\mathcal{R}_{12}(u - v)\mathcal{T}_1(u)\mathcal{T}_2(v) - \mathcal{T}_2(v)\mathcal{T}_1(u)\mathcal{R}_{12}(u - v)||. \tag{6.7}$$

Next, we have constraints that must be imposed on the R-matrix at $u = 0$. Following equation (1.27) and equation (1.34) in previous section, we require that [32]

$$R(0) = P, \qquad P\frac{d}{du}R(u)|_{u=0} = H, \tag{6.9}$$

where H is the two particle Hamiltonian. They both can be encoded in the loss function as

$$\mathcal{L}_{reg} = ||\mathcal{R}(0) - P||, \tag{6.10}$$

$$\mathcal{L}_H = ||P\frac{d}{du}\mathcal{R}(u)|_{u=0} - H||. \tag{6.11}$$

Here, we should mention that we have some flexibility in the manner in which we implement the Hamiltonian constraint $\mathcal{L}_H$. Firstly, one can fix the exact numerical values for the entries of H and learn corresponding R-matrix. We will also consider extensions of this loss function where we supply only algebraic constraints restricting the search space for target Hamiltonians to those with certain symmetries or belonging to certain gauge-equivalence classes. In general, such Hamiltonian constraints give us the requisite control to converge to the different classes of integrable Hamiltonians, and we will name such regime as a *exploration by attraction*.

In the same spirit, when working with the XYZ spin chain or its XXZ and XXX limits, we also require that the two-particle Hamiltonian computed from $R(u)$ is hermitian, i.e.,

$$H = H^\dagger, \tag{6.12}$$

We impose this condition by means of the loss function

$$\mathcal{L}_\dagger = ||H - H^\dagger||, \tag{6.13}$$

We shall therefore train our neural network with the loss function

$$\mathcal{L} = \mathcal{L}_{YBE} + \mathcal{L}_{reg} + \lambda_{RTT}\mathcal{L}_{RTT} + \lambda_H\mathcal{L}_H + \lambda_\dagger\mathcal{L}_\dagger, \tag{6.14}$$

---

[32]It is tempting to consider a variation of our method which involves *residual learning a la* the ResNet family of networks [120]. As opposed to learning deviations from identity, which is typically the approach adopted in the ResNet architecture, we may define

$$R(u) = P + \tilde{R}(u), \tag{6.8}$$

where $\tilde{R}(u)$ is the target function of the neural network, which we design to identically output $\tilde{R}(0) = 0$. While this is possible in principle, in practice it turns out that since the neural network is learning a function in the vicinity of P, which trivially minimizes the Yang-Baxter equation and all other constraints imposed, it almost invariably collapses to the trivial solution and learns $\tilde{R}(u) = 0$ across all u. It would nonetheless be interesting to identify such architectures that successfully learn non-trivial R-matrices and this is in progress.

where putting the coefficients λ_α, for $\alpha = \{RTT, H, \dagger\}$, to zero removes the corresponding loss term from being trained.

The loss function (6.14) produces a very complicated landscape and the NN should approach its minimum during the training. Usually, this search is performed with gradient based optimization methods. One might be skeptical about being stuck in some local minimum instead of finding the global minimum of such complicated loss function in a very high dimensional hypothesis space. However, recent analysis revealed that deep NNs end up having all their local minima almost at the same value as the global one [123], [124]. In other words, there are many different configurations of weights and biases resulting into a function of similar accuracy as the one corresponding to the global minimum. There are also many saddle points and some of them have big plateau and just a small fraction of descendent directions, making them practically indistinguishable from the local minima. However, most of their losses are close to the global minimum as well. Those with significantly higher losses have a bigger number of descendent directions and thus can be escaped during the learning [123], [124].

We find that the training converges to yield simultaneously low values for each of the above losses as applicable. Further, while the hyper-parameters $\{\lambda\}$ are tunable experimentally, setting them all to 1 is a useful default. However, for fine-tuning the training it is also useful to tune these parameters to reflect the specific task at hand. We provide the requisite details in Sections 6.3, where we discuss specific training methodologies and the corresponding results. We will also discuss there a new loss function

$$\mathcal{L}_{repulsion} = \exp\{(-||H - H_o||/\sigma)\}\,, \tag{6.15}$$

which is useful to fine-tune the training to access new integrable Hamiltonians H in the neighbourhood of previously known integrable Hamiltonians H_o, we will call such regime as a *exploration by repulsion*.

As a final observation on the choice of activation functions, we note that at the level of the discussion above, any holomorphic activation function such as `sigmoid`, `tanh`, and the `sinh` would suffice. In practice we find that the training converges faster and more precisely using the `swish` activation [119]. This is given by

$$\text{swish}\,(z) = z\,\sigma\,(z)\,, \qquad \sigma\,(z) = \frac{1}{1 + e^{-z}}\,. \tag{6.16}$$

We have provided some comparison tests across activation functions in Appendix F.2.

In the following sub-sections, we present our results for learning R-matrices within the restricted setting of two dimensional spin chains of difference form. Our analysis will be divided into three parts. First, we will learn hermitian XYZ model and its well-known XXZ and XXX limits, comparing our deep-learning results against the analytic plots. Then we remove hermiticity and reproduce all 14 classes of solutions from [118]. The last set of experiments demonstrates how our Neural Network in the Explorer mode can search for Integrable models exploring the space of Hamiltonians.

6.3 Specific integrable spin chains

In this sub-section we look at specific physical models, by imposing tailored conditions on the Hamiltonian derived from the training R-matrix. This includes constraints on the Hamiltonian entries at $u = 0$, and hermiticity of the Hamiltonian.

6.3.1 Hermitian models: XYZ spin chain and its isotropic limits

Imposing hermiticity on the 8-vertex Hamiltonian, we learn the classic XYZ integrable spin chain and its symmetric XXZ limit. We start with the following 8-vertex model ansatz for the R-matrix

$$R(u) = \begin{pmatrix} a & 0 & 0 & d \\ 0 & b & c & 0 \\ 0 & c & b & 0 \\ d & 0 & 0 & a \end{pmatrix} \tag{6.17}$$

and impose the loss functions for YBE, hamiltonian constraint, regularity, and hermiticity (see equation 6.14). The target Hamitonians comprise of a 2-parameter family $H_{XYZ}(J_x, J_y, J_z)$ given by

$$H_{XYZ}(J_x, J_y, J_z) = J_x S_1^x S_2^x + J_y S_1^y S_2^y + J_z S_1^z S_2^z = \begin{pmatrix} J_z & 0 & 0 & J_x - J_y \\ 0 & -J_z & 2 & 0 \\ 0 & 2 & -J_z & 0 \\ J_x - J_y & 0 & 0 & J_z \end{pmatrix},$$
$$\tag{6.18}$$

where we have set $J_x + J_y$ to be equal to 2. The symmetric limit of XXZ model is realised for $J_x = J_y = 1$. A useful reparametrisation for these models is in terms of (η, m) [125]

$$J_x = 1 + \frac{\sqrt{m}\,\mathrm{sn}\,(2\eta \mid m)}{2}, \quad J_y = 1 - \frac{\sqrt{m}\,\mathrm{sn}\,(2\eta \mid m)}{2}, \quad J_z = \mathrm{cn}\,(2\eta \mid m)\,\mathrm{dn}\,(2\eta \mid m) \tag{6.19}$$

The analytic solution for the XYZ R-matrix is given in terms of Jacobi elliptic functions as

$$a(u) = \frac{\mathrm{sn}\,(2\eta + \omega u \mid m)}{\mathrm{sn}\,(2\eta \mid m)} \exp\left(-\frac{\mathrm{cn}\,(2\eta \mid m)\,\mathrm{dn}\,(2\eta \mid m)}{2\,\mathrm{sn}\,(2\eta \mid m)} \omega u \right),$$

$$b(u) = \frac{\mathrm{sn}\,(\omega u \mid m)}{\mathrm{sn}\,(2\eta \mid m)} \exp\left(-\frac{\mathrm{cn}\,(2\eta \mid m)\,\mathrm{dn}\,(2\eta \mid m)}{2\,\mathrm{sn}\,(2\eta \mid m)} \omega u \right),$$

$$c(u) = \exp\left(-\frac{\mathrm{cn}\,(2\eta \mid m)\,\mathrm{dn}\,(2\eta \mid m)}{2\,\mathrm{sn}\,(2\eta \mid m)} \omega u \right),$$

$$d(u) = \sqrt{m}\,\mathrm{sn}\,(\omega u \mid m)\,\mathrm{sn}\,(2\eta + \omega u \mid m) \exp\left(-\frac{\mathrm{cn}\,(2\eta \mid m)\,\mathrm{dn}\,(2\eta \mid m)}{2\,\mathrm{sn}\,(2\eta \mid m)} \omega u \right), \tag{6.20}$$

where $\omega = 2\,\mathrm{sn}\,(2\eta \mid m)$, and m is the elliptic modular parameter[33]. Our model consistently learns the R-matrices for the XYZ model for generic values of the free parameters η, m. Figure 10 gives the time evolution of the different loss terms during training. Figure 11 plots the R-matrix component ratios with respect to R_{12} in terms of the spectral parameter, and compares them with the corresponding analytic functions for a generic choice of deformation parameters $\eta = \frac{\pi}{3}$ and $m = 0.6$. Letting $m = 0$, we recover the XXZ models for generic values of η.

6.3.2 Two-dimensional classification

Here, we lift the hermiticity constraint on the Hamiltonian, thus allowing for more generic integrable models. As we shall see below, the neural network successfully learns all the 14

---

[33]Usually, these expressions are written in terms of the elliptic modulus k instead of the modular parameter $m = k^2$, e.g. as in [122]. We have expressed them in terms of the modular parameter following the implementation in both Python and Mathematica.
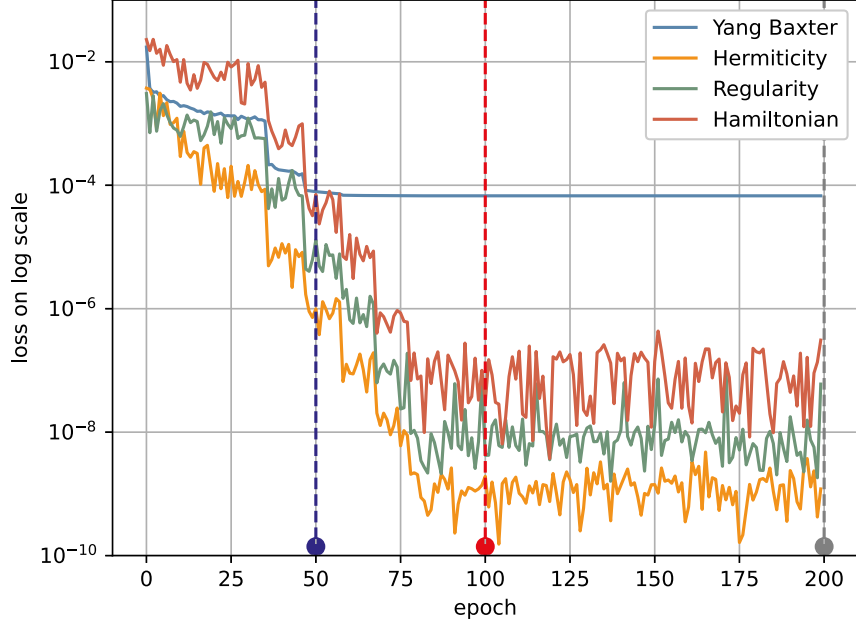
Figure 10: The evolution of training losses for the XYZ model, shown on the log scale. The losses tend to fall in a step-wise manner, which corresponds approximately to the learning rate schedule the network is trained with.
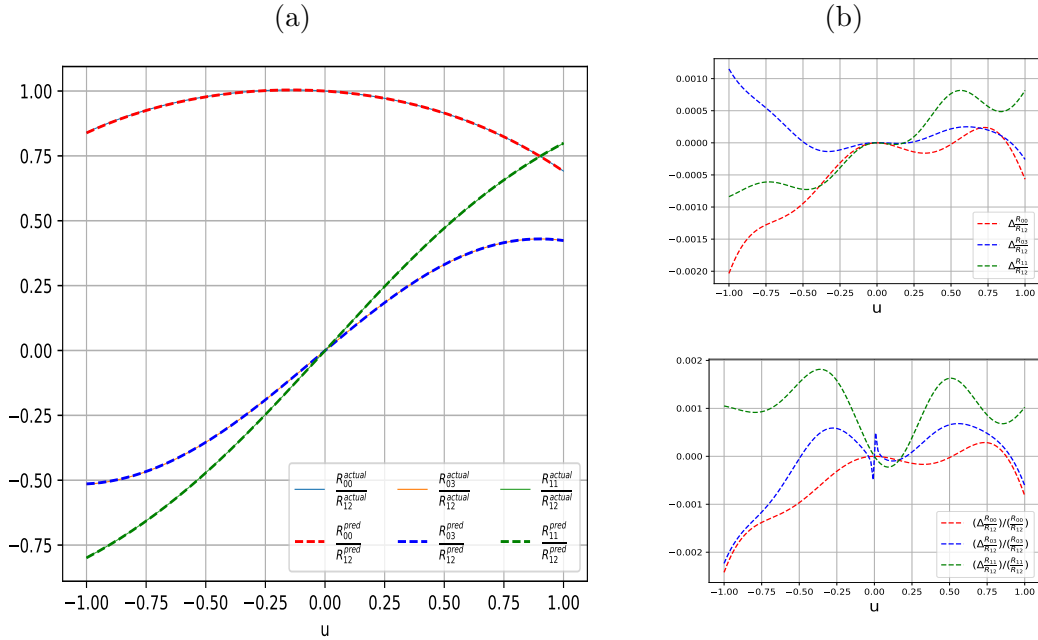
Figure 11: (a) XYZ R-matrix as ratios with respect to the (12) component for $\eta = \pi/3, m = 0.6$, (b) Relative and absolute errors for R-matrix.
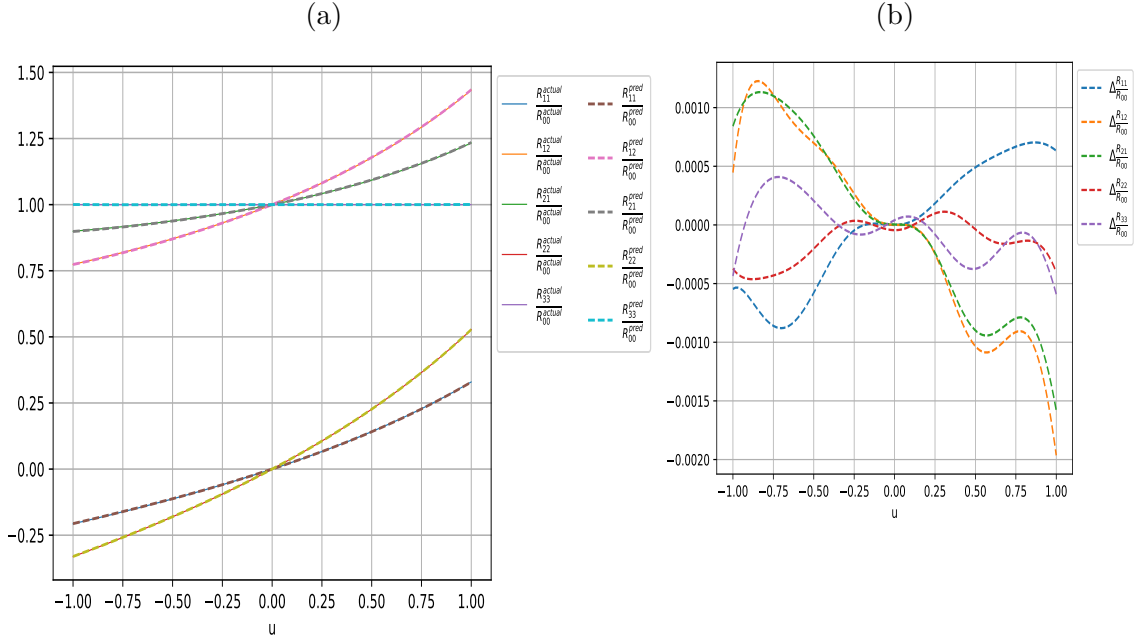
Figure 12: (a) Predicted vs actual R-matrix component ratio w.r.t. R_{00} for XXZ-type model with $a_1 = a_2 = 0.3, b_1 = 0.45, b_2 = 0.6, c_1 = 0.4, c_2 = 0.25$, (b) Absolute error between predicted and actual R-matrix component ratios

classes[118] of difference-form integrable (not necessarily Hermitian) spin chain models with 2-dimensional space at each site. The R-matrices corresponding to each of these classes are written down explicitly in appendix E. Towards the end of this sub-section, we also present results for learning solutions in generic gauge obtained by similarity transformation of integrable Hamiltonians from the aforementioned 14 classes. We shall discuss the results in two parts: XYZ type models, and non-XYZ type models.

The first set of Hamiltonians under consideration are generalisations of the XYZ model (discussed in the previous sub-section), with at most 8 non-zero elements in its Hamiltonian density

$$H_{8-\text{vertex}} = \begin{pmatrix} a_1 & 0 & 0 & d_1 \\ 0 & b_1 & c_1 & 0 \\ 0 & c_2 & b_2 & 0 \\ d_2 & 0 & 0 & a_2 \end{pmatrix} \tag{6.21}$$

where the coefficients can take generic complex values. The XYZ model corresponds to the subset with $a_1 = a_2, b_1 = b_2, c_1 = c_2, d_1 = d_2$. As discussed in section 6.1, these models can be further sub-divided into four, six, seven and eight vertex models. On the other hand, there are 6 distinct classes of non-XYZ type solutions. Here we will discuss the training results for one example each from the XYZ and non-XYZ type models, since the training behaviour is similar within these two types. Rest of the models will be presented in Appendix E. Figure 12 plots the R-matrix components as ratios with respect to R_{00} for a generic 6-vertex model with $d_1 = d_2 = 0$, and $a_1 = a_2$. The figure also includes the absolute and relative errors with respect to the corresponding analytic R-matrix (see equation (E.2)).

73
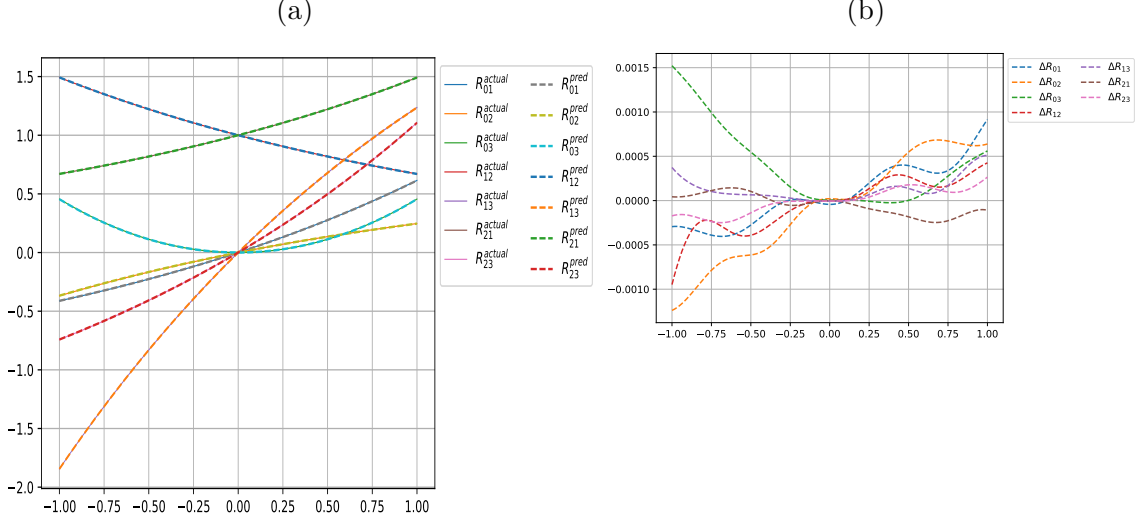
Figure 13: (a) Predicted vs actual R-matrix components for the Hamiltonian of class-1, with coefficients $a_1 = .5$, $a_2 = .3$, $a_3 = .9$, $a_4 = 1.5$, $a_5 = .4$. Note here the R-matrices are automatically normalised since R_{00} was fixed to the constant value of 1, (b) Absolute error between predicted and actual R-matrix components

From the non-XYZ classes, we will focus on the following 5-vertex Hamiltonians

$$H_{class-1} = \begin{pmatrix} 0 & a_1 & a_2 & 0 \\ 0 & a_5 & 0 & a_3 \\ 0 & 0 & -a_5 & a_4 \\ 0 & 0 & 0 & 0 \end{pmatrix} \tag{6.22}$$

For integrability, we require the additional condition

$$a_1 a_3 = a_2 a_4 \,. \tag{6.23}$$

Training the Hamiltonian constraint (6.11) for generic values $a_1 = 0.5, a_2 = 0.3, a_3 = 0.9, a_4 = 1.5, a_5 = 0.4$ satisfying the above integrability condition, we get over 99.9% accuracy for training over $\sim$100 epochs. Figure 13 plots the trained R-matrix components and absolute errors with respect to the analytic R-matrices in equation (E.20), for the above choice of target Hamiltonian. We have also surveyed more general solutions beyond the representative solutions of the 14 classes *a la* [118], by changing the gauge of the R-matrix as well as the corresponding Hamiltonian. As noted earlier in section 1.2.2, we can act with a 2×2 similarity matrix Ω on the R-matrix :

$$R(u) \rightarrow R^{\Omega}(u) = (\Omega \otimes \Omega)R(u)(\Omega^{-1} \times \Omega^{-1}) \tag{6.24}$$

$$H \rightarrow H^{\Omega} = (\Omega \otimes \Omega)H(\Omega^{-1} \times \Omega^{-1}) \tag{6.25}$$

If $R(u)$ satisfies Yang-Baxter equation, so does $R^{\Omega}(u)$. A generic similarity matrix Ω

$$\Omega = \begin{pmatrix} v_{11} & v_{12} \\ v_{21} & v_{22} \end{pmatrix} \tag{6.26}$$

with non-zero off-diagonal entries $v_{12}, v_{21} \neq 0$, results in conjugated R-matrices and Hamiltonians with all 16 non-zero entries. We trained 16-vertex Hamiltonians resulting

from XYZ model in the general gauge and recovered the corresponding R-matrix with a relative error of order $\mathcal{O}(0.1\%)$. Generic XYZ type models, as well as non-XYZ type models gave similar results for different gauges. Figure 14 plots the learnt R-matrix components for XXZ model with $\eta = \frac{\pi}{3}$ conjugated by the matrix $\Omega = \begin{pmatrix} 0.4 & 0.5 \\ -1.2 & 1 \end{pmatrix}$. For comparison with analytic formulae, we normalised our results by taking ratios with respect to a fixed component R_{00}, i.e. we plot $\frac{R_{ij}}{R_{00}}$. As a result of starting from the XXZ model, the R-matrix R_{XXZt} in the general gauge has following highly symmetric form

$$
R_{XXZg} = \begin{pmatrix} R_{00} & R_{01} & R_{01} & R_{03} \\ R_{10} & R_{11} & R_{12} & -R_{01} \\ R_{10} & R_{12} & R_{11} & -R_{01} \\ R_{30} & -R_{10} & -R_{10} & R_{00} \end{pmatrix}
\tag{6.27}
$$

Thus we only plot the entries $R_{00}, R_{01}, R_{03}, R_{10}, R_{11}, R_{12}, R_{30}$. Since there exists overall normalisation ambiguity, we should only compare ratio of R-matrix entries with the analytic solution written in the same gauge.

(a) (b)
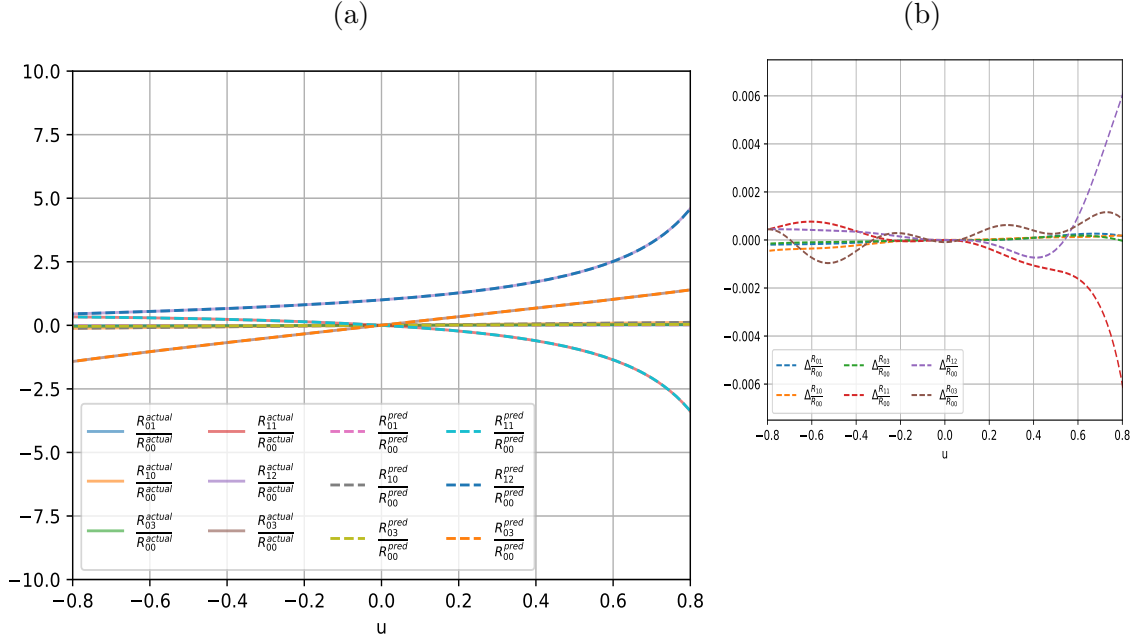
Figure 14: (a) Predicted R-matrix component ratios w.r.t. R_{00}, for conjugated XXZ model with $\eta = \frac{\pi}{3}$ and similarity matrix $\Omega = \begin{pmatrix} 0.4 & 0.5 \\ -1.2 & 1 \end{pmatrix}$, (b) Absolute error between predicted and actual R-matrix ratios

Next we discuss the difference in the training of integrable vs non-integrable models with our neural network. We will focus on two representative examples : 6-vertex model with Hamiltonian $H_{6v,1}$, and class 4 models with Hamiltonian $H_{class-4}$. Similar results hold across all the 14 classes.

For 6-vertex models with Hamiltonians following equation (6.21) with $d_1 = d_2 = 0$, generic values of the coefficients a_i, b_i, c_i, d_i for $i = 1, 2$ leads to non-integrable models, unless

$$
a_1 = a_2, \quad a_1 + a_2 = b_1 + b_2.
\tag{6.28}
$$
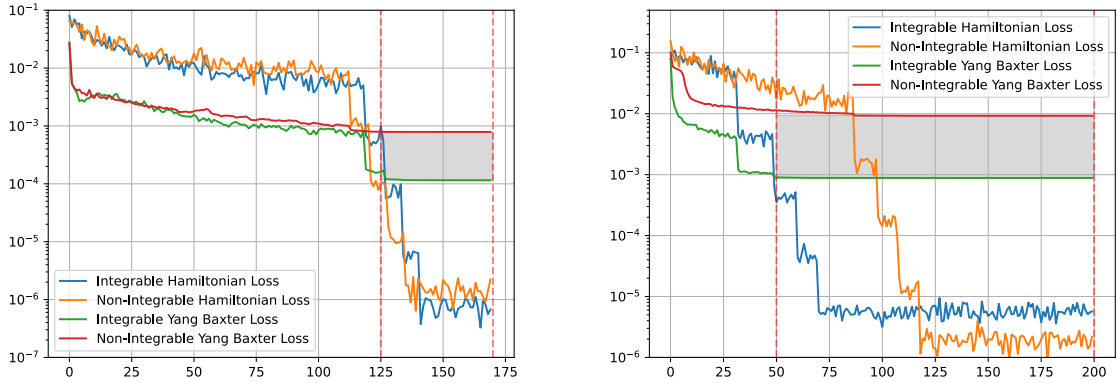
(a) Hamiltonian $H_{6v,1}$ vs non-integrable.　　(b) Hamiltonian $H_{\text{class}-4}$ vs non-integrable.

Figure 15: Comparing the training history of the Type XYZ and non-XYZ models against corresponding non-integrable Hamiltonians. There is approximately an order of magnitude difference between the Yang-Baxter losses for the integrable case vs the non-integrable case after the training saturates, indicated by the gray region in the graph. The step-wise drops in the loss functions approximately correspond to the learning rate schedule. The presented Hamiltonians are the same as on Fig.16 and Fig.17

These are the models with Hamiltonian $H_{6v,1}$, $H_{6v,2}$ in appendix E. Figure 15a compares the training for a generic Hamiltonian with coefficients satisfying none of the above conditions against the training for $H_{6v,1}$-type model. We see that while the Hamiltonian constraint (6.11) saturates to similarly low values in both cases, the Yang-Baxter loss saturates at approximately one order of magnitude higher. Similar behavior holds for the non-XYZ type models as well. The training for a generic class-4 Hamiltonian with coefficients $a_1 = 0.5, a_2 = 0.3, a_3 = 0.4, a_4 = 0.9$ (see Equation E.19) and a non-integrable deformation is shown in Figure 15b.

One can further discriminate between integrable and non-integrable models by checking the point-wise values of the Yang-Baxter losses in the two cases. Let us define the metric

$$\tilde{\mathcal{L}} = \frac{||\mathcal{R}_{12}(u-v)\mathcal{R}_{13}(u)\mathcal{R}_{23}(v) - \mathcal{R}_{23}(v)\mathcal{R}_{13}(u)\mathcal{R}_{12}(u-v)||}{||\mathcal{R}_{12}(u-v)\mathcal{R}_{13}(u)\mathcal{R}_{23}(v)||}, \qquad (6.29)$$

which measures the relative error in the approximate solution of the Yang-Baxter equation. This metric is evaluated for the trained R-matrix for both integrable and non-integrable models in Figure 16 (for $H_{6v,1}$ model), and Figure 17 (for $H_{class-4}$ model). We see that the normalized error can be up to two orders of magnitude larger for the non-integrable case. Note that irrespective of the choice of Hamiltonian, there are two lines along $u = v$ and $v = 0$ on which the Yang-Baxter equation is trivially satisfied, due to regularity. This metric also can detect anomalous situations when the learned solution once satisfied the Hamiltonian constraint at $u = 0$ quickly evolves to a true solution of Yang-Baxter equation producing relatively small YB loss (6.5). In this case we will see the big spike in (6.29) around zero which will indicate the fakeness of the found solution.

The above consideration shows that one can define the metrics which together indicate the closeness of the given system to the integrable Hamiltonian. However, the final conclusion in the binary form of "integrable/nonintegrable" regarding the given spin chain

76

(a) $H_{6v,1}$
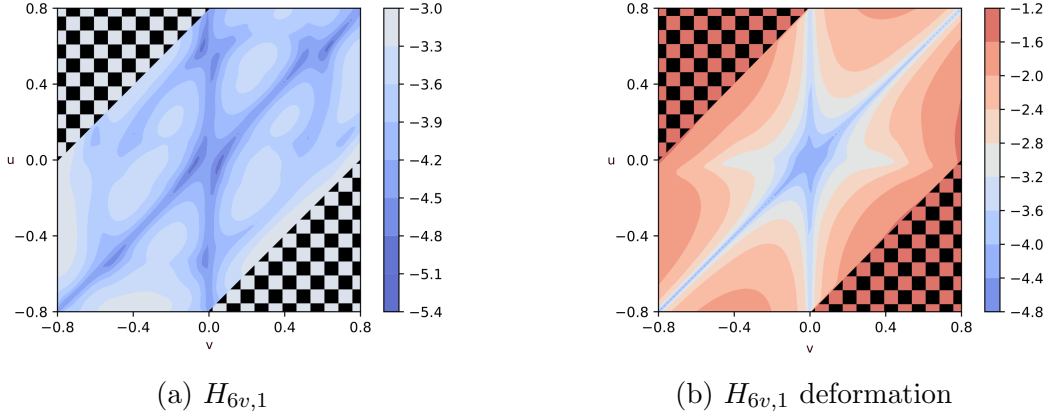
(b) $H_{6v,1}$ deformation

Figure 16: (a) The normalized Yang-Baxter error (6.29) plotted in the logarithmic scale at the end of training for the Hamiltonian $H_{6v,1}$ with $a_1 = 0.3, a_2 = 0.3, b_1 = 0.45, b_2 = 0.6, c_1 = 0.4, c_2 = 0.25$, and (b) its non-integrable deformation with $a_1 = -1.3, a_2 = 1.3$ and other parameters kept constant. In order to keep all three arguments appearing in YB equation inside the same inteval $|u|, |v|, |u-v| < 0.8$ we cut out the area $|u - v| > 0.8$ with chess-pattern triangles.

(a) $H_{\text{class}-4}$

(b) $H_{\text{class}-4}$ deformation
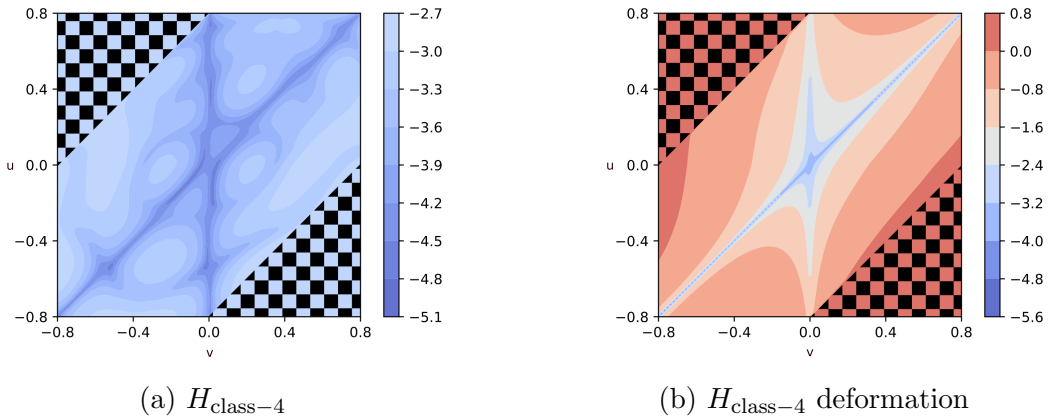
Figure 17: (a) The normalized Yang-Baxter error (6.29) plotted in the logarithmic scale at the end of training for the Hamiltonian $H_{class-4}$ from (E.19), with $a_1 = 0.5, a_2 = 0.3, a_3 = 0.4, a_4 = 0.9$, (b) Non-integrable deformation with same Hamiltonian parameters as in the integrable case, except for $H_{13} = -0.9$.

can be made only asymptotically, namely increasing the number of neurons, density of points and training time one can get the normalized YB loss (6.29) uniformly decreasing to zero for integrable Hamiltonians while for nonintegrable case it will be bounded from below by some positive value. Also let's stress that such problem is specific for the solver mode once we stick to a given Hamiltonian, while in the case of relaxed Hamiltonian restrictions as we will see in the next section, the neural network moves to the true solution of the Yang-Baxter equation.

6.4 Explorer: new from existing
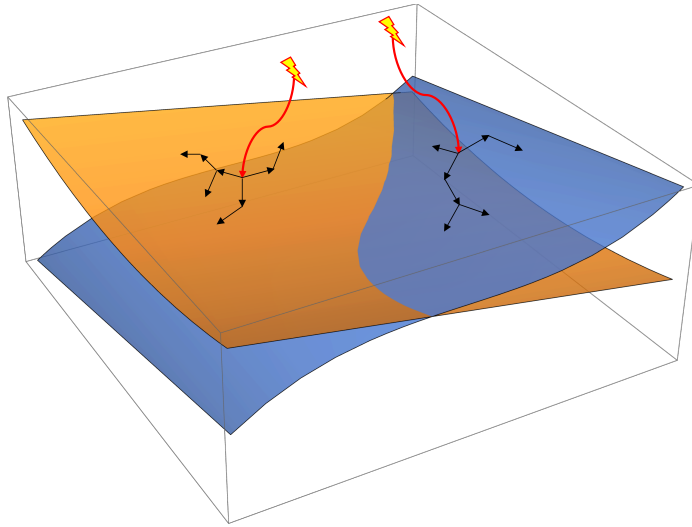
Figure 18: Visualizing the Explorer scheme. We start with random initializations, marked by lightning symbols, and perform solver learning represented by red curve arrows. Once we reach an submanifold of integrable Hamiltonians, we explore it using repulsion to identify new integrable models.

In this section we will present two kinds of experiments that illustrate how the neural network presented above can be used to scan the landscape of two-dimensional spin-chains for integrable models. The training schedule adopted in this section is visualized in Figure 18 and relies essentially on two new ingredients which distinguish it from the previous *solver* framework. These are *warm-start* and *repulsion*. We will illustrate each by an example. In the first case we shall simply use warm-start, and in the second, we shall combine warm-start with repulsion. Finally, we shall use unsupervised learning methods such as t-SNE and Independent Component Analysis to identify distinct classes of Hamiltonians within the set of integrable models thus discovered. Collectively, these strategies make up our *explorer* framework.

The first key new ingredient is a *warm-start initialization*. As mentioned previously, the standard solver framework of the previous section uses He initialization [120] to instantiate the weights and biases of the neural network. In warm-start initialization, we use the knowledge of integrable systems previously discovered by the neural network to
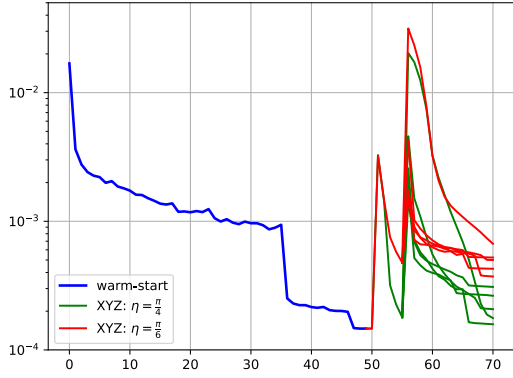
(a) Evolution of Yang-Baxter Loss　　　　(b) Evolution of Hamiltonian Loss
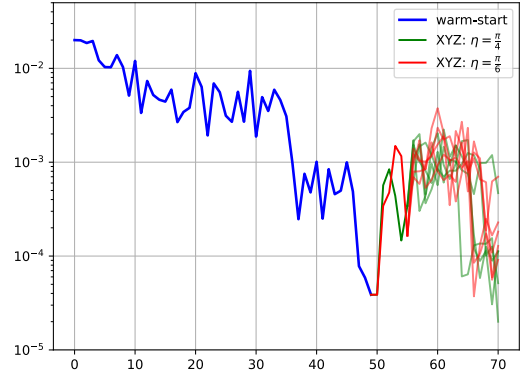
Figure 19: The convergence to XYZ models from XXZ models trained with different parameters. XXZ was trained for 50 epochs at $\eta = \frac{\pi}{3}$ and $m = 0$. Then, it was trained for 5 more epochs at $\eta = \frac{\pi}{4}$ and $\eta = \frac{\pi}{6}$, still with $m = 0$. After that, 5 non-zero values of m were used for each XXZ model, and we trained for another 15 epochs. Loss spikes occurred when the target hamiltonian values were reset. The final training was run in parallel for convenience, but it can be run sequentially.
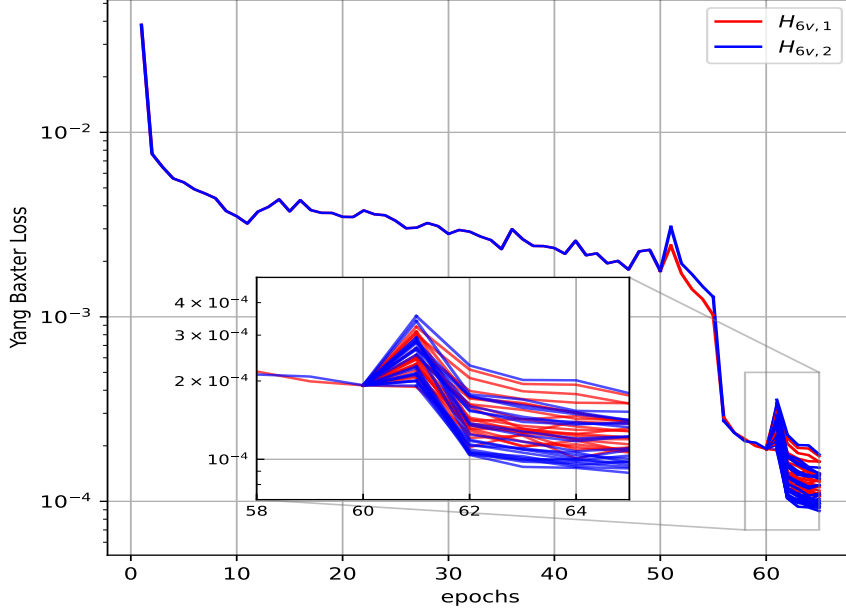
Figure 20: Time evolution of the Yang Baxter loss as the neural network explores the space of integrable Hamiltonians of 6-vertex models $H_{6v1,6v2}$ by repulsion. The loss evolves together until the 50th epoch after which it fragments slightly as the training converges to the two warm-start points on the 60th epoch. For the remaining epochs the losses fragment completely as the neural network seeks out different new Hamiltonians and is terminated when the loss reaches the neighborhood of 1×10^{-4}.

79
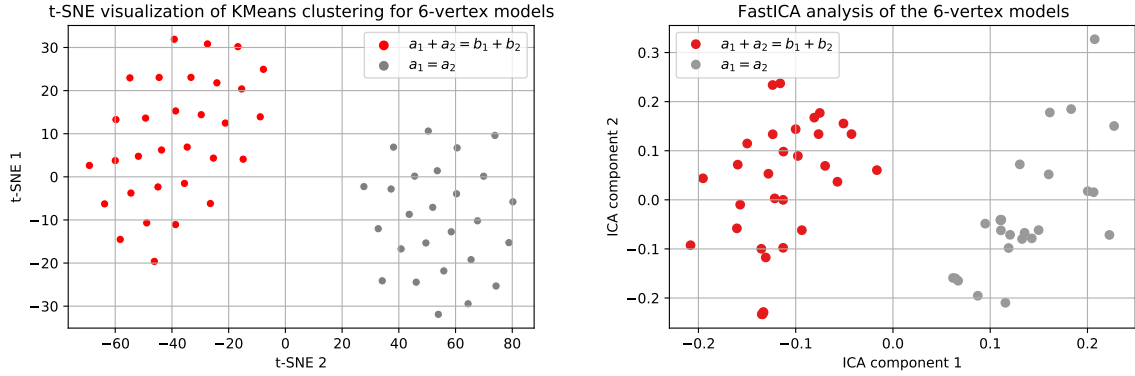
Figure 21: Clustering of Hamiltonians from the 2 classes of gauge-inequivalent 6-vertex models obtained by Explorer using repulsion from solution at intersection of both classes.
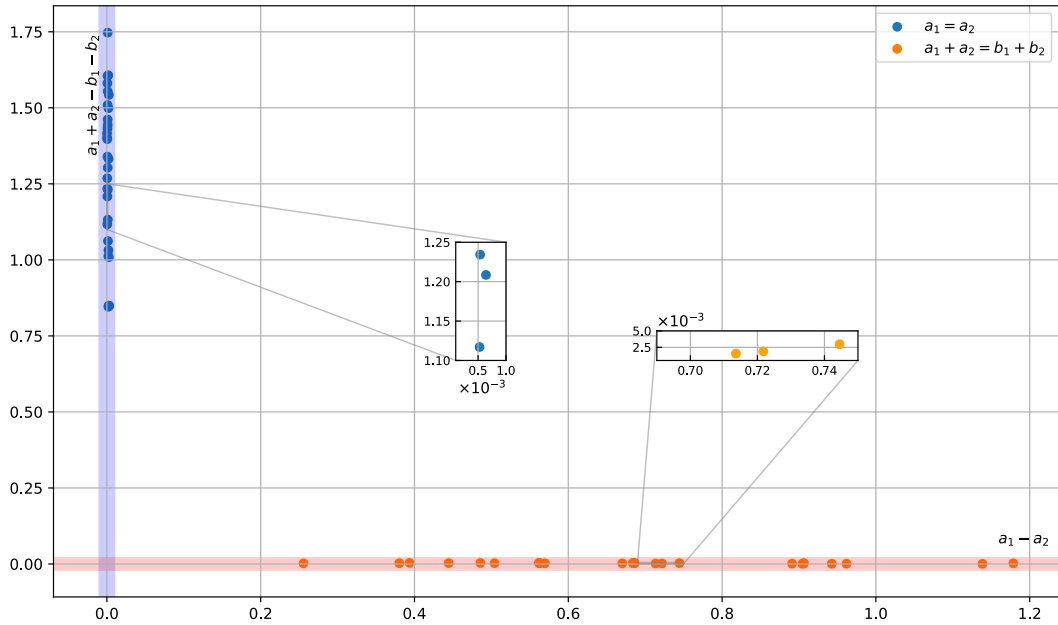
Figure 22: The 6-vertex models learnt by exploration. The graph visualizes the obtained Hamiltonians by plotting their values along the $a_1 + a_2 - b_1 - b_2$ and the $a_1 - a_2$ axes. The models $H_{6v,1}$ lie along the y-axis and the models $H_{6v,2}$ along the x-axis with an error margin of order 10^{-3} as shown in the telescoped inset plots.

find new systems in its vicinity. The idea, at least intuitively, is that it should be possible to find new integrable systems more efficiently than with the random initialization by exploring the vicinity in weight-space of previously determined solutions using an iterative procedure such as gradient-based optimization. On doing so, we find a significant acceleration in training convergence, with new solutions being discovered typically in about 5 epochs of training after warm-start initialization. For definiteness, we consider the hermitian XYZ model discussed earlier in Section 6.3.1. This has a two-parameter family of solutions, corresponding to independent choices for the parameters η and m of the Jacobi elliptic function, as seen from Equation (6.20). The XXZ model is embedded into this space as the $m = 0$ subspace of solutions.

We now describe how the above strategy can be used to quickly generate the cluster of XYZ R-matrices starting from a particular one which we choose from XXZ subclass. We begin with pre-training our neural network using the solver mode of the previous section, but with the learning rate of the `Adam` optimizer set to 10^{-3}. The pre-training is stopped when all losses saturate below $\mathcal{O}\left(10^{-3}\right)$, which typically requires about 50 epochs of training. We carried out this pre-training setting arbitrary reference values of η, but with m fixed to zero. The results shown here correspond to $\eta = \frac{\pi}{4}$. The weights thus obtained correspond to our warm-start values. Then we shift the target Hamiltonian values to correspond to $\eta \to \eta + \delta\eta$, where $\delta\eta$ are randomly chosen $\mathcal{O}\left(10^{-1}\right)$ numbers, and m can take on non-zero values as well. We then retrain the model with a smaller learning rate, 10^{-4} for a few epochs until all loss terms fall to $\mathcal{O}\left(10^{-4}\right)$, which typically takes about 5 epochs, upon which we update the target Hamiltonian by updating η and m and continue training. This strategy generates about 10 XYZ models within the same time-scale (i.e. about 100 to 200 epochs of training) as we earlier needed for a single model. For best results, while we randomly update η, we systematically anneal the modular parameter m to upwards of zero. A sample of this training is visualized in Figure 19b.

Our next key new ingredient for the Explorer mode is *repulsion*, which is added to the previous strategy of warm-start initialization. In principle, it should allow us to rediscover all 14 classes of integrable spin chains. However, for sake of simplicity, we will illustrate it now with a toy-model example and return to the general analysis later [126]. Namely, we consider the class of 6-vertex Hamiltonians with unrestricted a_1 and a_2. It includes both integrable 6-vertex classes $H_{6v,1}, H_{6v,2}$ (E.2, E.4) as well as nonintegrable models. In order to mimic the general situation when all integrable classes intersect at zero, we begin by pre-training the neural network to a Hamiltonian belonging to the intersection of the classes $H_{6v,1}$ and $H_{6v,2}$, i.e. whose matrix element satisfy the constraints $a_1 = a_2$ and $a_1 + a_2 = b_1 + b_2$ simultaneously. The results mentioned in this work correspond to setting

$$a_1 = a_2 = \frac{b_1 + b_2}{2}\,; \qquad b_1 = 0.6,\ b_2 = 0.8,\ c_1 = 0.5,\ c_2 = 0.9\,. \tag{6.30}$$

Having arrived at this model, we would like to navigate to neighboring models not by specifying target values of the Hamiltonian, but by scanning the neighborhood of the current model. To do so, we employ a two step strategy. First, we navigate to two[34] new 6-vertex integrable Hamiltonians by random scanning the vicinity of the current model without giving specific target values. We shall use these new models as our warm-start

---

[34]We stop the scanning once we found a representative from each of two classes because we know that there are only two integrable families here. In general case one of course should generate sufficiently many points in order to find all classes. We will return to this subtle point later in [126]

points. From each of them, we navigate away by using the *repulsion* loss term (6.15) for 1 epoch, followed by training for another 5 epochs. Note in this step, we still train within the restricted class of 6-vertex models by fixing the corresponding entries of the R-matrix to zero. We repeat this schedule 25 times starting from either of the saved models. This way, we generate fifty 6-vertex integrable Hamiltonians with over 1% accuracy[35]. The training curve displaying how the Yang-Baxter loss evolves is shown in Figure 20.

The learnt models are classified into two classes using clusterisation methods as shown in Figure 21. Figure 22 plots the trained models in terms of coordinates defined by the integrability conditions of the Hamiltonians $H_{6v,1}, H_{6v,2}$. Models lying near the two axes were classified correctly into the two classes in Figure 21 with 100% accuracy.

6.5 Conclusions and Future directions

In this work we constructed a neural network for solving the Yang-Baxter equation (1.26) in various contexts. Firstly, it can learn the R-matrix corresponding to a given integrable Hamiltonian or search for an integrable spin chain and the corresponding R-matrix from a certain class specified by imposed symmetries or other restrictions. We refer to this as the solver mode. Next, in the explorer mode, it can search for new integrable models by scanning the space of Hamiltonians.

We demonstrated the use of our neural network on two-dimensional spin chains of difference form. In the solver mode, the network successfully learns all fourteen distinct classes of R-matrices identified in [118] upto accuracies of the order of $99.9 - 99.99\%$. We demonstrated the work of the Explorer mode, restricting the search to the space of spin chains containing both classes of 6-vertex models as well as nonintegrable Hamiltonians. Starting from the hamiltonian at the intersection of two classes , Explorer found 50 integrable Hamiltonians which after clusterisation clearly fall into two families corresponding to two integrable classes of 6-vertex model. Working in the explorer mode, we find that warm-starting our training from the vicinity of a previously learnt integrable model greatly speeds up convergence, allowing us to identify typically about 50 new integrable models in the same time that random initialization takes to converge to a single model.

The main focus of this work was creating the neural network architecture and demonstrating its robustness in various solution generating frameworks using known integrable models as a testing ground. However, we expect that this program can be extended to various scenarios such as the exploration and classification of the space of integrable Hamiltonians in dimensions greater than two. This would be of great interest since the general classification of models is currently limited to two dimensions. Our experiments with exploration and clustering are a promising starting point in this regard. In our setup the strategy is quite straightforward [126]. Because all integrable families of Hamiltonians can be multiplied by arbitrary scalar, we should only scan the Hamiltonians on the unit sphere which is compact. Scanning over sufficiently dense set of points on the sphere will allow us to identify integrable Hamiltonians from various classes. Then we can use the Explorer to reconstruct the whole corresponding families and perform clusterisation in order to identify them. On another footing, it would also be interesting to extend our study to R-matrices of non-difference form as these are particularly relevant to the AdS/CFT correspondence [127, 54, 50, 128].

---

[35]If we further train the individual models for more epochs, we can improve the accuracy of the obtained solution to similar levels as obtained in the examples presented in Section 6.3, 6.4

While our network learns a numerical approximation to the R-matrix, it can also be useful for the reconstruction of analytical solutions using symbolic regression [129, 130]. Alternately, one may try to use the learnt numerical solution for the reconstruction of the symmetry algebra such as the Yangian and then arrive at the analytical solution. Remarkably, machine learning is already proving helpful in the analysis of symmetry in physical systems. In particular, one may verify the presence of a conjectured symmetry or even automate its search using machine learning [131, 114, 115, 116, 132, 133, 134]. It would be very interesting to explicate the interplay of our program in this broader line of investigation.

In addition, the flexibility of our approach would also allow us to implement various additional symmetries or other restrictions, both at the level of the R-matrix and the Hamiltonian. It would therefore be very interesting to develop an 'R-matrix bootstrap' in the spirit of the two-dimensional S-matrix bootstrap and analyze the interplay between various symmetries. For example, all 14 families of R-matrices considered in this work satisfy the condition of braided unitarity and it would be interesting to rediscover them from the use of braided unitarity and other symmetries without imposing the Yang-Baxter condition, similar to how integrable two-dimensional S-matrices have been identified in the S-matrix Bootstrap approach [135, 136, 137].

With mild modifications, we can adapt our architecture to the analysis of Yang-Baxter equation for the integrable S-matrices in two dimensions. The only new feature to implement is the analytic structure in the s-plane. It can be naturally realized with the use of holomorphic networks.

Learning solutions for different classes with the same architecture, we noticed that the number of epochs needed to reach the same precision varies for different classes while being roughly the same for the Hamiltonians from the same classes. Thus, it would be very tempting to use the training of losses to define the complexity of spin chains. Ideally, we should be able to go beyond the class of integrable models and see that they sit at the minima of complexity, matching common beliefs that the integrable models are the "simplest" ones.

7 Summary and outlook

Let us conclude this thesis with a summary of the works presented here and outlook for the ongoing research directions. Integrability and machine-learning are two sets of very different tools that have seen applications across fields in physics and mathematics, both in theory and in experiments. The goal of this thesis was to try to understand aspects of AdS/CFT duality in certain 3-dimensional backgrounds using integrability techniques, and to develop ML techniques to search for new integrable models. Besides these works, we have also presented successful use of ML to learn properties of Lie algebras which are ubiquitous in theoretical physics.

String theory in AdS backgrounds have provided a rich yet controlled playground to probe quantum gravity. Integrability assists even further, allowing us to learn properties of the theory that hold true across entire moduli spaces. Bringing these two together, AdS_3 backgrounds with 16 supersymmetries have been explored in the integrable limit, wherein a lot of non-perturbative information has been obtained. Unlike in AdS_5 and AdS_4 holographic dualities, AdS_3 has massless modes of excitations, plus the dual CFTs are not well-understood. Among other effects, the massless (fermionic) modes lead to a

degeneracy of protected spectrum on top of the BMN vacuum, which is the ground state encountered in AdS_5 integrability. In section 4, we use algebraic Bethe ansatz to study these states in various integrable AdS_3 backgrounds. We start out by computing some generic low-magnon massless states, which are generated by acting on the level-1 vacuum $|\chi^{\otimes N_0}\rangle$ with $\mathcal{B}^1, \mathcal{B}^3$ creation operators which are part of the two component $psu(1|1)^2_{c.e.}$ monodromy matrices $\mathcal{M}^I, I = 1, 3$. The transfer matrix eigenstates are obtained by solving the auxiliary Bethe equation for $y_{I,k}, I = 1, 3$(while freezing the massless momentum carrying roots $z_k^\pm$, which are determined by solving equations (2.53)). We then obtain the protected states in mixed flux $AdS_3 \times S^3 \times T^4$ backgrounds by taking the level-1 magnon-momenta to zero and solving for the auxiliary Bethe roots, which themselves converge to special values $y = s_\pm$. We also compute the protected spectrum in $AdS_3 \times S^3 \times K_3$ backgrounds, where K_3 is realised as an orbifold of T^4. Besides, we also compute the protected spectrum in mixed-flux $AdS_3 \times S^3 \times S^3 \times S^1$ and its $\mathbb{Z}_2$ orbifold.

Recently, the TBA equations have been worked out for ground state in $AdS_3 \times S^3 \times T^4$ background with pure RR flux [128]. It would be interesting to verify that the contour-deformation trick to access excited state TBA admits these protected states as singular solutions, just as BMN vacuum is a singular solution to the ground state TBA. Our analysis was done in mixed flux backgrounds, where the TBA is yet to be worked out. We are currently working on understanding the dressing factors in mixed flux $AdS_3 \times S^3 \times T^4$ backgrounds and preferred choice of spectral parameter to solve crossing equations for the same.

A parallel yet complementary set of works involved understanding applicability of modern machine-learning tools such as neural networks to assist computations in mathematical physics, esp. quantum integrability. The works presented here include employing NN for classification problems in Lie algebras like tensor product decomposition, and to search for quantum integrable R-matrices by solving for Yang-Baxter equation. The former work on Lie algebras showed the ability of NN to supervised learn tensor product decomposition of very high-dimensional representation of Lie algebras to reasonably high accuracies. Other similar works around supervised learning which have been omitted from this thesis include probing properties of polytopes, and Hilbert series. In all these scenarios, it would be interesting to see if one can generate new mathematical conjectures for the properties that seem to be better amenable (i.e. high accuracy) to machine-learning. The latter work on quantum integrability was the first of its kind, showing how one could search for quantum integrable spin chain models using neural networks. This work focused on 2-dimensional representations at the spin chain sites, wherein all the models have been classified using analytic methods. We managed to recover all the 14 distinct classes of regular difference-form integrable R-matrices with extremely high precision (99% within a compact interval around the origin on the real line in spectral parameter plane). Furthermore, we have presented a search algorithm to look for new R-matrices by rediscovering the two distinct classes of 6-vertex integrable Hamiltonians using K-means clustering. Currently, we are searching for new models in higher dimensional setting of 9×9 and 16×16 R-matrices. For this, we are employing modifications of the methods already discussed in section 6.3, plus employing new tools like symbolic regression, and new NN architectures. We are also looking at improving the accuracies by trying new optimisation tools like energy conserving descent. Besides the higher dimensional searches, we are also looking at other similar applications such as solving for boundary Yang-Baxter equations, generalised Yang-Baxter equations, etc. Another interesting direction that we are actively trying to probe as an extension of this

work, is to search for R-matrices of non-difference form, as well as non-regular R-matrices, which appear for spin-chains that cease to be nearest neighbour type.

Overall, I believe the works presented here shine some light into the power of integrability in string theory holography, and how modern tools of machine-learning can assist and accelerate our understanding of this field and others in mathematical physics.

A Derivation of Bethe equations in Zhukovski variables

In this section, we derive the Bethe equations (4.46), (4.49). We show this for a single copy of $\mathrm{psu}(1|1)^2_{\mathrm{c.e.}}$, labelled $I = 1$. The proof works the same way for the other copy of $\mathrm{psu}(1|1)^2_{\mathrm{c.e.}}$ $(I = 3)$, and hence the full $\mathrm{psu}(1|1)^4_{\mathrm{c.e.}}$. The reference state for the $\mathrm{psu}(1|1)^2_{\mathrm{c.e.}}$ ABA is

$$|\phi_{p_1} \ldots \phi_{p_{N_0}}\rangle \,. \tag{A.1}$$

The monodromy matrix $\mathcal{M}^1$ is defined as

$$\mathcal{M}^1(p_0|\vec{p}) = R_{0N}^{\mathrm{LL}}(x_{p_0}^{\pm}, x_{p_N}^{\pm}) \ldots R_{01}^{\mathrm{LL}}(x_{p_0}^{\pm}, x_{p_1}^{\pm}), \tag{A.2}$$

with R^{LL} given in equation (2.33). Above, the auxiliary space carries momentum p_0 and the sites of the physical sites carry momenta $\vec{p} = \{p_i\}_{i=1}^N$.

The auxiliary Bethe equation arises from requiring that the extra term $|X\rangle$ in the eigenstate condition (4.45) vanish. In order to write these terms explicitly, we need to use the RTT relation

$$R^{\mathrm{LL}}(x_{p_0}^{\pm}, x_{p_{0'}}^{\pm})\mathcal{M}^1(p_0|\vec{p})\mathcal{M}^1(p_0'|\vec{p}) = \mathcal{M}^1(p_0'|\vec{p})\mathcal{M}^1(p_0|\vec{p})R^{\mathrm{LL}}(x_{p_0}^{\pm}, x_{p_{0'}}^{\pm})\,, \tag{A.3}$$

where $0, 0'$ label two auxiliary spaces with momenta $p_0, p_{0'}$. The commutation relations between operators $(\mathcal{A}^1, \mathcal{B}^1)$, and $(\mathcal{D}^1, \mathcal{B}^1)$ follow from $(A.3)$ are

$$\mathcal{A}^1(p_0|\vec{p})\mathcal{B}^1(p_{0'}|\vec{p}) = \frac{1}{D_{p_{0'}p_0}}\mathcal{B}^1(p_{0'}|\vec{p})\mathcal{A}^1(p_0|\vec{p}) - \frac{E_{p_{0'}p_0}}{D_{p_{0'}p_0}}\mathcal{B}^1(p_0|\vec{p})\mathcal{A}^1(p_{0'}|\vec{p}),$$

$$\mathcal{D}^1(p_0|\vec{p})\mathcal{B}^1(p_{0'}|\vec{p}) = -\frac{F_{p_0p_{0'}}}{D_{p_0p_{0'}}}\mathcal{B}^1(p_{0'}|\vec{p})\mathcal{D}^1(p_0|\vec{p}) + \frac{C_{p_0p_{0'}}}{D_{p_0p_{0'}}}\mathcal{B}^1(p_0|\vec{p})\mathcal{D}^1(p_{0'}|\vec{p})\,, \tag{A.4}$$

where the coefficients in the right-hand side are entries of the R-matrix R^{LL} in equation (2.33). Subtracting the second equation from the first one in $(A.4)$ and substituting the coefficients from equation (2.34), we get

$$\mathcal{T}^1(p_0|\vec{p})\mathcal{B}^1(p_{0'}|\vec{p}) = \frac{x_0^+ - x_{0'}^-}{x_0^- - x_{0'}^-}\sqrt{\frac{x_0^-}{x_0^+}}\mathcal{B}^1(p_{0'}|\vec{p})\mathcal{T}^1(p_0|\vec{p}) + \frac{x_{0'}^- - x_{0'}^+}{x_0^- - x_{0'}^-}\sqrt{\frac{x_0^-}{x_0^+}}\frac{\eta_0}{\eta_{0'}}\mathcal{B}^1(p_0|\vec{p})\mathcal{T}^1(p_{0'}|\vec{p}),$$
$$\tag{A.5}$$

where $x_0^{\pm}, x_{0'}^{\pm}$ depend on the auxiliary momenta $p_0, p_{0'}$ respectively via equation (2.27). As discussed in section 4.2.3 (see footnote 17) it is simplest to keep the mass parameter of the auxiliary variable non-zero.

The above FCR implies that $|X\rangle$ can be expanded in the basis

$$|p_0, \hat{y}_{1,i}\rangle \equiv \mathcal{B}^1(p_0)\mathcal{B}^1(y_{1,1})\cdots\mathcal{B}^1(y_{1,i-1})\mathcal{B}^1(y_{1,i+1})\cdots\mathcal{B}^1(y_{1,N_1})|\phi_{p_1}\cdots\phi_{p_{N_0}}\rangle \tag{A.6}$$

as

$$|X\rangle = \sum_{i=1}^{N_1} M_i \, |p_0, \hat{y}_{1,i}\rangle \, . \tag{A.7}$$

The coefficients M_i in equation (A.7) can be obtained by performing the following set of steps. First, we commute $\mathcal{B}^1(y_{1,i})$ through to the front of the string of $\mathcal{B}$ operators by using the FCR $\mathcal{B}^1(p)\mathcal{B}^1(q) = \frac{F_{pq}}{A_{pq}}\mathcal{B}^1(q)\mathcal{B}^1(p)$ which follows from the RTT relation in equation (A.3). The next step involves commuting the transfer matrix $\mathcal{T}^1(p_0)$ through $\mathcal{B}^1(y_{1,i})$ and picking up the contribution from the second term on the right-hand side of equation (A.5) which involves swapping of the auxiliary parameters of $\mathcal{T}^1$ and $\mathcal{B}^1$. Next, we commute the $\mathcal{T}^1$ through the rest of the $\mathcal{B}^1$ string of operators without any further swapping of the auxiliary parameters, thus picking up contribution from the first term on the right-hand side of equation (A.5). Finally, we act with the $\mathcal{T}^1$ operator on the pseudo-vacuum.

Following the above steps, we end up with the coefficient M_i of $|p_0, \hat{y}_{1,i}\rangle$ in the expansion of $|X\rangle$ in equation (A.7) as

$$M_i = \left(\prod_{j=1}^{i-1} \frac{F_{q_{1,j}q_{1,i}}}{A_{q_{1,j}q_{1,i}}} \right) \left(\frac{C_{p_0 q_{1,i}}}{D_{p_0 q_{1,i}}} \right) \prod_{j \neq i}^{N_1} \left(-\frac{F_{q_{1,i}q_{1,j}}}{D_{q_{1,i}q_{1,j}}} \right) \Lambda_0^1(q_{1,i}|\vec{p}) \, , \tag{A.8}$$

where $\Lambda_0^1(q|\vec{p})$ is the eigenvalue of the pseudo-vacuum $|\phi_{p_1} \cdots \phi_{p_{N_0}}\rangle$ under $\mathcal{T}^1(q|\vec{p})$

$$\Lambda_0^1(q|\vec{p}) = \prod_{i=1}^{N_0} A_{qp_i} - \prod_{i=1}^{N_0} D_{qp_i} = 1 - \prod_{i=1}^{N_0} \sqrt{\frac{x_i^+}{x_i^-}} \frac{x_q^- - x_i^-}{x_q^- - x_i^+} \, . \tag{A.9}$$

The coefficients M_k will *all* be zero simultaneously only if $\Lambda_0^1(q_{1,i}|\vec{p})$ vanishes

$$\Lambda_0^1(q_{1,i}|\vec{p}) = 0, \quad \forall \, i = 1, 2, \ldots, N_1 \, . \tag{A.10}$$

Re-labelling the Zhukovski variables $x_{q_{1,i}}^- = y_{1,i}$ to match the convention in the main text, we recover the auxiliary Bethe equation (4.46). Note, the auxiliary Zhukovski variables $x_{q_{1,i}}^+$ can be obtained by using shortening condition in equation (2.25). However, this is unnecessary for our purpose, as $x_{q_{1,i}}^+$ only show up as overall factors in the Bethe states as discussed in footnote 20.

B $N_0 = 3$, $N_1 = N_3 = 1$ **state from equation** (4.61)

Here, we write down explicitly the highest-weight Bethe state with three sites at level $N_1 = N_3 = 1$, in terms of the basis kets

$$\begin{aligned}
\mathcal{B}^1(y_*)\mathcal{B}^3(y_*) \, |\chi_{p_1}\chi_{p_2}\chi_{p_3}\rangle \propto {}& \alpha^2 \, |\tilde{\chi}_{p_1}\chi_{p_2}\chi_{p_3}\rangle + \beta^2 \, |\chi_{p_1}\tilde{\chi}_{p_2}\chi_{p_3}\rangle + \gamma^2 \, |\chi_{p_1}\chi_{p_2}\tilde{\chi}_{p_3}\rangle \\
& - i\alpha\beta \left(|T_{p_1}^1 T_{p_2}^2 \chi_{p_3}\rangle + |T_{p_1}^2 T_{p_2}^1 \chi_{p_3}\rangle \right) - i\alpha\gamma \left(|T_{p_1}^1 \chi_{p_2} T_{p_3}^2\rangle - |T_{p_1}^2 \chi_{p_2} T_{p_3}^1\rangle \right) \\
& - i\beta\gamma \left(|\chi_{p_1} T_{p_2}^1 T_{p_3}^2\rangle + |\chi_{p_1} T_{p_2}^2 T_{p_3}^1\rangle \right) \, , \quad \text{(B.1)}
\end{aligned}$$

where coefficients $\alpha \, , \beta \, , \gamma$ are

$$\alpha = \frac{\eta_1}{y_* - x_1^+} \, , \quad \beta = \frac{\eta_2}{y_* - x_2^+} D_{q_* p_1} \, , \quad \gamma = \frac{\eta_3}{y_* - x_3^+} D_{q_* p_1} D_{q_* p_2} \, , \tag{B.2}$$

with $y_* = x^-(q_*)$ defined in equation (4.60), and $\eta_i \, , D_{q_* p}$ defined in equation (2.22), (2.34) respectively.

C   Pure RR limit: relativistic ABA

In this appendix, we will discuss the pure RR limit of our results from the main text in terms of a different spectral parameter γ. This alternate parameterisation manifests the relativistic invariance present in the pure RR limit, and allows for compact expressions for the Bethe wavefunctions to be written down. We shall review the $\mathrm{psu}(1|1)^4_{\mathrm{c.e.}}$ ABA in the relativistic variables and then compute the zero-momentum states that give rise to the protected spectrum. The subtleties involved with the zero-momentum limit, as discussed in the main text, are inherited by this alternate parameterisation.

The pure RR massless limit of the $\mathrm{psu}(1|1)^2_{\mathrm{c.e.}}$ R-matrices from equation 2.33,2.35, in relativistic variable γ, is of *difference form*

$$R^{\mathrm{LL}}_{\mathrm{psu}(1|1)^2}(\gamma_1 - \gamma_2) = \begin{pmatrix} 1 & 0 & 0 & 0 \\ 0 & -b & a & 0 \\ 0 & a & b & 0 \\ 0 & 0 & 0 & -1 \end{pmatrix}, \tag{C.1}$$

$$R^{\tilde{\mathrm{L}}\tilde{\mathrm{L}}}_{\mathrm{psu}(1|1)^2}(\gamma_1 - \gamma_2) = \begin{pmatrix} 1 & 0 & 0 & 0 \\ 0 & -b & -a & 0 \\ 0 & -a & b & 0 \\ 0 & 0 & 0 & -1 \end{pmatrix}, \tag{C.2}$$

with a and b defined in terms of the difference of rapidities $\gamma_{12} = \gamma_1 - \gamma_2$

$$a(\gamma_1, \gamma_2) = a(\gamma_1 - \gamma_2) = \operatorname{sech} \frac{\gamma_1 - \gamma_2}{2} \equiv \operatorname{sech} \frac{\gamma_{12}}{2},$$
$$b(\gamma_1, \gamma_2) = b(\gamma_1 - \gamma_2) = \tanh \frac{\gamma_1 - \gamma_2}{2} \equiv \tanh \frac{\gamma_{12}}{2}. \tag{C.3}$$

The rapidity γ is related with momentum p as

$$\gamma = \log \tan \frac{p}{4}. \tag{C.4}$$

Note the R-matrices in equation (C.1), (C.2) match those in equation 2.33,2.35 only when both momenta $p_1(\gamma_1)$, $p_2(\gamma_2)$ lie in the range between 0 and π. Although it is not going to be sufficient to build the monodromy matrices for level-matched momenta (since we are only considering positive momenta for the sites), it is a very similar setup. Later in the section, we will modify this setup while considering level-matched Bethe states.

Following equation (4.20), the $\mathrm{psu}(1|1)^4_{\mathrm{c.e.}}$ R-matrix is obtained by tensoring the above two matrices R^{LL}, $R^{\tilde{\mathrm{L}}\tilde{\mathrm{L}}}$. If we ignore the level-matching condition for now, we can use the the above two R-matrices to build monodromy matrices, and then perform the same steps for ABA construction as in section 4.2.3 to get the transfer matrix eigenstates. The Bethe states generated using the operators $\mathcal{B}^1$ and $\mathcal{B}^3$ (see equation (4.44)), are now labelled by the Bethe roots in relativistic variables

$$|\vec{\gamma}; \vec{\beta}_1; \vec{\beta}_3\rangle \equiv \prod_{i=1}^{N_3} \mathcal{B}^3(\beta_{3,i}) \prod_{j=1}^{N_1} \mathcal{B}^1(\beta_{1,j}) \, |\chi_{\gamma_1} .. \chi_{\gamma_{N_0}}\rangle \,, \tag{C.5}$$

where $\vec{\gamma} = \{\gamma_i\}$, $\vec{\beta}_I = \{\beta_{I,j}\}$ are the momentum-carrying, and auxiliary rapidities. These

auxiliary roots are constrained to satisfy the Bethe equations

$$e^{-iLp_k} = (-1)^{N_0-1} \prod_{i \neq k}^{N_0} S^2(\gamma_{kj}) \prod_{j=1}^{N_1} \coth \frac{\beta_{1,jk}}{2} \prod_{l=1}^{N_3} \coth \frac{\beta_{3,lk}}{2},$$

$$1 = \prod_{i=1}^{N_0} \tanh \frac{\beta_{1,ki}}{2}, \qquad\qquad k = 1, \ldots, N_1,$$

$$1 = \prod_{i=1}^{N_0} \tanh \frac{\beta_{3,ki}}{2}, \qquad\qquad k = 1, \ldots, N_3. \qquad (C.6)$$

Above, we have used the shorthand

$$\beta_{I,jk} \equiv \beta_{I,j} - \gamma_k, \qquad\qquad I = 1, 3, \qquad\qquad (C.7)$$

and $S(\gamma)$ is the famous Zamolodchikov sine-Gordon scalar factor [138], as shown in [94]. The proof follows from appendix A, with a change of variables.

In the rest of the section, we compute some of the Bethe states for a single $\mathrm{psu}(1|1)^2_{\mathrm{c.e.}}$ (with R^{LL} as the R-matrix), both at generic and zero momentum. The protected states are obtained by tensoring these Bethe states with ones coming from the other copy of $\mathrm{psu}(1|1)^2_{\mathrm{c.e.}}$ ABA (with $R^{\tilde{L}\tilde{L}}$ as the R-matrix). To avoid repetition, we will omit this final step since it works out the same way as in the Zhukovski variables (see section 4.3).

C.1 Level-matched $\mathrm{psu}(1|1)^2_{\mathrm{c.e.}}$ ABA

Here, we modify the above setup to allow negative momenta for the sites. This will allow us to impose level-matching for the low magnon solutions with $N_0 = 1, 2, 3, 4$, relevant for our protected states discussion. For two particles with mixed kinematics, i.e. $0 < p_1 < \pi$, $-\pi < p_2 < 0$, the R-matrix $R^{\mathrm{L}\ell}_{\mathrm{psu}(1|1)^2}(\gamma_1 - \gamma_2)$ coming from equation (2.33), again in *difference form*, is a slight modification of $R^{\mathrm{LL}}_{\mathrm{psu}(1|1)^2}(\gamma_1 - \gamma_2)$

$$R^{\mathrm{L}\ell}_{\mathrm{psu}(1|1)^2}(\gamma_1 - \gamma_2) = \begin{pmatrix} 1 & 0 & 0 & 0 \\ 0 & -b & -ia & 0 \\ 0 & -ia & -b & 0 \\ 0 & 0 & 0 & 1 \end{pmatrix}, \qquad (C.8)$$

where a, b are defined using equation (C.3), and the rapidity γ_2, for negative values of momentum $-\pi < p_2 < 0$, is defined as

$$\gamma_2 \equiv \log \tan \frac{p_2 + 2\pi}{4}. \qquad\qquad (C.9)$$

$R^{\mathrm{L}\ell}$ (where ℓ denotes L with world-sheet *right* kinematics) shows up whenever we consider a site with negative momentum $p_i < 0$. The monodromy matrix is a product of R-matrices, each of which is either R^{LL} or $R^{\mathrm{L}\ell}$ depending on the momenta at the sites

$$\mathcal{M}(\gamma_0|\vec{\gamma}) = R^{\mathrm{L}q_{N_0}}_{0N_0}(\gamma_0 - \gamma_{N_0}) R^{\mathrm{L}q_{N_0-1}}_{0N_0-1}(\gamma_0 - \gamma_{N_0-1}) \ldots R^{\mathrm{L}q_1}_{01}(\gamma_0 - \gamma_1), \qquad (C.10)$$

where $q_i = \mathrm{L}, \ell$ for momentum $p_i(\gamma_i) > 0$ or < 0.

The $\mathcal{B}$ operator generating the transfer matrix eigenstates on top of the pseudovacuum is $\mathcal{B}^1(\gamma_0)$ from equation (4.39). The auxiliary Bethe equation satisfied by the auxiliary

roots $\gamma_0 = \beta$, for system with k particles in mixed kinematics, is slightly modified with respect to equation (C.6) (which holds for all sites with positive momenta) by an overall factor of $(-1)^k$

$$\prod_{i=1}^{N_0} b(\beta - \gamma_i) = (-1)^k.$$

(C.11)

For $N_0 \geqslant 2$, this equation has two common solutions at $\beta = -\frac{i\pi}{2}, \frac{i\pi}{2}$ which translate to $y = 0, \infty$ respectively in Zhukovski variable. Expanding the $\mathcal{B}$ operator near these values of rapidity β, it behaves as supercharges of the $\mathrm{psu}(1|1)^2_{\mathrm{c.e.}}$ algebra (similar to equation (4.52)). Thus, the highest weight Bethe states of the $\mathrm{psu}(1|1)^2_{\mathrm{c.e.}}$ algebra are the ones without any roots at $\beta = \pm\frac{i\pi}{2}$. The momentum-carrying Bethe equation does not see any modification in its form w.r.t equation (C.6), upto the dressing phase which may get modified. It will still be of difference form in the appropriate variables since the R-matrix is. We leave its further investigation for future works, as it is irrelevant for our discussion here[36].

C.1.1 $N_0 = 1$

For a single site with rapidity γ_1, the auxiliary root $\gamma_0 = \beta$ satisfying the level-1 Bethe equation (C.11) gives

$$b(\beta - \gamma_1) = 1$$

(C.12)

which is solved for

$$\beta = \infty.$$

(C.13)

Thus the two Bethe states at generic rapidity γ_1 are

$$|\phi_{\gamma_1}\rangle, \quad \mathcal{B}^1(\infty)\,|\phi_{\gamma_1}\rangle \propto |\psi_{\gamma_1}\rangle.$$

(C.14)

Note, the above states are not level-matched for generic γ_1. The zero-momentum limit

$$p \to 0^+ \quad \Rightarrow \quad \gamma_1 \to -\infty$$

(C.15)

is special, since the auxiliary Bethe equation is trivially satisfied for all values of β. Following the discussion from section 4.3, we pick the auxiliary Bethe root $\beta \to -\infty$ in this limit. Thus, the zero-momentum 1-magnon Bethe states are

$$|\phi_{-\infty}\rangle, \quad \mathcal{B}^1(-\infty)\,|\phi_{-\infty}\rangle \propto |\psi_{-\infty}\rangle.$$

(C.16)

Taking tensor product of the above states with ones from the other $\mathrm{psu}(1|1)^2_{\mathrm{c.e.}}$ we recover states in equation (4.83), (4.84).

C.1.2 $N_0 = 2$

States with two sites satisfy the level-matching condition $0 < p_1 = -p_2 < \pi$. Using equation (C.10), the monodromy matrix is

$$\mathcal{M} = R^{\mathrm{L}\ell}(\gamma_0 - \gamma_2) R^{\mathrm{LL}}(\gamma_0 - \gamma_1), \qquad \gamma_2 = -\gamma_1 = \gamma.$$

(C.17)

---

[36]It will be a reduction of the known phase from [53].

The auxiliary Bethe equation for the rapidity $\gamma_0 = \beta$ is obtained by substituting $k = 1$, $N = 2$ in equation (C.11)

$$\prod_{i=1}^{2} b(\beta - \gamma_i) = -1 \,, \tag{C.18}$$

with solutions at

$$\beta = \pm \frac{i\pi}{2} \,. \tag{C.19}$$

The corresponding Bethe eigenstates are

$$
\begin{aligned}
&|\phi_\gamma \phi_{-\gamma}\rangle \,, \\
\mathcal{B}^1(\tfrac{i\pi}{2}) \, |\phi_\gamma \phi_{-\gamma}\rangle &\propto |\phi_\gamma \psi_\gamma\rangle + |\psi_\gamma \phi_\gamma\rangle \,, \\
\mathcal{B}^1(-\tfrac{i\pi}{2}) \, |\phi_\gamma \phi_{-\gamma}\rangle &\propto |\phi_\gamma \psi_\gamma\rangle - |\psi_\gamma \phi_\gamma\rangle \,, \\
\mathcal{B}^1(\tfrac{i\pi}{2}) \mathcal{B}^1(-\tfrac{i\pi}{2}) \, |\phi_\gamma \phi_{-\gamma}\rangle &\propto |\psi_\gamma \psi_{-\gamma}\rangle \,.
\end{aligned}
\tag{C.20}
$$

These states organise into a long $(2|2)$-dimensional multiplet of the $\mathrm{psu}(1|1)^2_{\mathrm{c.e.}}$ algebra.

Next, we look at the zero-momentum limit. Following the discussion in section 4.3, the auxiliary roots are located at rapidities $\beta = \pm\infty$. The Bethe states at these roots are

$$
\begin{aligned}
\lim_{\gamma \to -\infty} |\phi_\gamma \phi_{-\gamma}\rangle &\propto |\phi_{-\infty} \phi_\infty\rangle \,, \\
\lim_{\gamma \to -\infty} \mathcal{B}^1(\infty) \, |\phi_\gamma \phi_{-\gamma}\rangle &\propto |\psi_{-\infty} \phi_\infty\rangle \,, \\
\lim_{\gamma \to -\infty} \mathcal{B}^1(-\infty) \, |\phi_\gamma \phi_{-\gamma}\rangle &\propto |\phi_{-\infty} \psi_\infty\rangle \,, \\
\lim_{\gamma \to -\infty} \mathcal{B}^1(-\infty) \mathcal{B}^1(\infty) \, |\phi_\gamma \phi_{-\gamma}\rangle &\propto |\psi_{-\infty} \psi_\infty\rangle \,,
\end{aligned}
\tag{C.21}
$$

Since the auxiliaries generating the Bethe states are at $\pm\infty$ (and not at $\pm i\frac{\pi}{2}$), these states are no longer generated by the action of the supercharges and each of the four states are highest weight states of the SUSY algebra.

C.1.3 $N_0 = 3$

The level-matched rapidities $\gamma_i(p_i)$ for three sites satisfy can be chosen as

$$\gamma_1 = \log \tan \frac{p_1}{4}, \quad \gamma_2 = \log \tan \frac{p_2}{4}, \quad \gamma_3 = \log \tan \frac{p_3 + 2\pi}{4}, \tag{C.22}$$

with

$$\gamma_3 = \log \frac{\sinh \frac{-\gamma_1 - \gamma_2}{2}}{\cosh \frac{\gamma_1 - \gamma_2}{2}} \,. \tag{C.23}$$

In other words by selecting $p_1 > p_2 > 0$ and $p_3 < 0$. With this choice, the monodromy matrix in relativistic variables is a product of two R^{LL} and one $R^{\mathrm{L}\ell}$

$$\mathcal{M}(\gamma_0 | \vec{\gamma}) = R^{\mathrm{L}\ell}(\gamma_0 - \gamma_3) R^{\mathrm{LL}}(\gamma_0 - \gamma_2) R^{\mathrm{LL}}(\gamma_0 - \gamma_1) \,. \tag{C.24}$$

The auxiliary Bethe root β satisfies the Bethe equation

$$\prod_{i=1}^{3} b(\beta - \gamma_i) = -1 \,, \tag{C.25}$$

90

which has solutions

$$\beta = -\infty \,, \pm \frac{i\pi}{2} \,. \tag{C.26}$$

Dropping the γ_i subscripts for brevity, and introducing shorthand

$$\gamma_i^{\pm} \equiv \gamma_i \pm \frac{i\pi}{2} \tag{C.27}$$

the corresponding $N_1 = 1$ Bethe states are

$$\mathcal{B}^1(-\infty)\,|\phi\phi\phi\rangle \propto ie^{-\frac{\gamma_3}{2}}\,|\phi\phi\psi\rangle + e^{-\frac{\gamma_2}{2}}\,|\phi\psi\phi\rangle - e^{-\frac{\gamma_1}{2}}\,|\psi\phi\phi\rangle \,,$$

$$\mathcal{B}^1(\tfrac{i\pi}{2})\,|\phi\phi\phi\rangle \propto i\operatorname{sech}\!\left(\tfrac{\gamma_1^-}{2}\right)|\phi\phi\psi\rangle - \operatorname{sech}\!\left(\tfrac{\gamma_2^-}{2}\right)e^{-\frac{ip_2}{2}}\,|\phi\psi\phi\rangle - \operatorname{sech}\!\left(\tfrac{\gamma_3^-}{2}\right)e^{-\frac{ip_3}{2}}\,|\psi\phi\phi\rangle \,,$$

$$\mathcal{B}^1(-\tfrac{i\pi}{2})\,|\phi\phi\phi\rangle \propto i\operatorname{sech}\!\left(\tfrac{\gamma_1^+}{2}\right)|\phi\phi\psi\rangle - \operatorname{sech}\!\left(\tfrac{\gamma_2^+}{2}\right)e^{\frac{ip_2}{2}}\,|\phi\psi\phi\rangle - \operatorname{sech}\!\left(\tfrac{\gamma_3^+}{2}\right)e^{\frac{ip_3}{2}}\,|\psi\phi\phi\rangle \,. \tag{C.28}$$

The $N_1 = 2$ Bethe states are

$$\mathcal{B}^1(\tfrac{i\pi}{2})\mathcal{B}^1(-\infty)\,|\phi\phi\phi\rangle \propto \operatorname{sech}\!\left(\tfrac{\gamma_1^-}{2}\right)|\phi\psi\psi\rangle + \operatorname{sech}\!\left(\tfrac{\gamma_2^-}{2}\right)e^{\frac{ip_1}{2}}\,|\psi\phi\psi\rangle + i\operatorname{sech}\!\left(\tfrac{\gamma_3^-}{2}\right)e^{-\frac{ip_3}{2}}\,|\psi\psi\phi\rangle$$

$$\mathcal{B}^1(\tfrac{-i\pi}{2})\mathcal{B}^1(-\infty)\,|\phi\phi\phi\rangle \propto \operatorname{sech}\!\left(\tfrac{\gamma_1^+}{2}\right)|\phi\psi\psi\rangle + \operatorname{sech}\!\left(\tfrac{\gamma_2^+}{2}\right)e^{\frac{-ip_1}{2}}\,|\psi\phi\psi\rangle + i\operatorname{sech}\!\left(\tfrac{\gamma_3^+}{2}\right)e^{\frac{ip_3}{2}}\,|\psi\psi\phi\rangle$$

$$\mathcal{B}^1(\tfrac{i\pi}{2})\mathcal{B}^1(-\tfrac{i\pi}{2})\,|\phi\phi\phi\rangle \propto e^{-\frac{\gamma_1}{2}}\,|\phi\psi\psi\rangle + e^{-\frac{\gamma_2}{2}}\,|\psi\phi\psi\rangle + ie^{-\frac{\gamma_3}{2}}\,|\psi\psi\phi\rangle \tag{C.29}$$

while the $N_1 = 3$ state is

$$\mathcal{B}^1(\tfrac{i\pi}{2})\mathcal{B}^1(-\tfrac{i\pi}{2})\mathcal{B}^1(-\infty)\,|\phi\phi\phi\rangle \propto |\psi\psi\psi\rangle \,. \tag{C.30}$$

Care needs to be taken in the normalisation of states generated by $\mathcal{B}^1(\tfrac{i\pi}{2})\mathcal{B}^1(-\tfrac{i\pi}{2})$, since naively, this product is zero for generic values of rapidities γ_i. Such zeros did not arise in the main text, because we kept the auxiliary variable in a massive representation and we dropped y^+-dependent normalisation factors (see footnote 20 for details). Normalising the states carefully by removing overall factors of the type mentioned in footnote 20 gives the correct non-vanishing eigenstates of the transfer matrix.

In the zero-momentum limit of the above $N_0 = 3$ Bethe states the magnon rapidities approach $\gamma_1 \to -\infty$, and $\gamma_2 = -\gamma_3 \to -\infty$, while the auxiliary roots end up at $\beta = -\infty$, $-\infty \,, +\infty$.

C.1.4 $N_0 = 4$

For $N_0 = 4$ sites with two positive and two negative momenta (labelled a, i respectively), the level-matched rapidities $\gamma_i(p_i)$ satisfy

$$\gamma_a = \log \tan \frac{p_a}{4}, \quad \gamma_i = \log \tan \frac{p_i + 2\pi}{4}, \quad \text{s.t.} \quad \gamma_4 = \log \frac{-e^{\gamma_1} - e^{\gamma_2} - e^{\gamma_3} + e^{\gamma_1+\gamma_2+\gamma_3}}{1 - e^{\gamma_1+\gamma_2} - e^{\gamma_2+\gamma_3} - e^{\gamma_1+\gamma_3}}, \tag{C.31}$$

with $a = 1, 2$, and $i = 3, 4$. The monodromy matrix is

$$\mathcal{M}(\gamma_0|\vec{\gamma}) = R^{\text{L}\ell}(\gamma_0 - \gamma_4)R^{\text{L}\ell}(\gamma_0 - \gamma_3)R^{\text{LL}}(\gamma_0 - \gamma_2)R^{\text{LL}}(\gamma_0 - \gamma_1)\,. \tag{C.32}$$

The auxiliary Bethe equation and its solutions for level-matched rapidities are

$$\prod_{i=1}^{4} b(\beta - \gamma_i) = 1 \quad \Rightarrow \quad \beta = \pm\frac{i\pi}{2}, \pm\infty\,. \tag{C.33}$$

Using these we generate 1, 4, 6, 4, and 1 Bethe states with 0, 1, 2, 3, and 4 auxiliary roots that span the 16 dimensional space of states. As in the $N_0 = 3$ case, there are spurious zeroes one needs to take care of, arising from the product of $\mathcal{B}$ operators at $\frac{i\pi}{2}$, $-\frac{i\pi}{2}$.

The zero-momentum limit is approached by taking $\gamma_1 = -\gamma_3 = -\infty$, followed by $\gamma_2 = -\gamma_4 = -\infty$. The four auxiliary roots acting on the zero modes are at $\beta = -\infty, -\infty, +\infty, +\infty$.

D   Coordinate Bethe ansatz

Here we will briefly discuss how the coordinate Bethe ansatz can be used to obtain the wave functions we found using the algebraic Bethe ansatz in the above text. The construction we present here is based on the derivation presented in [103, 64] but formulated in a language similar to the free fermion construction of [139].

For simplicity we will restrict ourselves to a system with $\mathrm{psu}(1|1)^2_{\mathrm{c.e.}}$ symmetry and consider excitations transforming in the ρ_L representation, so that we have a boson ϕ and a fermion ψ. As in the algebraic Bethe ansatz, our starting point is a reference state where all excitations are of highest weight in their representations

$$|\phi_{p_1} \cdots \phi_{p_K}\rangle. \tag{D.1}$$

As in equation (4.23), this state can be made into an energy eigenstate by summing over all the permutations of the momenta by repeatedly acting with the S matrix

$$|\Psi(\sigma_1, \ldots, \sigma_K)\rangle = \sum_{\tau \in S_K} e^{i(p_{\tau_1}\sigma_1 + \cdots + p_{\tau_K}\sigma_K)} \mathcal{S}_\tau |\phi_{p_1} \cdots \phi_{p_K}\rangle. \tag{D.2}$$

Here $\mathcal{S}_\tau$ is a component of the full K-particle S matrix which permutes the momenta $p_k \to p_{\tau_k}$. Factorised scattering implies that this S matrix can be written as a product of two-particle S matrices, which have the action (see section 4.2.1)

$$\mathcal{S} |\phi_p \phi_q\rangle = A_{pq} |\phi_q \phi_p\rangle. \tag{D.3}$$

We impose periodicity through the condition

$$|\Psi(\sigma_1, \ldots, \sigma_K)\rangle = |\Psi(\sigma_2, \ldots, \sigma_K, \sigma_1 + L)\rangle, \tag{D.4}$$

Collecting terms with the same exponential prefactor, we can compare for example the term coming from the trivial permutation on the left-hand side, with the term coming from the cyclic permutation $(K \cdots 21)$ on the right-hand side, as illustrated in figure 23. The above equality then leads to the condition

$$e^{ip_1 L} \prod_{j \neq 1} A_{p_1 p_j} = 1. \tag{D.5}$$

In order to describe state which also contain ψ excitations we introduce the creation operator $\mathbf{Q}_y$ which acts by

$$\mathbf{Q}_y |\phi_p\rangle = \frac{\eta_p}{y - x_p^+} |\psi_p\rangle, \qquad \mathbf{Q}_y |\psi_p\rangle = 0, \tag{D.6}$$

	σ_1	σ_2	σ_3	σ_4	σ_5	$\cdots$	σ_K	σ_1+L
Identity	①	②	③	④	⑤	$\cdots$	Ⓚ	
$(K\cdots 21)$		②	③	④	⑤	$\cdots$	Ⓚ	①

Figure 23: The two configurations used to derive equation (D.5) from equation (D.4). The circled numbers represent the excitations ϕ_{p_1}, ϕ_{p_2}, ..., ϕ_{p_K}. To find equation (D.5) we pick out the identity permutation, as in the middle line of the figure, from the state on the left-hand side of (D.4), and the permutation $(K\cdots 21)$, as in the last line of the figure, from the state on the right-hand side.

with the coproduct

$$\Delta(\mathbf{Q}_y) = \mathbf{Q}_y \otimes 1 + \sqrt{\frac{x_p^+}{x_p^-}} \frac{y - x_p^-}{y - x_p^+} \otimes \mathbf{Q}_y. \tag{D.7}$$

The operator $\mathbf{Q}_y$ interpolates between the supercharges $\mathbf{Q}_{\mathrm{L}}$ (for $y = \infty$) and $\bar{\mathbf{Q}}_{\mathrm{R}}$ (for $y = 0$), as can be seen from equations (2.19) and (2.21), and satisfies the relations[37]

$$[\mathbf{Q}_y, \mathcal{S}_{i,i+1}] = 0, \qquad \{\mathbf{Q}_{y_1}, \mathbf{Q}_{y_2}\} = 0. \tag{D.8}$$

The first relation above in particular means that

$$\mathcal{S}_{i,i+1}\mathbf{Q}_y |\phi_{p_1}\cdots\phi_{p_i}\phi_{p_{i+1}}\cdots\phi_K\rangle = A_{p_i p_{i+1}}\mathbf{Q}_y |\phi_{p_1}\cdots\phi_{p_{i+1}}\phi_{p_i}\cdots\phi_K\rangle. \tag{D.9}$$

We can now build excited states by acting with some number of $\mathbf{Q}_y$ on $|\Psi(\sigma_1,\ldots,\sigma_K)\rangle$. Since $\mathbf{Q}_y$ commutes with the two-particle S matrix it does not matter if we act with it before or after summing over all permutations.

Adding excitations to the reference state changes the quantisation condition on the momenta p_i. We consider the same types of terms as above, with a trivial permutation on one side and the permutation $(K\cdots 21)$ on the other side. Let us first look at a term where no $\mathbf{Q}_y$ operator acts on ϕ_{p_1}. On the right hand side the $\mathbf{Q}_y$s do not have to commute through ϕ_{p_1} which means we have an extra phase

$$\prod_i \sqrt{\frac{x_{p_1}^-}{x_{p_1}^+}} \frac{y_i - x_{p_1}^+}{y_i - x_{p_1}^-}, \tag{D.10}$$

as illustrated in figure 24a. Hence we find that periodicity implies the condition

$$e^{ip_1 L} \prod_{j\neq 1} A_{p_1 p_j} \prod_i \sqrt{\frac{x_{p_1}^-}{x_{p_1}^+}} \frac{x_{p_1}^+ - y_i}{x_{p_1}^- - y_i} = 1. \tag{D.11}$$

Now consider a term where $\mathbf{Q}_{y_1}$ acts on ϕ_{p_1}. The extra factor on the right hand side then takes the form

$$\prod_{i\neq 1} \sqrt{\frac{x_{p_1}^-}{x_{p_1}^+}} \frac{y_i - x_{p_1}^+}{y_i - x_{p_1}^-} \prod_{j\neq 1} \sqrt{\frac{x_{p_j}^+}{x_{p_j}^-}} \frac{y_1 - x_{p_j}^+}{y_1 - x_{p_j}^-} = \prod_i \sqrt{\frac{x_{p_1}^-}{x_{p_1}^+}} \frac{y_i - x_{p_1}^+}{y_i - x_{p_1}^-} \prod_j \sqrt{\frac{x_{p_j}^+}{x_{p_j}^-}} \frac{y_1 - x_{p_j}^+}{y_1 - x_{p_j}^-} \tag{D.12}$$

---

[37]Here $\mathcal{S}_{i,i+1}$ is the two-particle S matrix acting on any two neighbouring excitations.
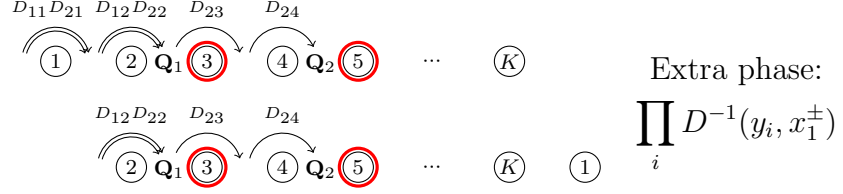
(a) Extra phase for creation operators not acting on ϕ_{p_1}.
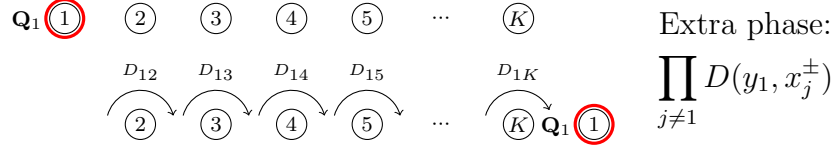
(b) Extra phase for creation operators acting on ϕ_{p_1}.

Figure 24: Illustration of the extra phases in the nested Bethe equations (D.14). The circled numbers represent the excitations ϕ_{p_1}, ϕ_{p_2}, ..., ϕ_{p_K} and the symbols $\mathbf{Q}_i$ represent the creation operator $\mathbf{Q}_{y_i}$ which acts on the following excitation to the right, as indicated by the thick red circles. Commuting the operator $\mathbf{Q}_{y_i}$ through the excitation ϕ_{p_j} gives a factor $D_{ij} = \sqrt{x_j^+/x_j^-}(y_i - x_j^-)/(y_i - x_j^+)$.

where the first product has the same origin as in the previous case (for all $\mathbf{Q}_{y_i}$ with $i \neq 1$), and the second factor comes from commuting $\mathbf{Q}_{y_1}$ through all ϕ_{p_j} with $j \neq 1$, see figure 24b. Compatibility of the resulting equations for p_1 then imposes the additional constraint

$$1 = \prod_j \sqrt{\frac{x_{p_j}^+}{x_{p_j}^-}} \frac{y_1 - x_{p_j}^+}{y_1 - x_{p_j}^-}. \tag{D.13}$$

Above we have considered the momentum p_1 and the auxiliary parameter y_1, but the same conditions of course apply for any other parameters and we find that the Bethe equations take the form

$$e^{ip_k L} = \prod_{j \neq 1} A_{p_k p_j}^{-1} \prod_j \sqrt{\frac{x_{p_k}^+}{x_{p_k}^-}} \frac{x_{p_k}^- - y_j}{x_{p_k}^+ - y_j}, \qquad 1 = \prod_j \sqrt{\frac{x_{p_j}^+}{x_{p_j}^-}} \frac{y_k - x_{p_j}^+}{y_k - x_{p_j}^-}. \tag{D.14}$$

These equations exactly match the $\mathrm{psu}(1|1)_{\mathrm{c.e.}}^2$ subsector (*i.e.*, setting $N_3 = 0$) of the Bethe equations (4.49), and (4.46).

It is now straight forward to obtain wave functions of excited states. For example, the action of a single $\mathbf{Q}_y$ operator on reference states with two and three excitations are given by

$$\mathbf{Q}_y |\phi_{p_1}\phi_{p_2}\rangle = \frac{\eta_1}{y - x_1^+} |\psi_{p_1}\phi_{p_2}\rangle + \frac{\eta_2}{y - x_2^+} \frac{y - x_1^-}{y - x_1^+} \sqrt{\frac{x_1^+}{x_1^-}} |\phi_{p_1}\psi_{p_2}\rangle, \tag{D.15}$$

and

$$\mathbf{Q}_y \ket{\phi_{p_1} \phi_{p_2} \phi_{p_3}} = \frac{\eta_1}{y - x_1^+} \ket{\psi_{p_1} \phi_{p_2} \phi_{p_3}} + \frac{\eta_2}{y - x_2^+} \frac{y - x_1^-}{y - x_1^+} \sqrt{\frac{x_1^+}{x_1^-}} \ket{\phi_{p_1} \psi_{p_2} \phi_{p_3}}$$
$$+ \frac{\eta_3}{y - x_3^+} \frac{y - x_1^-}{y - x_1^+} \frac{y - x_2^-}{y - x_2^+} \sqrt{\frac{x_1^+ x_2^+}{x_1^- x_2^-}} \ket{\phi_{p_1} \phi_{p_2} \psi_{p_3}} . \tag{D.16}$$

Comparing these expressions with equations (4.54) and (4.62) we see that the states obtained using the $\mathbf{Q}_y$ operator exactly match those obtained using the $\mathcal{B}$ operator, up to normalisation.[38] Similarly, we can check that the two formulation lead to identical wave functions also for states with longer reference states and more creation operators.[39]

E   2D integrable difference form spin chain classification

In this sub-section, we list our trained results for each of the 14 gauge-inequivalent integrable Hamiltonian classes of difference form and the corresponding R-matrices. Amongst the XYZ type models, the simplest solution is a diagonal 4-vertex model with Hamiltonians and R-matrices as follows:

$$H_{4v} = \begin{pmatrix} a_1 & 0 & 0 & 0 \\ 0 & b_1 & 0 & 0 \\ 0 & 0 & b_2 & 0 \\ 0 & 0 & 0 & a_2 \end{pmatrix} \quad \leftrightarrow \quad R_{4v}(u) = \begin{pmatrix} e^{a_1 u} & 0 & 0 & 0 \\ 0 & 0 & e^{b_2 u} & 0 \\ 0 & e^{b_1 u} & 0 & 0 \\ 0 & 0 & 0 & e^{a_2 u} \end{pmatrix} \tag{E.1}$$

Figure 25 plots the training curve for R-matrix components as ratios with respect to (00) component, against the analytic functions for parameters $a_1 = 0.9, b_1 = 0.4, b_2 = 0.6, a_2 = 0.75$.

In 6-vertex models, we have two distinct classes depending on whether the Hamiltonian entries H^{00} and H^{33} are equal or not. In the first case, the R-matrix $R_{6v,1}(u)$ and its associated Hamiltonian $H_{6v,1}$ are given by

$$H_{6v,1} = \begin{pmatrix} a_1 & 0 & 0 & 0 \\ 0 & b_1 & c_1 & 0 \\ 0 & c_2 & b_2 & 0 \\ 0 & 0 & 0 & a_1 \end{pmatrix} \quad \leftrightarrow \quad R_{6v,1}(u) = \begin{pmatrix} R_{6v,1}^{00}(u) & 0 & 0 & 0 \\ 0 & R_{6v,1}^{11}(u) & R_{6v,1}^{12}(u) & 0 \\ 0 & R_{6v,1}^{21}(u) & R_{6v,1}^{22}(u) & 0 \\ 0 & 0 & 0 & R_{6v,1}^{33}(u) \end{pmatrix} \tag{E.2}$$

---

[38]The extra signs in equations (4.54) and (4.62) compared to equations (D.15) and (D.16) appear because the $\mathrm{psu}(1|1)_{\mathrm{c.e.}}^4$ highest weight excitation χ is a fermion, while we here consider reference states with a bosonic excitation ϕ.

[39]The difference in normalisation of a general state is exactly given by the factor discussed in footnote 20 on page 47.
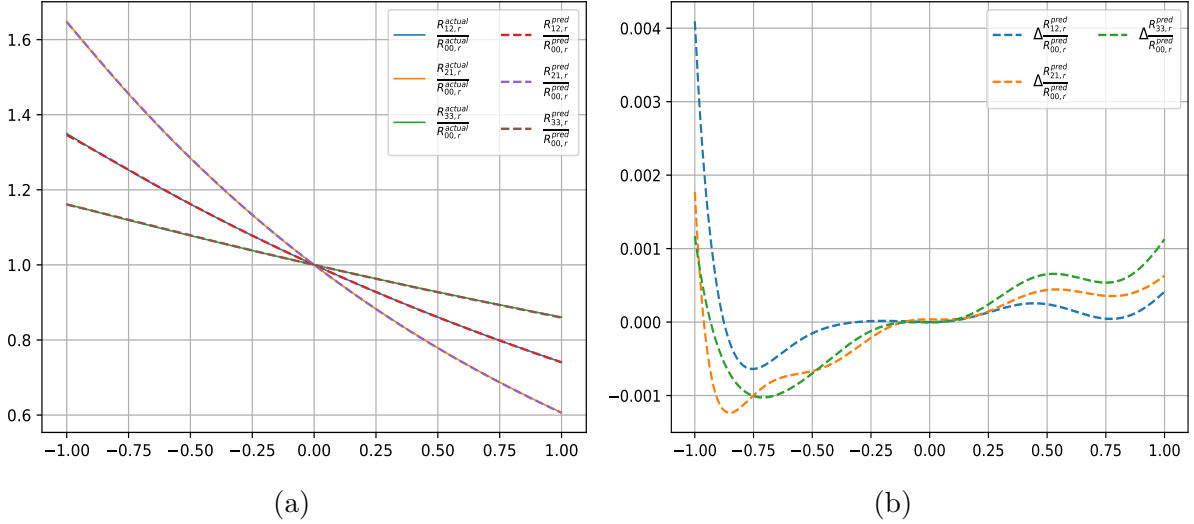
Figure 25: (a) 4-vertex model, with H_2 parameters $a_1 = 0.9$, $b_1 = 0.4$, $b_2 = 0.6$, $a_2 = 0.75$, (b) errors

where

$$R_{6v,1}^{00}(u) = R_{6v,1}^{33}(u) = e^{(b_1+b_2)u/2}(\cosh(\omega u) + \frac{2a_1 - b_1 - b_2}{2\omega} \sinh(\omega u))$$

$$R_{6v,1}^{11}(u) = \frac{c_2}{\omega} e^{(b_1+b_2)u/2} \sinh(\omega u)$$

$$R_{6v,1}^{12}(u) = e^{b_2 u}$$

$$R_{6v,1}^{21}(u) = e^{b_1 u}$$

$$R_{6v,1}^{22}(u) = \frac{c_1}{\omega} e^{(b_1+b_2)u/2} \sinh(\omega u), \qquad \omega = \frac{\sqrt{(2a_1 - b_1 - b_2)^2 - 4c_1 c_2}}{2} \tag{E.3}$$

Figure 12 gives a representative training vs actual plot for this class.

For the case $H^{00} \neq H^{33}$, the R-matrix $R_{6v,2}(u)$ is given by

$$H_{6v,2} = \begin{pmatrix} a_1 & 0 & 0 & 0 \\ 0 & b_1 & c_1 & 0 \\ 0 & c_2 & b_2 & 0 \\ 0 & 0 & 0 & a_2 \end{pmatrix} \leftrightarrow R_{6v,2}(u) = \begin{pmatrix} R_{6v,2}^{00}(u) & 0 & 0 & 0 \\ 0 & R_{6v,2}^{11}(u) & R_{6v,2}^{12}(u) & 0 \\ 0 & R_{6v,2}^{21}(u) & R_{6v,2}^{22}(u) & 0 \\ 0 & 0 & 0 & R_{6v,2}^{33}(u) \end{pmatrix} \tag{E.4}$$

where $a_2 = b_1 + b_2 - a_1$ and

$$R_{6v,2}^{00}(u) = e^{(a_1+a_2)u/2}(\cosh(\omega u) + \frac{a_1 - a_2}{2\omega} \sinh(\omega u))$$

$$R_{6v,2}^{11}(u) = \frac{c_2}{\omega} e^{(a_1+a_2)u/2} \sinh(\omega u)$$

$$R_{6v,2}^{12}(u) = e^{b_2 u}$$

$$R_{6v,2}^{21}(u) = e^{b_1 u}$$

$$R_{6v,2}^{22}(u) = \frac{c_1}{\omega} e^{(a_1+a_2)u/2} \sinh(\omega u)$$

$$R_{6v,2}^{33}(u) = e^{(a_1+a_2)u/2}(\cosh(\omega u) - \frac{a_1 - a_2}{2\omega} \sinh(\omega u)), \qquad \omega = \frac{\sqrt{(a_1 - a_2)^2 - 4c_1 c_2}}{2} \tag{E.5}$$

Figure 26 gives a representative training vs actual plot for Hamiltonian parameters $a_1 = 1., a_2 = 0.2, b_1 = 0.45, b_2 = 0.75, c_1 = 0.4, c_2 = 0.6$. Next we have the 7-vertex models,
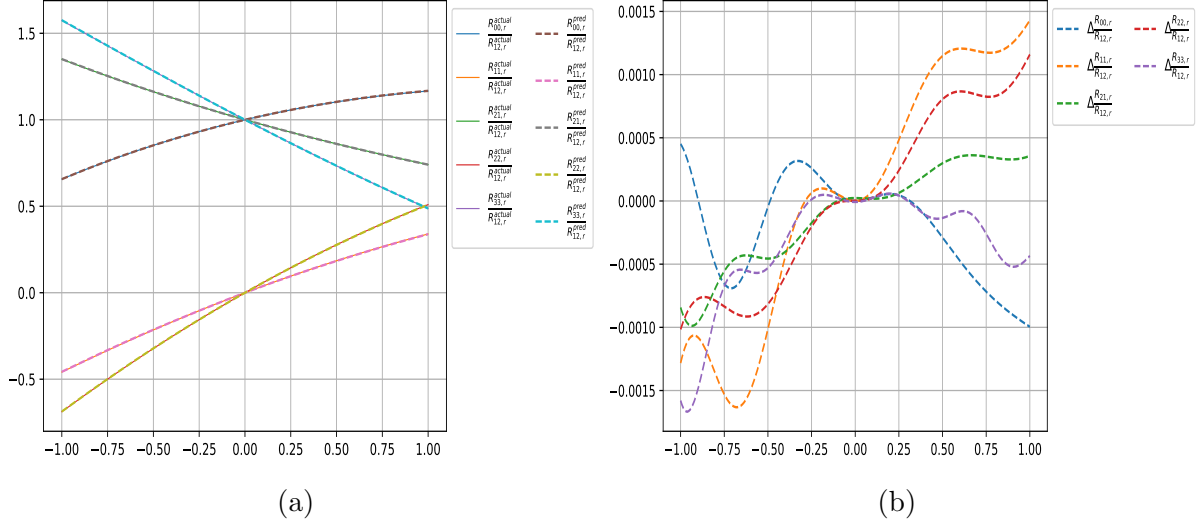
Figure 26: (a) 6-vertex model with Hamiltonian of type $H_{6v,2}$, with parameters $a_1 = 1, a_2 = 0.2, b_1 = 0.45, b_2 = 0.75, c_1 = 0.4, c_2 = 0.6$, (b)errors

which consists of two classes of solution distinguished by the Hamiltonian entries H^{00}, H^{33} being equal or not. In the first case, we have

$$
H_{7v,1} = \begin{pmatrix} a_1 & 0 & 0 & d_1 \\ 0 & a_1 + b_1 & c_1 & 0 \\ 0 & -c_1 & a_1 - b_1 & 0 \\ 0 & 0 & 0 & a_1 \end{pmatrix} \leftrightarrow R_{7v,1}(u) = \begin{pmatrix} R_{7v,1}^{00}(u) & 0 & 0 & R_{7v,1}^{03}(u) \\ 0 & R_{7v,1}^{11}(u) & R_{7v,1}^{12}(u) & 0 \\ 0 & R_{7v,1}^{21}(u) & R_{7v,1}^{22}(u) & 0 \\ 0 & 0 & 0 & R_{7v,1}^{33}(u) \end{pmatrix}
$$
(E.6)

where

$$
R_{7v,1}^{00}(u) = R_{7v,1}^{33}(u) = e^{a_1 u} \cosh(c_1 u)
$$
$$
R_{7v,1}^{11}(u) = -R_{7v,1}^{22}(u) = e^{a_1 u} \sinh(c_1 u)
$$
$$
R_{7v,1}^{12}(u) = e^{(a_1 - b_1)u}
$$
$$
R_{7v,1}^{21}(u) = e^{(a_1 + b_1)u}
$$
$$
R_{7v,1}^{03}(u) = -\frac{d_1}{2b_1}(e^{(a_1 - b_1)u} - e^{(a_1 + b_1)u})
$$
(E.7)

Figure 27 plots the predicted R-matrix components as ratios with respect to the (12) component against the above analytic results, and their differences for a generic choice of parameters $a_1 = 1, b_1 = 0.45, c_1 = 0.6, d_1 = 0.75$.
In the second case for $H^{00} \neq H^{33}$, we have

$$
H_{7v,2} = \begin{pmatrix} a_1 & 0 & 0 & d_1 \\ 0 & a_1 - c_2 & c_1 & 0 \\ 0 & c_2 & a_1 - c_1 & 0 \\ 0 & 0 & 0 & a_2 \end{pmatrix} \leftrightarrow R_{7v,2}(u) = \begin{pmatrix} R_{7v,2}^{00}(u) & 0 & 0 & R_{7v,1}^{03}(u) \\ 0 & R_{7v,2}^{11}(u) & R_{7v,1}^{12}(u) & 0 \\ 0 & R_{7v,2}^{21}(u) & R_{7v,1}^{22}(u) & 0 \\ 0 & 0 & 0 & R_{7v,1}^{33}(u) \end{pmatrix}
$$
(E.8)
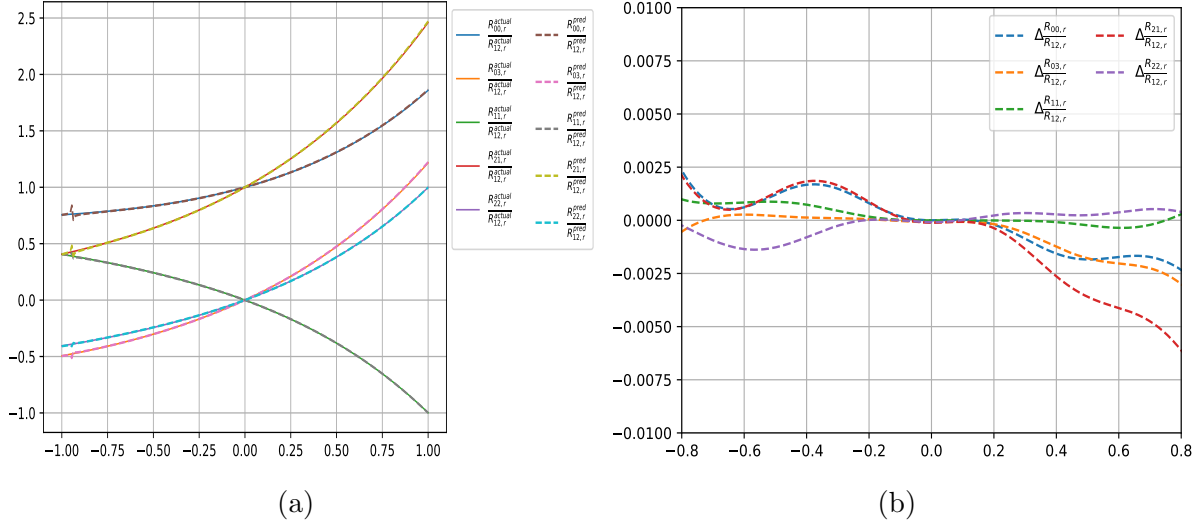
Figure 27: (a) 7-vertex model with Hamiltonian of type $H_{7v,1}$, with parameters $a_1 = 1, b_1 = 0.45, c_1 = 0.6, d_1 = 0.75$, (b)errors

where $a_2 = a_1 - c_1 - c_2$ and

$$R^{00}_{7v,2}(u) = \frac{e^{(a_1-\frac{c_1+c_2}{2})u}}{c_1 - c_2}((c_1 - c_2)\cosh{(\frac{c_1 - c_2}{2}u)} + (c_1 + c_2)\sinh{(\frac{c_1 - c_2}{2}u)})$$

$$R^{11}_{7v,2}(u) = \frac{2c_2}{c_1 - c_2}e^{(a_1-\frac{c_1+c_2}{2})u}\sinh{(\frac{c_1 - c_2}{2}u)}$$

$$R^{22}_{7v,2}(u) = \frac{2c_1}{c_1 - c_2}e^{(a_1-\frac{c_1+c_2}{2})u}\sinh{(\frac{c_1 - c_2}{2}u)}$$

$$R^{12}_{7v,2}(u) = e^{(a_1-c_1)u}$$

$$R^{21}_{7v,2}(u) = e^{(a_1+c_2)u}$$

$$R^{03}_{7v,2}(u) = \frac{2d_1}{c_1 - c_2}e^{(a_1-\frac{c_1+c_2}{2})u}\sinh{(\frac{c_1 - c_2}{2}u)}$$

$$R^{33}_{7v,2}(u) = \frac{e^{(a_1-\frac{c_1+c_2}{2})u}}{c_1 - c_2}((c_1 - c_2)\cosh{(\frac{c_1 - c_2}{2}u)} - (c_1 + c_2)\sinh{(\frac{c_1 - c_2}{2}u)}) \quad\text{(E.9)}$$

Figure 28 plots the predicted R-matrix components as ratios with respect to the (12) component against the above analytic results, and their differences for a generic choice of parameters $a_1 = 1, c_1 = 0.45, c_2 = 0.75, d_1 = 0.5$.

8-vertex models have 3 gauge-inequivalent classes labelled $H_{8v,i}, i = 1, 2, 3$. One of these models, namely $H_{8v,1}$, is a generalisation of the XYZ model

$$H_{8v,1} = \begin{pmatrix} a_1 & 0 & 0 & d_1 \\ 0 & b_1 & c_1 & 0 \\ 0 & c_1 & b_1 & 0 \\ d_2 & 0 & 0 & a_1 \end{pmatrix} \leftrightarrow R_{8v,1}(u) = \begin{pmatrix} R^{00}_{8v,1}(u) & 0 & 0 & R^{03}_{8v,1}(u) \\ 0 & R^{11}_{8v,1}(u) & R^{12}_{8v,1}(u) & 0 \\ 0 & R^{21}_{8v,1}(u) & R^{22}_{8v,1}(u) & 0 \\ R^{30}_{8v,1}(u) & 0 & 0 & R^{33}_{8v,1}(u) \end{pmatrix}$$
$$\text{(E.10)}$$
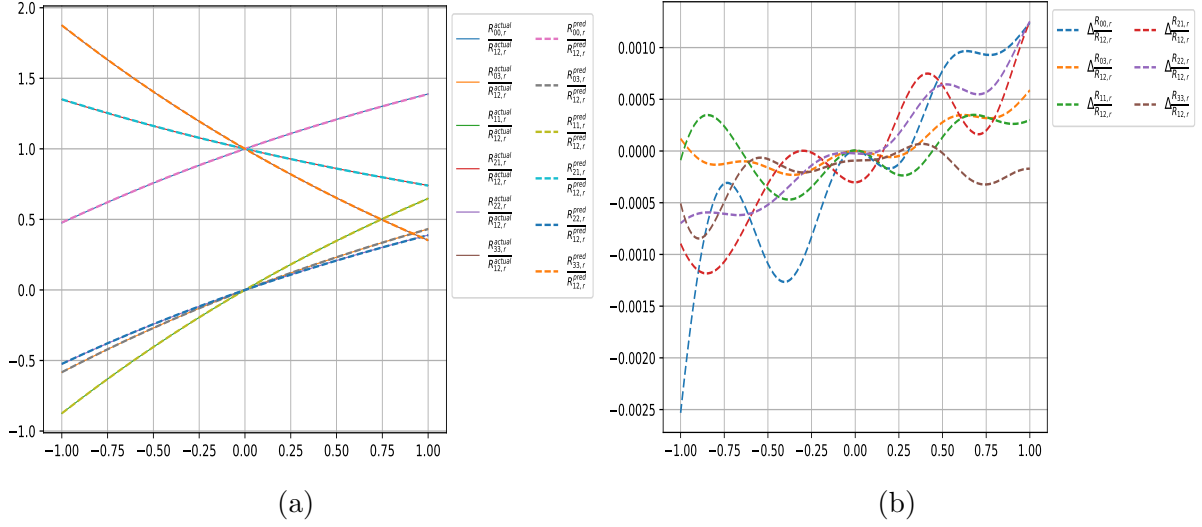
Figure 28: (a) 7-vertex model with Hamiltonian of type $H_{7v,2}$, with parameters $a_1 = 1, c_1 = 0.45, c_2 = 0.75, d_1 = 0.5$, (b)errors

where

$$R_{8v,1}^{00}(u) = R_{8v,1}^{33}(u) = \frac{\text{sn}(u + 2\eta, m)}{\text{sn}(2\eta, m)} e^{b_1 u}$$

$$R_{8v,1}^{11}(u) = R_{8v,1}^{22}(u) = \frac{\text{sn}(u, m)}{\text{sn}(2\eta, m)} e^{b_1 u}$$

$$R_{8v,1}^{12}(u) = R_{8v,1}^{21}(u) = e^{b_1 u}$$

$$R_{8v,1}^{03}(u) = \sqrt{\frac{d_1}{d_2}} \sqrt{m} \, \text{sn}(u + 2\eta, m) \text{sn}(u, m) e^{b_1 u}$$

$$R_{8v,1}^{30}(u) = \sqrt{\frac{d_2}{d_1}} \sqrt{m} \, \text{sn}(u + 2\eta, m) \text{sn}(u, m) e^{b_1 u} \tag{E.11}$$

with Hamiltonian coefficients given by

$$a_1 = b_1 + \frac{\text{cn}(2\eta, m) \text{dn}(2\eta, m)}{\text{sn}(2\eta, m)}, \quad c_1 = \frac{1}{\text{sn}(2\eta, m)},$$

$$d_1 = \sqrt{m} \, \delta_1 \, \text{sn}(2\eta, m), \quad d_2 = \sqrt{m} \, \delta_2 \, \text{sn}(2\eta, m) \tag{E.12}$$

for free parameters $b_1, \eta, m, \delta_1, \delta_2$. Figure 29 plots the predicted R-matrix components as ratios with respect to the (12) component against the above analytic results, and their differences for a generic choice of parameters $b_1 = 0.4, \eta = 0.8, m = 0.5, \delta_1 = 1.3, \delta_2 = 0.7$.

The second class of 8-vertex XYZ-type solution has Hamiltonian $H_{8v,2}$ and R-matrix $R_{8v,2}(u)$ defined as follows

$$H_{8v,2} = \begin{pmatrix} a_1 & 0 & 0 & d_1 \\ 0 & b_1 & c_1 & 0 \\ 0 & c_1 & b_1 & 0 \\ d_2 & 0 & 0 & 2b_1 - a_1 \end{pmatrix} \leftrightarrow R_{8v,2}(u) = \begin{pmatrix} R_{8v,2}^{00}(u) & 0 & 0 & R_{8v,2}^{03}(u) \\ 0 & R_{8v,2}^{11}(u) & R_{8v,2}^{12}(u) & 0 \\ 0 & R_{8v,2}^{21}(u) & R_{8v,2}^{22}(u) & 0 \\ R_{8v,2}^{30}(u) & 0 & 0 & R_{8v,2}^{33}(u) \end{pmatrix}$$

$$\tag{E.13}$$
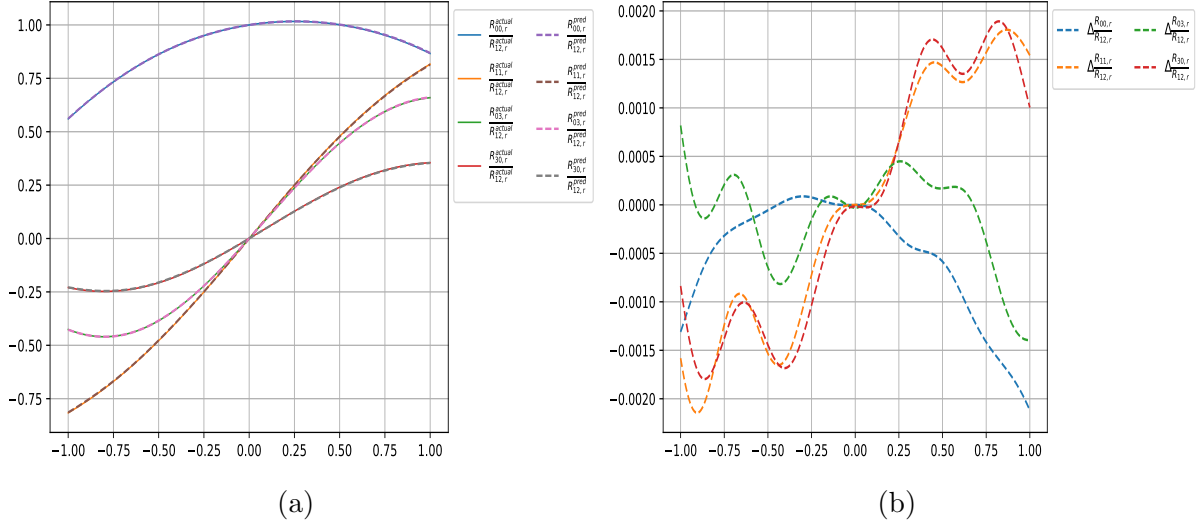
Figure 29: (a) 8-vertex model with Hamiltonian of type $H_{8v,1}$, with parameters $b_1 = 0.4, \eta = 0.8, m = 0.5, \delta_1 = 1.3, \delta_2 = 0.7$, (b)errors

where

$$R_{8v,2}^{00}(u) = (\frac{\text{cn}(u,m)}{\text{dn}(u,m)} + \frac{\text{sn}(u,m)\text{cn}(2\eta,m)}{\text{sn}(2\eta,m)})e^{b_1 u}$$

$$R_{8v,2}^{11}(u) = R_{8v,1}^{22}(u) = \frac{\text{sn}(u,m)}{\text{sn}(2\eta,m)}e^{b_1 u}$$

$$R_{8v,2}^{12}(u) = R_{8v,1}^{21}(u) = e^{b_1 u}$$

$$R_{8v,2}^{03}(u) = \frac{\delta_1}{\beta_1}\frac{\text{sn}(u,m)\text{cn}(u,m)}{\text{dn}(u,m)\text{sn}(2\eta,m)}e^{b_1 u}$$

$$R_{8v,2}^{30}(u) = \frac{\delta_2}{\beta_1}\frac{\text{sn}(u,m)\text{cn}(u,m)}{\text{dn}(u,m)\text{sn}(2\eta,m)}e^{b_1 u}$$

$$R_{8v,2}^{33}(u) = (\frac{\text{cn}(u,m)}{\text{dn}(u,m)} - \frac{\text{sn}(u,m)\text{cn}(2\eta,m)}{\text{sn}(2\eta,m)})e^{b_1 u} \qquad \text{(E.14)}$$

with the Hamiltonian coefficients given by

$$a_1 = b_1 + \frac{\text{cn}(2\eta,m)}{\text{sn}(2\eta,m)}, \ c_1 = \frac{1}{\text{sn}(2\eta,m)}, \ d_1 = \frac{\delta_1}{\beta_1 \text{sn}(2\eta,m)}, \ d_2 = \frac{\delta_2}{\beta_1 \text{sn}(2\eta,m)} \qquad \text{(E.15)}$$

$$m = \frac{\delta_1 \delta_2}{\alpha_1^2 - \beta_1^2}, \ \text{cn}(2\eta,m) = \frac{\alpha_1}{\beta_1}, \ \text{sn}(2\eta,m) = \sqrt{1 - \frac{\alpha_1^2}{\beta_1^2}} \qquad \text{(E.16)}$$

for free parameters $b_1, \alpha_1, \beta_1, \delta_1, \delta_2$. Figure 30 plots the predicted R-matrix components as ratios with respect to the (12) component against the above analytic results, and their differences for a generic choice of parameters $b_1 = 0.4, \alpha_1 = 0.5, \beta_1 = 0.7, \delta_1 = 0.3, \delta_2 = 0.2$.

The third class of 8-vertex XYZ-type solution has Hamiltonian $H_{8v,3}$ and R-matrix
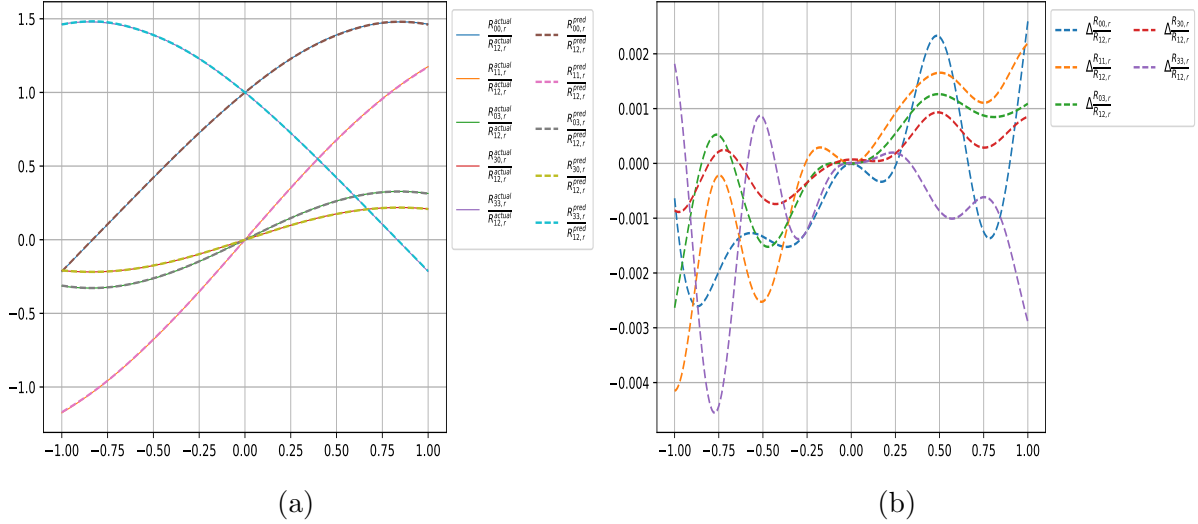
Figure 30: (a) 8-vertex model with Hamiltonian of type $H_{8v,2}$, with parameters $b_1 = 0.4, \alpha_1 = 0.5, \beta_1 = 0.7, \delta_1 = 0.3, \delta_2 = 0.2$, (b)errors

$R_{8v,3}(u)$ defined as follows

$$H_{8v,3} = \begin{pmatrix} a_1 & 0 & 0 & d_1 \\ 0 & a_1 & -b_1 & 0 \\ 0 & b_1 & a_1 & 0 \\ d_2 & 0 & 0 & a_1 \end{pmatrix} \leftrightarrow R_{8v,3}(u) = \begin{pmatrix} R_{8v,3}^{00}(u) & 0 & 0 & R_{8v,3}^{03}(u) \\ 0 & R_{8v,3}^{11}(u) & R_{8v,3}^{12}(u) & 0 \\ 0 & R_{8v,3}^{21}(u) & R_{8v,3}^{22}(u) & 0 \\ R_{8v,3}^{30}(u) & 0 & 0 & R_{8v,3}^{33}(u) \end{pmatrix}$$
(E.17)

where

$$R_{8v,3}^{00}(u) = R_{8v,1}^{33}(u) = \frac{\cosh(b_1 u)}{\cos(\sqrt{d_1 d_2} u)} e^{a_1 u}$$

$$R_{8v,3}^{11}(u) = -R_{8v,1}^{22}(u) = \frac{\sinh(b_1 u)}{\cos(\sqrt{d_1 d_2} u)} e^{a_1 u}$$

$$R_{8v,3}^{12}(u) = R_{8v,1}^{21}(u) = e^{a_1 u}$$

$$R_{8v,3}^{03}(u) = \sqrt{\frac{d_1}{d_2}} e^{a_1 u} \tan(\sqrt{d_1 d_2} u)$$

$$R_{8v,1}^{30}(u) = \sqrt{\frac{d_2}{d_1}} e^{a_1 u} \tan(\sqrt{d_1 d_2} u)$$
(E.18)

Figure 31 plots the predicted R-matrix components as ratios with respect to the (12) component against the above analytic results, and their differences for a generic choice of parameters $a_1 = 1$, $b_1 = -0.45$, $d_1 = 0.6$, $d_2 = 0.75$.

For non-XYZ type models, the 6 gauge-inequivalent Hamiltonians are of the form

$$H_{\text{class}-1} = \begin{pmatrix} 0 & a_1 & a_2 & 0 \\ 0 & a_5 & 0 & a_3 \\ 0 & 0 & -a_5 & a_4 \\ 0 & 0 & 0 & 0 \end{pmatrix}, \quad H_{\text{class}-2} = \begin{pmatrix} 0 & a_2 & a_3 - a_2 & a_5 \\ 0 & a_1 & 0 & a_4 \\ 0 & 0 & -a_1 & a_3 - a_4 \\ 0 & 0 & 0 & 0 \end{pmatrix},$$
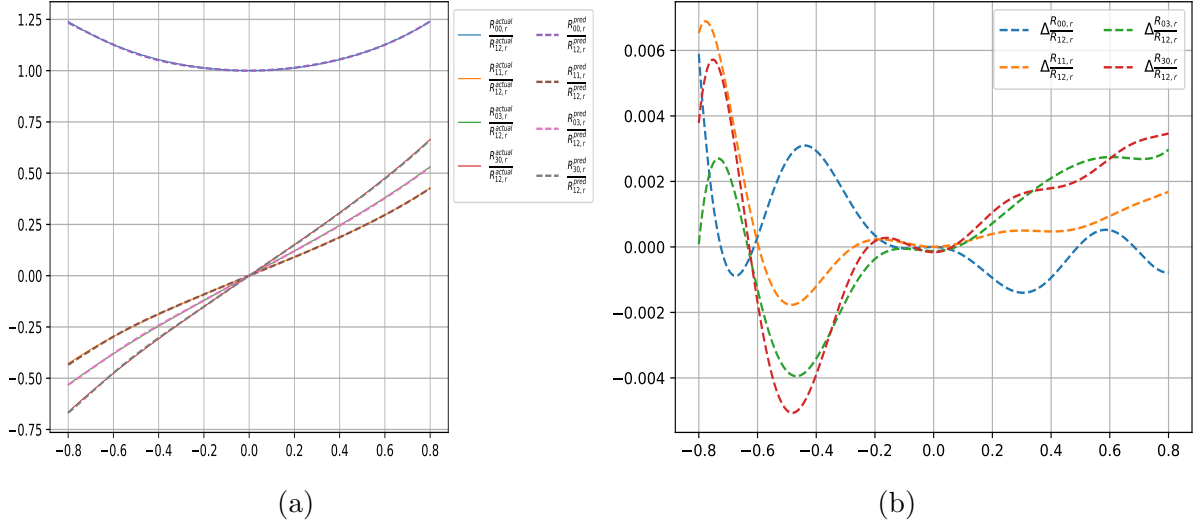
Figure 31: (a) 8-vertex model with Hamiltonian of type $H_{8v,3}$, with parameters $a_1 = 1$, $b_1 = -0.45$, $d_1 = 0.6$, $d_2 = 0.75$, (b)errors

$$H_{\text{class}-3} = \begin{pmatrix} -a_1 & (2a_1 - a_2)a_3 & (2a_1 + a_2)a_3 & 0 \\ 0 & a_1 - a_2 & 0 & 0 \\ 0 & 0 & a_1 + a_2 & 0 \\ 0 & 0 & 0 & -a_1 \end{pmatrix}, \quad H_{\text{class}-4} = \begin{pmatrix} a_1 & a_2 & a_2 & a_3 \\ 0 & -a_1 & 0 & a_4 \\ 0 & 0 & -a_1 & a_4 \\ 0 & 0 & 0 & a_1 \end{pmatrix}$$

$$H_{\text{class}-5} = \begin{pmatrix} a_1 & a_2 & -a_2 & 0 \\ 0 & -a_1 & 2a_1 & a_3 \\ 0 & 2a_1 & -a_1 & -a_3 \\ 0 & 0 & 0 & a_1 \end{pmatrix}, \quad H_{\text{class}-6} = \begin{pmatrix} a_1 & a_2 & a_2 & 0 \\ 0 & -a_1 & 2a_1 & -a_2 \\ 0 & 2a_1 & -a_1 & -a_2 \\ 0 & 0 & 0 & a_1 \end{pmatrix} \quad \text{(E.19)}$$

Corresponding R-matrices are

$$R_{\text{class}-1}(u) = \begin{pmatrix} 1 & \frac{a_1(e^{a_5 u}-1)}{a_5} & \frac{a_2(e^{a_5 u}-1)}{a_5} & \frac{(a_1 a_3 + a_2 a_4)}{a_5^2}(\cosh(a_5 u) - 1) \\ 0 & 0 & e^{-a_5 u} & \frac{a_4(1 - e^{-a_5 u})}{a_5} \\ 0 & e^{a_5 u} & 0 & \frac{a_3(1 - e^{-a_5 u})}{a_5} \\ 0 & 0 & 0 & 1 \end{pmatrix} \quad \text{(E.20)}$$

$$R_{\text{class}-2}(u) = uP\left(\frac{a_1}{\sinh(a_1 u)} + H_{class-5} + \frac{\tanh(a_1 u)}{a_1} H_{class-5}^2\right), \quad P = \begin{pmatrix} 1 & 0 & 0 & 0 \\ 0 & 0 & 1 & 0 \\ 0 & 1 & 0 & 0 \\ 0 & 0 & 0 & 1 \end{pmatrix} \quad \text{(E.21)}$$

$$R_{\text{class}-3}(u) = \begin{pmatrix} e^{-a_1 u} & a_3(e^{(a_1 - a_2)u} - e^{-a_1 u}) & a_3(e^{(a_1 + a_2)u} - e^{-a_1 u}) & 0 \\ 0 & 0 & e^{(a_1 + a_2)u} & 0 \\ 0 & e^{(a_1 - a_2)u} & 0 & 0 \\ 0 & 0 & 0 & e^{-a_1 u} \end{pmatrix} \quad \text{(E.22)}$$

$$R_{\text{class}-4}(u) = \begin{pmatrix} e^{a_1 u} & \frac{a_2 \sinh(a_1 u)}{a_1} & \frac{a_2 \sinh(a_1 u)}{a_1} & \frac{e^{a_1 u}(a_2 a_4 + a_1 a_3 \coth(a_1 u))\sinh^2(a_1 u)}{a_1^2} \\ 0 & 0 & e^{-a_1 u} & \frac{a_4 \sinh(a_1 u)}{a_1} \\ 0 & e^{-a_1 u} & 0 & \frac{a_4 \sinh(a_1 u)}{a_1} \\ 0 & 0 & 0 & e^{a_1 u} \end{pmatrix} \quad \text{(E.23)}$$

$$R_{\text{class}-5}(u) = (1 - a_1 u) \begin{pmatrix} 2a_1u + 1 & a_2u & -a_2u & a_2a_3u^2 \\ 0 & 2a_1u & 1 & -a_3u \\ 0 & 1 & 2a_1u & a_3u \\ 0 & 0 & 0 & 2a_1u + 1 \end{pmatrix} \tag{E.24}$$

$$R_{\text{class}-6}(u) = (1 - a_1 u) \begin{pmatrix} 2a_1u + 1 & a_2u(2a_1u + 1) & a_2u(2a_1u + 1) & -a_2^2u^2(2a_1u + 1) \\ 0 & 2a_1u & 1 & -a_2u(2a_1u + 1) \\ 0 & 1 & 2a_1u & -a_2u(2a_1u + 1) \\ 0 & 0 & 0 & 2a_1u + 1 \end{pmatrix} \tag{E.25}$$

In the class-2 solution above, the non-zero R-matrix components are explicitly given by

$$R^{00}_{\text{class}-2}(u) = R^{33}_{\text{class}-2}(u) = \frac{a_1u}{\sinh u}$$

$$R^{01}_{\text{class}-2}(u) = a_2u(1 + \tanh\left(\frac{a_1u}{2}\right)),$$

$$R^{02}_{\text{class}-2}(u) = (a_2 - a_3)u(-1 + \tanh\left(\frac{a_1u}{2}\right))$$

$$R^{03}_{\text{class}-2}(u) = a_5u(1 + \frac{((a_4 - a_3)(a_2 - a_3) + a_2a_4)\tanh\frac{a_1u}{2}}{a_1a_5})$$

$$R^{12}_{\text{class}-2}(u) = a_1u(-1 + \frac{1}{\sinh(a_1u)} + \tanh\frac{a_1u}{2})$$

$$R^{13}_{\text{class}-2}(u) = (a_4 - a_3)u(-1 + \tanh\left(\frac{a_1u}{2}\right))$$

$$R^{21}_{\text{class}-2}(u) = a_1u(1 + \frac{1}{\sinh(a_1u)} + \tanh\frac{a_1u}{2})$$

$$R^{23}_{\text{class}-2}(u) = a_4u(1 + \tanh\left(\frac{a_1u}{2}\right)) \tag{E.26}$$

Amongst the above non-XYZ type models, we have already looked into the training for Class 1 model in section 6.3. Figure 32, 33, 34 plot the training vs actual R-matrix components for classes 2,3,4, class 5, and class 6 respectively, with generic Hamiltonian parameters. Also we note that allowing for complex parameters results in generically complex R-matrices. We compare the predictions against the actual formulae by taking ratios with respect to the real part of the (00) component for classes 2-5, and (12) component for class 6.

F Designing the Neural Network

We begin with an overview of the architecture of our neural network solver, as well as details of the hyperparameters with which the network is trained. Our starting point is the close analogy between our problem of machine learning R-matrices by imposing constraints and the design of the Siamese Neural Networks [140, 141]. These were designed to function in settings where the canonical supervised learning approach of (3.5), (3.6) for classification becomes infeasible due to the large number of target classes $\{y\}$ and the paucity of training examples $\{x_\alpha\}$ corresponding to each class y_α. In such a situation, one may instead define a similarity relation

$$x_{\alpha_1} \sim x_{\alpha_2} \qquad \Longleftrightarrow \qquad y(x_{\alpha_1}) = y(x_{\alpha_2}), \tag{F.1}$$
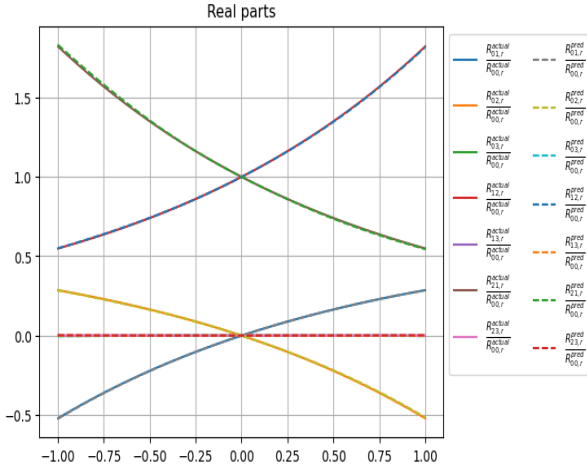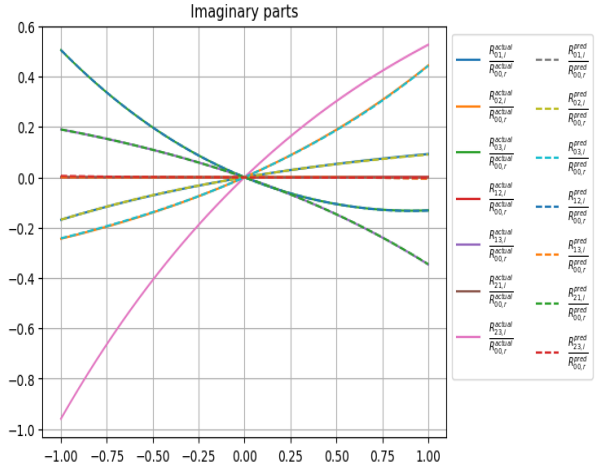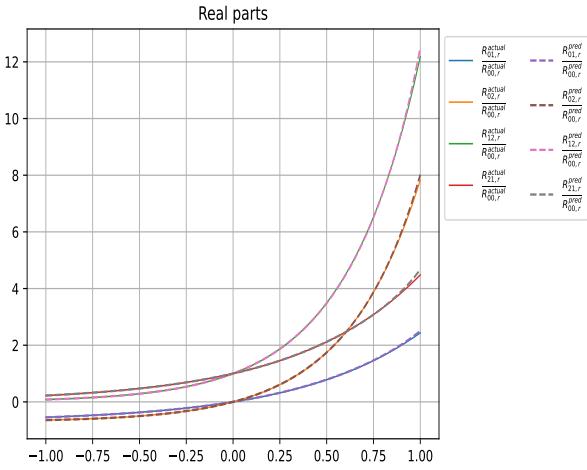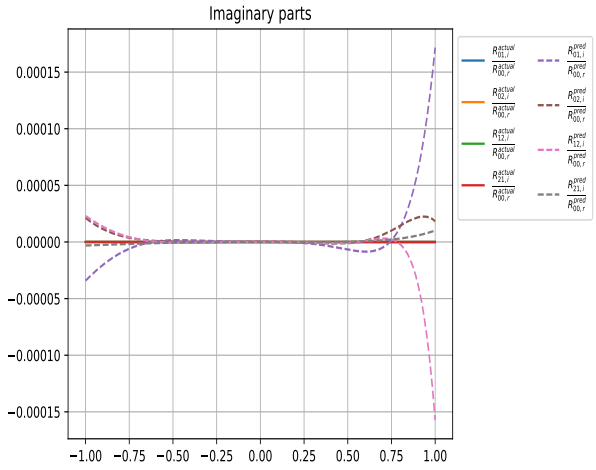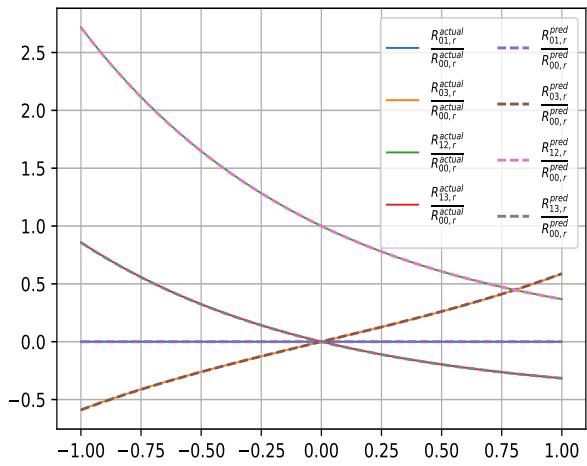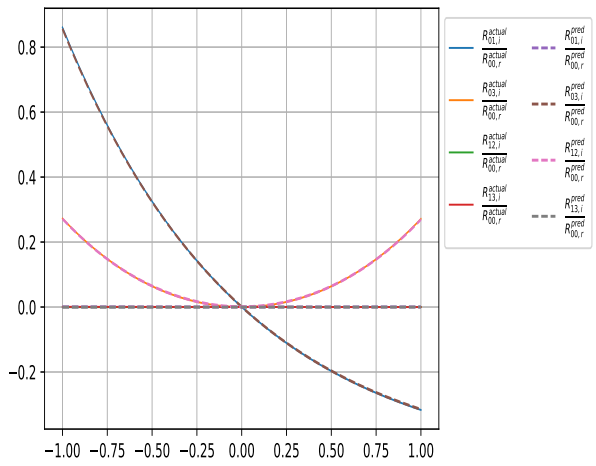
Figure 32: (a,b) class 2, with H_2 parameters $a_1 = -0.6$, $a_2 = 0.381 + 0.123\,i$, $a_3 = 0.447\,i$, $a_4 = 0.7\,i$, $a_5 = -0.3\,i$: real and imaginary parts, (c,d) class 3, with H_2 parameters $a_1 = 1$, $a_2 = 0.5$, $a_3 = 0.7$: real and imaginary parts, (e,f) class 4, with H_2 parameters $a_1 = 0.5$, $a_2 = -0.5\,i$, $a_3 = 0.5$, $a_4 = -0.5$: real and imaginary parts
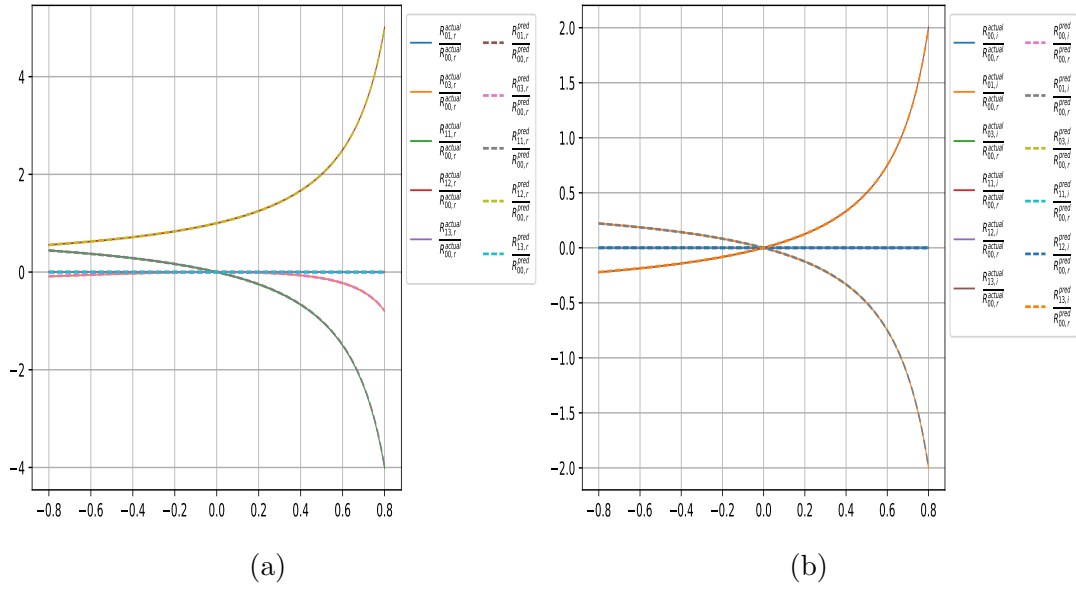
Figure 33: (a,b) class 5, with H_2 parameters $a_1 = -0.5$, $a_2 = -0.5\,i$, $a_3 = -0.5\,i$: real and imaginary parts
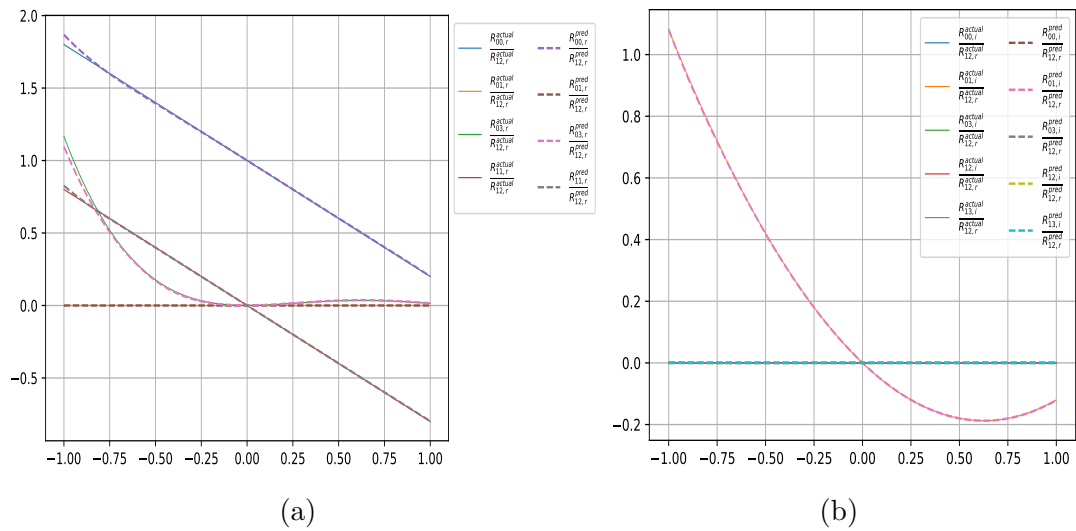
Figure 34: (a,b) class 6, with H_2 parameters $a_1 = -0.4$, $a_2 = -0.6\,i$: real and imaginary parts
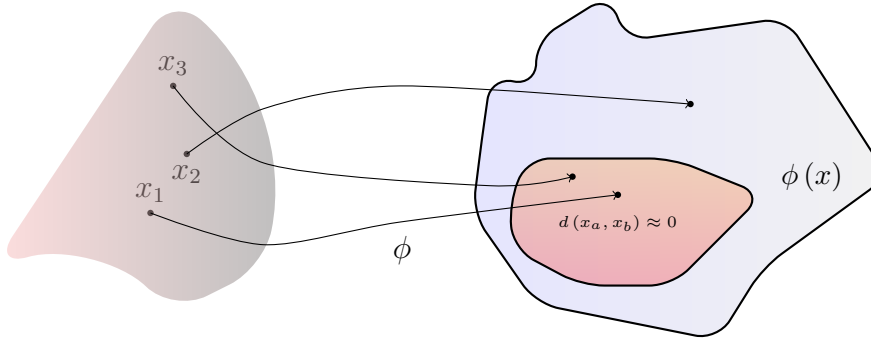
Figure 35: Visualizing the map ϕ which is learnt by the Siamese architecture. The points x_1 and x_3 are similar to each other while x_2 is dissimilar to both of them.

and train the neural network to learn a function $\phi(x) : \mathbb{R}^D \to \mathbb{R}^d$ such that the Euclidean distance between representatives $\phi(x)$ of two input vectors x_1, x_2 that are similar to each other is small, while the distance between dissimilar data is large. Schematically,

$$d(x_a, x_b) = |\phi(x_a) - \phi(x_b)|^2 \approx 0 \qquad \Longleftrightarrow \qquad x_a \sim x_b. \tag{F.2}$$

This is visualized in Figure 35.

There are many loss functions by which such networks may be trained, see for example [140, 141, 142, 143]. For definiteness, we mention the *contrastive loss* function of [140, 141], given by

$$\mathcal{L} = Y d(x_1, x_2) + (1 - Y) \max(r_o - d(x_1, x_2), 0), \tag{F.3}$$

where $Y = 1$ if $x_1 \sim x_2$ and $Y = 0$ otherwise. Clearly this loss function causes the network to learn a function ϕ such that similar inputs x are clustered together while dissimilar inputs are pushed at least a distance r_o apart. This therefore realizes our naive criterion for ϕ laid out in Equation (F.2). We also see very explicitly that the loss function in Equation (F.3) does not directly depend on the values y in contrast to Equation (3.5). Instead, the network is trained to learn a function $\phi(x)$ which obeys a property which is not given point-wise for each input x but instead is expressed as a non-linear constraint (F.2) on $\phi(x)$ evaluated at *two* points x_1 and x_2.

F.1 The Neural Network Architecture and Forward Propagation

We now provide some more details about our implementation of $\mathcal{R}(u)$ and the training done to converge to solutions of the Yang-Baxter equation (1.26) consistent with additional requirements such as regularity (1.27). As already mentioned in Section 6.2, each matrix element $\mathcal{R}_{ij}$ is decomposed into the sum $a_{ij} + i\, b_{ij}$ which are individually modeled by MLPs. In principle each MLP is independent of the rest and can be individually designed. We shall however take all MLPs to contain two hidden layers of 50 neurons each, followed by a single output neuron which is `linear` activated [40]. The possible activations

---

[40] One might also construct an alternate formulation of the neural network where a single MLP of the kind shown in Figure 1 accepts a real input u and outputs all the requisite real scalar functions that comprise $\mathcal{R}(u)$. So far we have observed that such a network does not perform as well as our current formulation of independent neural networks for each real function. Nonetheless, it is possible that this formulation may eventually prove competitive with our current one and the question remains under investigation currently.
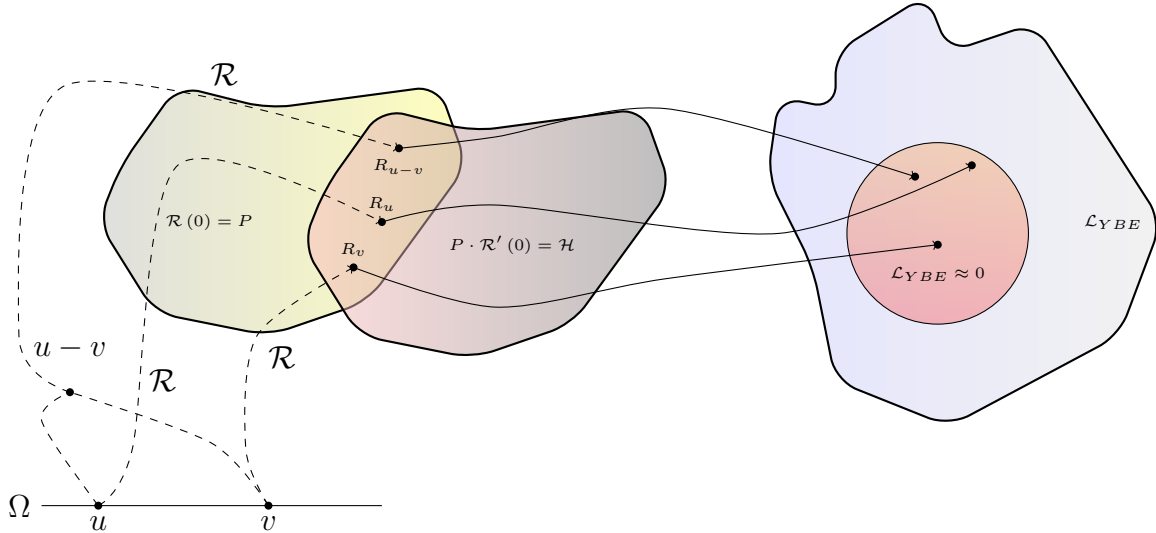
Figure 36: Visualizing the forward propagation of the neural network $\mathcal{R}(u)$. This has a very strong parallel to Figure 35, with the function $\mathcal{R}(u)$ playing the role of the map ϕ. The only difference is that $\mathcal{R}(u)$ also has additional constraints on $\mathcal{R}(0)$ and $\mathcal{R}'(0)$ which are unique to our problem.

for the hidden layers are compared in Appendix F.2 below. To proceed further, note that our loss function involves a term (6.5) which takes arguments $\mathcal{R}(u)$, $\mathcal{R}(v)$ and $\mathcal{R}(u-v)$ where u, v are valued in Ω. This clearly has a very strong parallel with the Siamese Networks introduced above. At least intuitively, one may regard our problem as training a 'triplet' of identical neural networks $\mathcal{R}$ to optimize the loss function (6.5). In addition however, we also have to train the function on loss functions such as (6.10) and (6.11). These constraints, along with the Siamese schematic shown in Figure 35 motivate our design visualized in Figure 36. During the forward propagation we sample a minibatch of u and v values, from which the corresponding $u-v$ is constructed. Next, the $\mathcal{R}$ matrix is constructed at u, v and $u-v$ via Equation (6.4). We also evaluate $\mathcal{R}(0)$ and $\mathcal{R}'(0)$ thus completing the forward propagation. Next, we compute the losses (6.5), (6.10) and (6.11) as well as possibly (6.13). The loss function is trained on by using the `Adam` optimizer [72], with an initial learning rate η of 10^{-3} which is annealed to 10^{-8} in steps of 10^{-1} by monitoring the saturation in the Yang-Baxter loss computed for the validation set over 5-10 epochs. The effect of this annealing in the learning rate is also visible in the training histories in Figures 10 and 37 where the step-wise falls in the losses correspond to the drops in the learning rate. Across the board, training converges in about 100 epochs and is terminated by early stopping.

F.2 Comparing different activation functions

We now turn to a brief comparison of the performance of different activation functions with the above set up. Again for uniformity, we will use one activation throughout for all the MLPs a_{ij} and b_{ij}, but for the output neuron which is linearly activated. We then compared the performance of this neural network architecture while learning the

Activation	Final Yang-Baxter Loss	Final Hamiltonian Loss	Saturation Epoch
sigmoid	2.5×10^{-3}	6.12×10^{-7}	150
tanh	1.90×10^{-4}	5.25×10^{-7}	125
swish	6.49×10^{-5}	1.51×10^{-7}	75
elu	2.75×10^{-4}	5.63×10^{-7}	100
relu	5.52×10^{-4}	4.63×10^{-7}	100

Table 5: Performance of different activation functions on learning the Hamiltonian (F.4). The saturation epoch is the approximate epoch after which the model did not train further. The final values of the Yang-Baxter and Hamiltonian losses after saturation is also mentioned. We observed that the `swish` activation converges sooner and to lower losses. This is stable across multiple runs. See also Figure 37.

Hamiltonian

$$H_{6v,1} = \begin{pmatrix} 0.3 & 0 & 0 & 0 \\ 0 & 0.45 & 0.4 & 0 \\ 0 & 0.25 & 0.6 & 0 \\ 0 & 0 & 0 & 0.3 \end{pmatrix}, \tag{F.4}$$

which is 6-vertex Type 1 in the classification of [118], see Equation (E.2) above. The neural network was trained with the loss functions (6.5), (6.11) and (6.10) and setting λ_H and λ_{reg} to 1 each. The training was carried out for 200 epochs on observing that the networks did not perform better on training for longer. Further, we set a batch size of 16 and optimized using `Adam` with a starting learning rate of 10^{-3} which was annealed to 10^{-8} using the saturation in the Yang-Baxter loss over the validation set as the criterion as mentioned above. We conducted this training using the activations `sigmoid`, `tanh`, `swish`, all of which are holomorphic, as well as `elu` and `relu`. The last two are not holomorphic but have been included for completeness. The evolution of the Yang-Baxter and the Hamiltonian loss for all these activations is shown in Figure 37 and Table 5. On the whole, we see that the `swish` activation tends to outperform the others quite significantly. While these are the results of a single run, we found that the result is consistent across several runs and tasks, leading us to adopt the `swish` activation uniformly across the board for all the analyses shown in this work.
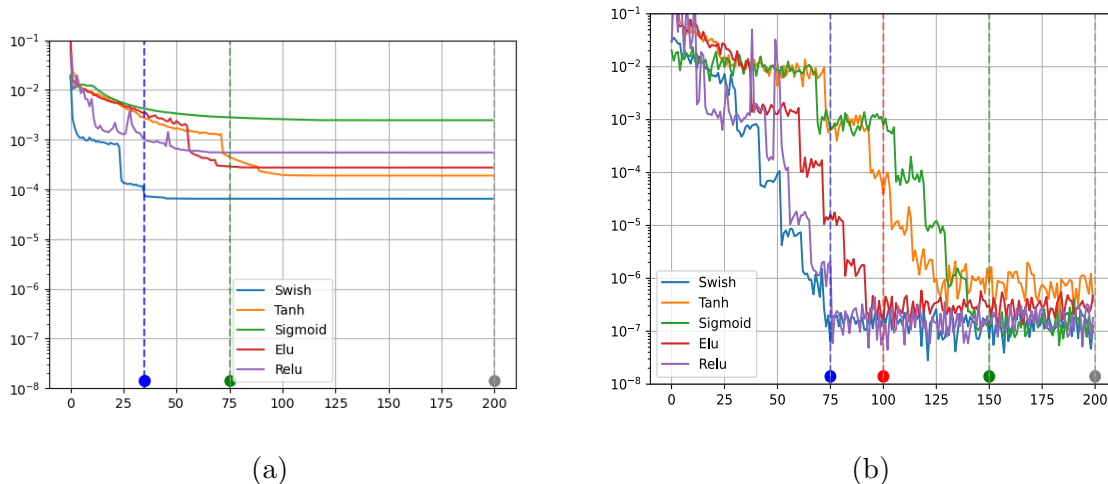
Figure 37: The evolution of the Yang-Baxter loss (left) and the Hamiltonian loss (right) for a variety of activation functions when training for 200 epochs. The swish activation tends to outperform the others. The precise numbers are given in Table 5.

References

[1] J. A. Minahan and K. Zarembo. The Bethe-ansatz for $\mathcal{N} = 4$ super Yang-Mills. JHEP, 0303:013, 2003.

[2] Iosif Bena, Joseph Polchinski, and Radu Roiban. Hidden symmetries of the $AdS_5 \times S^5$ superstring. Phys. Rev., D69:046002, 2004.

[3] R. R. Metsaev and A. A. Tseytlin. Type IIB superstring action in $AdS_5 \times S^5$ background. Nucl. Phys., B533:109–126, 1998.

[4] Diego M. Hofman and Juan M. Maldacena. Giant magnons. J. Phys., A39:13095–13118, 2006.

[5] Gleb Arutyunov, Sergey Frolov, Jan Plefka, and Marija Zamaklar. The off-shell symmetry algebra of the light-cone $AdS_5 \times S^5$ superstring. J. Phys., A40:3583–3606, 2007.

[6] Niklas Beisert and Matthias Staudacher. Long-range $PSU(2, 2|4)$ Bethe ansaetze for gauge theory and strings. Nucl. Phys., B727:1–62, 2005.

[7] Niklas Beisert. The su(2|2) dynamic S-matrix. Adv. Theor. Math. Phys., 12:945–979, 2008.

[8] Niklas Beisert, Burkhard Eden, and Matthias Staudacher. Transcendentality and crossing. J. Stat. Mech., 0701:P01021, 2007.

[9] Thomas Klose. Review of AdS/CFT integrability, Chapter IV.3: $\mathcal{N} = 6$ Chern-Simons and strings on $AdS_4 \times CP^3$. Lett. Math. Phys., 99:401–423, 2010.

[10] A. Babichenko, B. Stefański, jr., and K. Zarembo. Integrability and the AdS_3/CFT_2 correspondence. JHEP, 1003:058, 2010.

109

[11] O. Ohlsson Sax and B. Stefański, jr. Integrability, spin-chains and the AdS$_3$/CFT$_2$ correspondence. JHEP, 1108:029, 2011.

[12] Alessandra Cagnazzo and Konstantin Zarembo. B-field in AdS$_3$/CFT$_2$ correspondence and integrability. JHEP, 1211:133, 2012.

[13] Andrei Babichenko, Amit Dekel, and Olof Ohlsson Sax. Finite-gap equations for strings on AdS$_3 \times$ S$^3 \times$ T^4 with mixed 3-form flux. JHEP, 1411:122, 2014.

[14] Juan Martin Maldacena. The large N limit of superconformal field theories and supergravity. Adv. Theor. Math. Phys., 2:231–252, 1998.

[15] Sergei Gukov, Emil Martinec, Gregory W. Moore, and Andrew Strominger. The search for a holographic dual to AdS$_3 \times$ S$^3 \times$ S$^3 \times$ S^1. Adv. Theor. Math. Phys., 9:435–525, 2005.

[16] Olof Ohlsson Sax and Bogdan Stefański, jr. Closed strings and moduli in AdS$_3$/CFT$_2$. JHEP, 05:101, 2018.

[17] Olivier Babelon, Denis Bernard, and Michel Talon. Introduction to classical integrable systems. Cambridge University Press, 2003.

[18] L. D. Faddeev. How algebraic Bethe ansatz works for integrable model. In Les Houches School of Physics: Astrophysical Sources of Gravitational Radiation, pages pp. 149–219, 5 1996.

[19] M. Lüscher. Volume dependence of the energy spectrum in massive quantum field theories. 1. Stable particle states. Commun. Math. Phys., 104:177, 1986.

[20] M. Lüscher. Volume dependence of the energy spectrum in massive quantum field theories. 2. Scattering states. Commun. Math. Phys., 105:153–188, 1986.

[21] Niklas Beisert et al. Review of AdS/CFT integrability: An overview. Lett. Math. Phys., 99:3–32, 2012.

[22] Stijn J van Tongeren. Introduction to the thermodynamic bethe ansatz. Journal of Physics A: Mathematical and Theoretical, 49(32):323005, 2016.

[23] Gleb Arutyunov and Sergey Frolov. Foundations of the AdS$_5 \times$ S^5 superstring. Part I. J. Phys. A, A42:254003, 2009.

[24] Juan Martin Maldacena and Hirosi Ooguri. Strings in AdS$_3$ and SL$(2, R)$ WZW model. I. J. Math. Phys., 42:2929–2960, 2001.

[25] Andrei Mikhailov and Sakura Schafer-Nameki. Perturbative study of the transfer matrix on the string worldsheet in AdS(5) x S**5. Adv. Theor. Math. Phys., 15(4):913–971, 2011.

[26] Warren Siegel. Hidden local supersymmetry in the supersymmetric particle action. Physics Letters B, 128(6):397–399, 1983.

[27] Michael B Green and John H Schwarz. Covariant description of superstrings. Physics Letters B, 136(5-6):367–370, 1984.

[28] Michael J Duff, T Inami, Kellogg S Stelle, and Paul S Howe. Superstrings in d= 10 from supermembranes in d= 11. Phys. lett. B, 191(CERN-TH-4664-87):70–74, 1987.

[29] David Eliecer Berenstein, Juan Martin Maldacena, and Horatiu Stefan Nastase. Strings in flat space and pp waves from $\mathcal{N} = 4$ super Yang Mills. JHEP, 0204:013, 2002.

[30] S. S. Gubser, I. R. Klebanov, and Alexander M. Polyakov. A semi-classical limit of the gauge/string correspondence. Nucl. Phys., B636:99–114, 2002.

[31] S. Frolov and Arkady A. Tseytlin. Semiclassical quantization of rotating superstring in $AdS_5 \times S^5$. JHEP, 0206:007, 2002.

[32] S. Frolov and A. A. Tseytlin. Multi-spin string solutions in $AdS_5 \times S^5$. Nucl. Phys., B668:77–110, 2003.

[33] V. A. Kazakov, A. Marshakov, J. A. Minahan, and K. Zarembo. Classical/quantum integrability in AdS/CFT. JHEP, 5:24, 2004.

[34] V. A. Kazakov and K. Zarembo. Classical / quantum integrability in non-compact sector of AdS/CFT. JHEP, 0410:060, 2004.

[35] N. Beisert, V. A. Kazakov, K. Sakai, and K. Zarembo. The algebraic curve of classical superstrings on $AdS_5 \times S^5$. Commun. Math. Phys., 263:659–710, 2006.

[36] Sakura Schafer-Nameki. Review of AdS/CFT integrability, Chapter II.4: The spectral curve. Lett. Math. Phys., 99:169–190, 2010.

[37] Changrim Ahn and Rafael I. Nepomechie. Review of AdS/CFT integrability, Chapter III.2: Exact world-sheet S-matrix. Lett. Math. Phys., 99:209–229, 2010.

[38] Pedro Vieira and Dmytro Volin. Review of AdS/CFT integrability, Chapter III.3: The dressing factor. Lett. Math. Phys., 99:231–253, 2012.

[39] Gleb Arutyunov and Sergey Frolov. String hypothesis for the $AdS_5 \times S^5$ mirror. JHEP, 0903:152, 2009.

[40] Gleb Arutyunov and Sergey Frolov. Thermodynamic Bethe ansatz for the $AdS_5 \times S^5$ mirror model. JHEP, 0905:068, 2009.

[41] Gleb Arutyunov, Sergey Frolov, and Ryo Suzuki. Exploring the mirror TBA. JHEP, 1005:031, 2010.

[42] Justin R. David and Bindusar Sahoo. Giant magnons in the D1-D5 system. JHEP, 0807:033, 2008.

[43] Justin R. David and Bindusar Sahoo. S-matrix for magnons in the D1-D5 system. JHEP, 1010:112, 2010.

[44] Per Sundin and Linus Wulff. The low energy limit of the $AdS_3 \times S^3 \times M_4$ spinning string. JHEP, 1310:111, 2013.

[45] Jerome P. Gauntlett, Robert C. Myers, and P. K. Townsend. Supersymmetry of rotating branes. Phys. Rev., D59:025001, 1998.

[46] Thomas Lloyd and Bogdan Stefański, jr. AdS$_3$/CFT$_2$, finite-gap equations and massless modes. JHEP, 1404:179, 2014.

[47] Michael C. Abbott and Inês Aniceto. Macroscopic (and microscopic) massless modes. Nucl. Phys., B894:75–107, 2015.

[48] Olof Ohlsson Sax, Bogdan Stefański, jr., and Alessandro Torrielli. On the massless modes of the AdS$_3$/CFT$_2$ integrable systems. JHEP, 1303:109, 2013.

[49] Marco Baggio, Olof Ohlsson Sax, Alessandro Sfondrini, Bogdan Stefański, jr., and Alessandro Torrielli. Protected string spectrum in AdS$_3$/CFT$_2$ from worldsheet integrability. JHEP, 04:091, 2017.

[50] Suvajit Majumder, Olof Ohlsson Sax, Bogdan Stefański, and Alessandro Torrielli. Protected states in AdS3 backgrounds from integrability. J. Phys. A, 54(41):415401, 2021.

[51] Riccardo Borsato, Olof Ohlsson Sax, and Alessandro Sfondrini. All-loop Bethe ansatz equations for AdS$_3$/CFT$_2$. JHEP, 1304:116, 2013.

[52] Riccardo Borsato, Olof Ohlsson Sax, and Alessandro Sfondrini. A dynamic su(1|1)^2 S-matrix for AdS$_3$/CFT$_2$. JHEP, 1304:113, 2013.

[53] Riccardo Borsato, Olof Ohlsson Sax, Alessandro Sfondrini, Bogdan Stefański, jr., and Alessandro Torrielli. Dressing phases of AdS$_3$/CFT$_2$. Phys. Rev., D88:066004, 2013.

[54] Riccardo Borsato, Olof Ohlsson Sax, Alessandro Sfondrini, Bogdan Stefański, jr., and Alessandro Torrielli. The all-loop integrable spin-chain for strings on AdS$_3$ × S^3 × T^4: the massive sector. JHEP, 1308:043, 2013.

[55] Riccardo Borsato, Olof Ohlsson Sax, Alessandro Sfondrini, and Bogdan Stefański, jr. Towards the all-loop worldsheet S matrix for AdS$_3$ × S^3 × T^4. Phys. Rev. Lett., 113:131601, Sep 2014.

[56] Riccardo Borsato, Olof Ohlsson Sax, Alessandro Sfondrini, and Bogdan Stefański, jr. The complete AdS$_3$ × S^3 × T^4 worldsheet S-matrix. JHEP, 1410:66, 2014.

[57] Thomas Lloyd, Olof Ohlsson Sax, Alessandro Sfondrini, and Bogdan Stefański, jr. The complete worldsheet S matrix of superstrings on AdS$_3$ × S^3 × T^4 with mixed three-form flux. Nucl. Phys., B891:570–612, 2015.

[58] Riccardo Borsato, Olof Ohlsson Sax, Alessandro Sfondrini, and Bogdan Stefański, jr. The AdS$_3$ × S^3 × S^3 × S^1 worldsheet S matrix. J. Phys., A48(41):415401, 2015.

[59] Sergey Frolov and Alessandro Sfondrini. New dressing factors for AdS3/CFT2. JHEP, 04:162, 2022.

[60] Andrea Cavaglià, Simon Ekhammar, Nikolay Gromov, and Paul Ryan. Exploring the Quantum Spectral Curve for AdS$_3$/CFT$_2$. 11 2022.

[61] Sergey Frolov and Alessandro Sfondrini. Massless S matrices for AdS3/CFT2. JHEP, 04:067, 2022.

[62] Mirjam Cvetič, Hong Lü, C. N. Pope, and K. S. Stelle. T-duality in the Green-Schwarz formalism, and the massless/massive IIA duality map. Nucl. Phys., B573:149–176, 2000.

[63] Andrea Dei and Alessandro Sfondrini. Integrable S matrix, mirror TBA and spectrum for the stringy $AdS_3 \times S^3 \times S^3 \times S^1$ WZW model. JHEP, 02:072, 2019.

[64] Riccardo Borsato, Olof Ohlsson Sax, Alessandro Sfondrini, Bogdan Stefański, jr., and Alessandro Torrielli. On the dressing factors, Bethe equations and Yangian symmetry of strings on $AdS_3 \times S^3 \times T^4$. J. Phys., A50(2):024004, 2017.

[65] George Cybenko. Approximation by superpositions of a sigmoidal function. Mathematics of control, signals and systems, 2(4):303–314, 1989.

[66] Kurt Hornik, Maxwell Stinchcombe, and Halbert White. Multilayer feedforward networks are universal approximators. Neural networks, 2(5):359–366, 1989.

[67] Zhou Lu, Hongming Pu, Feicheng Wang, Zhiqiang Hu, and Liwei Wang. The expressive power of neural networks: A view from the width. Advances in neural information processing systems, 30, 2017.

[68] Judy Hoffman, Daniel A Roberts, and Sho Yaida. Robust learning with jacobian regularization.

[69] Sejun Park, Chulhee Yun, Jaeho Lee, and Jinwoo Shin. Minimum width for universal approximation.

[70] Yann LeCun, Léon Bottou, Yoshua Bengio, and Patrick Haffner. Gradient-based learning applied to document recognition. Proceedings of the IEEE, 86(11):2278–2324, 1998.

[71] Alex Krizhevsky, Geoffrey Hinton, et al. Learning multiple layers of features from tiny images. 2009.

[72] Diederik P Kingma and Jimmy Ba. Adam: A method for stochastic optimization.

[73] Giuseppe Bruno De Luca and Eva Silverstein. Born-infeld (bi) for ai: energy-conserving descent (ecd) for optimization. In International Conference on Machine Learning, pages 4918–4936. PMLR, 2022.

[74] G Bruno De Luca, Alice Gatti, and Eva Silverstein. Improving energy conserving descent for machine learning: Theory and practice. arXiv preprint arXiv:2306.00352, 2023.

[75] Maziar Raissi, Paris Perdikaris, and George Em Karniadakis. Physics informed deep learning (part i): Data-driven solutions of nonlinear partial differential equations. 2017.

[76] Maziar Raissi, Paris Perdikaris, and George Em Karniadakis. Physics informed deep learning (part ii): Data-driven solutions of nonlinear partial differential equations. 2017.

[77] Harold Erbin and Atakan Hilmi Fırat. Characterizing 4-string contact interaction using machine learning. arXiv preprint arXiv:2211.09129, 2022.

[78] Alan S Cornell, Anele Ncube, and Gerhard Harmsen. Using physics-informed neural networks to compute quasinormal modes. Physical Review D, 106(12):124047, 2022.

[79] Karan Shah, Patrick Stiller, Nico Hoffmann, and Attila Cangi. Physics-informed neural networks as solvers for the time-dependent schr\" odinger equation. arXiv preprint arXiv:2210.12522, 2022.

[80] Gergely Kántor, Vasilis Niarchos, and Constantinos Papageorgakis. Conformal bootstrap with reinforcement learning. Physical Review D, 105(2):025018, 2022.

[81] Gergely Kántor, Vasilis Niarchos, Constantinos Papageorgakis, and Paul Richmond. 6d (2, 0) bootstrap with the soft-actor-critic algorithm. Physical Review D, 107(2):025005, 2023.

[82] V. Niarchos, C. Papageorgakis, P. Richmond, A. G. Stapleton, and M. Woolley. Bootstrability in Line-Defect CFT with Improved Truncation Methods. 6 2023.

[83] James Halverson, Brent Nelson, and Fabian Ruehle. Branes with brains: exploring string vacua with deep reinforcement learning. Journal of High Energy Physics, 2019(6):1–60, 2019.

[84] Sergei Gukov, James Halverson, Fabian Ruehle, and Piotr Sułkowski. Learning to unknot. Machine Learning: Science and Technology, 2(2):025035, 2021.

[85] VV Sivak, A Eickbusch, B Royer, S Singh, I Tsioutsios, S Ganjam, A Miano, BL Brock, AZ Ding, L Frunzio, et al. Real-time quantum error correction beyond break-even. arXiv preprint arXiv:2211.09116, 2022.

[86] Zoltán Bajnok. Review of AdS/CFT integrability, Chapter III.6: Thermodynamic Bethe ansatz. Lett. Math. Phys., 99:299–320, 2010.

[87] Riccardo Borsato, Olof Ohlsson Sax, Alessandro Sfondrini, and Bogdan Stefański, jr. On the spectrum of $AdS_3 \times S^3 \times T^4$ strings with Ramond-Ramond flux. J. Phys., A49(41):41LT03, 2016.

[88] Jan de Boer. Six-dimensional supergravity on $S^3 \times AdS_3$ and 2d conformal field theory. Nucl. Phys., B548:139–166, 1999.

[89] Lorenz Eberhardt, Matthias R. Gaberdiel, Rajesh Gopakumar, and Wei Li. BPS spectrum on $AdS_3 \times S^3 \times S^3 \times S^1$. JHEP, 03:124, 2017.

[90] Atish Dabholkar and Ari Pakman. Exact chiral ring of AdS_3/CFT_2. Adv. Theor. Math. Phys., 13(2):409–462, 2009.

[91] Marco Baggio, Jan de Boer, and Kyriakos Papadodimas. A non-renormalization theorem for chiral primary 3-point functions. JHEP, 07:137, 2012.

[92] Michael C. Abbott and Inês Aniceto. Massless Lüscher terms and the limitations of the AdS_3 asymptotic Bethe ansatz. Phys. Rev., D93(10):106006, 2016.

[93] Michael C. Abbott and Inês Aniceto. Integrable field theories with an interacting massless sector. Phys. Rev. D, 103(8):086017, 2021.

[94] Diego Bombardelli, Bogdan Stefański, and Alessandro Torrielli. The low-energy limit of AdS$_3$/CFT$_2$ and its TBA. JHEP, 10:177, 2018.

[95] Andrea Fontanella, Olof Ohlsson Sax, Bogdan Stefański, jr., and Alessandro Torrielli. The effectiveness of relativistic invariance in AdS$_3$. JHEP, 07:105, 2019.

[96] Michael B. Green, J.H. Schwarz, and Edward Witten. Superstring Theory. Vol. 1: Introduction. Cambridge University Press, 1987.

[97] B. Hoare, A. Stepanchuk, and A.A. Tseytlin. Giant magnon solution and dispersion relation in string theory in AdS$_3 \times$ S$^3 \times$ T^4 with mixed flux. Nucl. Phys., B879:318–347, 2014.

[98] N. A. Slavnov. Introduction to the nested algebraic Bethe ansatz. SciPost Phys. Lect. Notes, 19:1, 2020.

[99] Justin R. David, Gautam Mandal, and Spenta R. Wadia. Microscopic formulation of black holes in string theory. Phys. Rept., 369:549–686, 2002.

[100] Cumrun Vafa and Edward Witten. A strong coupling test of S duality. Nucl. Phys., B431:3–77, 1994.

[101] Mark A. Walton. The heterotic string on the simplest Calabi-Yau manifold and its orbifold limits. Phys. Rev., D37:377, 1988.

[102] Andrea Fontanella and Alessandro Torrielli. Geometry of massless scattering in integrable superstring. JHEP, 06:116, 2019.

[103] Riccardo Borsato. Integrable strings for AdS/CFT. PhD thesis, Imperial Coll., London, 2015.

[104] S. Yamaguchi, Y. Ishimoto, and K. Sugiyama. AdS(3) / CFT(2) correspondence and space-time N=3 superconformal algebra. JHEP, 02:026, 1999.

[105] Lorenz Eberhardt and Ida G. Zadeh. $\mathcal{N} = (3,3)$ holography on AdS$_3 \times$ (S$^3 \times$ S$^3 \times$ S^1)/$\mathbb{Z}_2$. JHEP, 07:143, 2018.

[106] Linus Wulff. Constraining integrable AdS/CFT with factorized scattering. JHEP, 04:133, 2019.

[107] Heng-Yu Chen, Yang-Hui He, Shailesh Lal, and Suvajit Majumder. Machine learning Lie structures & applications to physics. Phys. Lett. B, 817:136297, 2021.

[108] R. Slansky. Group theory for unified model building. Phys. Rept., 79:1–128, 1981.

[109] Yang-Hui He. Machine-learning the string landscape. Physics Letters B, 774:564–568, 2017.

[110] Rehan Deen, Yang-Hui He, Seung-Joo Lee, and Andre Lukas. Machine learning string standard models. Phys. Rev. D, 105(4):046001, 2022.

[111] Yang-Hui He and Shing-Tung Yau. Graph Laplacians, Riemannian Manifolds and their Machine-Learning. 6 2020.

[112] Brian W Matthews. Comparison of the predicted and observed secondary structure of t4 phage lysozyme. Biochimica et Biophysica Acta (BBA)-Protein Structure, 405(2):442–451, 1975.

[113] Shailesh Lal, Suvajit Majumder, and Evgeny Sobko. The r-matrix net. arXiv preprint arXiv:2304.07247, 2023.

[114] Ziming Liu and Max Tegmark. Machine learning hidden symmetries. Physical Review Letters, 128(18):180201, 2022.

[115] Ziming Liu and Max Tegmark. Machine learning conservation laws from trajectories. Physical Review Letters, 126(18):180604, 2021.

[116] Roberto Bondesan and Austen Lamacraft. Learning symmetries of classical integrable systems.

[117] Sven Krippendorf, Dieter Lust, and Marc Syvaeri. Integrability Ex Machina. Fortsch. Phys., 69(7):2100057, 2021.

[118] Marius De Leeuw, Anton Pribytok, and Paul Ryan. Classifying integrable spin-1/2 chains with nearest neighbour interactions. Journal of Physics A: Mathematical and Theoretical, 52(50):505201, 2019.

[119] Prajit Ramachandran, Barret Zoph, and Quoc V Le. Searching for activation functions.

[120] Kaiming He, Xiangyu Zhang, Shaoqing Ren, and Jian Sun. Deep residual learning for image recognition. pages 770–778, 2016.

[121] MG Tetel'man. Lorentz group for two-dimensional integrable lattice systems. Soviet Journal of Experimental and Theoretical Physics, 55(2):306, 1982.

[122] RS Vieira. Solving and classifying the solutions of the yang-baxter equation through a differential approach. two-state systems. Journal of High Energy Physics, 2018(10):1–50, 2018.

[123] Anna Choromanska, Mikael Henaff, Michael Mathieu, Gérard Ben Arous, and Yann LeCun. The loss surfaces of multilayer networks. pages 192–204, 2015.

[124] Yann N Dauphin, Razvan Pascanu, Caglar Gulcehre, Kyunghyun Cho, Surya Ganguli, and Yoshua Bengio. Identifying and attacking the saddle point problem in high-dimensional non-convex optimization. Advances in neural information processing systems, 27, 2014.

[125] LA Takhtadzhan and Lyudvig D Faddeev. The quantum method of the inverse problem and the heisenberg xyz model. Russian Mathematical Surveys, 34(5):11, 1979.

[126] Shailesh Lal, Suvajit Majumder, and Evgeny Sobko. Drawing the map of integrable spin chains. in progress.

[127] Niklas Beisert and Matthias Staudacher. The n= 4 sym integrable super spin chain. Nuclear Physics B, 670(3):439–463, 2003.

[128] Sergey Frolov and Alessandro Sfondrini. Mirror thermodynamic bethe ansatz for ads3/cft2. Journal of High Energy Physics, 2022(3):1–29, 2022.

[129] Silviu-Marian Udrescu and Max Tegmark. Ai feynman: A physics-inspired method for symbolic regression. Science Advances, 6(16):eaay2631, 2020.

[130] Michael Schmidt and Hod Lipson. Distilling free-form natural laws from experimental data. science, 324(5923):81–85, 2009.

[131] Heng-Yu Chen, Yang-Hui He, Shailesh Lal, and M. Zaid Zaz. Machine Learning Etudes in Conformal Field Theories. 6 2020.

[132] Sebastian J. Wetzel, Roger G. Melko, Joseph Scott, Maysum Panju, and Vijay Ganesh. Discovering symmetry invariants and conserved quantities by interpreting siamese neural networks. Phys. Rev. Res., 2:033499, Sep 2020.

[133] Roy T Forestano, Konstantin T Matchev, Katia Matcheva, Alexander Roman, Eyup Unlu, and Sarunas Verner. Deep learning symmetries and their lie groups, algebras, and subalgebras from first principles.

[134] Robin Quessard, Thomas Barrett, and William Clements. Learning disentangled representations and group structure of dynamical environments. Advances in Neural Information Processing Systems, 33:19727–19737, 2020.

[135] Miguel F. Paulos, Joao Penedones, Jonathan Toledo, Balt C. van Rees, and Pedro Vieira. The S-matrix bootstrap II: two dimensional amplitudes. JHEP, 11:143, 2017.

[136] Yifei He, Andrew Irrgang, and Martin Kruczenski. A note on the S-matrix bootstrap for the 2d O(N) bosonic model. JHEP, 11:093, 2018.

[137] Miguel F. Paulos and Zechuan Zheng. Bounding scattering of charged particles in $1 + 1$ dimensions. JHEP, 05:145, 2020.

[138] Alexander B. Zamolodchikov and Alexei B. Zamolodchikov. Factorized S-matrices in two dimensions as the exact solutions of certain relativistic quantum field models. Annals Phys., 120:253–291, 1979.

[139] Marius De Leeuw, Chiara Paletta, Anton Pribytok, Ana L. Retore, and Alessandro Torrielli. Free Fermions, vertex Hamiltonians, and lower-dimensional AdS/CFT. JHEP, 02:191, 2021.

[140] Jane Bromley, James W Bentz, Léon Bottou, Isabelle Guyon, Yann LeCun, Cliff Moore, Eduard Säckinger, and Roopak Shah. Signature verification using a "siamese" time delay neural network. International Journal of Pattern Recognition and Artificial Intelligence, 7(04):669–688, 1993.

[141] Raia Hadsell, Sumit Chopra, and Yann LeCun. Dimensionality reduction by learning an invariant mapping. 2:1735–1742, 2006.

[142] Gal Chechik, Varun Sharma, Uri Shalit, and Samy Bengio. Large scale online learning of image similarity through ranking. Journal of Machine Learning Research, 11(3), 2010.

[143] Florian Schroff, Dmitry Kalenichenko, and James Philbin. Facenet: A unified embedding for face recognition and clustering. pages 815–823, 2015.